Analysis of wind turbine aerodynamics and aeroelasticity using vortex-based methods

Branlard, Emmanuel Simon Pierre

Publication date:
2015

Document Version
Publisher's PDF, also known as Version of record

Analysis of wind turbine aerodynamics and aeroelasticity using vortex-based methods

DTU Wind Energy PhD Thesis 2015

Emmanuel Branlard
DTU Wind Energy PhD-0052 (EN)
April 2015

DTU Wind Energy
Department of Wind Energy

Author: Emmanuel S.P. Branlard
Title: Analysis of wind turbine aerodynamics and aeroelasticity using vortex based methods

Department: DTU Wind Energy

The dissertation was submitted to the Technical University of Denmark, in partial fulfilment of the requirements for the obtainment of the PhD degree from the PhD School DTU Wind Energy.
The PhD project was carried out between the 1st of April 2012 and the 31st of March 2015 at the Aeroelastic Design Section of DTU Wind Energy, Department of Wind Energy (formerly Risø DTU, Wind Energy Department). The dissertation was submitted on the 1st of April 2015, and successfully defended on the 8th of June 2015.

Main Supervisor:
Mac Gaunaa, DTU Wind Energy

DTU Wind Energy PhD-0052 (EN)
ISBN: 978-87-93278-44-8
Revision: *1.0-109-g915418a*
April 2015

Pages: 218
References: 229
Technical University of Denmark
DTU Wind Energy
Risø Campus
Frederiksborgvej 399
Building 118
DK-4000 Roskilde
ebra@dtu.dk
www.vindenergi.dk

Abstract

Momentum analysis through Blade Element Momentum (BEM) and Computational Fluid Dynamics (CFD) are the two major paths commonly followed for wind turbine aerodynamic and aeroelastic research. Instead, the current PhD thesis focuses on the application of vortex-based methods. Vortex-based methods are understood as both simple vortex models and advanced numerical vortex methods. Prandtl's tip-loss factor and Coleman's yaw model are examples of features that were obtained using simple vortex models and implemented in BEM-based codes. Low-order vortex lattice codes and high-order vortex particle methods have regained interest in wind energy applications over the last two decades. The current work derives and illustrates some of the potential benefits of vortex-based analyses.

The two key wake geometries used in this study to derive simple vortex models are the cylindrical and helical wake models. Both models can be attributed to the work of Joukoswki. They are further studied in this thesis. The cylindrical wake model is detailed for the finite-tip speed ratio case. A superposition of such models is used to investigate the effect of wake rotation. A proper implementation of this effect in BEM codes is suggested. The application to yawed conditions leads to the derivation of a new yaw model applicable in BEM codes. Further applications of the cylindrical wake model considered include the study of unsteady inflow and sheared inflow. The helical wake model is used to derive a new-tip loss factor intended to be used in BEM implementations.

The current thesis also presents the implementation of a vortex code to further investigate wind turbine aerodynamics. The code consists of both low-order and high-order formulations. The implementation features are described and illustrated through different validation cases. Analytical results, measurements and CFD simulations are used for comparison and validation. Low-order methods are used to validate the simple vortex models. The vortex particle method is applied to model a turbulent field and investigate the impact of a wind turbine on the inflow turbulence. The code is coupled to the in-house aero-servo-elastic code in order to obtain a "next generation" aeroelastic simulation tool.

Abstract in Danish

Momentum analyse, som er hjørnestenen i Blade Element Momentum (BEM) beregninsværktøjer, og Computational Fluid Dynamics (CFD) er de to hovedretninger som størstedelen af den vindmølle-aerodynamiske og -aeroelastiske forskning baseres på. Den nærværende PhD afhandling fokuserer i stedet på anvendelsen af hvirvelbaserede metoder. Med hvirvelbaserede metoder menes der både på de simple analytiske hvirvelmodeller og de avancerede numeriske hvirvelmetoder. Prandtl's tip-tabsfaktor og Coleman's yaw model er eksempler på udvidelser af de BEM-baserede beregningsmodeller, der er opstillet ved hjælp af analytiske hvirvelmodeller. Lav-ordens hvirvelbaserede panelkoder (vortex-lattice methods) og højere-ordens hvirvelpartikelmetoder (vortex particle methods) har fået mere opmæksomhed fra forskningsmiljøerne indenfor de sidste to årtier. Den nærværende afhandling illustrerer nogle af de potentielle fordele ved hvirvelbaserede analyser.

De to vigtigste kølvandsgeometrier der i denne undersøgelse er anvendt til at udlede de simplere analytiske hvirvelmodeller er cylindriske og spiralformede kølvandsmodeller. Begge modeller kan spores tilbage til Joukowski. Den cylindriske kølvandsmodel bliver opstillet for et endeligt tiphastighedsforhold. Superposition af sådanne elementarmodeller bruges til at undersøge effekter fra rotation af kølvandet efter rotoren, hvorved en konsistent implementation af denne effekt i BEM baserede koder er udviklet. Applikation af hvirvelmodellen på vindmøller under krøjende forhold har resulteret i udviklingen af en ny krøjeaerodynamikmodel til BEM baserede koder. Yderligere anvendelse af den cylindriske kølvandesmodel omhandler studiet af instationære forhold samt shearet anstrømning. Den spiralformede kølvandsmodel er anvendt til at udlede en ny-tip tabskorrektion til applikation i BEM-baserede koder.

Denne afhandling omhandler også udvikling og implementation af en numerisk hvirvelkode til yderligere analyse af vindmølleaerodynamik. Koden har både lav-ordens og høj-ordens formuleringer af hvirvelelementer. Kodens funktionalitet er beskrevet og illustreret gennem forskellige valideringstilfælde, hvor analytiske resultater, måledata samt CFD simuleringer er blevet brugt til sammenligning og validering. Analytiske hvirvelmodeller er anvendt til validere de simplere hvirvel modeller i koden. Partikelversionen af hvirvelmetoden er anvendt til at modellere en turbulent indstrømning og undersøge effekten af en vindmølle på den indstrømmende turbulens. Koden er derudover koblet til DTU's aero-servoelastiske kode for herved at opnå et "next generation" aeroservoelastisk simuleringsværktøj.

Contents

Abstract i
Introduction v
Dissemination during the period of the PhD xiii
Aknowledgments xvi
List of symbols xviii

I Vortex models for rotors in uniform inflow

1 Cylindrical vortex model for finite and infinite tip-speed ratios 3
2 Superposition of cylindrical models - Effect of wake rotation 9
3 Helical vortex model applied to tip-losses 15

II Vortex models for rotors in yaw

4 Yaw-modeling using a skewed vortex cylinder model 23
5 Simple implementation of a new yaw model 29
6 Advanced implementation of the yaw model - Pre-study 35

III Vortex models for rotors in shear and unsteady inflow

7 Shear-model of Gaunaa et al. 43
8 Model for unsteady circulation and inflow 47

IV Implementation of a vortex code for aero-elastic simulations

9 Description of the implemented vortex code 53
10 Vortex code validation and illustration 63
11 Examples of wind energy validation cases 69

V Vortex methods for complex inflow and aero-elastic simulations

12 Reconstruction of a velocity field using vortex particles 77
13 Effect of wind turbines on the turbulent inflow 83
14 Aeroelastic simulation of a wind turbine under turbulent and sheared conditions 89

VI Final remarks and Bibliography

Conclusion 97
References 102

VII Appendices

A Vortex cylinders and vortex disk 123
B Helical vortex filaments 147
C Kutta-Joukowski theorem applied to a rotor with straight lifting lines 151
D Vortex theory for rotors: Helical wake, optimal circulation, tip-losses and wake expansion . 157
E Right cylindrical vortex model applied to wind energy - Complements 181
F Application of the helical and cylindrical models - comparison with Actuator disk 189

Introduction

This thesis summarizes the work of the author during a three year PhD project performed at the "Aero-Elastic Design" (AED) section of the Wind Energy department of the Technical University of Denmark (DTU) from the 1st of April 2012 to the 31st of March 2015. The project was entitled: "Analysis of wind turbine aerodynamics and aeroelasticity using vortex-based methods". The topic is further introduced below. Paragraphs marked with an asterix (∗) are un-conventional but slightly more human since they are the manifestation of the author taking liberties and pleasure in writing this introduction. They can be safely skipped.

(∗) **Where to start •** Four questions are hidden in the title of this paragraph depending on what the symbol "•" stands for: "the writing of this thesis", "this PhD project", "if you read this thesis and are disappointed it doesn't cover all what the title promise", "if you are new to the field". The first question is now implicitely answered. The three remaining questions are addressed in this paragraph by suggesting four sources of information. The author is constantly learning from the first two of them. First, a list of references most cited in this thesis is given in table 1. The list gives an indication of the work on which this thesis is built on. Second, a list of reference books associated to each of the keyword of the PhD title is given in table 2. None of the content of this thesis could supplement the reading of the references mentioned in these two tables. Third, a summary of the understanding of the field by the author was written in a separate document [21]: The reading of this document can be seen as a starting point to the reading of this thesis for someone with a wind-energy aerodynamics background. Last, the following paragraph introduces the main notions used.

(∗) **Main notions involved** This paragraph attemps to introduce a simplified description of the different notions and methods used in this thesis.
The notions of vortex and vorticity are strongly linked. *Vorticity* is a measure of the local rotation of a fluid particle. A *vortex* represents a coherent flow structure which can be characterized by a large scale rotation of the fluid. A tornado can be thought as an example of a 3D vortex of tubular shape. If one could imagine that there is such a thing as an ideal tornado, then one could picture the air rotating in a perfectly circular motion around it. Far from it, the rotation should be zero since a tornado is only felt in a local area. The velocity can then be thought to be inversely proportional to the distance to the tornado center. If this is the case though, the velocities near the core would reach infinity. *Viscous forces* prevent this and a physical solution is reached where the velocity smoothly drops to zero at the center. It can be shown that in this case the vorticity is zero everywhere except close to the core of the tornado. This is a property which may come as a surprise if one forgets that vorticity measures a local rotation and not a global rotation.
Circulation is an integrated value of vorticity over an open surface, say a disk. One could simplify the tornado further by concentrating all the vorticity carried in the core into a straight vertical tube such that the circulation of a cross section of the core and a cross section of the tube have the same value of circulation. Reducing the cross section of the tube to a point while keeping the circulation constant results in a straight vertical line that contains all the vorticity. In this idealization process, the area where the viscous forces were taking place has been reduced to zero and the resulting velocity field does tend to infinity towards the center. This can be seen as the price one has to pay when too much simplicity is sought: *inviscid* solutions do not have the physical smoothness we are used to. The gain is great though since outside of the area where viscosity is

Table 1: List of most cited references in this thesis

Reference		Citations
Hansen 2008	[79]	25
Cottet and Koumoutsakos 2000	[52]	18
Okulov and Sørensen 2008	[150]	14
Burton et al. 2002	[34]	12
Katz and Plotkin 2001	[96]	12
Coleman et al. 1945	[46]	12
Wald 2006	[218]	11
Voutsinas 2006	[217]	11
Goldstein 1929	[72]	11
Winckelmans and Leonard 1993	[221]	10
Saffman 1992	[170]	8
Glauert 1935	[71]	8
Gaunaa et al. 2015	[67]	8
Theodorsen 1948	[203]	7
Lewis 1991	[116]	7
Batchelor 1967	[9]	7
Wrench 1957	[223]	6
Burton et al. 2011	[35]	6
Winckelmans 2004	[220]	6
Papadakis 2014	[155]	6
Øye 1990	[152]	6
Hejlesen et al. 2013	[84]	6
van Garrel 2003	[211]	6
Beale and Majda 1985	[12]	6
Beale and Majda 2011	[13]	6

Table generated with:

```
cat *.aux|grep -oPoPoP '(?<=\\citation\{).*(?=\})'|tr , '\n'|sort|uniq -c|
    sort -nr|grep -v branlard|head -25|awk '{print "\\citeAY{"$2"}&\\cite{"$2
    "}&"$1"\\\\"}'>RefList.tex
```

known to be at play, the results from the simplified model are valid to a high degree and most of the time can be obtained at a lower cost. The velocity field of this idealized model can be determined from the knowledge of the vorticity strength by means of the *Biot-Savart law*. Under the context of applicability of this law, there is a causal link between vorticity and velocity and one will talk of velocity *induced* by the vorticity. The current thesis will greatly make use of this idealization approach. In most contexts, the terms vortex and vorticity will be blurred together in light of the idealized-vortex/concentrated-vorticity tornado example.

Vorticity is present at every scale of fluids: in the agitations of heated molecules, in the wake of a tea spoon, in the turbulent eddies of the sea or atmosphere, up to the plasma and gas motion in the formation of a star. Certainly it can be found in the wind energy context.

Let us first consider the wind on planet Earth. The atmosphere is heated by the sun and is cooled by radiation to outer space. Difference of temperatures in the atmosphere implies difference of pressure and air density. Just like the air flows out of a pressure cooker, the wind tends to flow from areas of high pressure to areas of low pressure in the atmosphere. Since the wind does not go through the ground and is zero inside the earth, the velocity at its boundary has to drop smoothly to zero. This once again is the effect of the viscous forces that drag down the wind velocity near

Table 2: Reference books used and suggested by the author for each of the keyword of the PhD title

Keyword	Reference book	
Wind turbines	Burton et al. 2011	[34]
Wind turbines	Manwell et al. 2003	[133]
Aerodynamics	Lamb 1932	[108]
Aerodynamics	Batchelor 1967	[9]
Wind turbines aerodynamics	Hansen 2008	[79]
Aeroelasticity	Bisplinghoff et al. 1996	[18]
Vorticity	Saffman 1992	[170]
Vortex methods	Cottet and Koumoutsakos 2000	[52]
Vortex methods	Katz and Plotkin 2001	[96]

the boundary. The region where this effect predominates is called the *boundary layer*. The fact that the wind velocity is not uniform but drops to zero will be referred to as *shear*. A shear is associated with vorticity generation, a bit like pushing a shopping cart with one arm stronger than the other will make the cart rotate, the difference of wind speed with height makes the fluid particles rotate. The boundary layer is characterized by a mean shear profile, but perturbations about the mean are to be expected. The perturbations can be due for instance to: changes of temperature in the atmosphere, obstacles for the wind or the roughness and the temperature of the ground and water surfaces. A perturbed pendulum will eventually stop due to the friction of the air. Similarly, a perturbation, or an irregular displacement of the air at any scale will progressively decay under the effect of viscous diffusion. Yet, the sources of perturbations being so numerous and the viscosity having only limited power, the atmospheric flow field is constantly in a perturbed state. The perturbations in the velocity field are called *turbulence*. A turbulent field contains large and small scale vortex structures depending on the source of perturbation and the age of the perturbation. The presence of shear facilitates the propagation of perturbations and gives more energy to turbulence. Shear and turbulence are the two main components that affects the wind experienced by a wind-turbine. The vertical wind-direction change induced by the Coriolis force and referred to as *veer* is a third one.
Just like planet Earth, a wind turbine is a solid that does not let the wind pass through it. Boundary layers are present on all the wind turbine surfaces exposed to the wind and each of them contributes to adding vorticity to the wind. The difference is that the wind turbine is immersed in the wind and thus there is a continuation of the boundary layers after the surfaces, named *wakes*. The airfoils forming the blades play a special role. The idealization procedure applied to an airfoil will condense the vorticity contained within the boundary layer and reduce it to the surface of the airfoil. The vorticity in the wake would be condensed into a vortex sheet. The vorticity carried by the airfoil is referred to as the *bound vorticity*. This vorticity at the boundary of the body is a *generalized vorticity* since it is of different nature than the one defined within the fluid. In a *steady* case, the vorticity in the wake is only composed of one component which is referred to as *trailed vorticity*. In an *unsteady* case, a change of configuration of the airfoil with time will result in a change of its boundary layer and thus a change of generalized vorticity. This change of vorticity, called *shed vorticity* should exit the airfoil. This release naturally occurs at a point of least resistance and can be assume to merge with the wake vortex sheet behind the airfoil. The turbine wake tends to roll-up around the stronger vortices, which are usually generated around the tip and root of the blade. This information can be used to further simplify the wake vorticity model. Just like the tornado, the airfoil can be simplified down to a vortex surface or a vortex line. Further simplifications can be obtained by assuming that the turbine has an infinite number of blades. The rotors is then modelled by an *actuator disk* (AD) of vorticity.

The air molecules impact and induce friction on the wind turbine blades. Both actions from the inflow produce an integrated aerodynamic force. This force is decomposed into two components perpendicular and parallel to the inflow, respectively called the *lift* and *drag* forces. In an inviscid approach, the vorticity carried by the airfoil is responsible for the lift force and the relation between the airfoil circulation and the steady lift force is given by the *Kutta-Joukowski* (KJ) relation. The effective work of the aerodynamic forces is used to rotate the turbine and generate electricity. The source of this energy is the kinetic energy of the wind. The fact that the wind turbine extracts energy from the wind implies a reduction of the wind speed upstream and downstream of the turbine. This velocity reduction can be understood in a vorticity formulation as the effect induced by the bound and wake vorticity. The deformation of the turbine under the effect of the aerodynamic forces is referred to as an *aero-elastic* response. Most aero-elastic investigations are unsteady.
By idealizing the bodies with concentrated vorticity, it was shown that the entire problem of a wind turbine and its inflow can be characterized by vorticity. The current thesis will make use of this aspect.

Vortex-based methods The notion of vortex-based methods, as understood by the author and his supervisor, needs clarification before further presentation of the topic. Vortex-based methods focus on the generation and tracking of vorticity (ω) as opposed to *conventional* fluid dynamics formulations that solve for the velocity (u) and pressure (p). Another example of non-conventional formulation is given by *spectral methods*. All approaches are mathematically equivalent under the same assumptions. Simple u-p analyses of actuator disks are referred to as *momentum theory* by the community. Algorithms have been devised based on these analyses leading to the development of *Blade Element Momentum* (BEM) codes which are widely used for aero-elastic wind turbine design. Grid-based implementation of advanced velocity-pressure formulations will be further referred to as traditional or conventional *computational fluid dynamics* (CFD) codes. As mentioned in the previous paragraph, a vortex is a coherent structure of the flow which is partially characterized by a strong value of vorticity. Most vortex methods deals with elementary functions which produces a flow that can be assimilated, mathematically or physically, to an elementary vortex. This probably explains why the term "vortex methods" was historically retained compared to a more correct appellation such as "vorticity-based methods". The scientific community working in the field traditionally uses the term "vortex methods" to refer to high-order Lagrangian particle methods. Particle methods offers great advantages for performing long-term simulations of high-accuracy thanks to, e.g., the implementation of remeshing techniques and viscous effects. Vortex lattice methods using vorticity segments cannot handle these effects in an easy way since they require a handling of the connectivity between elements. Simple vortex lattice methods made of rectilinear segments are thus regarded as low-order methods, and the term "vortex-model" is sometimes preferred by the community of high-order vortex methods. In the current thesis, this distinction will not be made and the above definition of "vortex-model" will not be adopted. Instead, the terms "vortex-model" and "vortex-theory" will be used indifferently to refer to even lower order methods, viz.: methods that simplify a problem using prescribed vorticity support of simple geometrical shapes. The numerical complexity of vortex models is null or negligible compared to the one of vortex methods. The term "vortex-based methods" will be used in this thesis to cover both "vortex methods" and "vortex models".

Justification of the PhD topic Before detailing the scope of the topic, its justification as a research topic is presented.
Curiosity (& Co.) Curiosity is the main factor that drove this investigation. Knowledge's sake, if ethical, is believed to be enough of a justification to the author for a research topic. Economical justifications follows from the fact that a better understanding of wind turbine aerodynamics and

aeroelasticity will result in the development of better-suited and cheaper wind turbines and participate to the reduction of the cost of energy. Environmental motives are indirect justifications but direct motivations. As mentioned above, the choice of using vortex-based analysis is a key to make this research topic unique. Main justifications of this choice follow.

A good alternative. BEM codes and conventional CFD codes are the two major paths that are currently followed for wind turbine aerodynamic and aeroelastic research. Vorticity has to be expressed into velocity gradients in a *u-p* formulation. The vortices are then exposed to numerical diffusion when a grid-based CFD method is used. Lagrangian vortex methods on the other hand are known to present less diffusion of vorticity [52]. In a problem where many vortices are present (turbulence, turbine wakes), it appears of interest to have vorticity as primary variable and use grid free numerical methods. Lagrangian vortex methods offer both options. Furthermore, classical aerodynamic theories like the lifting line or lifting surface ones, are also formulated in terms of vorticity and thus the presence of a wind turbine can be readily introduced in a unified vorticity way. Vortex-based methods have been extensively used in aircraft and helicopter aerodynamics but to a lesser degree within wind turbine research. Inviscid panel methods and lifting line codes have been used for many years for aircraft and helicopter modelling [113]. Wind energy applications differs from the fact that induced velocities in the wake keep the vorticity close to the rotor. The accuracy of the near-wake description is thus of greater importance than for helicopter and aircrafts. Vortex theory has been used to derive key results of wind turbine aerodynamics and derive simple engineering models used in BEM codes. Vortex methods have regained interest in wind energy applications over the last two decades (see [80]). Yet, vortex-based methods have not been used to their fullest.

Compromises. A wide range of formulations are possible in vortex methods and different level of complexity and accuracy may be achieved [52]: At a similar computational cost, a cylindrical vortex wake model gives results similar to those of a BEM code [**26**], and high-order vortex methods can reach accuracy of the same order as traditional CFD or spectral methods [53, 222, 225].

Low-order vortex methods on the other hand can be seen as an intermediate between BEM and CFD codes: They offer the possibility to introduce compromises such that their computational cost is lower than for CFD codes while the actual physics are better resolved than in the case of the computationally lighter BEM-based codes. Examples of compromises are for instance: representing a 3D wing by a lifting surface or a lifting line, simplifying the far-wake of an object by simple vortex elements such as vortex points or a vortex cylinder, assuming a prescribed vorticity support, etc. This trade-off between computational time and physical modelling allows low-order vortex methods to be used for optimizations. The key drivers can then be identified before using higher-order fidelity tools. The broad spectrum of compromises possible with vortex-based methods is one of its key advantage.

Causality. Vortex theory and low-order vortex methods offer the possibility to pinpoint driving mechanisms and separate effects within different physical phenomena. Indeed, as previously mentioned, the Biot-Savart law introduces a mathematical and causal link between vorticity and velocity. A given vorticity patch *induces* a velocity field in the entire domain and may be identified as the source explaining a given observed phenomenon. For example, one can identify the effect of the shed and trailed vorticity behind a wing separately, or the effect of tangential and longitudinal vorticity of a wind turbine wake. This approach yields to a better understanding of many situations for both steady and unsteady rotor aerodynamics. With this better understanding of the physics at play, vortex-based methods can open up possibilities for improving existing models and developing new models for BEM-based codes.

BEM codes extensions As mentioned above, the physical modelling and the computational time requirement of low-order vortex codes may be seen as a compromise between the ones of BEM codes and the traditional CFD codes. Performance of low-order lifting-line codes have shown

to give results within the same range of accuracy as BEM codes [174, 76, 28] but it is usually difficult to prove better performance. The physical modelling of such vortex codes is of greater complexity but they usually suffer from their singular behavior and results are usually dependent on the choice of the viscous core model [209]. Higher-order vortex methods do not present this problem. For unsteady flow, non-uniform inflow or yawed cases, BEM-based codes rely to a high degree on empirical correlations. The knowledge that can be extracted using vortex methods can be used to improve existing engineering design-and-analysis models, which are mostly based on BEM theory. Vortex methods of any-order furthermore allow the investigation of the effects of sweep and non-planar rotors, which is impossible with the BEM-based tools currently used. Also, since most structural codes currently rely on BEM methods for their aerodynamic computations, a significant improvement can be obtained by coupling them with a vortex code for advanced aeroelastic studies.

Topic and main objectives The PhD topic offers many possible applications and the chosen fields of investigation need to be further defined. The scope of the study was restrained in the early stage of the PhD. The description, taken from the PhD application, is given below.

> The aim of the project is to investigate the potential gain one can obtain from vortex-based analysis as opposed to traditional analysis. The PhD project should focus on the implementation of a flexible vortex-based code and the development of mathematical models which should be used to investigate fundamental issues and phenomena linked to steady and unsteady wind turbine aerodynamics. Specifically, operation in the computationally challenging unsteady conditions of yaw, shear and turbulent inflow are defined as the field of application of this work. The overall goals of the project are threefold:
>
> 1. Developing and implementing a flexible, unsteady vortex-based aerodynamic model to investigate the unsteady effects of yaw, shear and turbulent inflow.
> 2. Coupling this model to the structural model in *HAWC2* [110] to obtain a "next generation" aeroelastic simulation tool.
> 3. Analysis of the predicted rotor aerodynamics for cases with yaw, shear and turbulent inflow with the aim of using vortex code results and results from simple models in order to improve engineering BEM based models.

Approach chosen In the early literature-review stage of the PhD it was assessed that the implementation of a high-order vortex code would take a significant amount of programming time since the implementation would have to start from scratch. Furthermore, at the early stage of the PhD, high-order vortex methods appeared really hard to comprehend and the author had to admit that it would be unrealistic to expect to contribute to the field of vortex methods (e.g. implementing a new solver, using new projection functions, different divergence-free corrections, etc.) without drifting away from the wind-turbine topic. Instead, it was chosen to implement a flexible low-order code in order to fulfill the two first aims of the PhD presented in the previous paragraph as early as possible. Even then, the contribution to the field would imply a strong dedication since medium-to-low order vortex codes were already coupled to aeroelastic codes, as e.g. the coupling of GAST and GenUVP developed by NTUA [168, 132] or the use of a mixed vortex-filaments/vortex-rings code by NTNU [57]. The rest of the time would be used to focus on the third goal: apply vortex-based methods to the specific topics of yaw, shear and turbulence. The two key advantages of vortex-based methods to the author's opinion, namely compromises and causality, would then be exploited for these analyses. It was thought it would be more realistic to contribute to the field by using this approach rather than doing direct application of the vortex code to the different fields since the former is less common than the latter.

(∗) **What really happened** Let us set I = *the author* in this paragraph. I chose to alternate between the different goals and topics in a difficult attempt to discuss them all. The first few months of the PhD were dedicated to a literature review on vortex theory. The reading of the book of Theodorsen [203] and the article of Wrench [223] led to the continuation of a previous work **[20, 28]** on the topic of optimal circulation (unpublished but given in Appendix D) and tip-losses **[22]**. The implementation of the low-order vortex code and its coupling to *HAWC2* followed within the first year of the project. Then, the topic of yaw was chosen as a first field of investigation. The discovery of the article of Coleman et al. [46] was illuminating: It raised interest into the derivations of vortex theory results related to vortex rings and vortex cylinders. It appeared possible to contribute to existing work by focusing on the case of finite tip-speed ratio, both for right and skewed cylinders. This led to a study of nine months on the topic. On the side, I worked in collaboration with a colleague from the department DTU Compute in order to parallelize the $O(N^2)$ part of the vortex code with MPI and GPU technologies. After nine months, the vortex code reached a computational time low-enough to perform long term simulations. It was thus chosen to take a break from vortex theory and focus on the vortex code. To my opinion, one disadvantage of low-order vortex methods was the singular behavior and the absence of viscosity handling. One month and a half were dedicated to implement different viscous models and compare the results to actuator disk simulations. Turbulent simulations were also performed using the wind module of *HAWC2*. Satisfying results were obtained with the low-order vortex code but I realized that high-order vortex particles methods would be required to further perform viscous and turbulent simulations with high-accuracy. Another one month and a half was dedicated to set up and investigate a BEM yaw model based on the vortex theory results obtained from a skewed vortex cylinder. The study revealed that a superposition of cylinders would potentially improve the results. I thus returned to "vortex-theory" analysis to investigate the possibility to use a superposition of vortex cylinders. The case of right cylinders were considered first. At a time corresponding to about 2 years and two months into the PhD, a master student started a six months project in view of accelerating the vortex code by implementing a tree-code algorithm for the vortex particles interaction. At this stage of the PhD, the topic of shear had still not been investigated. Fortunately, I got involved in a vortex model work on the topic by my supervisor and briefly contributed. Later attempts to investigate shear using low-order vortex methods revealed difficult: Such investigation requires a proper account of the boundary conditions since the support of the shear vorticity is infinite but the computational domain is finite. The topic of shear was thus put aside, waiting to see if time will remain in the PhD to implement a high-order particle vortex code with a Poisson solver that could be used to satisfy such boundary conditions. In the mean time, the work on the superposition of cylinders led to the idea of using the model for simple unsteady simulations. I then had the opportunity to visit the department of Gregoire Winckelmans at the University Catholic of Louvain, Belgium, whose group focuses on high-order vortex methods. This visit further convinced me on the need to use high-order particle methods. I stayed one month at the University of Victoria, Canada, and focused on learning and implementing tools needed by 2D high-order vortex methods. I then had the great opportunity to visit the department of professor Spyros Voutsinas at NTUA, Greece, for a period of one month. During this period, I worked on applying the newly implemented tree-code to study the impact of a wind turbine on turbulence using vortex particles. A month was then dedicated to the writing of this thesis. After that, I visited NTUA again to work on the topic of shear. I was given access to a Poisson solver developed at NTUA to perform efficient particle-mesh simulations. The solver was coupled with the vortex code during this period. Due to time constraint though, the study on the topic of shear and turbulence had to be performed using the tree-algorithm and not the Poisson solver. The remaining two weeks of the PhD were dedicated to reviewing and shortening the text of the appendix. The thesis was delivered on the serious date of the 1st of April 2015.

Structure of the document The main corpus of the PhD thesis will focus on the contributions of the author. Background information necessary to apprehend the different vortex models and vortex code features were gathered in a different document [21]. The appendix features extra details that complement the results given in the different publications. Significantly less time was dedicated to the appendix than to the work of the different publications.
The main corpus consists in six parts, each part being divided into 2 to 3 chapters, each chapter consisting in 4 pages (except for chapter 9, and only for the a4-version). The chapters have a limited scope and it was chosen to keep the literature reviews within each chapter instead of gathering all of them into an introductory part. Most chapters correspond to a publication. The article is mentioned at the beginning of the chapter when it is the case. The literature review and conclusions are directly taken from the publication with slight modifications to ensure the cohesion of the thesis. To futher reduce the length of this thesis, only the key results of the papers are developed in the corpus with limited details. For further concision, the information given in figure captions is not repeated in the text.
The three first parts are dedicated to vortex models and are divided according to the different flow situations investigated, namely: uniform inflow, yawed inflow, sheared inflow and unsteady inflow. The fourth part introduces the vortex code implemented, the choices made and the validation cases run. The vortex code is yet used in parts *I* to *II* and careful reference to the implementations of part *IV* are made. Part *V* focuses on advanced applications of the vortex code. The last part of the corpus summarize the conclusions and envisages future work topics.

Dissemination during the period of the PhD

Publications during the period of the PhD

The symbol • refers to publications published or accepted while publications in parentheses were submitted before the 1stst of April 2015.

Publications directly related to this thesis:

Journal

(•) Branlard, E., Gaunaa, M, Machefaux, E., Mercier, P., Voutsinas, S.
'Impact of a wind turbine on turbulence: un-freezing the turbulence by means of a simple vortex particle approach'
Submitted to *Journal of Wind Engineering and Industrial Aerodynamics* in February 2015 [25]

(•) Gaunaa, M., Troldborg N., Branlard E.
'Modelling the influence of wind shear using a simple vortex rotor model'
To be submitted to *Wind Energy* in March 2015 [67]

- Branlard, E., Gaunaa, M
'Superposition of vortex cylinders for steady and unsteady simulation of rotors of finite tip-speed ratio'
In: *Wind Energy*, doi:10.1002/we.1899, 2015. [26]
- Branlard, E., Gaunaa, M
'Cylindrical vortex wake model: skewed cylinder, application to yawed or tilted rotors'
In: *Wind Energy*, doi:10.1002/we.1838, 2015, [24]
- Branlard, E., Gaunaa, M
'Cylindrical vortex wake model: right cylinder'
In: *Wind Energy*, vol 524, no. 1, 2014. [23]

Journal - Conference series

- Branlard, E., Gaunaa, M. Machefaux, E.
'Aeroelastic large eddy simulations using vortex methods: un-frozen turbulent and sheared inflow'
In: *Journal of Physics: Conference Series* (Online), vol 625, 2015. [31]
- Branlard, E., Gaunaa, M. Machefaux, E.
'Investigation of a new model accounting for rotors of finite tip-speed ratio in yaw or tilt'
In: *Journal of Physics: Conference Series* (Online), vol 524, no. 1, 2014. [29]
- Branlard, E, Gaunaa, M.
'Development of new tip-loss corrections based on vortex theory and vortex methods'
In: *Journal of Physics: Conference Series* (Online), vol 555, 2014. [22]

Conference

- Branlard, E., Machefaux E., Gaunaa M., Brandenborg Sørensen H.H., Troldborg N.
'Validation of vortex code viscous models using lidar wake measurements and CFD'
In: *Proceedings of EWEA 2014 - European Wind Energy Conference & Exhibition*, 2014. [30]

Publications indirectly related to this thesis:

Journal

- Branlard, E., Dixon, K, Gaunaa, M.
  'Vortex methods to answer the need for improved understanding and modelling of tip-loss factors'
  In: *IET Renewable Power Generation* - Special Issue: EWEA 2012, 2013. [28]

Conference

- Branlard, E, Dixon, K, Gaunaa, M.
  'An improved tip-loss correction based on vortex code results'
  In: *Proceedings of EWEA 2012 - European Wind Energy Conference & Exhibition*, 2012. [27]

Publications on a different topic:

Journal

- Branlard, E, Pedersen, AT, Mann, J, Angelou, N, Fischer, A, Mikkelsen, T, Harris, M, Slinger, C & Montes, BF
  'Retrieving wind statistics from average spectrum of continuous-wave lidar'
  In: *Atmospheric Measurement Techniques*, vol 6, pp. 1673-1683, 2013. [32]

Conferences - Symposia

- 2012 - European Wind Energy Conference & Exhibition - Poster
- 2012 - The science of making torque from wind - Poster
- 2013 - North American Wind Energy Association Symposium - Oral Presentation
- 2014 - European Wind Energy Conference & Exhibition - Poster
- 2014 - The science of making torque from wind - Oral presentation

External stays

- 2014 - Sustainable Systems Design Laboratory - University of Victoria, Canada - 5 weeks
- 2014 - School of Mechanical Engineering, National Technical University of Athens, Greece - 8 weeks

Other visits of laboratories

- Norwegian University of Science and Technology, Norway
- Université catholique de Louvain, Belgium
- ONERA, Department of Applied Aerodyanmics (DAAP), France
- Pontifical Catholic University of Rio de Janeiro, Brasil

Summer school

- NORCOWE 2013: Offshore wind - challenges, data analysis and interpretation

Teaching and supervision

- Supervision of master student P. Mercier for his 6 months masters' thesis on the topic: "Fast vortex method for large scale wind energy simulations" [136].
- Teaching assistant for the 3 weeks DTU course: "Planning and Development of Wind Farms".

Open-source and programming projects

- Annex to this thesis (vortex theory and methods for wind energy).
- Preliminary development of a license manager for linux to be used with HAWC2.
- matlab2fortran: perform some simple conversions from matlab code to fortran.
- simple-fortran-parser: fortran parser to automatically generate derived type source code and generate library call headers
- vim-matlab-behave: reproduce matlab editor behavior (e.g. run functionality) for vim.
- vim-simple-comment: simple comment plugin for vim.
- vim-simple-compile: compile/run/view current file with or without a makefile.
- fuzzy-run: launch applications/commands with a minimum of key-pressed (vim bindings).
- par-latex: reformat latex document or paragraphs to a fixed width.

Aknowledgments

The words in this section are chronologically the last ones that were written. The current PhD project wouldn't have been possible without a part or the totality of the persons and each of the person mentioned below. To avoid conflicts, trying to be as politically and emotionally correct as possible, I will list these persons by order of appearance in the list.

sup I want to thank my supervisor, Mac Gaunaa, who has supported me all along the PhD: always available and ready to help, never out of illuminating ideas and constructive feedback, and always ready to crack a joke. Fun, smart, encouraging and kind. Whenever I've been asked, I've always described Mac as the best PhD supervisor possible. This PhD would not have been such a pleasant experience without him. Thank you Mac.

prf There is two professors at DTU I'd like to thank in particular: Jakob Mann who first introduced me to the research environment at DTU (Risø) and Niels Sørensen. Both of them have help me with fruitful discussions.

clg I want to thank my colleagues at DTU for helping me out in this project. Torben Larsen and Anders Hansen for setting me up with the development of *HAWC2*; Georg Pirrung for some interesting discussions, work and fun related, and exchanges of input files. We unfortunately never get to compare our similar models but it's good to keep some for the future; Niels Troldborg for his useful CFD experience, his trust in the cylindrical model and his sense of humor; Frederik Zahle for accepting my annoying random requests once in a while and my teasing pro-linux remarks. Ewan Machefaux for running CFD cases in really short time-frames, and way more on the non-work part of life. Mads Hejlesen for his advises and for being so open about code sharing. I would like to thank Henrik Brandenborg Sørensen for his help in accelerating the code. It was a delightful experience to collaborate with him. I'm grateful to Philippe Mercier who I co-supervised for his master thesis. I'm really glad I got to supervise someone for the first time, and he was a great student.

gov I'd like to thank the people that were involved in the decision of the travel grant I received, even if they might never read this thesis, they influenced it, and I thank them for their trust.

lab I had the opportunity to visit different labs during my PhD. I am infinitely grateful for the time Spyros Voutsinas has spent answering my questions and supervising my work during my stay at NTUA. It was a great chance to work with Spyros. I also would like to thank his colleague Papis (Giorgios Papadakis), whom I had the opportunity to work closely with, briefly unfortunately. Thank you to both of you for your nice explanations and for making my stay in Athens enjoyable. I want to thank Thomas Lewiner for answering my emails, exchanging source code with me on LIC, and eventually accepting my visit in his university. It was a pleasure to meet you. I want to thank Gerald Carrier for accepting my visit at the DAAP department of ONERA. I was lucky to perform a lovely external stay at the University of Victoria with the dynamic group of Curran Crawford, who I would like to thank a lot for this opportunity. I wish I could have stayed longer to exchange more with the team. Thanks to Ozi, Mike, Manuel and Mana for taking good care of me there. I'm really glad I got to visit Jabus (Jacobus De Vaal) at NTNU, for the interesting hopes of collaboration but also for an awesome time escaping in the mountains. Last, I would like to thank Philippe Chatelain and Gregoire Winckelmans for welcoming me at the UCL. Despite my short impromptu visits, they took the time to address all of my questions. I am really thankful for their inputs on vortex methods.

off Even if I do enjoy quietness in the office, I most certainly also enjoy some of the relaxing, geeky, fun, random life-reshaping discussions I had with my office mates. In 115, Lorenzo. In 101, Christian. In 115, Ewan, Juan and Alexander. In Victoria, Ozi and Manuel. Ozi I definitely owe you one for making my stay in Victoria so pleasant! Thanks a lot to you all of you guys for supporting my geekiness and for making our shared offices a pleasant place where everything can be discussed.

prg On the programming side, I need to thank Medina and the green danish robot for helping me writing these lines of code.
grl Thank you to Rosa, Jhannety, Mariah, Mana, Nanna, each of you for being a woman, shaping my life, and making me work less.
frd Thank you to Ewan, Philippe, Jeanne and Alessandro for being there all the time. Thank you to François for becoming my new La Fontaine partner. Thank you to the more geographically remote friends, for keeping track of the long-term fluctuations: Touille, Dim, Julie, Kiki, Loic, Milou, Romain.
fam The PhD time has been the period I've contacted my family the least and I am sorry for that. Nonetheless, I want to express my love to them for their continuous support. Thank you to my siblings Sophie and Julien for helping me grow up. Thank you, papa et maman, for bringing me to life!

List of symbols

Lower case letters

a	Axial induction factor
a_B	Axial induction factor local to the blade
$\hat{a}$	Axial induction factor from 2D MT
a'	Tangential induction factor
c	Chord
h	Helix pitch
h_B	Apparent pitch h/B
$\overline{h}$	Normalized pitch h/R
k^2	Elliptical parameter for elliptic integrals
k_t	Turbulent kinetic energy
l	Helix torsional parameter
$\overline{l}$	Normalized torsional parameter l/R
m	Elliptical parameter for elliptic integrals
n_{rot}	Rotational speed in RPM: $\Omega/(2\pi)$
p	Static pressure
q	Heat flux
r	Radial position
t	Time
t_0	Parameter in the core-spreading model
$\overline{r}$	Dimensionless radial position r/R
$\tilde{r}$	Dimensionless radial position r/R
s	Sign
u_θ	Tangential induced velocity
u_z	Axial induced velocity
u	x-component of velocity
v	y-component of velocity
w	z-component of velocity
w	Wake relative longitudinal velocity (Betz)
z_0	Surface roughness length

Upper case letters

$\boldsymbol{A}$	Angular Impulse
A	Area
AR	see Abbreviations
B	Number of blades
C_Γ	Dimensionless circulation
C_d	Drag coefficients
C_l	Lift coefficients
C_n	Normal aerodynamic coefficient
C_p	Power coefficient
C_q	Local torque coefficient
C_Q	Total torque coefficient
C_t	Tangential aerodynamic coefficient
C_t	Local thrust coefficient
C_T	Total thrust coefficient
D	Drag force
D	Rotor diameter
$\mathcal{D}$	Deformation matrix
E	Complete elliptic integral of the 2^{nd} kind
E	Energy
$\mathcal{E}$	Enstrophy
F	Tip-loss factor
F_a	Tip-loss factor based on axial induction
F_Γ	Tip-loss factor based on circulation
F_{C_l}	Performance tip-loss factor
F_{Go}	Goldstein's tip-loss factor
F_{Gl}	Glauert's tip-loss factor
F_{Pr}	Prandtl's tip-loss factor
F_{Sh}	Shen's tip-loss factor
$\mathcal{F}$	Complex velocity potential in 2D
I_t	Turbulence intensity
$\boldsymbol{I}$	Linear Impulse
$\mathcal{J}$	Helicity
$G_\bullet$	Green function associated to the operator $\bullet$
H	Heaviside function
$K_\bullet$	Kernel (associated to a given operator $\bullet$)
K	Complete elliptic integral of the 1^{st} kind
L	Lift force
Ma	Mach number
P	Power
$\mathcal{P}$	Palinstrophy
Q	Rotor torque
$\mathcal{Q}$	Vortical Helicity
R	Rotor radius
Re	Reynolds number
S	Surface
S	Energy density spectrum
S_d	Volume of the unit-spere in $\mathbb{R}^d$
T	Thrust force
T	Temperature
U	Longitudinal velocity at the rotor in 1D
$\boldsymbol{U}$	Relative velocity at the rotor
U_0	Longitudinal velocity far upstream
U_i	Induced velocity in 1D
U_n	Velocity normal to the rotor
U_t	Velocity tangent to the rotor
V	Velocity vector
V_{r}	Rotor velocity Ωr
V_{rel}	Relative velocity
$\mathcal{V}$	Volume
$\boldsymbol{W}$	Induced velocity vector at the rotor

Lower case Greek letters

$\boldsymbol{\alpha}$	Point/Blob vorticity intensity
α	Angle of attack
β	Twist angle
γ	Surface vorticity - Distributed circulation
γ_t	Vortex cylinder tangential vorticity
γ_l	Vortex cylinder longitudinal vorticity
γ_b	Bound vorticity

δ	Dirac function
ϵ	Pitch angle of the wake helix screw
ϵ	Regularization parameter
$\varepsilon_{l/d}$	Lift-over-drag ratio
ζ	Regularisation/cut-off function
η	Efficiency
θ	Azimuthal coordinate
κ	Goldstein's factor
λ	Tip speed ratio $= \Omega R/U_0$
λ_r	Local speed ratio $= \lambda r/R$
λ	First Lamé's coefficient
μ	Second Lamé's coefficient
ν	Kinematic viscosity $= \mu/\rho$
ρ	Air density ≈ 1.225 kg/m^3
σ	Local blade solidity $= Bc/2\pi r$
σ	Cauchy stress tensor
τ	Shear stress, viscous stress tensor
ϕ	Flow angle
χ	Wake skew angle, in yaw conditions
ψ	Azimuthal coordinate
$\boldsymbol{\psi}$	Vector potential
ω	Rotational speed of the wake
ω	Vorticity

Upper case Greek letters

Γ	Circulation
Δ	Laplacian operator ∇^2
Θ	Dilatation
Π	Gate function
Π	Complete elliptic integral of the 3$^{\text{rd}}$ kind
Φ	Velocity Potential
Ψ	Stream function (2D)
Ψ	Stokes stream function (3D)
Ω	Rotational speed of the rotor
Ω	Rotation matrix (fluid kinematics)
Ω	Solid angle
$\boldsymbol{\Omega}$	Total vorticity

Scandinavian letters

$\varnothing$	Empty set

Abbreviations

1D	One dimension
2D	Two dimensions
3D	Three dimensions
AD	Actuator Disk
AEP	Annual Energy Output
AED	Aeroelastic Design (section at DTU)
AL	Actuator Line
AR	Aspect ratio of a wing (b^2/S)
BEM	Blade Element Momentum
BET	Blade Element Theory
CFD	Computational Fluid Dynamics
CPU	Central Processing Units
DOF	Degree of Freedom
DTU	Technical Universtiy of Denmark
ECN	Energy Center of the Netherlands
GPU	Graphical Processing Units
HSS	High Speed Shaft
IEC	International Electrotechnical Commission
KJ	Kutta-Joukowski
LE	Leading edge
LES	Large Eddy Simulation
LHS	Left Hand Side
LSS	Low Speed Shaft
MT	Momentum Theory
NTUA	National Technical University of Athens
PSE	Particle Strength Exchange
VC	Vortex Code
VC	Vortex Cylinder (depending on context)
VL	Vortex Lattice
RHS	Right Hand Side
SGS	Sub-grid scale model
ST	Stream-tube Theory
TE	Trailing edge
TKE	Turbulent Kinetic Energy
WD	Wind direction
WS	Wind speed
WT	Wind Turbine

Operators

${}^t\!X$	Transpose
X^T	Transpose
∇	Del operator, "nabla"
div	Divergence, $\operatorname{div} \boldsymbol{X} = \nabla \cdot \boldsymbol{X}$
	$\operatorname{div} \underline{\underline{\boldsymbol{T}}} = \partial_j(T_{ij})\boldsymbol{e}_i$
grad	Gradient, $\operatorname{grad} X = \nabla X$
grad	Gradient of first order tensor
curl	Rotational, $\operatorname{curl} \boldsymbol{X} = \nabla \times \boldsymbol{X}$

Part I

Vortex models for rotors in uniform inflow

1 Cylindrical vortex model for finite and infinite tip-speed ratios 3
- 1.1 *Introduction and Context*
- 1.2 *Contribution and key results*
- 1.3 *Conclusions*

2 Superposition of cylindrical models - Effect of wake rotation 9
- 2.1 *Context*
- 2.2 *Contribution and key results*
- 2.3 *Conclusions*

3 Helical vortex model applied to tip-losses 15
- 3.1 *Introduction and Context*
- 3.2 *Contribution and key results*
- 3.3 *Conclusions*

Chapter 1

Cylindrical vortex model for finite and infinite tip-speed ratios

This chapter is based on the following publication: 'Cylindrical vortex wake model: right cylinder' [**23**].

Prologue A simple vortex model of a rotor with infinite number of blade is presented in this chapter. It will form the basis for the analysis performed in several chapters of this thesis: chapters 2, 4, 7 and 8.

1.1 Introduction and Context

The vortex model consisting of a circular cylinder with uniform circulation, introduced by Joukowski [94] in 1912, may be seen as the simplest vortex model of the wake of a rotor. In 1935, Glauert noted that this model gives similar results to the 2D momentum theory (MT) [71, p. 230]. The right vortex cylinder with tangential vorticity is not only a classical fluid-dynamic but also magnetostatic problem. In 1926, Müller [143] derived analytical formulae for the magnetic field of a finite solenoid based on the mutual inductance of two circular rings. In 1960, Callaghan and Maslen [37] presented formulae based on the derivation of the vector potential. Their work can be applied in fluid-dynamics to obtain the velocity field induced by the tangential vorticity of a right vortex cylinder. In 1974, analytical formulae were derived by Gibson [69] for the velocities induced by the tangential and longitudinal vorticity of a semi-infinite circular cylinder. Gibson followed a different approach than the previous authors. His results are based on a general Lemma and the use of integration by parts. Conway derived expressions for the system using Bessel functions and provided expressions for an arbitrary radial loading using integral relations [51, 47]. Conway also provided results for the velocity on the axis for different analytical radial distributions. In 1980, George [68] presented induced velocities formulae for a cylinder which cross section is an ellipse that deviates only slightly from a circle. Investigations of the vortex cylinder model were also applied to yawed configurations as will be seen in chapter 4.
Further improvement of the cylindrical wake model includes the addition of a root-vortex and a bound vorticity disk to complete the representation of the rotor and its wake. In 1912, Joukowski [94] presented analytical results for the entire system and in the entire domain. Direct integration of the Biot-Savart law was used, but the results were left in integral form and not explicitly written in elliptic integral. The author nevertheless mentioned this possibility. Formulae for the axial induction were derived for points in the vicinity of the cylinder surface. The bound vortex disk was considered but the full velocity field was not computed. The author provided important results for the induction in the rotor plane, the far field and the cylinder surface. Snel and Schepers [191, p. 226] used numerical integration to include the contribution of the longitudinal component of vorticity and the root vortex. Results from numerical integration of the influence of the vortex

cylinder, the bound vortex disk and the root vortex are found in the book of Burton et al. [35].

The assumptions of constant circulation and rigid wake envelope were also successfully relaxed. Heyson and Katsoff [86] used a superposition of cylinders of uniform circulation to study rotors with radially varying but azimuthally constant circulation. The ECN cylindrical differential equation model [191, p. 240] includes the time-history of the wake vorticity distribution in the Biot-Savart integration. The idea of superposition of vortex rings by Castles and de Leeuw was used by Øye to study wake expansion and non-uniform wake convection velocity [152]. The effect of expansion was studied using helical vortex filaments for rotors with finite and infinite number of blades by the present author and his supervisor **[22]**.

Results from vortex theory are often used to derive engineering models that can be implemented in BEM codes. This is partly due to the existence of relations between the momentum and vortex theories (see e.g. Glauert [71, p. 230], Burton et al. [35, p. 50-52], Johnson [93, p. 76] and the following section). Several BEM code yaw models are for instance based on the derivations of Coleman et al. (see e.g. Hansen [79, p. 98]). Recently, suggestions for using in a BEM code the induced velocities found by numerical integration of the cylindrical wake were presented by Crawford [54]. Sant [174] used the results of a free-wake lifting line code to derive BEM-compatible engineering models.

The similarity of results obtained with the cylindrical vortex model compared to the momentum theory (MT) of an actuator disk partially justifies the use of the model. The limitations and possible inconsistencies of both the momentum and vortex theories should yet be borne in mind and the reader is referred to the articles of van Kuik and Sørensen [214, 193] for further considerations. Radial velocities through the vortex cylinder surface are present as a result of the absence of wake expansion. Yet it was observed by Øye [152] that a fully resolved vortex system with wake expansion provides results in the rotor plane which are consistent with the simplified vortex system presented. This further justifies the application of the model.

1.2 Contribution and key results

Contributions It was chosen to investigate further the model of Joukowski consisting of: a cylinder with longitudinal and tangential vorticity, a bound vortex disk and a root vortex (see figure 1.1). The article consisted of the following contributions: the derivation of the induced velocities from a bound vortex disk; the derivation of the induced velocities from the tangential and longitudinal vorticity in a different way than in the current literature; the proof of annuli-independence (used in Blade element theory and stream-tube analyses) using a superposition of concentric cylindrical systems; and an illustration of the application of the model for the estimation of velocity deficits upstream of a wind turbine.

Vortex model The cylindrical vortex model considered and the coordinate system used are shown in figure 1.1. The vortex system represents a rotor with an infinite number of blades and its wake. The total circulation of the rotor is constant and such that the circulation of each infinitesimal blade is radially constant. The rotor operates at a finite tip-speed ratio. The incoming wind is steady and uniform. The cylindrical wake doesn't expand. The justification of the generation of a closed vortex system behind an actuator disk is discussed by van Kuik [213]. If the tip-speed ratio tends to infinity while the thrust remains constant, then the bound vorticity, and thereby also the longitudinal vorticity and root vortex strength, tend to zero. In this case therefore the only non-negligible component is the tangential vorticity.

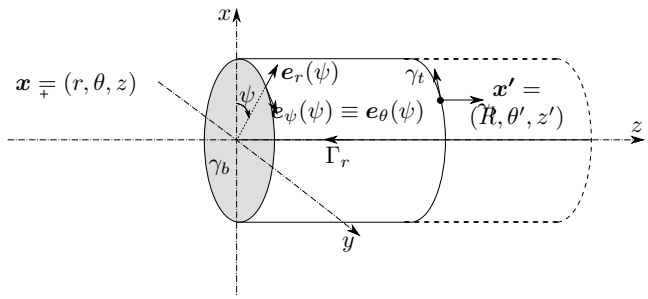

Figure 1.1: Vortex model and coordinate system. The rotor is represented by a gray disk and the infinite wake represented by dashes extends from $z = 0$ to $+\infty$. The model consists of a root vortex, a right semi-infinite vortex cylinder with tangential γ_t and longitudinal vorticity γ_l, and a bound vortex disk with radial vorticity γ_b.

Induced velocities in the entire domain The different strengths of the root vortex, the bound vorticity, the tangential and longitudinal vorticity are respectively:

$$\boldsymbol{\Gamma}_r = -\Gamma_{\text{tot}}\,\boldsymbol{e}_z, \qquad \boldsymbol{\gamma}_b(r) = \frac{\Gamma_{\text{tot}}}{2\pi r}\,\boldsymbol{e}_r, \qquad \boldsymbol{\gamma}_t = -\frac{\Gamma_{\text{tot}}}{h}\,\boldsymbol{e}_\psi, \qquad \boldsymbol{\gamma}_l = \frac{\Gamma_{\text{tot}}}{2\pi R}\,\boldsymbol{e}_z, \tag{1.1}$$

where Γ_{tot} is the total circulation of the rotor, R is the rotor radius, and h is the pitch of the helical wake formed by the combination of the two tip-vorticity components. The notation $u_{\bullet,\diamond}$ will refer to the $\bullet$-component of the velocity induced by the vortex element $\diamond$, where $\bullet \in \{r, \psi, z\}$ and $\diamond \in \{r, t, l, b\}$. The velocity field induced by the full vortex system is: $u_r = u_{r,t}$, $u_z = u_{z,t}$, $u_\psi = u_{\psi,l} + u_{\psi,r} + u_{\psi,b}$. The expressions of the different components were obtained by direct integration of the Biot-Savart law as:

$$u_r(r,z) = -\frac{\gamma_t}{2\pi}\sqrt{\frac{R}{r}}\left[\frac{2-\mathrm{k}^2(r,z)}{\mathrm{k}(r,z)}K\left(\mathrm{k}^2(r,z)\right) - \frac{2}{\mathrm{k}(r,z)}E\left(\mathrm{k}^2(r,z)\right)\right]$$

$$u_z(r,z) = \frac{\gamma_t}{2}\left[\frac{R-r+|R-r|}{2|R-r|} + \frac{z\mathrm{k}(r,z)}{2\pi\sqrt{rR}}\left(K\left(\mathrm{k}^2(r,z)\right) + \frac{R-r}{R+r}\Pi\left(\mathrm{k}^2(r,0), \mathrm{k}^2(r,z)\right)\right)\right]$$

$$u_\psi(r,z) = \begin{cases} -\Gamma_{\text{tot}}/4\pi r, & r < R \text{ and } z = 0 \quad \text{, or,} \quad r = R \text{ and } z > 0 \\ -\Gamma_{\text{tot}}/2\pi r, & r < R \text{ and } z > 0 \\ 0, & \text{otherwise} \end{cases}$$

where E, K and Π are the complete elliptic integrals of the first, second and third kind respectively, which elliptic parameter k is given by

$$\mathrm{k}^2(r,z) = m(r,z) = \frac{4rR}{(R+r)^2+z^2}, \qquad n_1 = \frac{2r}{r+\sqrt{r^2+z^2}}, \qquad n_2 = \frac{2r}{r-\sqrt{r^2+z^2}}. \tag{1.2}$$

and where n_1 and n_2 are used below. The different components forming the tangential velocity are:

$$u_{\psi,l}(r,z) = \frac{\gamma_l}{2}\frac{R}{r}\left[\frac{r-R+|R-r|}{2|R-r|} + \frac{z\mathrm{k}(r,z)}{2\pi\sqrt{rR}}\left(K\left(\mathrm{k}^2(r,z)\right) - \frac{R-r}{R+r}\Pi\left(\mathrm{k}^2(r,0), \mathrm{k}^2(r,z)\right)\right)\right] \tag{1.3}$$

$$u_{\psi,r}(r,z) = -\frac{\Gamma_{\text{tot}}}{4\pi r}\left[1 + \frac{z}{\sqrt{r^2+z^2}}\right] \tag{1.4}$$

$$u_{\psi,b}(r,z) = \frac{\Gamma_{\text{tot}}}{4\pi}\left\{\frac{1}{r}\left[\frac{z}{\sqrt{r^2+z^2}} - \frac{|z|}{z}\right] - \frac{1}{\pi z}\sqrt{\frac{r}{R}}\frac{z^2}{r^2}\sqrt{m}\left[K(m) + T_1\,\Pi(n_1,m) - T_2\,\Pi(n_2,m)\right]\right\} \tag{1.5}$$

$$T_1 = \frac{\left(\sqrt{r^2+z^2}-r\right)(r+R)-z^2}{2z^2}, \qquad T_2 = \frac{\left(\sqrt{r^2+z^2}+r\right)\left(\sqrt{r^2+z^2}+R\right)}{2z^2}, \tag{1.6}$$

The above results were presented in **[23]**. The velocity induced by the tangential vorticity, the longitudinal vorticity and the bound vortex disk are respectively studied in details in Appendix A, section A.3.3, and section A.4. The velocity field induced by the root-vortex is directly obtained from the Biot-Savart formula for a semi-infinite vortex filament **[23]**.

Combined influence and rotor inductions On the rotor disk, the bound vorticity has no induction and the combined influence of all components is such that $u_z = -\frac{\gamma_t}{2}$ and $u_\psi(r) = -\frac{\Gamma_{\text{tot}}}{4\pi r}$. From geometrical arguments, the induced velocities at the rotor plane are half the ones that would be obtained if the cylindrical system was infinite, i.e. half the induced values in the far-wake. This result is consistent with results from momentum theory of an actuator disk (see e.g. [71]). Introducing Ω the rotational speed of the actuator disk, U_0 the incoming free stream, a the axial induction factor positive along $\boldsymbol{e}_z$ and a' the tangential induction factor negative along $\boldsymbol{e}_\psi$, the vortex system leads:

$$aU_0 = -\frac{\gamma_t}{2}, \qquad a'\Omega r = \frac{\Gamma_{\text{tot}}}{4\pi r}, \tag{1.7}$$

Large tip-speed ratio - Relation to 1D MT Under the assumption of large tip-speed ratio, the helix pitch corresponds to the distance travelled by the wake vorticity in one rotor rotation. Using the convection velocity V_c of the vortex cylinder sheet in the far-wake (assumption used by Øye [152]) the pitch is then: $h = 2\pi V_c/\Omega = 2\pi(U_0+\gamma_t/2)/\Omega$. Inserting the pitch into the expression of γ_t leads to:

$$k = 4\frac{-\overline{\gamma}_t}{2}\left[1 - \left(-\frac{\overline{\gamma}_t}{2}\right)\right], \tag{1.8}$$

where $k = \Omega\Gamma_{\text{tot}}/\pi U_0^2$ and $\overline{\gamma}_t = \gamma_t/U_0$. By consideration of the Kutta-Joukowski relation it can be shown that k is equal to the local and total thrust coefficients under the assumption of large tip-speed ratio (see e.g. chapter 2, **[26, 67]** and Appendix C). The vortex theory result from equation (1.8) is then identical to the momentum theory analysis $C_T = 4a(1-a)$. Identical results are also found when considering the power coefficient as obtained by both theories **[67]**. Solving equation (1.8) for γ_t leads to $\gamma_t = U_0\left(-1+\sqrt{1-k}\right)$. The helix pitch may then be written: $h = \pi R[1+\sqrt{1-k}]/\lambda$. This relation was obtained using 1D momentum theory in a previous work [28], and is closely related to the relation obtained by Okulov and Sørensen [151] in the context of optimal circulation.

Large tip-speed ratio - Relation to 2D MT - Superposition of cylindrical vortex systems Glauert [71, p. 230] pointed out the existence of a link between vortex theory and 2D momentum theory. A formal derivation is presented in the article corresponding to the current section **[23]**, while the scope of this result is further studied in chapter 2 and **[26]**. In **[23]** it is shown that a vortex theory analysis can obtain the independence of annuli which is implied by Blade Element Theory and stream-tube analysis, in the case of an infinite tip-speed ratio. This result is not presented here since it is in fact a particular case of the more general case that will be presented in chapter 2.

Application to the upstream velocity reduction The vortex system provides more information than the momentum theory since the entire velocity field is known. In particular, the velocity on the disk axis is:

$$U_z(r=0,z) = U_0\left[1 - a\left(1 + \frac{z/R}{\sqrt{1+(z/R)^2}}\right)\right]. \tag{1.9}$$

This model reveals for instance that the wind speed measured at the recommended distance $5R$ [90] in front of a wind turbine operating at the canonical induction $1/3$ is $0.99\,U_0$. Further improvement

can be obtained using a superposition of vortex cylinders and consideration of the entire velocity field as will be shown in the following chapter.

1.3 Conclusions

The vortex system presented in this study can be used for simple models of wind turbines with infinite number of blades and finite tip-speed ratios. The main analytical contribution of this study consisted of the derivation of induced velocity formulae for the bound vortex disk. Also, a novel approach based on direct integration was presented to derive the inductions of a right vortex cylinder. The results obtained were consistent with existing work on the vortex cylinder. The study of the combined contributions from the longitudinal and bound vorticity validated the bound vorticity formulae derived. Relations between momentum theory and vortex theory were presented to justify the implementation in BEM codes of engineering models based on vortex theory results. In the case of infinite tip-speed ratio, it was shown that a superposition of concentric cylindrical systems predicts the independence of annuli which is assumed in Blade element theory and stream-tube analyses.

Chapter 2

Superposition of cylindrical models - Effect of wake rotation

This chapter is based on the following publication: 'Superposition of vortex cylinders for steady and unsteady simulation of rotors of finite tip-speed ratio' **[26]**. At the time of writing, the article is under review. Details of derivation are provided in Appendix E, and the Kutta-Joukowski loads for an actuator disk are defined in Appendix C.

Prologue The model presented in chapter 1 assumes a constant circulation along each infinitesimal blade. This assumption can be relaxed using a superposition of concentric cylindrical models. The case of infinite tip-speed ratio is a limiting case of the finite tip-speed ratio case but the two situations will be seen to have different implications.

2.1 Context

Infinite tip-speed ratio Only the tangential vorticity of the cylindrical vortex model remains under the assumption of infinite tip-speed ratios. A superposition of such models under this assumption was presented in **[23]** as mentioned in the previous chapter. It will be seen in chapter 4 that the assumption of infinite tip-speed ratio was for instance used by Coleman et al. [46] in 1945 to study the wake of a yawed rotor. In 1956, Heyson and Katsoff [86] used a concentric superposition of cylinders to study yawed rotors with radially varying but azimuthally constant circulation. Numerical integration had to be performed to obtain the full velocity field from a single cylinder. Results of the continuous superposition of vortex cylinders at infinite tip-speed ratio are found in integral form in the books of Johnson [92, p. 80], [93, p. 76].

Finite tip-speed ratio The actuator disk of finite tip-speed ratio was studied in details by Conway [51, 47]. Conway derived expression for an arbitrary radial loading using integral forms. Several of the main assumptions of the cylindrical vortex model have been successfully relaxed in the case of finite tip-speed ratio. In 1929, Goldstein [72] solved the potential flow around a rigid helical surface of vorticity, obtaining the circulation distribution of an "optimal" rotor with a finite number of blades. In this context, the assumptions of infinite number of blades and constant circulation are relaxed simultaneously but the result only applies to the specific "optimal" configuration. Relaxing the assumption of infinite number of blades, leads to the helical vortex system of Joukowski (see e.g. chapter 3 and Appendix F). Wrench [223] derived in 1957 approximate formulae for the velocities induced by helical filaments. A model using a superposition of helical filaments allows for a radially varying circulation: This concept was for instance used to study tip-losses **[22]**, or study the optimal rotor configuration [151]. Yet, the definition of the helical pitch becomes a crucial parameter of the model [147]. The relation between momentum theory and 2D vortex theory mentioned by Glauert [71, p. 230] (see also Burton et al. [35, p. 52], Johnson [93, p. 76]) is a powerful result,

that does not hold in the case of finite tip-speed ratio. The importance of the pressure drop due to wake rotation was revealed using momentum analysis by e.g. Sørensen and van Kuik [193], and using vortex theory by Øye in the work of Madsen et al. [126]. Corrections to BEM algorithm to include this pressure drop were suggested based on comparisons with actuator disk simulations by Madsen et al. [123].

2.2 Contribution and key results

Contributions A superposition of vortex cylinder models in the case of (in)finite tip-speed ratio was not presented in the literature to the authors knowledge. This study led to the following contributions: the identification of the pressure drop due to wake rotation from this system; the determination of the pitch required to form a consistent vortex system; the extension of the model to a continuous superposition of cylinders; the identification of the similarity between the BEM algorithm and the cylindrical vortex model and the equivalence in the case of infinite tip-speed ratio; an indication of how to correct BEM to include the effect of wake rotation according to the obtained result; the extension of the model to high-thrust case; and an illustration of application of the method to determine the velocity field in the entire domain, in particular upstream of a wind turbine. The model was also extended to unsteady simulations (see chapter 8).

Introduction Stream-tube Theory (ST) will refer to momentum analyses that assume radial independence of the stream-tubes (for others see e.g. [218]). The local thrust and torque coefficients found using ST are [79]: $C_{t,\mathrm{ST}} = 4a(r)\left[1-a(r)\right]$, $C_{q,\mathrm{ST}} = 4a(r)\left[1-a(r)\right]a'(r)\lambda_r$, where $\lambda_r \equiv \frac{\Omega r}{U_0}$. The BEM algorithm relates Blade Element Theory (BET) and ST results using three links. The 1st link uses a velocity triangle (see e.g. [219]) to relate the azimuthally averaged velocities from ST to the velocities on the blade:

$$4a'(r)[1+a'(r)] = 4a(r)[1-a(r)]\frac{1}{\lambda_r^2} \quad \Leftrightarrow \quad \exists\, \phi \in \mathbb{R}, \qquad \frac{[1-a(r)]}{[1+a'(r)]\lambda_r} = \frac{a'(r)\lambda_r}{a(r)} = \tan\phi \quad (2.1)$$

Both parts of the second equation should be satisfied. It can be solved for a' (see e.g. [82, p.26]) as: $a' = \frac{1}{2}\left[\sqrt{1+\frac{4a(1-a)}{\lambda_r^2}}-1\right]$. Yet, a different expression for a' is often used in BEM implementations (see e.g. [79, p. 53]). The 2nd and 3rd links relate the local thrust and torque coefficients from both theories. It is noted that the BET and the Kutta-Joukowski (KJ) loads are identical when the drag term is omitted in the loads. Several authors [219, 59] argue that this is indeed the proper way to derive the BEM algorithm. The KJ loads for an actuator disk are (see Appendix C):

$$C_{t,\mathrm{KJ}}(r) = k(r)[1+a'(r)], \quad C_{q,\mathrm{KJ}}(r) = \frac{k(r)}{\lambda_r}[1-a(r)], \quad C_{p,\mathrm{KJ}}(r) = k(r)[1-a(r)], \quad k(r) = \frac{\Omega\Gamma(r)}{\pi U_0^2} \quad (2.2)$$

Model and assumptions The support of vorticity around a rotor will be assumed to reduce to a superposition of concentric elementary cylindrical vortex systems. The elementary cylindrical system was presented in chapter 1, from which the notations are further adopted. The different components of the elementary vortex system are shown in figure 2.1a and the superposition is illustrated in figure 2.1b. A superposition of elementary systems allows for a radially varying circulation along the span of the blade.

Discrete superposition of cylindrical vortex systems The circulation is assumed to be piecewise continuous with the radius. The i-th circulation change, occurring at $r = R_i$, is associated with an elementary vortex system extending from $R_0 = 0$ to R_i of intensity $\tilde{\Gamma}_i = \Gamma_i - \Gamma_{i+1}$. The

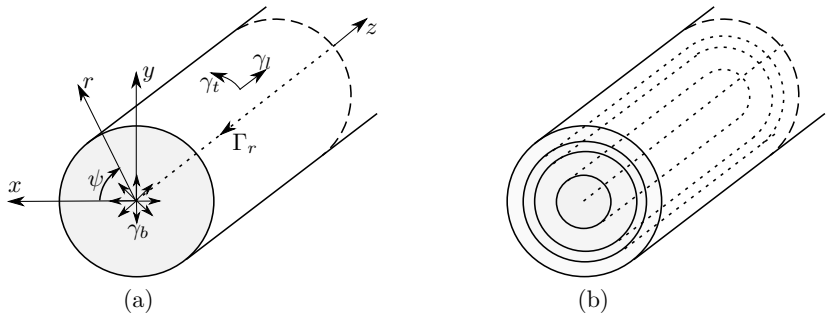

Figure 2.1: Sketch and notations for the vortex cylinder model. (a) Elementary model consisting of: a root vortex, a bound vortex disk, and a cylindrical vorticity surface with tangential and longitudinal components. (b) Superposition of concentric elementary models.

last cylinder, indexed n, extends radially from 0 to R. For convenience the ghost index $n+1$ is introduced such that $\Gamma_{n+1} = 0$. The tangential vorticity of the cylinder i is $\gamma_i = -\tilde{\Gamma}_i/h_i$, where h_i is the local helical pitch to be determined to form a consistent vortex system. The axial and tangential inductions in the rotor plane are directly obtained from the properties of an elementary vortex cylinder. For $R_{i-1} < r < R_i$ the induction factors are:

$$a_i = -\sum_{j=i}^{n} \frac{\gamma_j}{2U_0} \qquad , \qquad a'_i(r) = -\sum_{j=1}^{n} \frac{\tilde{\Gamma}_j}{4\pi\Omega r^2} = -\frac{\Gamma_i}{4\pi\Omega r^2} \tag{2.3}$$

It is seen that the tangential induction is only a function of the circulation of the closest surrounding cylinder. The axial induction requires the solving of a system for the tangential vorticity. Indeed, the tangential vorticity depends on the helical pitch, which depends on the far-wake convection velocity, which in turn depends on the tangential vorticity. The solving of the system, detailed in section E.5, leads to:

$$a_i = \frac{1}{2} - \frac{1}{2}\sqrt{1 - C_{t,i}(R_i) + C_{t,\mathrm{rot},i}} \quad \Rightarrow \quad C_{t,i}(R_i) = 4a_i(1-a_i) + C_{t,\mathrm{rot},i} \tag{2.4}$$

with

$$C_{t,i}(r) \equiv k_i \left(1 + \frac{k_i}{4\lambda_r^2}\right), \qquad k_i \equiv \frac{\Omega\Gamma_i}{\pi U_0^2}, \qquad C_{t,\mathrm{rot},i} = \sum_{j>=i+1} \left(\frac{k_j}{2}\right)^2 \left[\frac{1}{\lambda^2_{R_{j-1}}} - \frac{1}{\lambda^2_{R_j}}\right], \tag{2.5}$$

From [26, 126], the term $C_{t,\mathrm{rot},i}$ can be interpreted as the thrust coefficient of the force exerted on the disk by the wake rotation of the surrounding cylinders. With equation (2.3) and equation (2.4), a'_i and a_i are known for a given distribution of k_i, and the thrust and power coefficients over the entire radius can be determined according to the KJ relation from equation (2.2):

$$C_{t,\mathrm{KJ}}(R_{i-1} < r < R_i) = k_i \left(1 + \frac{k_i}{4\lambda_r^2}\right) \ , \qquad C_{p,\mathrm{KJ}}(R_{i-1} < r < R_i) = k_i \left(1 - a_i\right) \tag{2.6}$$

Continuous distribution of cylinders The results from the discrete superposition are extended to the continuous case by considering infinitesimal cylinders of extent dr trailing a circulation $\tilde{\Gamma} = d\Gamma/dr$. The thrust coefficient for a continuous superposition of cylinders is then:

$$C_{t,\mathrm{KJ}}(r) \equiv k(r) \left(1 + \frac{k(r)}{4\lambda_r^2}\right) = 4a(r)[1-a(r)] + C_{t,\mathrm{rot}}(r), \quad \text{with} \quad C_{t,\mathrm{rot}} = 2\int_r^R \frac{u_\psi^2}{U_0^2}\frac{dr}{r} \tag{2.7}$$

with $k(r) = \frac{\Omega\Gamma}{\pi U_0^2}$. The power coefficient can be expressed in any of the following forms:

$$C_{p,\mathrm{KJ}}(r) \equiv k(r)\left[1-a(r)\right] = \frac{C_{t,\mathrm{KJ}}(r)}{1+a'}\left[1-a(r)\right] = 4a(r)\left[1-a(r)\right]^2\frac{1}{1+a'(r)} + C_{t,\mathrm{rot}}(r)\frac{1-a(r)}{1+a'(r)} \tag{2.8}$$

The torque coefficient can be directly obtained from the power coefficient:

$$C_{q,\mathrm{KJ}}(r) \equiv \frac{C_{p,\mathrm{KJ}}(r)}{\lambda_r} = \frac{k(r)}{\lambda_r}\left[1-a(r)\right] \tag{2.9}$$

The axial and tangential inductions for a continuous distribution of cylinders are obtained as:

$$a(r) = \frac{1}{2} - \frac{1}{2}\sqrt{1-C_{t,\mathrm{eff}}(r)}\ , \quad a'(r) = \frac{\Gamma(r)}{4\pi\Omega r^2} \qquad \text{with:} \qquad C_{t,\mathrm{eff}} = C_{t,\mathrm{KJ}} - C_{t,\mathrm{rot}} \tag{2.10}$$

It is seen that the axial induction at a given location is a function of the induction of all the surrounding cylinders. In the infinite tip-speed ratio case though ($C_{t,\mathrm{rot}} = 0$), only the closest surrounding cylinder contributes and the annuli-independence is satisfied.

Vortex cylinder model and BEM algorithm The definition of a' from equation (2.10) can be inserted into the KJ torque coefficient given in equation (2.2), leading to: $C_{q,\mathrm{KJ}}(r) = \frac{\Gamma(r)}{\pi r U_0}[1 - a(r)] = 4\frac{\Omega r}{U_0}a'(r)[1-a(r)]$ which is also equal to $C_{q,\mathrm{ST}}$. On the other hand, $C_{t,\mathrm{KJ}}(r)$ contains an additional term, namely $C_{t,\mathrm{rot}}$ compared to the one obtained from ST . If the tip-speed ratio is infinite, then $C_{t,\mathrm{rot}}$ is zero and the thrust coefficients from both theories are equal. The orthogonality condition given in equation (2.1) becomes irrelevant when the tip-speed ratio is infinite.
For an infinite tip-speed ratio, the above showed that the BEM algorithm and the vortex cylinder models are equivalent, provided: an infinite number of blades, an azimuthally constant loading and the absence of drag terms in the computation of the induction coefficients. In the finite tip-speed ratio case, the vortex cylinder model with proper system closure revealed that the traditional BEM implementation that uses only the ST thrust lacks the loading from the wake rotation and assumes erroneously that annuli are independent.
The singularity in $C_{t,\mathrm{rot}}$ at the root can easily be avoided using a circulation that smoothly drops to zero towards the root. The current study reveals how a BEM implementation should include the effect of wake rotation: The thrust and axial induction should be computed according to equation (2.7) and equation (2.10) respectively. This implementation is then different than the one suggested by Madsen [123].

Momentum breakdown - Correction for high thrust Equation (2.10) is valid as long as the effective C_t is below unity. Drawing an analogy with Spera's correction [79], this equation can be modified as **[26]**:

$$a_{\mathrm{eff}} = \frac{C_{t,\mathrm{eff}} - 4a_c^2}{4\left(1-2a_c\right)} \qquad (\text{with } a_c \text{ chosen as } 0.34 \text{ in [79]}) \tag{2.11}$$

Results An iterative vortex cylinder code using tabulated profile data is implemented similar to a BEM code. The steps required for the calculation of the helical pitches are given in section E.7. The Risø-10MW reference rotor [227] is used to compare different algorithms. Results from the BEM code and the vortex cylinder (VC) code are shown in figure 2.2. The operating conditions are: $U_0 = 10$ m/s, $\lambda = 7.5$, $C_T = 0.83$ and a zero pitch angle. It is possible to set up an erroneous VC model equivalent to a BEM implementation (see section E.6 or **[26]**). The equivalence between the two codes is confirmed in the numerical implementation (BEM and VC-erroneous). Discrepancies between the BEM code and the proper VC model increases towards the root where the thrust due to wake rotation has a larger influence. This is expected for the axial induction but also the tangential

induction due to iterative nature of the algorithm: $a' = f(\Gamma) = f(a, a', \cdots)$. The discrepancies will increase for lower values of the tip-speed ratio where the relative wake rotation increases.

The curve labelled 'VC-pitch' does not use the pitch determined by the closure of the system. Instead it uses the velocity triangle behind the blade to assess the local pitch as: $h = 2\pi U_0(1 - a)/\Omega(1 + 2a')$. This formulation was used in a previous work [22] to determine the pitch of helical vortex filaments for a model similar to the current one but defined for a finite number of blades. From the current study it appears that using this velocity triangle introduces a large error. This error is expected to be smaller for simulations at low thrust coefficients.

The VC version offers the advantage of providing the velocity field in the entire domain and not only in the rotor plane. This is illustrated in figure 2.2.

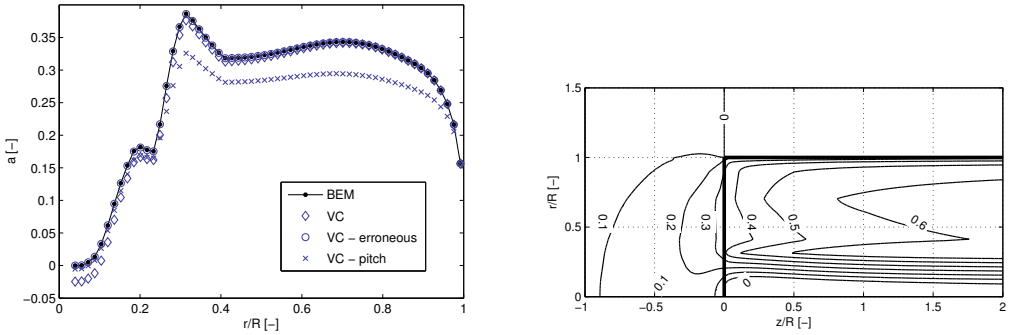

Figure 2.2: Axial inductions obtained for the DTU-10MW rotor [227] at a moderate tip-speed ratio $\lambda = 7.5$. Left: Simulations from BEM and Vortex cylinder (VC). Right: Contours computed using a superposition of 100 cylinders. Due to the absence of wake expansion results for $z > 0$ and $r > R$ are likely to differ from actutor disk simulations.

2.3 Conclusions

A vortex cylinder model was studied under the assumptions of constant circulation, infinite number of blades, but finite tip speed ratio. The relations between the vortex intensities and the rotor performance parameters required to form a consistent system were provided. The model was extended for radially varying circulation using a superposition of elementary systems. Relations to ensure the overall consistency of the model were also derived. Using the Kutta-Joukowski relation to relate to rotor loads, it was shown that this model was strongly related to the BEM algorithm. The additional term present in the vortex cylinder model was identified to be the thrust associated with the pressure drop occurring due to the wake rotation. This contribution can easily be added to a BEM algorithm and the current study reveals in which expressions the thrust due to wake rotation should be added. It was possible to extend the vortex cylinder model to cases of large local thrust coefficient using the empirical Spera correction. The analytical formulae available for the system make it possible to compute the velocity field in the entire domain, as opposed to BEM computations which are limited to the rotor plane and far-wake. The relaxation of the azimuthally constant circulation is a great challenge for the vortex cylinder model. The relaxation of the assumption of infinite number of blades can easily be done using the analytical formulae of semi-helical filaments. This will be the topic of chapter 3. Future work will focus on the comparisons of

the vortex cylinder model with results from actuator disk and BEM codes using Madsen's correction for the effect of wake rotation.

Chapter 3

Helical vortex model applied to tip-losses

This chapter is based on the following publication: 'Development of new tip-loss corrections based on vortex theory and vortex methods' [**22**].

Prologue The *cylindrical vortex wake model* presented in chapter 1 applies to a rotor with an infinite number of blades. When the number of blades is finite the model for the rotor and its wake consists in: lifting lines of constant circulation, a root vortex and helical filaments trailed from the tip of each blade. This *helical vortex wake model* is also attributed to the work of Joukowski (see [94] and Appendix F). It should be noted that if the helices are not rigid the system is unconditionally unstable for all pitch values [151]. The induced velocities from a helical vortex are detailed in Appendix B. Similar to the superposition of vortex cylinders done in chapter 2, a superposition of helical filaments is here applied. Semi-analytical formulae and numerical studies are used to investigate the effect of tip-losses. Further applications of the model in the context of optimal circulation are given in Appendix D where formulae for wake expansions are also given.

3.1 Introduction and Context

Tip-losses commonly refer to kinematic and/or dynamic differences between a two-dimensional and a three dimensional configuration of a lifting device. The main source of these differences for a wing of finite span or for a rotating device of finite number of blades is the circulation flow driven by the pressure equalization which arises at the tip of the lifting device. Prandtl used vortex theory analysis to assess the proportion of these losses for both a wing [162] and a propeller blade [161] at the beginning of the 20^{th} century. The latter study was introduced as a correction factor to be applied to Betz's optimal circulation [16] extending the applicability of Betz's result from an infinite to a finite number of blades. Betz optimal circulation is obtained from a far-wake consisting of a infinitely dense system of helical vortex sheets moving as a rigid-body translation. Prandtl's tip-loss factor corresponds to an approximation of the ratio between the total blade circulation Γ_B and the circulation for an infinite number of blades Γ_∞ for the optimal Betz rotor. Prandtl's model considers the axi-symmetric wake flow about a series of semi-infinite rigid lines as an approximation to the system of finite helical vortex sheets. The exact circulation distribution Γ_B corresponding to the system of finite helical vortex sheets was obtained by Goldstein in 1929 [72]. Goldstein's tip-loss factor can be obtained from this solution [20]. Glauert [71] suggested a modification to Prandtl's tip-loss factor for a convenient numerical implementation and it is his model which has been retained to this day in most BEM codes. A generalization of Prandtl's tip-loss factor and its different implementations can be found in [28, 20]

A superposition of semi-infinite helical filaments can be used to represent the optimal helical wake (see e.g. Okulov et al. [149]) or a more general wake shape. The velocity potential corresponding to a system of B equally-spaced infinite helices was derived by Kawada [97]. Exact analytical formulae for the velocity field induced involve modified Bessel functions (see e.g. [81]). Lerbs [115], derived an approximation of Kawada's expression. Later, Wrench [223] added a correction term to improve

the accuracy of this approximation. The velocity field at the rotor plane from a superposition of semi-infinite helical filaments can be obtained with great accuracy with Wrench's formula.
Recently, a free wake lifting-line code (see e.g. [28], **[27]**) was used to derive tip-loss corrections accounting for wake expansion, roll-up and distortion, and applicable to a wide range of operation conditions.

3.2 Contribution and key results

Contributions This study made use of analytical vortex results to derive a new analytical tip-loss factor, derive various numerical counterparts and study the influence of wake expansion on tip-losses. The study led to the following contributions: the derivation of a new analytical tip-loss factor more representative of the wake shape; different definitions of the tip-loss factor; three-vortex theory results; the link between the formulae of Wrench and the ones of Okulov; the application of the Theodorsen wake-expansion function; the study of the effect of wake-expansion on tip-losses.

Introduction - Tip-loss factors and vortex theory Prandtl's tip-loss factor $F_\Gamma = \Gamma_B/\Gamma_\infty$ can be interpreted as a correction term applied to induction factors, $F_a = a_\infty/a_B$, and $F_{a'} = a'_\infty/a'_B$, where the subscript ∞ refers to the induction value for an infinite number of blades, and the subscript B refers to the value on the blade. This definition will be called the *natural* tip-loss factor. In most BEM codes, the tip-loss factor represents the proportion in which the axial induction at the blades differs from the momentum theory value. The 2D momentum value is the azimuthally averaged value written $\langle \bullet \rangle_\theta$. The *planar* tip-loss factor is defined as $F_{\langle a \rangle} = \langle a \rangle_\theta / a_B$, and $F_{\langle a' \rangle} = \langle a' \rangle_\theta / a'_B$. , consistent with e.g. [185, 79]. In the case of an axi-symmetric wake and by assuming that the wake shape is the same for any number of blades, the natural tip-loss factor and the planar tip-loss factors are equal **[22]**. These assumptions are satisfied in particular in the case of a non-expanding wake consisting in different trailed helical filaments (see figure 3.1). It

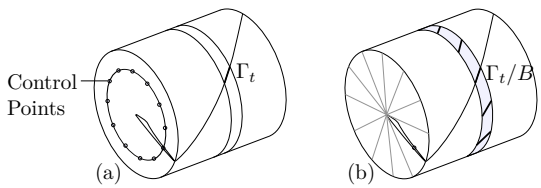

Figure 3.1: Planar and natural tip-loss factor computed using a large number of control points (a) or blades (b).

was also shown that the azimuthal average of the induced velocities on a plane perpendicular to the helix axis and from which a semi-infinite helix is emitted is half the value found for an infinite helix.

Elementary helical vortex model The elementary helical vortex model consists of B straight lifting-lines of constant circulation Γ representing the blades, B regular semi-infinite helical vortex filament of pitch h and circulation Γ trailed at the tip of each blade, and a root vortex of intensity $-B\Gamma$. The induced velocities from the B helix on the rotor plane are obtained from the formulae of Wrench. The formulae can be identically obtained using a summation of the approximate solution of Okulov [145] (see Appendix B).

Four vortex models - Radially varying circulation The model consisting of a superposition of elementary helical vortex model will be referred to as the *analytical vortex wake model* since the induced velocities in the rotor plane are indeed obtained using closed form formulae. The 2nd model is a numerical analog to the analytical helical wake model which include wake expansion. In a very simple fashion, an expansion factor as function of the downstream location is applied to the trailed vortex filament. Different expansion factors have been used including the theoretical one from Theodorsen [203], illustrated in figure 3.2. This method requires the determination of far wake parameters, for which an iterative procedure along the same line as the methodology presented in [150] and [218] was used. The helix pitches for the 1st and 2nd models are computed from the

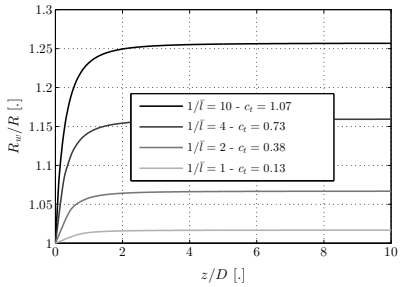

Figure 3.2: Wake Expansion factor computed using Theodorsen's theory for different far wake pitch $\bar{l}$ and a far wake convection velocity $\overline{w} = 0.4$. The thrust coefficient in the far-wake c_t is determined according to the far wake parameters and Goldstein's circulation [203].

velocity triangle immediately downstream of the blade (see figure 3.3) as:

$$h(r) \equiv 2\pi r \tan\epsilon(r) = \frac{2\pi U_0(1-a(r))}{\Omega(1+2a'(r))} \tag{3.1}$$

The 3rd model is the numerical prescribed wake model from Gaunaa [66]. It includes wake expansion

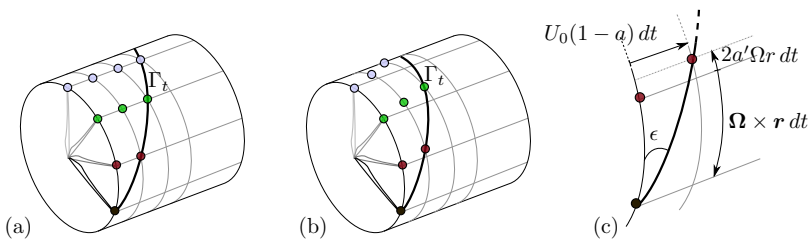

Figure 3.3: Trailed vorticity path for a one-bladed rotor. Four Lagrangian particles (of different colors) that passed through the tip of the blade at four different times are plotted. The line joining these particles at a given time is the trailed vorticity line. (a) Without tangential induction - (b) With tangential induction - (c) Helix angle.

and distortion with varying pitches along the wake and different convection velocities and rotational velocities of the vortex elements. This model was established based on the results from free wake computations. The 4th model consists of the free-wake vortex code as described in chapter 9 (Configuration 2-1, see section 9.3).

New tip-loss factor based on the analytical vortex wake model At a given radial position on the blade, the tip-loss is the ratio between the total induced velocity from the helical vortex filaments of the infinitely-bladed case to the induced velocity of the finite case:

$$F(r) = F_a(r) = \frac{\lim_{B_l \to \infty} \int_0^R u_{z,B_l}\left(r, r_0, h(r_0), \Gamma(r_0)/B_l\right) dr_0}{\int_0^R u_{z,B}\left(r, r_0, h(r_0), \Gamma(r_0)\right) dr_0} = \frac{\int_0^R \Gamma(r_0)/2h(r_0) dr_0}{\int_0^R u_{z,B}\left(r, r_0, h(r_0), \Gamma(r_0)\right) dr_0} \quad (3.2)$$

where $u_{z,B}$, given in [22] and equation (B.7), is the sum of induced velocities from B equally azimuthally-spaced helical filaments emitted at the radial position r_0. For each radial position, the proper circulation Γ and helical pitch $h = 2\pi l$ as defined by equation (3.1) is used. In practice the flow angle is known at finite positions and the integral is replaced by a summation. The limit in equation (3.2) was removed using vortex cylinder theory results. The tip-loss factor was given using the natural definition but the planar definition could be used indifferently in this context.

Results The different vortex wake models were used to determine the tip-loss factor from two different prescribed circulation shapes and different operating conditions. When the analytical vortex wake model is applied, the tip-loss factor from equation (3.2) is directly obtained. Results were reported in a table [22] and are commented below. A variable referred to as the *lost area*, noted A_F, is introduced. The lost area is the difference between the area of the unit-square and the area below the tip-loss curve $F_\bullet(r/R)$. A large lost area signifies large tip-losses.
All models captured the trend that tip-losses are reduced (A_F decreases) with increasing tip-speed ratio and increasing C_T. This trend can be explained by the increased proximity of the vortex sheets occurring with the increase of these parameters. Indeed, using 1D momentum theory (or an elementary cylindrical model) under the assumption of high tip-speed ratio ($a' = 0$) the proximity of the sheets is $h_B = \frac{\pi R}{\lambda B}\left[1 + \sqrt{1 - C_T}\right]$ [28].
Comparisons between BEM code and free-wake code results give the same conclusions as a previous study [28]: The tip-loss factors obtained with Glauert's formulation often have a larger lost area than the one obtained by the free-wake code. Yet, since the nature of the two codes is different the comparison can be quite abstruse. On the contrary, comparisons amongst vortex models are justified and offer great potential. From the table given in [22], it was observed that the lost area is always reduced when going from the simplest model to the more advanced free-wake model suggesting that both expansion and distortion of the wake tend to decrease the proportion of tip-losses. The sole effect of expansion on the tip-loss function is illustrated on the right of figure 3.4. In both cases, the prescribed wake models with expansion show a lower lost area. Gaunaa's advanced prescribed wake model gave similar tip-loss functions than the simpler helical wake model with Theodorsen's wake expansion, showing coherence between the expansion models and suggesting that the expansion model is more influential than the distortion model for the study of tip-losses.

3.3 Conclusions

Distinctions and clarifications between different possible definitions of tip-losses have been presented. By superposition of semi-infinite helical filaments whose pitches depend on the velocity triangle after the rotor, a tip-loss factor can be computed using analytical formulae. This new analytical tip-loss factor is easily implemented in a BEM code. The method is physically more advanced than the one originally presented by Prandtl. The two analytical methods give coherent results. The expansion factor from Theodorsen has been successfully applied to wind energy for the first time. The influence of wake expansion on the tip-loss factor has been studied with vortex methods. It was seen that the wake expansion has a greater influence on the tip-losses than the

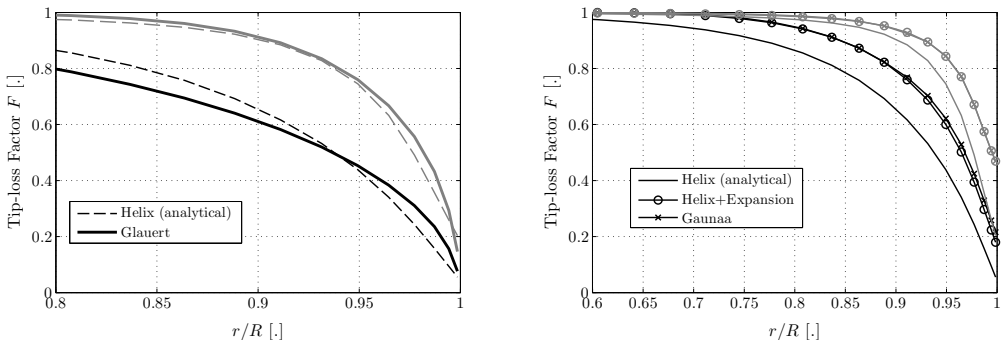

(a) (b)

Figure 3.4: Tip-loss factors for different tip-speed ratios and for $C_T = 0.6$. Left: Comparison of the two analytical tip-loss factors. Right: Effect of expansion. The darker curve corresponds to $\lambda = 3$ and the lighter one to $\lambda = 12$.

wake distortion. Despite the simplicity of the prescribed wake model used, it was possible to capture the fact that wake expansion reduces tip-losses. This result was confirmed by using free-wake simulations. Development of advanced numerical methods and accurate measurements of flow in the rotor plane will help reveal which of the methods assesses best the phenomenon of tip-losses.

Epilogue In a unsteady simulation where each blade have a different circulation, the tip-loss factor can still be independently determined for each blade using equation (3.2). The tip-loss factor of each blade is then obtained as if each blade was part of a system where all B blades had the same circulation. This is also the approach applied when using Glauert's tip-loss factor. A more representative value of the tip-loss can be obtained using the planar definition of the tip-loss factor.

$$F_a(r) = \frac{\langle \sum_{k=1}^{B} \int_0^R u_{z,1}\left(r, r_0, h_k(r_0), \Gamma_k(r_0)\right) dr_0 \rangle_\theta}{\sum_{k=1}^{B} \int_0^R u_{z,1}\left(r, r_0, h_k(r_0), \Gamma_k(r_0)\right) dr_0} \tag{3.3}$$

The formulae of the pitch obtained from the superposition of vortex cylinders presented in chapter 2 should preferably be used instead of the one from the velocity triangle (i.e. equation (3.1)). This choice would potentially improve the new-tip-loss model at low tip-speed ratios.
Another effect occurring at the tip of a blade which affects the inflow and thus the performance of the airfoil is the "de-cambering" effect. This effect was for instance studied by Sørensen et al. using vortex based tools and linear theory [195]. A tip-loss factor accounting for this specific effect is suggested by the authors.

Part II

Vortex models for rotors in yaw

4 Yaw-modeling using a skewed vortex cylinder model 23
- 4.1 *Introduction and Context*
- 4.2 *Key results and contributions*
- 4.3 *Conclusions*

5 Simple implementation of a new yaw model 29
- 5.1 *Context*
- 5.2 *Contribution and key results*
- 5.3 *Conclusions*

6 Advanced implementation of the yaw model - Pre-study 35
- 6.1 *Introduction*
- 6.2 *Models for the velocity field outside of the skewed cylinder*
- 6.3 *Helical pitch for the superposition of skewed cylinders*
- 6.4 *Yaw model implementation using a superposition of skewed cylinders*
- 6.5 *Partial approach - focus on the inboard part of the blade*
- 6.6 *Conclusions*

Chapter 4

Yaw-modeling using a skewed vortex cylinder model

This chapter is based on the following publication: 'Cylindrical vortex wake model: skewed cylinder, application to yawed or tilted rotors' [**24**].

Prologue The cylindrical vortex wake model presented in chapter 1 for the case of uniform inflow is extended to the case of yawed inflow. The bound vorticity is assumed to be as before but the vortex cylinder and the root vortex are skewed with respect to the normal of the rotor disk. Closed form formulae for the induced velocities only exist for a limited part of the domain. Semi-empirical models need to be established in particular to obtain the velocity at the rotor disk. Results from this analysis will be applied in chapter 5 to derive a BEM yaw model. The novelty of this approach is that the assumption of infinite tip-speed ratio is relaxed. Detailed derivations are provided in section A.5.

4.1 Introduction and Context

The yawed configuration of a wind turbine is similar to the case of an helicopter in forward-flight so that wind turbine aerodynamics benefit from the extensive study of the latter case. Glauert's study of the "autogyro concept" in 1926 [70] is among the earliest investigations. Glauert used a lifting line analysis where the rotor is assumed highly yawed and is modelled as a circular wing. The induced velocity normal to the rotor can be decomposed into a constant component and a component that varies linearly with the radius and sinusoidally with the azimuth angle. This form can be regarded as the zeroth and first sinusoidal component of a Fourier decomposition. The amplitude of the zeroth component corresponds to the induction value in the non-yawed case. The component attributed to yaw is referred to as the flow expansion function in the book of Burton et al. [34, p. 108]. Further refinements of the model may be obtained by adding higher harmonics of sine and cosine terms. The determination of the Fourier components may be done by various methods, for instance: experimentally [180] or using vortex analyses similar to the one of Coleman [46]. To this day, the work of Glauert and Coleman form the basis of yaw-model implementations for Blade Element Momentum(BEM) codes, see e.g. Hansen [79, p. 98].
In 1945, Coleman et al. [46] used a skewed cylindrical wake to study yawed rotors. They restricted their study to the component of vorticity tangential to the rotor. They derived far-wake relations and computed the normal induced velocity along the horizontal diameter of the rotor analytically. In 1954, Castles and de Leeuw computed the normal induced velocity at any point by modeling the cylinder as vortex rings and using a solid angle approximation of the far-wake [38]. Two years later, Castles and Durham improved the method by integrating the Biot-Savart law analytically along the axis and numerically over the azimuth [39].
The idea of Castles and de Leeuw consisting in modeling the vortex cylinder with rings was also

used by Øye to find a polynomial fit to the flow expansion factor [153]. This approach was also followed to compare the model with Computational Fluid Dynamic (CFD) simulations of wind turbines in yaw [206] and tilt configurations [75].
Vortex models of higher complexity followed the work of Coleman and his co-authors. In a combined publication by Heyson and Katsoff [86], Heyson used a superposition of cylinders to study yawed rotors with radially-varying but azimuthally-constant circulation [86]. Heyson later compared his results with experiments [87] finding good agreement in the near-wake, but decreasing accuracy in the far-wake due to wake distortion. Chaney et al. [41] used a superposition of two skewed cylinders to model the stalled inner-part of the rotor. Despite its simplicity the cylindrical vortex model with a step circulation was shown to reveal important features that other models would not capture. The case of a sinusoidal variation of the circulation with azimuth was studied by Drees [60] who found an approximate formulation for the first sine and cosine harmonics of the normal induced velocity. The effect of expansion was studied for a skewed rotor with a cylindrical wake by Chaney et al. [40]
Recently, suggestions for using in a BEM code the induced velocities found by numerical integration of the skewed cylindrical wake were presented by McWilliam et al. [134]. More advanced vortex wake models imply the prescription of complex wake geometries and the numerical integration of the Biot-Savart law as for example in the work of Egolf and Landgrebe [62]. Haans [77] used an extensive amount of experimental data to determine with precision the position and intensity of the vortex system in axial and yawed conditions. The author then decomposed the wake system to investigate the influence of the individual components of the wake such as the tip and root vortex or the shed vorticity. The final level of wake complexity is reached using free-wake methods. Sant [174] used the results of a free-wake lifting line code to develop BEM-compatible engineering models for wind turbine in yawed configuration.
In the above review, only the work related to vortex theory was presented since it is the method which will be used in this chapter. A great amount of work was done for yawed rotor using acceleration potential methods [129, 210], which led to the development of the Pitt and Peters model [159]. More detailed reviews may be found in the literature covering helicopters in forward-flight [113, 92] and wind turbines in yawed condition [191, 34].

4.2 Key results and contributions

Contributions This study focused on the extension of the work of Castles et al. and Coleman et al. in order to relax the assumption of infinite tip-speed ratio used in their studies. The study of the skewed cylinder model led to the following contributions: the derivation of all the components of the velocity field induced by the tangential vorticity (Castles et al. focused on the z-component); the justification of the use of the engineering model for the tangential vorticity presented in [35]; the derivation of semi-analytical formulae and engineering model for the velocity induced by the longitudinal vorticity; the derivation of far-wake properties for the longitudinal vorticity, namely that the velocity field is zero inside the cylinder ellipse and that the streamlines are confocal ellipses.

Presentation of the vortex wake model The vortex model consists of the same components as the right cylinder model presented in chapter 1 except that the wake direction vector forms an angle χ with the z-axis. The notation of chapter 1 are adopted. The different components are represented in figure 4.1, and the coordinate system is shown in figure 4.2. The angle χ is referred to as the *skew angle*. It is equal to zero in non-yawed condition and is usually higher than the yaw angle. Relations between the yaw angle and the skew angle may be found for instance in [153, 34, 91]. The different strengths of the root vortex, the bound vorticity, the tangential and

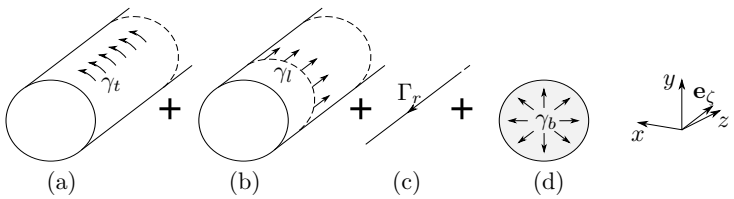

Figure 4.1: Vortex wake model used in this study. The influence of the tangential vorticity (a), the longitudinal tip-vorticity (b), the root-vortex (c) and the bound vorticity (d) is studied independently. The cylinder and root-vortex are directed along $\boldsymbol{e}_\zeta$

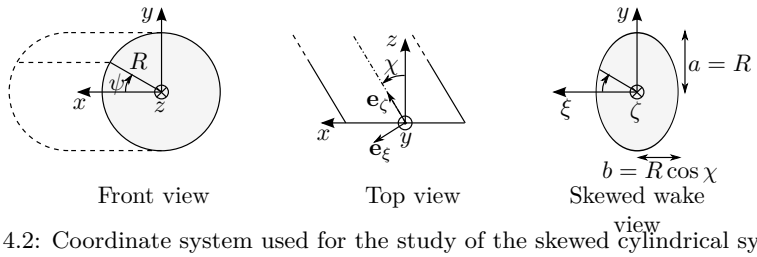

Figure 4.2: Coordinate system used for the study of the skewed cylindrical system

longitudinal vorticity are respectively:

$$\boldsymbol{\Gamma}_r = -\Gamma_{\text{tot}}\,\boldsymbol{e}_z, \qquad \boldsymbol{\gamma}_b(r) = \frac{\Gamma_{\text{tot}}}{2\pi r}\,\boldsymbol{e}_r, \qquad \boldsymbol{\gamma}_t = -\frac{\Gamma_{\text{tot}}}{h/\cos\chi}\,\boldsymbol{e}_\psi, \qquad \boldsymbol{\gamma}_l = \frac{\Gamma_{\text{tot}}}{2\pi R}\,\boldsymbol{e}_z, \tag{4.1}$$

Velocities induced by the tangential vorticity Coleman et al. derived in 1945 [46] an analytical expression for the axial velocity induced by the tangential vorticity along the fore-aft diameter: $u_{z,t}(r, \psi = 0, z = 0)$. In 1956, Castles and Durham [38] obtained the axial component of velocity at any point using an analytical integration over z and a numerical integration over the azimuthal variable. This approach is extended in the current study to derive all components of the induced velocity as:

$$u_{\bullet,t}(r,\psi,z) = \frac{\gamma_t}{4\pi}\int_0^{2\pi} \frac{2\left(a'_\bullet\sqrt{c} + b'_\bullet\sqrt{a}\right)}{\sqrt{a}\,(2\sqrt{ac}+b)}\,d\theta', \quad \{a'_z,\ b'_z\} = R\,\{R - r\cos(\theta'-\psi),\ m\cos\theta'\} \tag{4.2}$$

$$\{a'_r,\ b'_r\} = R\,\{z\cos(\theta'-\psi),\ -\cos(\theta'-\psi)\}, \quad \{a'_\psi,\ b'_\psi\} = R\,\{z\sin(\theta'-\psi),\ -\sin(\theta'-\psi)\}, \tag{4.3}$$

$$\{a,\ b,\ c\} = \left\{R^2 + r^2 + z^2 - 2rR\cos(\theta'-\psi),\ 2mR\cos\theta' - 2mr\cos\psi - 2z,\ 1+m^2\right\} \tag{4.4}$$

where the symbol $\bullet$ stands indifferently for r, ψ, z and where $m = \tan\chi$. Properties in the far-wake and in the rotor disk are further shown in [24]. The velocity field in the rotor plane was approximated with:

$$u_{z,t} \approx \frac{\gamma_t}{2}\left[1 + 2F_t\tan\frac{\chi}{2}\cos\psi\right], \quad u_{r,t} \approx u_{z,t}\tan\frac{\chi}{2}\cos\psi - \frac{\gamma_t}{2}F_t\sec^2\frac{\chi}{2}, \quad u_{\psi,t} \approx -u_{z,t}\tan\frac{\chi}{2}\sin\psi \tag{4.5}$$

where $F_t(r,\chi) = \frac{K_{z,t}(r,\chi)}{2\tan\frac{\chi}{2}} \approx r/2R$. Coleman et al. derived a closed form solution for $K_{z,t}$ and provided a linear approximation. The axial and tangential functions take exact values on the vertical and horizontal diameters while the radial component takes exact value only on the horizontal diameter.

Velocities induced by the root-vortex The velocity is directly obtained from the Biot-Savart formula of a semi-infinite vortex filament (see e.g. [23]), as:

$$u_{z,r} = \frac{\Gamma_r}{4\pi r(1-\cos\psi\sin\chi)}\sin\psi\sin\chi, \qquad u_{\psi,r} = \frac{\Gamma_r}{4\pi r(1-\cos\psi\sin\chi)}\cos\chi. \tag{4.6}$$

Velocities induced by longitudinal part of the tip-vortices The velocity is also obtained from the induction of a semi-infinite vortex filament as:

$$u_{\bullet,l} = \frac{\gamma_l}{4\pi}\int_0^{2\pi} \frac{N_\bullet}{D_1\left(D_2+\sqrt{1+m^2}D_1\right)}\,d\theta',\ N_z = m\left(-\sin\theta'+\tilde{r}\sin\psi\right),\ N_\psi = -m\tilde{z}\cos\psi-\cos(\theta'-\psi)+\tilde{r}$$
$$N_r = -m\tilde{z}\sin\psi+\sin(\theta'-\psi),\ D_1 = \sqrt{1+\tilde{r}^2+\tilde{z}^2-2\tilde{r}\cos(\theta'-\psi)},\ D_2 = m\cos\theta'-m\tilde{r}\cos\psi-\tilde{z} \tag{4.7}$$

with $\tilde{r} = r/R$, $\tilde{z} = z/R$. Properties in the far-wake and the rotor plane are derived in the article. In particular it is shown that the velocity is zero within the vortex cylinder of longitudinal vorticity in the far-wake and that the streamlines outside of the elliptical cross-section are confocal ellipses in a plane perpendicular to the wake direction. The following engineering model is suggested for the velocity field in the rotor plane:

$$u_{z,l} \approx -\gamma_l F_l(r)\tan^2\left(\frac{\chi}{2}\right)\sin(2\psi), \quad u_{\psi,l} \approx \frac{\gamma_l}{2}\tan\left(\frac{\chi}{2}\right)\left[1+G_l(r)-F_l(r)\sec^2\left(\frac{\chi}{2}\right)\right]\cos\psi \tag{4.8}$$

where $G_l \approx 0.1(\tilde{r}+7\tilde{r}^5)$ and $F_l \approx 0.1(\tilde{r}-2\tilde{r}^3+6\tilde{r}^5)$.

Velocities induced by the bound-vortex disk Due to the assumption of constant rotor circulation, the induced velocity from the bound-vortex disk is identical to the one obtained in the right-cylinder case from chapter 1.

Contribution of each component to the whole system From the derivations above it is possible to compute the velocity field induced by the entire system in the whole domain using numerical integration, and in the rotor plane using the approximate formulae. A study of the contribution of each component to the whole system for different pitch values is illustrated in figure 4.3. The pitch and tip-speed ratio are assumed for simplicity to be related by[1] $h \propto \frac{\pi R}{\lambda}[1+\sqrt{1-C_T}] \approx 4\pi R/(3\lambda)$, using $C_T = 8/9$. The induced velocities of each vortex component are linear with respect to their corresponding vorticity intensity. As seen in equation (4.1), only γ_t varies with h and χ. In the figure, u_z is scaled with $u_{z,0} = \gamma_t/2$ which is therefore a function of h. It is observed that $u_{z,l}$ is negligible and $u_{\psi,l}$ modest for the range of pitch displayed. Yet, for higher pitch, i.e. lower a tip-speed ratio the influence becomes non-negligible. If the tip-speed ratio approaches infinity, $u_{z,t}$ clearly predominates the other vortex components. This justifies the work of Coleman et al. who considered only this component. For finite tip-speed ratios though, the influence of the root-vortex in both the axial and tangential direction is significant. The root-vortex has a greater influence closer to the root while the tangential and longitudinal vorticity have a greater influence towards the rim of the disk. For large radii, the influence of the tangential vorticity and longitudinal vorticity have a comparable magnitude which is not a negligible proportion of the root vortex influence. These components should be taken into account in BEM computations of yawed rotors.

[1]The relation $h-\lambda$ presented here is a simplified measure for qualitative assessment. It uses the axial induction at the rotor and $a' = 0$ to assess the pitch, instead of a more correct formulation that would consider the far-wake induction.

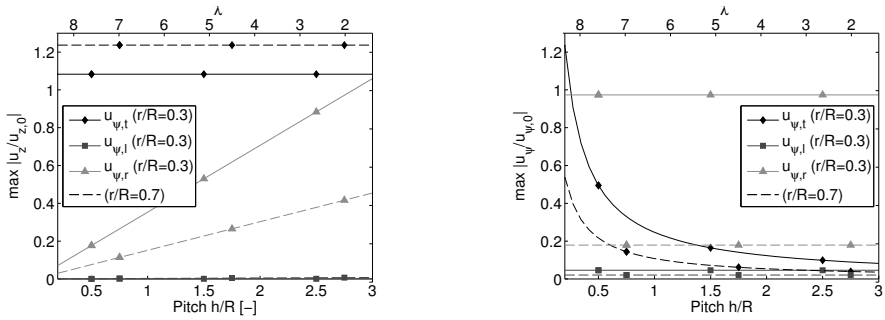

Figure 4.3: Comparison of the maximum azimuthal influence of each vortex components for a skew angle of $\chi = 30°$, different helix pitches and two radial positions: $r/R = 0.3$ (in black) and $r/R = 0.7$ (in grey). Left: Axial induction scaled with the axial induction at the middle of the rotor $u_{z,0}$. Right: Tangential induction scaled by $u_{\psi,0} = \Gamma_{\text{tot}}/2\pi r$.

4.3 Conclusions

The vortex model of Coleman et al. was extended for cases of finite tip-speed ratio by including the influence of the longitudinal tip-vorticity and the root-vortex. The analysis was not restricted to the axial component but included all the Cartesian and/or polar components. The influence of the bound vorticity was also mentioned so that the total velocity field induced by this vortex system can be determined in the entire domain. Results for an infinite elliptical cylinder (appendix A.5.4) were derived as part of this study.

The contribution of the longitudinal vorticity as a second harmonic term is consistent with observations and empirical formulae derived in the literature. On the one hand, the influence of the longitudinal tip vorticity appears to be of second order as long as the tip-speed ratio is large compared to unity. On the other hand, the influence of the root-vortex and the tangential vorticity on both the axial and tangential velocities should be included in BEM code yaw- or tilt-models. The inclusion of the tangential velocity component induced by the longitudinal vorticity is recommended. Simple engineering models were provided for each of the velocity components. The application of the model and its implementation into a BEM code for comparison with experiments and/or CFD calculations will be the topic of chapter 5.

Chapter 5

Simple implementation of a new yaw model

This chapter is based on the following publication: 'Investigation of a new model accounting for rotors of finite tip-speed ratio in yaw or tilt' [**29**].

Prologue The skewed vortex cylinder system studied in chapter 4 is used to derive a new BEM yaw model consistent with existing models. Results from BEM, CFD and vortex methods simulations are compared with measurements. The limitations of the new yaw model are studied.

5.1 Context

The analytical studies from Glauert in 1926 [70] and Coleman et al. in 1945 [46] form the basis of most yaw-models implemented in BEM codes. Yet, these models strictly apply to rotors of infinite tip-speed ratios. Coleman et al. used a skewed vortex cylinder to represent the wake behind a rotor. The ratio between the right cylinder induction and the skewed cylinder induction provides a correction factor that is applied in BEM codes.
Coleman's vortex system was extended to assess the effect of finite tip-speed ratio in chapter 4 [**24**]. Semi-analytical formulae and corresponding engineering models were provided for each velocity and vorticity components. The model can be applied both to yaw and tilt configurations of a rotor.
The MEXICO rotor [181] with data from the test case 2.1 of the IEA Task 29, first post-processed by Pascal [156] and finalized by Schepers et al. [179], will be used in the current study. Results from the in-house flow solver *EllipSys3D* [138, 197] were presented in a previous study by Sørensen [198] using geometry-resolving CFD, and in a study by Shen [187] using Actuator Line (AL) simulations [196]. Offsets between these high fidelity tools and the measurements were observed in previous studies [182, 198, 186]. Priority will be therefore given to the azimuthal trends when comparing with the measurement data.

5.2 Contribution and key results

Contributions The implementation of a new yaw model based on the skewed vortex cylinder results is established. Measurements from the MEXICO experiments [181] are compared to BEM, CFD and vortex methods simulations. The limitations of the model are studied.

Yaw model implementation It is assumed that the differences in induced velocities between the right and skewed vortex systems reflect the change of induced velocities that should be applied to correct momentum theory results in yawed configuration. It is chosen to use one single vortex cylinder representative of the rotor. This is the option chosen when using Coleman or Glauert yaw-models. The notations and engineering models from chapter 4 are adopted. The values of $u_{z,t}$

and $u_{\psi,r}$ for $\chi = 0$ are assimilated to AD momentum theory inductions. Using equation (4.5) and equation (4.6), the ratios between these induced velocities for a given χ and for $\chi = 0$ provides the following factors:

$$R_{z,t} = 1 + 2F_t(r,\chi)\tan\frac{\chi}{2}\cos\left(\psi - \psi_0\right), \qquad R_{\psi,r} = \frac{1}{1 - \cos\left(\psi - \psi_0\right)\sin\chi}\cos\chi \tag{5.1}$$

The above factors are applied to the momentum theory induced velocities aU_0 and $a'\Omega r$. They imply a redistribution of the inductions over the AD without changing their azimuthal averages. The former factor corresponds to the classical BEM yaw model. The total induced velocities to be used in the velocity triangle are $u_z = aU_0R_{z,t} + u_{z,r}$ and $u_\psi = a'\Omega r R_{\psi,r} + u_{\psi,t} + u_{\psi,l}$. The added components are absent in the non-yawed case. To further close the system, the vorticity distributions γ_l, γ_t and Γ_r need to be computed, which in turn require the knowledge of Γ_{tot}, h and χ. The skew angle can be determined using different methods (see e.g. [79, p. 99]), it is here assumed given. The value Γ_{tot} is taken as the average integrated value of circulation on the rotor blades. For simplicity, the helical wake pitch is assessed using the distance run by the tip-vortex in one rotor rotation: $h = \frac{2\pi R}{\lambda}\cos\chi$.

Preliminary results - comparison with measurements The conditions of the experiments are: $U_0 = 15$ m/s, $\Omega = 424.5$ RPM, $\rho = 1.237$ kg/m^3, $\lambda = 6.67$, $C_T = 0.75$. The yaw angle is $\theta_{\text{yaw}} = -30°$ using the sign convention of figure 5.1 and the blade pitch is $-2.3°$. Results from the

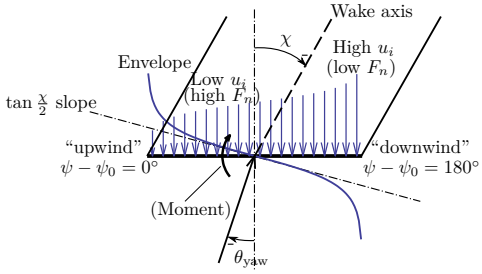

Figure 5.1: Top-view of the wake cross-section laying in the plane $y = 0$, data for $\chi = -30°$. The velocities induced by the tangential vorticity along the fore-aft diameter of the rotor ($z = 0$) are shown. Their relative fluctuations around the mean induction, or envelope, has a slope of $\tan\frac{\chi}{2}$. The distribution of velocity produces normal forces that can possibly (e.g. below stall) generate a restoring moment.

BEM yaw-model are compared with numerical simulations from geometry-resolving CFD, AL-CFD and a free-wake vortex-code. The new BEM model and the free-wake vortex-code were included in the aerodynamic module of *HAWC2* [110]. An AL simulation of the rotor using *EllipSys3D* was performed for the current study. The vortex code (VC) simulations are performed using the lifting-line formulation of the *OmniVor* library (Configuration 2-1, see section 9.3). The BEM-, AL- and VC implementations use the same airfoil data. The angle χ is determined from the free-wake code as $\chi = -36°$, a value consistent with the model $\chi = 1.2\,\theta_{\text{yaw}}$ [189]. The following observations were made: the mid-part of the blade (shown in figure 5.2) is well described by all codes; the vortex and AL code, which both use the same airfoil coefficient data, are in reasonable agreement at the blade root and in excellent agreement elsewhere.

Investigations on the implementation The VC is used as a reference to evaluate the performance of the new yaw-model since the latter is also vortex-based. Results are shown in figure 5.3. The new model performs best when the corrections to the inductions are applied outside of the BEM convergence loop ("BEM new(out.)" as opposed to "BEM new(in.)"). The concentrated root vortex, $u_{z,r}$ have a strong influence on the axial velocity. It is expected that an implementation using a superposition of vortex cylinders will moderate the influence of the root vortex (see chapter 6). The terms acting in the tangential direction were all observed to give a significant contribution to u_ψ. They can be listed from the most influential to the least as: $u_{\psi,t}$, $R_{\psi,r}$ and u_{ψ_l}. The amplitude of u_ψ with the new model is in good agreement with the one obtained from

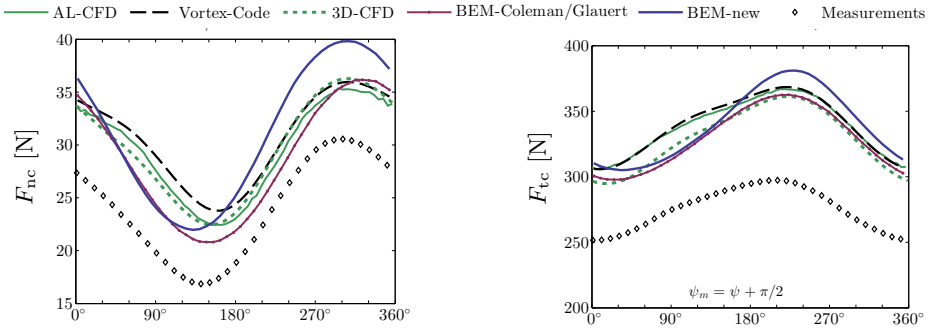

Figure 5.2: Tangential (left) and normal (right) loads (w.r.t. chord line) over the azimuth at $r = 0.6R$

the VC due to the contribution of $u_{\psi,t}$. The induced velocity in the tangential direction is nevertheless small compared to the wind contribution $U_0 \sin\theta_{\text{yaw}} \cos\psi$. The overall performance of the new yaw-model and Coleman/Glauert model compared to VC results is assessed using correlations and mean-square differences. The mean correlation coefficient of the tangential and normal loads compared to VC results is about 0.94 for both yaw-models. Yet, the relative squared distance to the VC loads is divided by two using the new yaw-model. The average correlation coefficient of the induced velocities increases from 0.36 to 0.90 using the new model. This gain is mainly due to the improved modelling of the tangential induction. The maximum squared distance to the VC inductions is divided by 1.2 by using the new yaw-model. Overall, the loads and induced velocities are closer to the vortex code results with the new model than with the Coleman/Glauert model.

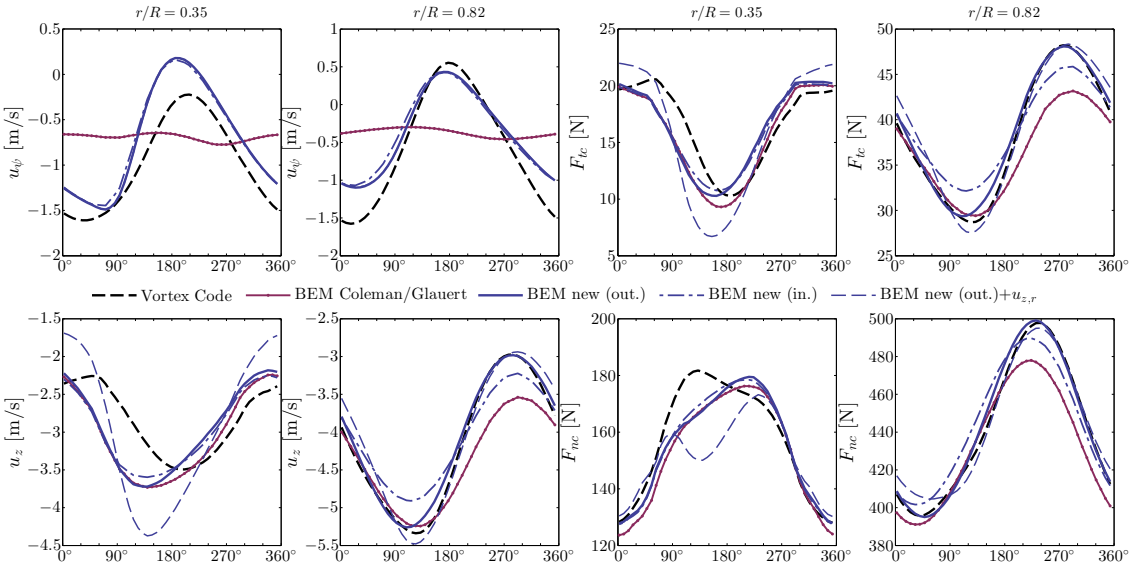

Figure 5.3: Induced velocities (left) and loads (right) over the azimuth $\psi_m = \psi + \pi/2$, for two radial positions. No dynamic stall model is used. Results at the inner part of the blade can be further improved using a superposition of cylinders.

The conclusions that follow were obtained using the results given in the article [29]. The effect of dynamic stall and stall delay are not included for the results of figure 5.3. BEM simulations with a

dynamic-stall model [114] and VC simulations without shed vorticity[1] were performed with focus on the inboard section. In [179], an increase of loading occurring at $\psi = 270°$ for $r = 0.25R$ was observed in the measurements. In [29], it was seen that this could not be explained by the influence of the root vortex but is partly due to the effect of shed vorticity. Also, the analysis revealed that the shift of loading towards lower azimuth at the inboard part of the blade cannot be due to the influence of a single root vortex. This shift is yet captured using a superposition of cylinders (see chapter 6).

Relaxation of assumptions and extension of the model The model presents four main assumptions which are: an infinite number of blades, a rigid wake, a constant circulation over the radius, and a constant circulation over the azimuth. Figure 5.4 illustrates the effect of wake distortion (left) and finite number of blades (right) for u_z (similar conclusions are drawn for u_ψ). The vortex code *OmniVor* with its prescribed-circulation formulation was used (Configuration 1, see section 9.3).
The wake distortion introduces phase and amplitude shifts along the blade which could potentially be modelled in a BEM extension. The rigid-wake assumption appears justified to a first order approximation since the main azimuthal and radial trends are captured.
Figure 5.4(right) shows the induction that is obtained for a number of blade of 1 and 3 when the tip-loss factors from Prandtl (Pr.) or Glauert (Gl.) [28] is used together with the new yaw-model (derived for an infinite number of blades). Glauert's formula appears satisfactory to model the effect of finite number of blades on the axial induction but over-predicts the changes in tangential induction [29]. The yaw-model derived for an infinite number of blades can be applied with sufficient accuracy together with Glauert's tip-loss factor for three-bladed rotors.

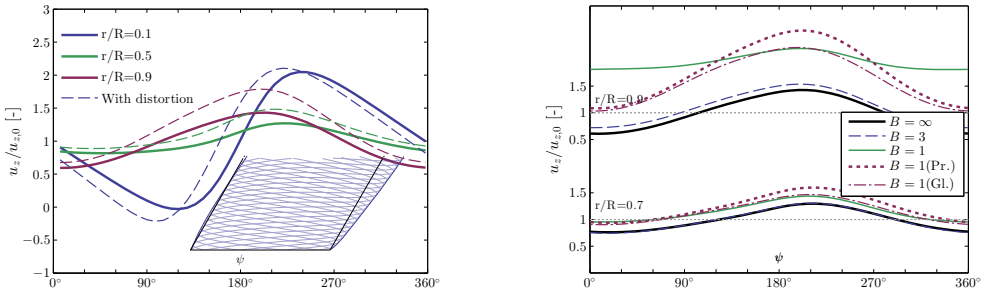

Figure 5.4: Numerical investigation of the model limitations. Left: Effect of wake distortion on the vortex model for a number of blades of 10 representing an infinite number of blades (99% accuracy). The inset figure shows the outline of the wake with and without distortion. Right: Azimuthal variation of the axial induced velocities with the number of blades for two radial positions.

5.3 Conclusions

The implementation of a new yaw-model based on recently developed vortex-theory results was presented. The model relaxes the assumption of infinite tip-speed ratios used in current BEM yaw-models. Three tools using the same 2D airfoil coefficient data were used in this study. Good agreement was found between the actuator-line and the vortex code simulations. The latter was

[1] In these simulations, the shed vorticity is fully removed: It doesn't contribute to the wake rollup and to the rotor inductions. Ideally only the latter contribution should be removed.

used as a reference to validate the new vortex-based yaw-model. The induced velocities and loads obtained with the new BEM yaw-model showed better agreement with the vortex code than the standard yaw-model implementation. The influence of a single root vortex was not seen to be the source of the shift of loading towards lower azimuth at the inboard part of the blade. The new yaw-model combined with the effect of dynamic stall showed reasonable agreement for the inner part of the blade which is usually difficult to model. The limitations due to the assumptions of infinite number of blades and rigid-wake were briefly discussed. These effects could be accounted for using engineering models. The assumption of rigid wake was seen to be justified to a first order approximation while the effect of finite number of blades can be consistently modelled using Glauert tip-loss factor. Future work will address the relaxation of the assumption of constant circulation along the blade azimuth[2]. The next chapter addresses the relaxation of the constant circulation along the blade radius.

[2]Chapter 7 relaxes this assumption for the case of infinite tip-speed ratio.

Chapter 6

Advanced implementation of the yaw model - Pre-study

This chapter is partially based on results given in the following publication: 'Investigation of a new model accounting for rotors of finite tip-speed ratio in yaw or tilt' [**29**].

Prologue The BEM yaw model presented in Chapter 5 can be improved by using a superposition of skewed vortex cylinders. The pitches of the different cylinders can be determined using the results from the superposition of right cylinders shown in Chapter 2. Engineering formulae for the velocity field outside of the skewed cylinder are required for fast numerical evaluation.

Contributions The velocity field on the fore-aft diameter for $r > R$ is given analytically. The elements necessary to implement a more advanced yaw models are given. A preliminary application is shown.

6.1 Introduction

In a combined publication by Heyson and Katsoff [86], Heyson used a superposition of cylinders to study yawed rotors with radially-varying but azimuthally-constant circulation. Heyson later compared his results with experiments [87] finding good agreement in the near-wake, but decreasing accuracy in the far-wake due to wake distortion. Heyson used numerical integration to compute the axial induction from the tangential vorticity of the different cylinders. The study consisted in a pure vortex model and was not linked to a BEM code. Chaney et al. [41] used a superposition of two skewed cylinders to model the stalled inner-part of the rotor. Despite its simplicity the cylindrical vortex model with a step circulation was shown to reveal important features that other models would not capture.

The current study will present the elements needed to determine the velocity field from a superposition of skewed cylinders in view of implementing a BEM yaw model. Preliminary elements are given in this chapter but further work is required to complete the study. The current chapter will be structured as follows. First, engineering formulae for the velocity field outside of the skewed vortex cylinder will be presented. Second, the determination of the helical pitch of the vortex cylinder is discussed. Third, the implementation of the yaw model using a superposition of cylinders is given. Third, results from the partial implementation done in [**29**] will be discussed.

6.2 Models for the velocity field outside of the skewed cylinder

Unlike the right vortex cylinder, the induced velocities are not zero outside of the skewed vortex cylinder. Care should then be taken when using a superposition of skewed cylinders to include the influence of the cylinders outside of their radii. Despite the fact that the full velocity field can be obtained from the results of Chapter 4 using numerical integration, closed form engineering models are preferred for their lighter computational cost. The models derived at the time of writing are presented in this section.

Velocity induced by the root vortex The closed-form analytical formulae from equation (4.6) can directly be used. In practice though, the influence of the root vortex can be neglected since the circulation usually drops to zero towards the root of the rotor. The "root-vortex-circulation" is then carried by and distributed amongst the first inner cylinders.

Velocity induced by the tangential vorticity Following the approach of Coleman et al. [46] the velocity on the fore-aft diameter is sought. The three integrals Coleman et al. introduced are here evaluated for $r > R$,

$$u_{z,t}(r > R, \psi = 0) = \frac{\gamma_t}{2}(1 + K_2 + K_3) \tag{6.1}$$

$$K_3(r, \chi) = 2F_t(r, \chi) \tan\frac{\chi}{2} \tag{6.2}$$

$$K_2(r, \chi) = -\frac{r\sqrt{1+m^2}}{2m^2\left(r^2 - R^2\right)}\left(\frac{r\left(\sqrt{C-B} + \sqrt{B+C}\right)}{\sqrt{r^2 + m^2R^2}} + \frac{\sqrt{C-B} - \sqrt{B+C}}{\sqrt{1+m^2}}\right) \tag{6.3}$$

with

$$B = 2r\sqrt{(1+m^2)(r^2+m^2R^2)}, \quad C = (2+m^2)r^2 + m^2R^2 \tag{6.4}$$

The azimuthal variation of the axial velocity is modelled based on the value at the fore-aft diameter as:

$$u_{z,t}(r < R, \psi) \approx \frac{\gamma_t}{2}(1 + K_3(r))\cos(\psi) \tag{6.5}$$

$$u_{z,t}(r > R, \psi) \approx \frac{\gamma_t}{2}(1 + K_2(r))\cos(2\psi) + K_3(r)\cos\psi \tag{6.6}$$

The model values are exact for $\psi = 90°$. The comparison between the model and the numerical integration on the rotor plane is shown in figure 6.1.

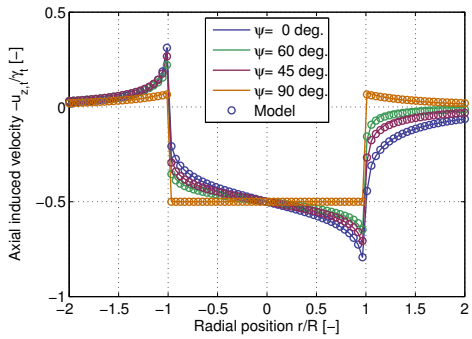

Figure 6.1: Comparison between engineering model and numerical integration on the rotor plane. The engineering model values are represented by circles.

Velocity induced by the longitudinal vorticity No models were derived so far.

6.3 Helical pitch for the superposition of skewed cylinders

Performing the system closure in the case of the skewed cylinder is more complexed than in the right cylinder case. A proper account of the convection velocities in the far wake is required. To a first approximation, it is thus suggested to determine the intensities of each vortex systems as if the cylinders were not skewed. The results from Chapter 2 could then be applied to determine the helical pitches. More details for the discrete implementation of the system closure can be found in section E.5. The steps required for the calculation of the helical pitches are given in section E.7.

6.4 Yaw model implementation using a superposition of skewed cylinders

The notations of Chapter 2 are adopted and partially reproduced in figure E.1. The intensity of each vortex system are determined according to equation (1.1),

$$\boldsymbol{\Gamma}_r = -\sum_i \tilde{\Gamma}_i \boldsymbol{e}_z = -\Gamma_1 \, \boldsymbol{e}_z, \qquad \boldsymbol{\gamma}_{t,i} = -\frac{\tilde{\Gamma}_i}{h_i} \boldsymbol{e}_\psi, \qquad \boldsymbol{\gamma}_{l,i} = \frac{\tilde{\Gamma}_i}{2\pi R_i} \boldsymbol{e}_z, \tag{6.7}$$

and the system closure discussed in section 6.3 is used to fully determined $\gamma_{t,i}$. A single root vortex represents the superposition of all the other root vortices. The total induction from all the vortex

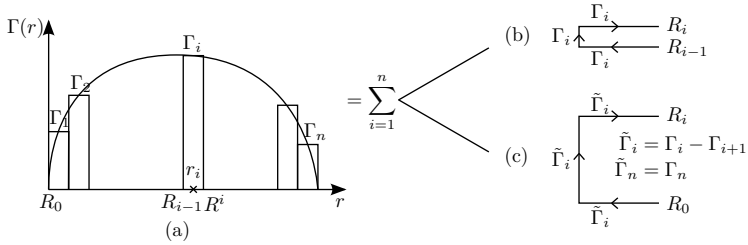

Figure 6.2: Principle of superposition for a radially varying bound circulation (a): decomposition using two cylinders (b) or using one cylinder and a root vortex (c). The latter allows a convenient application of the constant circulation model.

systems for the $\diamond$-component at a control point j is:

$$u_\diamond(r_j, \chi, \psi) = u_{\diamond,r}(r_j, \chi, \psi) + \sum_i \left[u_{\diamond,t,i}(r_j, \chi, \psi) + u_{\diamond,l,i}(r_j, \chi, \psi) \right] \tag{6.8}$$

Similar to the implementation presented in section 5.2, the momentum theory inductions are corrected by comparing the inductions from the right and the skewed cylinder models. The velocities induced by a superposition of right cylinders is given by equation (2.3):

$$u_z(r_j, \chi = 0) = -\sum_{j=i}^{n} \frac{\gamma_j}{2} \qquad , \qquad u_\psi(r_j, \chi = 0) = -\sum_{j=1}^{n} \frac{\tilde{\Gamma}_j}{4\pi r} = -\frac{\Gamma_i}{4\pi r} \tag{6.9}$$

The difference between the superposition of right cylinder and the single right cylinder case is that both the longitudinal tip-vorticity and the root vortex contribute to the tangential induction in the former case whereas the longitudinal tip-vorticity does not contribute in the latter. On the other hand, the tangential vorticity is the only one to contribute to the axial induction in both cases.

The correction factors applied to the momentum theory inductions are:

$$R_z(r_j,\chi,\psi) = \frac{\sum_i u^i_{z,t}(r_j,\chi,\psi)}{u_{z,t}(r_j,\chi=0)}, \qquad R_\psi(r_j,\chi,\psi) = \frac{u_{\psi,r}(r_j,\chi,\psi) + \sum_i u_{\psi,l,i}(r_j,\chi,\psi)}{u_\psi(r_j,\chi=0)}. \tag{6.10}$$

The remaining induced velocities present in the skewed cylinder case that are absent in the right cylinder case are: $u_{z,r}$, $u_{z,l}$ and $u_{\psi,t}$. The influence of the other axial components are added to the total induction in a way similar to the single cylinder case (see section 5.2). For simplicity the influence of the root vortex may be omitted at once since the circulation usually drops to zero towards the root of the rotor. The "root-vortex-circulation" is then carried by and distributed amongst the first inner cylinders. The component $u_{z,l}$ can also be neglected for simplicity since its influence is negligible compared to the other components (see Chapter 4).

6.5 Partial approach - focus on the inboard part of the blade

A superposition of skewed cylinder was used in [29] to investigate the possible improvement on yaw modelling compared to the case with a single cylinder. The study presented two limitations: the velocity field outside of the vortex cylinders were not modelled and the different cylinders had the same helical pitch for simplicity. A constant pitch value simplifies the derivations but violates the kinematic condition across the vortex cylinders (see section 6.3). Preliminary results using only the inner induced velocities are shown in figure 6.3 to illustrate the applicability of the method. The operating conditions correspond to the test case used in Chapter 5 for the MEXICO experiment. The error introduced by using only the inner velocities is expected to be small closer to the root

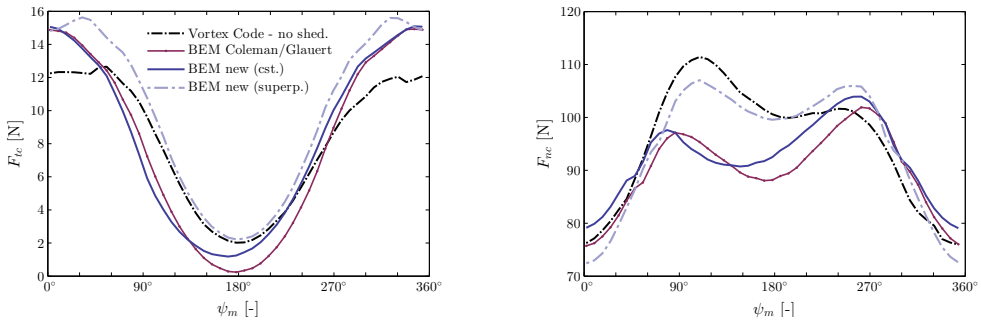

Figure 6.3: Normal and tangential loads with respect to the chord line for $r/R = 0.25$. The yaw-model using a superposition of vortex cylinders shows improved agreement with the vortex code.

since few cylinders have a radius lower than the control point at this location. The comparison of the constant-circulation yaw-model and the varying-circulation yaw-model reveals a clear improvement when using the second model since this model shows closer agreement with the vortex code results. The increased normal loading around the 90°-azimuth is well captured by the model. Yet, further investigation using both inner and outer velocities are required to fully assess the performance of the model.

6.6 Conclusions

The possibility of using a superposition of skewed cylinders to improve yaw-modelling was considered. The assumption of constant circulation can be relaxed at a relatively low cost. To achieve this, engineering models were provided for the velocity field outside of the skewed cylinder. The use

of the helical pitches from the superposition of right cylinders is suggested as a first approximation. The implementation of the yaw-model was discussed. Preliminary results showed that improved accuracy can be obtained. The shift of loading towards lower azimuth at the inboard part of the blade was captured using a superposition of cylinders and can thus not be attributed to the influence of the root vortex. Further work is required to fully model the velocity field outside of the skewed cylinder and fully implement this more advanced yaw model.

Part III

Vortex models for rotors in shear and unsteady inflow

7 Shear-model of Gaunaa et al. 43
- 7.1 *Context*
- 7.2 *Key-results and contributions*
- 7.3 *Conclusions from the article*

8 Model for unsteady circulation and inflow. 47
- 8.1 *Context*
- 8.2 *Contributions and key results*
- 8.3 *Conclusions*

Chapter 7

Shear-model of Gaunaa et al.

This chapter is entirely based on results given in the following publication: 'Modelling the influence of wind shear using a simple vortex rotor model' - [67]. The author had only a modest contribution to the article. The content will hence only be briefly presented without proof.

Prologue Due to the friction of the atmosphere with the earth surface, the wind profile is not uniform. The fact that the velocity increases with height induces shear stresses in the fluid and vorticity is present in the transverse direction. By extension, one will refer to wind shear or sheared inflow to describe such velocity profile. The simplest model of a shear profile consists in a step of wind speed, which in turn can be modelled by a vortex sheet. The current chapter will add the effect of this vortex sheet to the vortex cylinder model from Chapter 1.

7.1 Context

Wind shear plays a significant role on the loads and power production of a wind turbine. However, previous studies have shown significant deficiencies in state-of-the-art models attempting to include the effect of wind shear on wind turbine performance [127]. Madsen et al. [127] used different BEM models to simulate a wind turbine operating in a strongly sheared inflow and compared the results to the ones of more advanced codes. Shen et al. [188], Sezer-Uzol and Uzol [183] used free-wake vortex simulation to investigate the aerodynamic loads and performance of a horizontal axis wind turbine in non-uniform inflow. These three studies found that the power output in a sheared inflow is lower than in uniform inflow. However, the full Navier-Stokes computations conducted by Zahle and Sørensen [226] showed an increase in power production when operating in shear, which was largely proportional to the increase in the available power in the incoming flow. An analysis of the local power coefficient (based on local far upstream velocities) showed that the efficiency was highest on the lower half of the rotor and it was explained to be due to the differences in local angle of attack and tip speed ratio. Micallef et al. [137] used oblique ring elements to model the wake of a turbine in shear flow and to obtain an analytical solution of the deflection of the wake. Due to the inclination of the vortex rings, a vertical velocity component is induced from the low velocity side to the high velocity side. Thus, the model predicted an upward movement of the wake in agreement with predictions by various free-wake vortex simulations [183, 73].
The current study employ a simple analytical rotor model based on vortex theory to investigate and explain some of the main mechanisms at play for an idealized wind turbine rotor operating in a sheared inflow.

7.2 Key-results and contributions

Contribution from the author The author only contributed to the result concerning the induction of an infinite vortex cylinder of tangential vorticity of arbitrary cross section. The result is

usually found in the literature using solid angle arguments (see e.g.[200, p. 155], [93, p 76], [212]). Different arguments are used in this article.

Models studied Gaunaa et al. considered three different models: rotor in uniform flow with uniform loading; rotor in uniform flow with a step in loads; rotor in step-shear with a step in loads. Only the results from the last model will be presented here and the reader is referred to the reference for more details.

Cylindrical vortex model of a rotor in shear with large tip-speed ratio The velocity profile upstream is assumed to be equal to $U_0 - \gamma_{s,0}/2$ for $y < 0$ and $U_0 + \gamma_{s,0}/2$ for $y > 0$. This step of velocity is induced by an infinite vortex sheet at $y = 0$ of intensity $\gamma_{s,0}$. Due to the step in velocity the rotor loading is different in both regions[1]. The label 1 is attributed to the "lower" domain and 2 to the "upper" domain. The thrust coefficient, the circulation and far-wake velocity in the region $i = 1..2$ are noted C_{t_i}, Γ_i and U_{w_i} (see figure 7.1) with $C_{t_i} = \frac{\Gamma_i \Omega}{\pi U_{0_i}}$. The wind turbine wake is represented using a vortex cylinder with different tangential intensities in the upper and lower parts. The shear vorticity and the change of wake vorticity between the two regions is represented with an infinite vortex sheet of varying intensity. The system is analysed using values at infinity upstream and downstream. The continuous variation of vorticity is not accounted for. Further, the possible vertical displacement of the shear vortex sheet upstream and downstream of the rotor is disregarded. The system may be viewed as consisting of the following vortex sheets:
• an infinite vortex sheet of intensity $\gamma_{s,0}\boldsymbol{e}_x$ at $y = 0$ inducing the "backbone" step of wind speed
• two semi-infinite "open-half-pipes" of tangential vorticity γ_{0-1} and γ_{0-2} respectively
• a rectangular vortex sheet within the cylinder of intensity $\gamma_{1-2}\boldsymbol{e}_x$, located at $y = 0$ and extending from $x = [-R; R]$ and $z = [0; +\infty[$, resulting from the change of loading and vorticity between the two semi-infinite half-pipes
• a rectangular vortex sheet within the cylinder of intensity $\Delta\gamma_s \boldsymbol{e}_x$, located at $y = 0$ and extending from $x = [-R; R]$ and $z = [0; +\infty[$, which corresponds to the variation in shear intensity due to the lower convection velocity within the cylinder

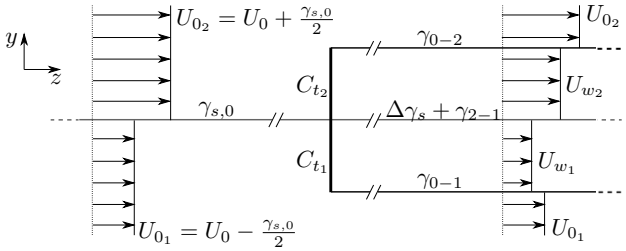

Figure 7.1: Side view of the vortex model and coordinate system. A consistent system is obtained when the velocities in the far wake are as represented in this figure (see Gaunaa et al. [67]).

The presence of the vortex cylinder slows down the shear vorticity which is then assumed to evolve from $\gamma_{s,0}$ upstream to $\gamma_{s,w} = \gamma_{s,0} + \Delta\gamma_s$ downstream (see figure 7.2). By conservation of vorticity the shear vorticity strength upstream and downstream verifies $\gamma_{s,0}V_{c,0} = \gamma_{s,w}V_{c,w}$, where V_c is the convection velocity of the vortex sheet.

Vorticity strengths - Results only By consideration of the convection velocity of the vortex cylinder sheet far downstream the vortex strengths are (a positive convention is adopted as opposed

[1]In the paper, the case of different loadings without a step of velocity is also considered.

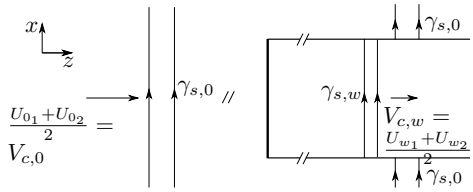

Figure 7.2: Top view of the model of the shear vortex sheet intensity as it passes through the vortex cylinder

to the other chapters):

$$\gamma_{0-1} = \frac{\Omega}{2\pi}\frac{\Gamma_1}{V_{c,0-1}}, \quad \gamma_{0-2} = \frac{\Omega}{2\pi}\frac{\Gamma_2}{V_{c,0-2}}, \quad \gamma_{2-1} = \frac{\Omega}{2\pi}\frac{(\Gamma_1 - \Gamma_2)}{V_{c,w}} \tag{7.1}$$

It can be shown [67] that a consistent vortex system is obtained when the far wake velocities within the half cylinders are constant and equal to

$$U_{w_i} = U_{0_i} - \gamma_{0-i} \tag{7.2}$$

and with the following vorticity strength:

$$\gamma_{0-i} = U_{0_i}\left(1 - \sqrt{1 - C_{t_i}}\right) \quad \Rightarrow \quad U_{w_i} = U_{0_i}\sqrt{1 - C_{t,i}} \tag{7.3}$$

$$\gamma_{2-1} = \frac{C_{t_1}U_{0_1}^2 - C_{t_2}U_{0_2}^2}{U_{w_1} + U_{w_2}} \tag{7.4}$$

Since the velocities in the far wake are constant, the condensation of the shear vorticity is:

$$\Delta\gamma_s = \gamma_{s,0}\left(\frac{U_0}{V_{c,w}} - 1\right) = \gamma_{s,0}\left(\frac{2U_0}{U_{w_2} + U_{w_1}} - 1\right) \tag{7.5}$$

Rotor variables The axial induction is defined in each region with respect to the "local" free-stream U_{0_i} as:

$$a_i \equiv \frac{U_{0_i} - U_{w_i}}{2U_{0_i}} \tag{7.6}$$

Using for each region of the rotor the "local" free-stream velocity, a KJ analysis leads to:

$$C_{t_i} = 4\,a_i\,(1 - a_i)\,, \qquad C_{p_i} = 4\,a_i\,(1 - a_i)^2 \tag{7.7}$$

The results have the same form as 1D momentum theory results indicating the independence of the two rotor regions.

Balance of longitudinal vorticity - Result only Both the wake vorticity and the shear vorticity are stretched in the axial direction. The wake vorticity in regions 1 and 2 are stretched due the difference of wind speeds in each regions. The shear vorticity is stretched due to the wind-speed reduction within the wake. This axial stretching results in the formation of axial vorticity. It is shown in [67] that the two effects are of opposite sign and equal strength and they thus cancel out.

7.3 Conclusions from the article

Application of the model to a non-uniformly loaded rotor in non-uniform inflow showed that 1D momentum theory is valid in a local sense. Thus, when defined according to the local free-stream velocity, the power coefficient of an ideal rotor was found to be unaltered by the presence of shear. Finally, a study of the influence of the inherent deformation of the vorticity sheets generated by the rotor and the wind shear revealed that there is no generation of axial vorticity and hence no cross-shear induced velocities. Thus, the model, unlike most free-wake vortex models, does not

predict any cross-shear deflection of the wake. All free-wake analyses in shear known to the authors have not taken into account the deformation of the shear vorticity. Such account is considered in the current vortex code implementation as discussed in Chapter 14.

Chapter 8

Model for unsteady circulation and inflow

This chapter is based on results given in the following publication: 'Superposition of vortex cylinders for steady and unsteady simulation of rotors of finite tip-speed ratio' [**26**]. At the time of writing the article is under review.

Prologue The superposition of cylindrical vortex wake models for finite tip-speed ratios presented in Chapter 2 is extended for unsteady simulations. The term unsteady is here understood as a change in time of the rotor circulation between two azimuthally constant circulation distributions. This case can correspond to a uniform change of wind speed on the rotor area, or a synchronous pitching of the blades. Results from Chapter 2 [**26**] (with details provided in Appendix E) will be used. Similar to the approach chosen in Chapter 2, an elementary system is introduced first before using a superposition of elementary systems.

8.1 Context

An equilibrium between loads and velocity inductions is not reached instantaneously if a change occurs in the rotor conditions. Changes at the rotor propagates downstream and it takes time for the wake to adapt to the new conditions. This can be understood in terms of the vorticity which is shed by the rotor in response to time changes of bound circulation. BEM codes implement these effects using dynamic inflow models. Øye [79, p. 94] and Pitt and Peters [159] are examples of contributors to the development of dynamic inflow models currently in use. Despite their theoretical grounds, the models require a certain level of empiricism. The model by Øye uses first order systems which time constants need tuning. The time constants were determined using an unsteady vortex ring model of a given wind turbine [79, p. 94]. Similar implementation of the model [128, 112] rely on tuning based on actuator disk simulations.
The current study will investigate the possibility to use the vortex cylinder model to study uniform unsteady changes in the rotor conditions. The model was partially inspired by the electromagnetic study of Protheroe regarding the transient field outside a solenoid [163].

8.2 Contributions and key results

Contributions The key elements required to implement an unsteady cylindrical model were introduced. A proof of concept of the model was presented. The crude assumptions applied appeared satisfactory. The model can e.g. be applied to tune dynamic inflow models.

Elementary unsteady model The elementary unsteady vortex model for a step change of circulation is illustrated in figure 8.1. A steady state solution of the rotor is assumed at $t = 0$, where the total rotor circulation is Γ_0 and the free-stream is U_0. The wake hence consists of a semi-infinite cylinder and a root vortex with intensities determined by equation (1.1). At $t = t_1$,

the rotor circulation is assumed to jump to the value Γ_1. The wind speed may also change to the value U_1. The change of circulation will then be assumed to be convected at the velocity that the far-wake cylindrical sheet would have for a steady state condition of intensity Γ_1 and under the free-stream wind condition U_1. At a given instant $t > t_1$, the wake consists in two vortex cylinders, two root vortices, and one wake vortex disks. The convection velocities of the two systems, labelled 0 and 1, are different. In this study, it will be assumed that the two systems remain adjoin. More advanced implementations and choices of advection velocities could be done, but simplicity is here preferred. The location z_1 where the change of circulation is present in the wake is thus modelled

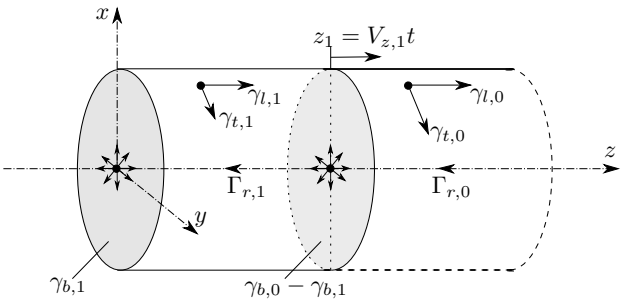

Figure 8.1: Illustration of the unsteady vortex cylinder model. The wake consists of several finite cylinders along z (two represented here), and a superposition of cylinders radially (one represented here). Each cylinder in the wake has a different circulation intensity. A vortex disk is present in between each cylinder. It is here assumed that the systems do not overlap even if their convection velocity is different.

using the convection velocity of the system 1, as given in Chapter 2

$$z_1(t) = V_{z,1}\, t = \frac{U_1}{2}\left(1 + \sqrt{1 - C_1}\right) t \tag{8.1}$$

where $C_1 \equiv \frac{\Omega\Gamma_1}{\pi U_1^2}(1 + a'_{c,1})$. It is noted that the index refers to the vortex system 1 and is not a radial index (handled in the next paragraph). The tangential velocity will be assumed to reach the steady state value instantaneously but the axial velocity is assumed to be influenced by both the finite and infinite vortex systems. The induced velocity from a finite cylinder of tangential vorticity $\gamma_{t,1}$, extending between z_0 and z_1 can be found in [**23**]:

$$u_r(r, z, z_0, z_1) = \frac{\gamma_{t,1}\sqrt{R}}{2\pi\sqrt{r}}\left[\frac{2 - k^2(r,z)}{k(r,z)} K\left(k^2(r,z)\right) - \frac{2}{k} E\left(k^2(r,z)\right)\right]_{\zeta_0}^{\zeta_1}, \tag{8.2}$$

$$u_z(r, z, z_0, z_1) = \frac{-\gamma_{t,1}}{4\pi\sqrt{rR}}\left[\zeta k(r,z)\left(K\left(k^2(r,z)\right) + \frac{R - r}{R + r}\Pi\left(k^2(r,0), k^2(r,z)\right)\right)\right]_{\zeta_0}^{\zeta_1} \tag{8.3}$$

where $k(r, z)$ is defined in equation (1.2) and where the brackets stand for the primitive integral, function of ζ, to be evaluated between $\zeta_1 = z - z_1$ and $\zeta_0 = z - z_0$. The tangential vorticity $\gamma_{t,0}$ and $\gamma_{t,1}$ of the two systems are determined from the results of Chapter 2 (see also equation (E.5)). The total axial velocity is obtained by summation of the two systems

$$u_z(r, z, t) = u_z(r, z, z_0, z_1(t)) + u_z(r, z, z_1, +\infty) \tag{8.4}$$

and the loads can directly be obtained from the Kutta-Joukowski relation.

Model for a step change between two circulation distributions A step change of circulation distribution is modelled using a superposition of elementary models presented above. The circulations $\Gamma_0(r)$ and $\Gamma_1(r)$ are discretized into the values $\Gamma_{i,0}$ and $\Gamma_{i,1}$. The free-stream velocity is assumed to be uniform and is respectively noted U_0 and U_1 before and after t_1. The two values

may be different. Using equation (E.30), the convection velocity of the cylinder i is

$$z_{i,1}(t) = V_{z,i,1}\, t = \left(U_1 + \sum_{j=i+1}^{n} \gamma_{t,j,1} + \frac{\gamma_{t,i,1}}{2} \right) t \tag{8.5}$$

where the values of $\gamma_{t,i,1}$ have to be determined according to the procedure of Chapter 2 (detailed in section E.5 and section E.7).

Unsteady simulation To assess the performance of the unsteady vortex cylinder model, the experimental test case of the pitch change of the Tjæreborg wind turbine is used. This case is described in details in the book of Hansen [79, p. 94-95]. The blades of the turbines undergo two pitch steps at $t = 2$s and $t = 32$s between the angles 0° and 3.7° for a wind speed of 8.7m/s. In the mentioned reference, the experimental results are compared with BEM code results. An identical BEM implementation to the one presented by Hansen was used for the current study. Based on this implementation a vortex cylinder (VC) code was developed. Tip-losses were included in the BEM results. On the other hand the vortex cylinder model does not include tip-losses. Consequently, the pitch values used for the vortex cylinder model were slightly adjusted to match the steady state values of the torque obtained with the BEM code. It was observed that the steady vortex cylinder model reproduced well the steady state values of the torque if pitch angles of 1° and 4.7° were used instead of 0° and 3.7°. Since the change of pitch values is moderate, it can be assumed that the inflow behavior obtained with the vortex cylinder model with infinite number of blades will still be similar to the one measured. The steady state values of the circulation and convection velocities obtained by the steady vortex cylinder model for these two pitch angles are shown in figure 8.2(left).

In both the BEM and VC models the pitch is assumed to change instantaneously, but the induced velocities adapt progressively. In the VC model, the tangential induction adapts instantenously[1]. The BEM code implementation use Øye dynamic inflow model [79, p. 94]. The model is based on two first order filters that govern the time behavior of the induced velocities. For the unsteady vortex cylinder model, it is assumed that the circulation instantaneously takes the steady state value. Yet, this change of circulation is progressively propagated downstream.

Results from the two codes are displayed with the measured values in figure 8.2(right). Since the simulations were not aero-elastic simulations, the oscillations observed in the measurements cannot be captured by either of the codes. Comparing the BEM code results with the ones from the BEM code used in figure 9.8 of [79], it is seen that the two implementations are indeed returning identical values, hence validating the current BEM implementation. From figure 8.2(right) it is seen that both the vortex cylinder (VC) and the BEM results agree to a high degree with the measurements. The vortex cylinder model posses three main advantages. First, the VC model does not rely on empirical constants as opposed to the BEM dynamic inflow model. In fact, as mentioned in the book of Hansen [79], the BEM dynamic inflow time-constants were tuned using a simple vortex model based on vortex rings. Second, unlike the BEM model, the results from the VC model are independent of the value of the time-step. Third, the VC model provide the unsteady velocity field in the entire domain. From the agreement of the VC model with the measurements, it appears that the different assumptions in the unsteady model are fair. The model can thus be used to tune dynamic inflow models in BEM codes

[1] The tangential induction within a finite cylinder of longitudinal vorticity bounded by two vorticity disks and with a root vortex is constant (using the axisymmetry and Ampere's theorem).

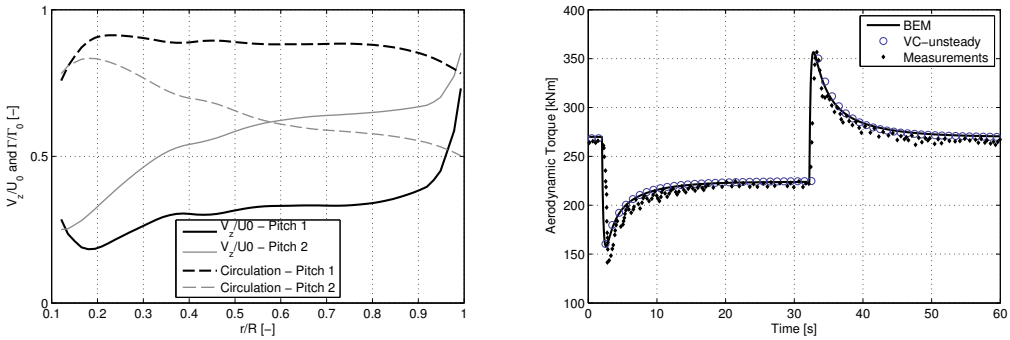

Figure 8.2: Simulation of the Tjæreborg turbine. Left: Steady values of the circulation and convection velocity for two values of the pitch angle obtained with a superposition of 60 cylinders. Right: Unsteady simulation showing the aerodynamic torque while the turbine undergoes a pitch step at $t = 2$s and $t = 32$s. Both the BEM and Vortex cylinder (VC) codes agree to a high degree with the measurements. The VC cylinder does not use a dynamic inflow model and do not rely on empirical constants as opposed to the BEM code.

8.3 Conclusions

A vortex cylinder model was described to model a rotor of infinite number of blades and finite tip-speed ratio under uniform unsteady conditions. For simplicity only uniform step changes in time of the rotor circulation were considered. The circulation on the rotor was allowed to change radially using a superposition of cylinders. Analytical formulae for the finite length cylinder were used. Simulations showed good agreement with both measurements and unsteady BEM simulations. The unsteady vortex cylinder model has the advantage of not requiring an empirical dynamic inflow model, unlike its BEM counter part. Also, the unsteady velocity field is available in the entire domain thanks to closed form formulae. The model can be used to tune or develop new dynamic inflow models.

Epilogue The model can be extended such that an elementary vortex cylinder is emitted at each time step. In such case, the use of vortex cylinders may be replaced by vortex rings carrying the same vorticity (see e.g.de Vaal et al. [57]).

Part IV

Implementation of a vortex code for aero-elastic simulations

9 Description of the implemented vortex code 53
9.1 *Introduction*
9.2 *Implementation and features*
9.3 *Specific configurations used in publications*
10 Vortex code validation and illustration. 63
10.1 *Simple validation of the vortex particle method*
10.2 *Lifting Line*
10.3 *Lifting surface*
10.4 *Thick bodies*
10.5 *Unit-tests*
10.6 *Further validation*
11 Examples of wind energy validation cases 69
11.1 *Comparison with BEM and Actuator-Line simulations*
11.2 *Wakes and flow field for uniform inflows*
11.3 *Effect of Viscosity - Comparison with AD*
11.4 *Effect of Turbulence - Comparison with Lidar and AD*
11.5 *Conclusions*

Chapter 9

Description of the implemented vortex code

This chapter presents contents given in the following article: 'Validation of vortex code viscous models using lidar wake measurements and CFD' **[30]**. Additional features were implemented since this article was written. Theses changes were directly incorporated in the current chapter.

Prologue The term vortex-based method is understood as both vortex models and vortex methods. The previous chapters of this thesis (in Part I to Part III) focused on simple vortex models developed during this work. The remaining chapters of this thesis will focus on the application of vortex methods to the topic. The current chapter presents the vortex code implemented during the PhD. More details about vortex methods are found in the book of Cottet and Koumoustakos [52].

9.1 Introduction

The purpose of the implemented vortex code is twofold. First, it is implemented in view of its application to aeroelastic simulation of wind turbines in complex inflows (see Part V). Second, the vortex code is intended to be used as a research tool to study various vortex configurations and study the contributions of different vortex components separately. The first condition requires the code to support long time-series simulation for standard load cases applications while remaining as computationally inexpensive as possible. Indeed, aero-elastic simulations require time-series of length varying from 10 min to 1 hour. Small time steps are also required to capture the structural frequencies and a reasonable range of the turbulence spectrum. The second condition requires the code to stay as general as possible so that it could be used to improve BEM models or investigate concepts such as kites, tip-rotors, tip-vanes, shrouded rotors, or vertical axis wind-turbines.
The first part of this chapter will describe the individual features of the code. The second part will highlight the different configurations (combination of features) that were used within this thesis.

9.2 Implementation and features

Presentation of the code The implemented library, named *OmniVor*[1], is a vortex code for computation of 2D and 3D incompressible fluid dynamics. Vortex methods are a particular set of Lagrangian methods that use the vorticity $\boldsymbol{\omega}$ as a primary variable. Traditional CFD uses velocity-pressure variables in an Eulerian formulation. The vorticity (transport) equation, for an incompressible homogeneous Newtonian fluid under conservative forces is

$$\frac{\partial \boldsymbol{\omega}}{\partial t} + \underbrace{(\boldsymbol{u}\cdot\nabla)}_{\text{convection}}\boldsymbol{\omega} \overset{\wedge}{=} \frac{d\boldsymbol{\omega}}{dt} = \underbrace{(\boldsymbol{\omega}\cdot\nabla)\boldsymbol{u}}_{\text{strain}} + \underbrace{\nu\Delta\boldsymbol{\omega}}_{\text{diffusion}} = \operatorname{div}(\boldsymbol{u}\otimes\boldsymbol{\omega}) + \nu\Delta\boldsymbol{\omega} \tag{9.1}$$

[1] *OMNIVOR* Means Numerics Involving VORticity

where $\boldsymbol{u}$ is the velocity field and ν the kinematic viscosity. The second form uses a conservative formulation implying the identity $\operatorname{div}\boldsymbol{\omega} \equiv 0$. The term $\operatorname{div}(\boldsymbol{u} \otimes \boldsymbol{\omega}) = (\boldsymbol{\omega} \cdot \nabla)\boldsymbol{u} + \boldsymbol{u}\operatorname{div}\boldsymbol{\omega}$ is the divergence of a tensorial product[2]. Vortex methods use Lagrangian markers as quadrature points to integrate the vorticity field. The method focuses on the resolution of equation (9.1) together with its boundary conditions and the convection equation of each marker: $d\boldsymbol{x}/dt = \boldsymbol{u}$ where $\boldsymbol{x}$ is the position of such marker. *OmniVor* achieves this using an extended vorticity field formulation discretized into a superposition of elementary solutions, further referred to as "elements". The positions and intensities of the vortex elements approximate the continuous vorticity field. The velocity field is obtained by inversion of the vorticity definition $\boldsymbol{\omega} = \operatorname{curl}\boldsymbol{u}$ either using the Biot-Savart law or using a Poisson solver. Inviscid boundary conditions on solid walls are solved as a Neumann problem. Vorticity is shed from lifting bodies based on the satisfaction of the Kutta-condition. The code includes features from grid-free and grid-based vortex methods. The book of Katz and Plotkin [96] describes the theory and implementation of panel methods with vortex-segment-based wake. The book of Cottet and Koumoutsakos [52] provides more details on particle-based vortex methods and grid-based formulations. The current vortex code combines aspects from these different vortex-methods. Implementation details follow.

Elements (Elementary solutions) The vortex code mainly uses the following low-order elements with low order geometrical representation: straight constant-strength vortex segments, vortex particles (blobs), flat constant-strength source panels, and constant-strength doublet panels. The two first elements are used for instance to represent wakes, while the two last are used for thick bodies. In the 2D formulation, these elements are mapped to their 2D projections.
Low-order elements usually have lower computational requirements than high-order elements [96]. Yet, higher spatial resolution is required to reach the same level of accuracy. Since high temporal and spatial resolution is required by the aero-elastic simulation, the choice of low-order element appeared appropriate.
Fixing the choice of elements allows for the code to be optimized and thus tackles the computational time challenge. Yet, this does not allow enough flexibility for using it as a research tool. As a result of this, elements are gathered into four categories: particles, segments, panels and miscellaneous elements. The last category adds flexibility to the code at the price of less optimization. The miscellaneous elements currently implemented are: vortex rings, vortex cylinders, helical vortex segments, point sources, 2D periodic vortex points, Lagrangian Markers, and Eulerian markers[3]. The list may be extended without altering the core of the code.
No specific topology of the vorticity is assumed in the implementation. Vortex elements are not stored as grid or lattice in the memory but instead connectivity tables are used. This allows for the panelling of bodies of arbitrary shapes and arbitrary segment arrangements.

Smooth/regularization models The simplification of the vorticity field into sheets, lines and points introduces singularities. For validation against theoretical results, it is often necessary to maintain this singular behavior. For arbitrary flows, numerical implementation will tend to chaotic behavior [17]. To circumvent this problem, the singularity is either removed directly in the expression ([43], [211]), or removed by convolution with a regularization/cut-off function ζ, sometimes chosen as a mollifier [52, p. 20]. Both approaches are implemented in *OmniVor*. The purpose of ζ is on one hand to regularize the velocity field that is numerically produced and on the other to improve the convergence of the method [221]. Regularization is essential for vortex methods that relies on the Biot-Savart law. Methods that use a Poisson solver do not require regularization since

[2]The convention $\operatorname{div}_2(\boldsymbol{\omega} \otimes \boldsymbol{u}) = (\boldsymbol{\omega} \cdot \nabla)\boldsymbol{u} + \boldsymbol{u}\operatorname{div}\boldsymbol{\omega}$ is found e.g. in the book of Cottet and Koumoutsakos [52]).
[3]Markers are not elementary solutions and they do not induce a velocity. Lagrangian markers are convected like any other elements.

the Poisson solver will introduce an inherent regularization (see [45, p. 9093]). The exponential and compact cut-off functions presented in [217] are implemented for particles, together with the 2D and 3D functions obtained by Beale and Majda [12, 84]. Cut-off functions similar to the ones described by Leishman [113, p. 592] are used for segments. The segments regularization functions are named after Rankine, Lamb-Oseen and Vatistas in this reference. The regularization function are all expressed as function of a smooth parameter ϵ. This smoothing parameter, or core size, should be related to the discretization of the continuous vorticity field. If h denotes the typical distance between particles, or the grid spacing when applicable, the choice $\epsilon \approx 1.5h$, is an accepted rule of thumb. In the context of core-spreading, the core size is related to a viscous representation of vortices (see the paragraph on viscous models below).

Viscous-splitting Vortex methods rely on the assumption that vortex elements are transported as material fluid elements. This assumption is only exact under the assumptions of Helmholtz's theorem, which comprise the assumption of inviscid fluid. The Lagrangian tracking of vorticity in viscous methods is justified within the context of viscous-splitting (see e.g. the work of Beale and Majda [11]). In such context, the convection/deformation step and the diffusion steps are done separately. Increased accuracy can be obtained by using sub-steps within a time step. This effectively decouples the hyperbolic part (convection/deformation) and the parabolic part (diffusion) of the equation.

Convection and numerical schemes A vortex element located at $\boldsymbol{x}_v$ is transported according to the convection equation $d\boldsymbol{x}_v/dt = \boldsymbol{u}(\boldsymbol{x}_v)$, where $\boldsymbol{u}$ is the fluid velocity consisting of the contribution from the free-stream, the free-vorticity and the influence of bodies. The determination of the velocity is detailed in the following paragraphs. The convection equation is integrated numerically as:

$$\boldsymbol{x}_v(t + \Delta t) = \boldsymbol{x}_v(t) + \boldsymbol{\Delta x}_v^{\text{conv}}(t) \tag{9.2}$$

where $\boldsymbol{\Delta x}_v^{\text{conv}}$ may be determined using different numerical schemes. The following schemes are implemented in *OmniVor*: forward first order Euler [63, p. 424], Forward second order Taylor-Euler [36], second order Adams-Bashforth [8] or fourth order Runge-Kutta [169, 107]. Second order schemes are given in the work of Cocle, with in particular the use of a Leap-Frog scheme for convection [45]. Third order Runge-Kutta schemes with adaptive time-step are also popular in vortex methods (see e.g. Chatelain et al. [42]). In most applications presented in this work the first-order scheme is used but accuracy can be greatly improved using higher order methods. The numerical schemes are also used for the resolution of the vorticity equation (stretching, diffusion). The convection and vorticity transport do not necessary use the same schemes (see e.g. Cocle et al. [45]).

Grid-free and grid-based methods The way the convection velocities and the RHS of equation (9.1) are computed leads to two main families of vortex methods: grid-free codes and grid-based codes. Both versions are available in the current code. General considerations follow and more details will be given in specific paragraphs below.

• In grid-free methods kinematics are easily handled using the Biot-Savart law: the Poisson equation is solved using the unbounded Green's function approach. Scalability of the computational time can become an issue for large scale problems: The convection of N elements requires N^2 computations of induced velocities using a direct interaction algorithm. Tree-based algorithms applied on the vortex elements can be used to accelerate the computation to $O(N \log N)$ and even down to $O(N)$ when a tree on the control points is also built (fast-multipole methods). Vorticity dynamics are not straightforward in 2D and 3D viscous methods since the viscous diffusion requires the computation of the

Laplacian operator without a grid. Vorticity dynamics in 3D particle methods present the problem that the vorticity field is not solenoidal [221]. The quality of the simulation deteriorates with time if no divergence-free correction is applied. Different methods were developed to handle these difficulties in grid free methods [221]. The convection of vortex segments automatically satisfies the strain of the vorticity lines. The strain term needs to be computed when vortex particles are present. LES modelling in a consistent way is not straight-forward and would require "surgical" techniques such as the Hairpin removal technique [44].

• In grid-based methods, the information is carried by Lagrangian markers but the vorticity equation is solved on an Eulerian grid. This requires the projection of the vorticity value carried by the vortex elements onto a grid at each time step. Kinematics are handled on the grid by means of the resolution of the Poisson equation $\nabla^2\boldsymbol{\psi} = -\boldsymbol{\omega}$ and the subsequent computation of $\boldsymbol{u}_\omega = \operatorname{curl}\boldsymbol{\psi}$ using finite differencing. Alternatively, the equation $\nabla^2\boldsymbol{u}_\omega = -\nabla\times\boldsymbol{\omega}$ can be solved for $\boldsymbol{u}_\omega$ directly. Efficient Poisson solvers with various boundary conditions handling can be used. The values of $\boldsymbol{\omega}$ and $\boldsymbol{u}$ being known on the grid, the RHS of equation (9.1) is easily obtained by means of finite differencing. It is preferred to use a conservative form of the stretching term in the RHS to reduce numerical errors [52]. The convection velocity and the evolution of the intensity of each vortex element are then obtained by projecting the information back from the grid to the elements. The difficulties found in grid-free methods are easily solved in grid-based methods: Divergence-free correction, viscous-diffusion, simple LES models are easily implemented. The projection steps from the grid to the elements and from the elements to the grid are easily implemented using vortex particles. On the other hand, projecting from the grid value to a vortex segment is not obvious since it would result in a loss of connectivity. A proper definition of the volume represented by each element is required to be able to project an intensity value into a vorticity value. Vortex element shed from the trailing edge of a wing may be attributed a volume representative of the boundary layer height of the wing section.

Each formulation possess its pros and cons and the choice between one or the other is a matter of compromises to be chosen or accepted for a given problem. Grid-based particle methods have clearly been adopted by the community as the method to be chosen for high-order computations. The second order Poisson solver, *Yaps*, developed at NTUA by Papadakis is used [155, 154] and is coupled to the *OmniVor* library. In order to facilitate performance of the Poisson solver, the method of local corrections from Anderson et al. is applied [2] together with a domain decomposition method described by Balls et al. [6].

Lifting and non-lifting bodies Lifting and non-lifting bodies can be present in the flow. Bodies are allowed to move and deform and their structural deformation may be determined by an elastic code such as *HAWC2* [110]. *OmniVor* may also prescribe rigid body motions to the various bodies and allow body coordinates systems to be linked to each other. Lifting bodies are divided into lifting patches. Three different representations of a lifting patch are available: a thick representation using doublet panels or a combination of source and doublet panels, a surface representation using doublet panels forming a vortex-lattice, and a lifting line representation. Different solving methods are applied for each representation. For the thick and surface representation, the inviscid non-flow through condition is used to determine the intensity of the vortex elements modelling the body (see e.g. Katz and Plotkin [96]). Viscous effects on solid boundaries can be included using a method similar to the one of Chorin [43]. For the lifting line representation, 2D or 3D-corrected (see e.g. Bak [5]) tabulated airfoil coefficient data are used to determine the aerodynamic loads within an iteration procedure. Bound, shed and trailed vorticity are approximated as vortex segments. At every time step a local angle of attack is determined and tabulated airfoil data are used in combination with a form of the Beddoes-Leishman dynamic inflow model [114]. The implementation of the lifting line code is similar to the one in AWSM [211]. The main parameters for the lifting

line algorithm are the relaxation factor, the maximum number of iterations and the criteria for convergence. The lifting-line technique is the only one compatible with the current grid-based implementation: lifting, shed and trailed segments are all converted to particles before projection on the grid. Non-lifting bodies follow the Hess-Smith [85] implementation method using flat source panels. A final method available which applies to all body representations consists in prescribing the intensity of the panels. This option allows a focus on specific aspect of the flow while also reducing the computational time since no solving step is required.

Wake and free-vorticity Free-vorticity is released from lifting bodies upon satisfaction of the Kutta-condition. The process of emitting free-vorticity from thick and thin lifting bodies is identical to the one used in the lifting-line formulation of AWSM [211]. "Near-wake" panels of unknown intensity are attached to the bodies at their trailing-edges. The unknown intensity of each panel is determined at each time step depending on the solving method of the "patch" to which the near-wake panel is attached. A panel is converted to vortex segments such that sides shared with other panels are merged into one segment and such that Kelvin's theorem is satisfied for the shed vorticity. The vorticity from this near-wake panel is then convected as free-vorticity. The size of the near-wake panel is kept as a parameter usually chosen according to be a proportion of the distance covered by the trailing edge between two time steps.
At any time, a collection of vortex segments or horse-shoes of three vortex segments may be converted to one or several vortex particles. It may be chosen for instance to convert the near-wake panels directly to particles as described by Voutsinas [217]. A mixed formulation of segments and particles is possible for the free vorticity in *OmniVor*. The original connectivity of the segments forming the near-wake panels is stored if later required. In general though, segments are considered to be independent. The independence of elements allows for "segments-surgery" or vortex-splitting algorithms (see e.g. Spalart [199, p. 47] and Winckelmans and Leonard[221]) where vortex elements that are too strained are divided into several elements or where segments are converted to particles. Due to Lagrangian distortion, the vortex elements should be periodically redistributed in order to maintain accuracy [52, p. 235]. This option is only available for particles. Better performance is obtained when the particles are placed at regular positions (see Beale and Majda [13]). The information can be projected on a grid at regular time interval in order to redistribute the vortex particles. Different interpolation kernels can be used for this projection step (see e.g. the book of Cottet and Koumoutsakos [52, p. 226]).

Wake growth handling The vortex shedding occurring in problems with lifting bodies implies that the vorticity domain extends with time, which result in a increase of the computational time per time step. Several options are available in *OmniVor* to moderate this.
• The wake may be cut all together. This can be achieved based on the wake age or based on the wake position (a domain is defined and elements outside of this domain are deleted).
• A convection domain can be defined outside of which elements are assumed to convect with the free-stream velocity. If N is the total number of elements and M is the number of elements within the convection domain ($M \leq N$), then a direct computation would require NM calculations instead of N^2.
• Remeshing on a non-uniform grid can also be used to reduce the resolution and the number of computational elements in the far wake. Changes in grid size should be progressive for the projection schemes to be applied. For now, only rectilinear and regular grids are supported but more complex geometries can be envisaged (like the trumpet mapping of Daeninck [55, p. 259]).
• A hybrid-wake concept similar to the one described by Voutsinas [217] is implemented to achieve constant computational time per time-step when active. The hybrid-wake concept consists in recording the induced velocity from the far-wake on a Cartesian grid. Once the recording is done,

the far-wake is removed and the vortex elements going outside of the grid at each time step are simply deleted. The parameters of this algorithm are the distance chosen to define the far-wake, the resolution of the grid, and the recording period used. The recording period may be chosen to correspond to one rotor rotation, so that once the recording is done, the recorded far-wake influence is chosen at each time-step depending on the azimuthal position of a reference blade. Similar implementations store the main Fourier components associated with the rotational period in order to avoid storing the entire recorded velocity and focus on the "steady" wake effects [217]. Such approach is only possible for problems with a given periodicity (e.g. constant rotational speed of a turbine).

Vortex splitting and merging Different schemes were implemented to split and merge vortex elements.
• Segment merging: For simulations with really small time steps, a high resolution of vortex segments is kept near the blade but these segments are merged and averaged together after a given time and for each n time steps.
• Segment splitting: When a segment has extended more than a given proportion it is split into n sub-segments.
• Particle splitting: When a particle strength has extended more than a given proportion it is split into n sub-particles.

Strain in grid-free particle methods The convection of the vortex segment points extremity satisfies the strain equation to first order approximation (e.g. Cottet and Koumoutsakos [52, p. 69]). This is nevertheless not the case for the vortex particles. The vortex particles strengths $\boldsymbol{\alpha}_p$ have to be updated according to the strain equation (see e.g. Voutsinas [217] and equation (9.1)):

$$\frac{d\boldsymbol{\alpha_p}}{dt} = (\boldsymbol{\alpha}_p \cdot \nabla)\, \boldsymbol{u} \tag{9.3}$$

In the absence of viscosity or higher order terms such as hyper-viscosity, the stretching term will tend to make the simulation "blow-up", independently of the solenoidal quality of the particle vorticity field (see e.g. Winckelmans and Leonard or Chorin [221, 44]). Different schemes exist to compute the stretching term: direct, transposed and mixed (see [220]). The problems that might result from the stretching term are rarely discussed in the literature. A starting vortex behind a wing can be challenging due to its strong intensity. Remeshing, vortex splitting, adaptive time-stepping or specific stretching implementation[4] may be required. The following option is available in *OmniVor*'s implementation: the magnitude of the stretching of a vortex particle can be limited to a given percentage between two time-steps while preserving the change of direction. This approach is used in Chapter 13 and Chapter 14 to avoid the simulation blow-up but also provide an artificial account of the unresolved scales of turbulence.
As the particles evolve the flow field will loose its divergence-free nature (see Cottet and Koumoutsakos [52, p. 60 and p. 84]). Corrections are not used for the results presented in the current thesis but will be considered in the future.

Diffusion - Viscous models The models for the account of diffusion related to the free-vorticity are discussed here. Vorticity generation and modelling of viscous effects arising at solid boundaries [175] will not be discussed. Under the assumption of viscous-splitting the convection step and diffusion step are treated separately [11]. Four models for the resolution of the diffusion equation $\frac{\partial \boldsymbol{\omega}}{\partial t} = \nu \Delta \boldsymbol{\omega}$ were implemented.

[4] Winckelmans, Chatelain, Voutsinas, private communications.

• Grid-based method: the diffusion equation is solved using a finite difference scheme on a structured grid after projection of the vorticity onto the grid.
• Random-walk method: the diffusion step is applied by introducing a random displacement of standard deviation proportional to the viscosity to the vortex element.
• Core-spreading method: the method intends to solve the diffusion equation by changing the core size of the regularization function with time. This method comes from the analogy between the Gaussian regularization function and Lamb's [108] Gaussian vorticity distribution which is an exact solution of the 2D-Navier-Stokes equation for a single viscous vortex.
• Particle-strength exchange: the Laplacian operator is replaced by an integral operator for which the particle approximation can be applied (see [220]).
References to more methods are found in the review presented in the PhD thesis of Barba [7].

Coupling with aero-servo-elastic code Three different coupling methods are available: strong, soft, or loose coupling. The strong coupling solves the flow for each sub-iteration of the structural code. The soft coupling only solves the flow once at each time-step and the loose coupling does so only after a given number of structural time steps. Obviously the strong coupling is preferred for an accurate aero-elastic simulation, and this was used in all studies. Coordinates, orientation and velocities of each of the bodies cross-sections are provided by the structural code at each sub-iteration. The *OmniVor* library solves the flow for this new configuration and returns the lift, drag and moment at each cross-section. When the sub-iteration process of the structural code has converged, the aerodynamic convection and diffusion step is performed. The *OmniVor* library has been coupled to DTU's aero-servo-elastic code *HAWC2* [111].

Free-stream and external inflow The library may use its own wind module or the wind module present in the aero-elastic tool to determine the free stream velocity at a given point in time and space. Such module contains for instance shear, turbulence inflow and standard gust inflow. On one hand, non-uniform and non-constant inflow do not fall into the potential flow theory and such application should be taken with care. On the other hand, the same holds for the momentum theory on which BEM codes are based. The investigation of these complex inflows within the context of vortex methods will be the topic of Part V.

Matrix solver Boundary elements methods (panel methods) requires the inversion of a matrix,. This step can be performed using a library implemented by the author, or using the following LAPACK implementations: standard library, MKL sequential or MKL threaded.

Acceleration techniques Three directions were successively chosen to reduce the computational time of the computationally expensive part of the code, i.e. the wake-relaxation step.
• Direct method (N^2): The induced velocity functions were parallelized using OpenMP and MPI. Further improvements were obtained by in-lining and porting this part to C, obtaining an average speed-up of 1.5 between the Fortran and the in-lined C implementation. Finally, the C-code was parallelized on Graphical Processing Units (GPU) using the CUDA framework. An average speed-up of 3.5 was obtained between the OpenMP C-version run on 64 threads and the GPU version run on a Tesla K20c device with double precision. This led to a speed-up factor of 200 between the sequential Fortran code and the CUDA implementation. It should nevertheless be noted that the full vectorization potential of the CPU-version was not exploited. Further improvement may be obtained by using AVX intrinsics for vectorization or multi-GPUs setups. This implementation was done in collaboration with H.H. Brandenborg Sørensen from *DTU Compute*. Results from the scaling of a computational step with the number of cores is shown in figure 9.1 for a problem of 0.6M particles.

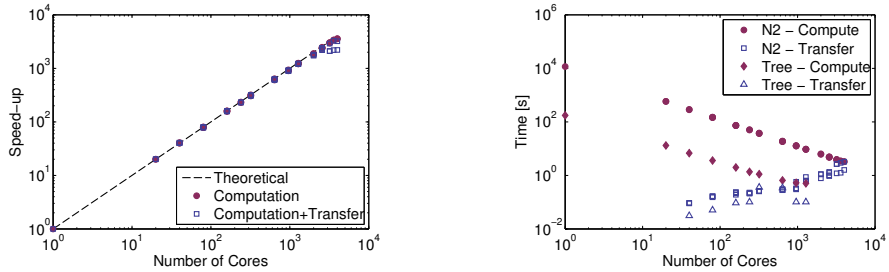

(a) (b)

Figure 9.1: Scaling of the parallelization of the wake-relaxation step. Results obtained for 0.6M particles. (a) Speed up for the N^2 step. (b) Comparison of computational times between the parallel N^2 and parallel tree implementations. Transfer times corresponds to communications between the different CPUs. The problem is here too small for the tree code and the transfer times soon becomes as important as the computational time.

• Tree-based method ($N \log N$): A tree-based multipole method [74, 172] was implemented to reduce the algorithm complexity to $O(N \log N)$. Second order multipole expansions were used for both the velocity and the velocity gradient computations (see e.g. Salmon et al.[172]). Using 0.6M particles, a speed-up of about 50 was obtained compared to the direct method (see figure 9.1b) for an average relative error estimated at about 0.02% for the velocity and 0.04% for the gradient. This implementation was done in collaboration with P. Mercier [136]. Results from the scaling of the code is shown in figure 9.2. The tree algorithm has been further improved and parallelized since these results were obtained.

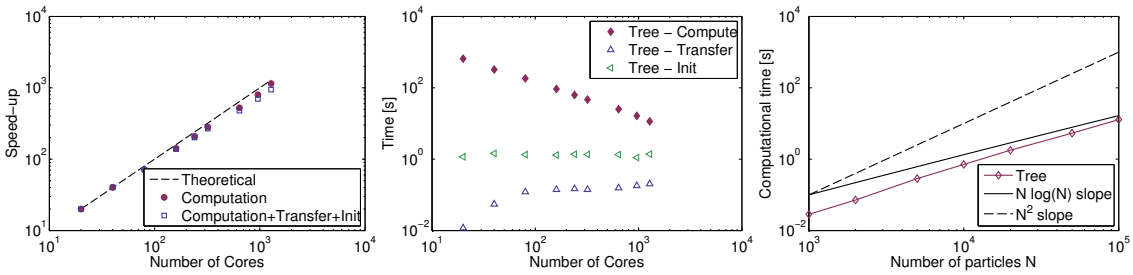

(a) (b) (c)

Figure 9.2: (a) Scaling and (b) computational time related to the multipole-tree implementation obtained using 1.1M particles and different number of cores. (c) Algorithm scaling for different number of particles on a single machine.

• Grid-based code: The vortex code includes a grid-based formulation which can make use of Fast Fourier Poisson solver (see e.g. [176]). Such codes have a computational cost in $O(N \log N)$ and are usually faster than a tree code. At the time of writing the Poisson solver developed by G. Papadakis at NTUA is used [155]. G. Papadakis greatly eased the coupling with his Poisson solver and provided post- and pre-processing functions.

Implementation The *OmniVor* library consists of several library-layers built upon each other. The library was originally developed in Matlab. Each layer was then progressively ported to Fortran

with the help of a matlab-to-fortran converter developed by the author. The code was tested against five different compilers and on multiple platforms to ensure its portability. Each library layer possess C-binding functions that facilitates its call from other programming languages. A Python and Matlab class have been implemented to wrap the library such that test scripts from both languages will have the same syntax. The name and description of the different library layers of *OmniVor* are given below.
• Layer 0 (*chipmunk*): contains induced velocity functions
• Layer 1 (*ze mouffette*): computes the evolution of a "user model" (set of vortex elements and wings).
• Layer 2 (*raccoon*): generates and handles a "user model" based on a set of bodies of given motion
• Layer 3 (*coyote*): ensures the coupling between the raccoon layer and an elastic code (e.g. *HAWC2*)
• Layer 4 (*bear*): tools (BEM, vortex code, aero-elastic code) wrapper for wind energy simulations (parametric study, power curves, optimization). This layer is still under development.
The *human* is the ultimate known layer of *OmniVor*, so far.

9.3 Specific configurations used in publications

Configuration 1 (Prescribed lifting-line, segment wake) In this configuration the circulation on the lifting line is prescribed. The circulation may be constant in time or time-varying. In the first case no shed vorticity is emitted. The wake consists of vortex segments which convect and roll-up. No viscous diffusion or remeshing is used.

Configuration 2-1 (Lifting-line, segment wake) The circulation is determined at each time step using an iterative procedure such that the induction at the blades is in equilibrium with the blade and near wake circulation (see [211]). The circulation at the blade is determined using the KJ relation and 2D tabulated airfoils data (or analytical expressions such as $C_l = 2\pi \sin\alpha$). A dynamic stall model can be applied. The wings emit vortex segments representing the trailed and shed vorticity. The effect of shed vorticity may be removed if desired. The wake consists exclusively of these vortex segments. They convect and roll-up. No remeshing is used. Viscous diffusion may be modelled to some extent using random walks and core-spreading methods. Turbulence and shear may be included in the "free-stream", but the vorticity associated to it is not accounted for.

Configuration 2-2 (Lifting-line, segment to particles wake) Same as 2-1 but the wake vortex segments are converted to particles after a given wake age (assumed non zero, since this is the case of configuration 3). No remeshing is used. For viscous simulations, the core-spreading and random-walk models are available for both segments and particles.

Configuration 3 (Lifting-line, pure particle wake) Same as 2-2 but the trailed and shed vorticity is immediately converted to particles. For viscous simulations, the core-spreading and random-walk models are still available but more physical models are obtained using the grid-based method or the PSE method.

Configuration 2-1-turb (2-1 + turbulent vortex particles) Same as 2-1 but turbulence is modelled using vortex particles. Remeshing can be used (it affects only the turbulence). The amount of stretching is limited.

Configuration 3-turb (3 + turbulent vortex particles) Same as 3 but turbulence is modelled using vortex particles. The amount of stretching is limited. The particles are periodically redistributed. The M'4 kernel interpolation kernel (see [52]) is used for this projection step. The multipole tree algorithm is used.

Configuration 3-map (3 + external map) Same as 3 with the possibility to add the contribution of an external Neumann-to-Dirichlet map (or generalized Helmholtz decomposition surface term) which accounts for the vorticity outside of the computational domain (see e.g. the discussion around equation (12.4) and Chapter 14).

Configuration 2D-0 (2D vortex particles only) The vorticity is projected onto 2D vortex particles. No bodies are present.

Chapter 10

Vortex code validation and illustration

Prologue Several of the validation cases run for the vortex code described in Chapter 9 will be presented in this chapter. The current vortex code implementation, *OmniVor*, originated from the re-writing, improving and extension of a previous vortex code from the author [20]. It was checked that both versions give identical results. Most of the test cases that are presented here were studied in more details for the previous implementation. The main new features that are presented in this chapter compared to the previous study are: vortex blobs and source panels; gradients of the velocity fields; thick bodies; square flat-plate results.

10.1 Simple validation of the vortex particle method

The accuracy of vortex particle methods depends to a large extent on the determination of the velocity $\boldsymbol{u}_\omega$ and deformation $[\boldsymbol{\nabla u}].\boldsymbol{\omega}$ from the distribution of vorticity. The accuracy of both the grid-free Biot-Savart law and the Poisson solver approaches are studied by comparison with the analytical formulae of the Hill's spherical vortex [88, 1]. The particles are initialized using the analytical vorticity value on a regular grid of spacing h/a where a is the radius of the Hill's sphere. The domain extends from $-1.2a$ to $1.2a$ in all directions. The velocity is then computed by the two methods on two control volumes: one entirely located inside the sphere and one crossing the sphere surface. Both volumes are made of 1000 control points that remain unchanged for the different grid spacings tried. The second control volume is more challenging since the vorticity experiences a discontinuity at the sphere boundary. The mean relative error between the numerical and analytical velocity and deformation on the two control volumes are shown in figure 10.1 (from [31]) . The Poisson solver uses a grid of the same spacing as the particle spacing. Different grid spacing h were used, the lowest grid resolution corresponding to 2000 particles and the highest to 14M. Resolutions up to 628M particles were also tried. Both methods are seen to be second order as expected. Better performance of the Poisson solver was observed in the determination of the velocity. For the grid-free approach, the accuracy can easily be improved by using higher order 3D regularization kernels ζ [12, 84] as long as the vorticity distribution has sufficient continuous derivatives [11]. For the Poisson solver, both the order of the solver and the order of the differentiation scheme are important.

10.2 Lifting Line

Elliptical wing The lifting line implementation and its iterative algorithm is validated using the exact same test case as the one used by van Garrel [211]. The condition corresponds to an elliptical wing of span $b = 5$, and max chord $c_0 = 1$ at $\alpha = 5.7106$, which profile coefficients are given by $C_l = 2\pi \sin\alpha$. This implies the following theoretical values: $C_l = 0.4765$, $\Gamma_{\max} = 0.2395$. The geometry is such that the aspect ratio is $\mathrm{AR} = 6.3662$ and the wing area is 3.9270. The free stream is set to $V_0 = [0\ 0.1\ 1]$. Results for a discretization of 20, 40 and 80 span points distributed using

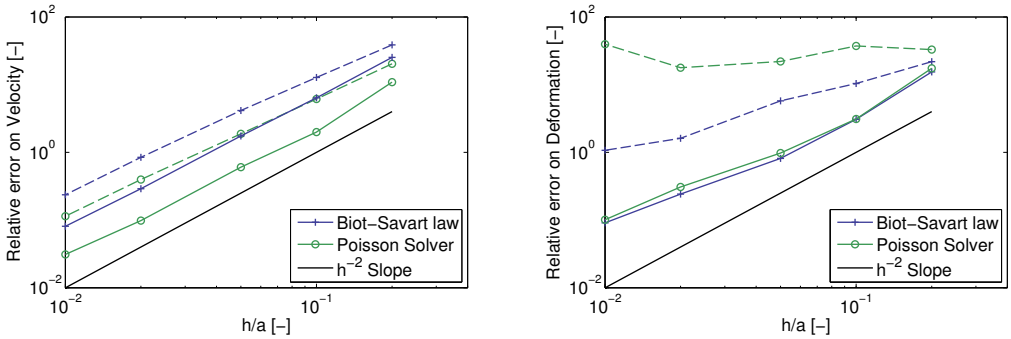

Figure 10.1: Accuracy of the current particle method using the Biot-Savart law or the Poisson solver by comparison with the analytical solution from the Hill's vortex. Relative error in velocity (left) and deformation (right). The errors were evaluated in a domain inside the Hill's vortex (plain lines), and in a domain surrounding part of the boundary of the vortex (dashed lines). The latter present more challenges due to the discontinuity of the vorticity across the boundary.

.

an approximate "full-cosine spacing" (see [211]) are shown in in figure 10.2. They are in perfect agreement with the work from van Garrel.

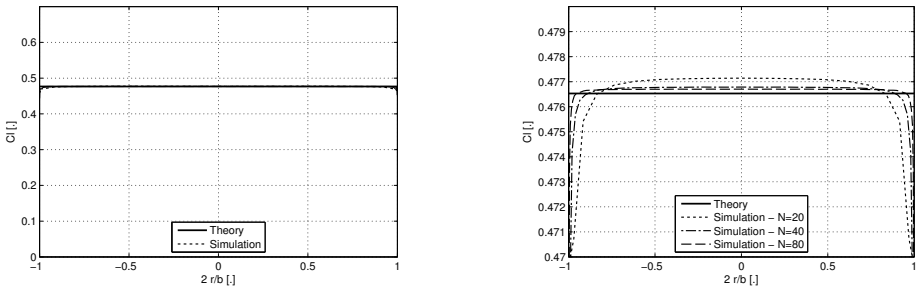

Figure 10.2: Validation of the lifting line implementation using an elliptical wing. The Figure to the right is a zoom of the left one.

10.3 Lifting surface

Flat plate Validation results for a rectangular flat plate of different aspect ratios are shown in figure 10.3b. Values are compared with experimental data [96] and various theories. More informations can be found in previous work from the author [20] but also from the analysis of Tuck [208]. Perfect agreement is found with the semi-analytical result from Tuck at high aspect ratio, and good agreement is found with the vortex lattice code from Jones 1960 [96]. Differences between the lifting surface results and the lifting line results from Prandtl are expected due to the difference in formulation.

Elliptical wing The analytical derivation from Kida [100, 208] provides the exact lift coefficient C_{l_α} of an elliptical wing from the three-dimensional lifting surface theory. Comparison with the

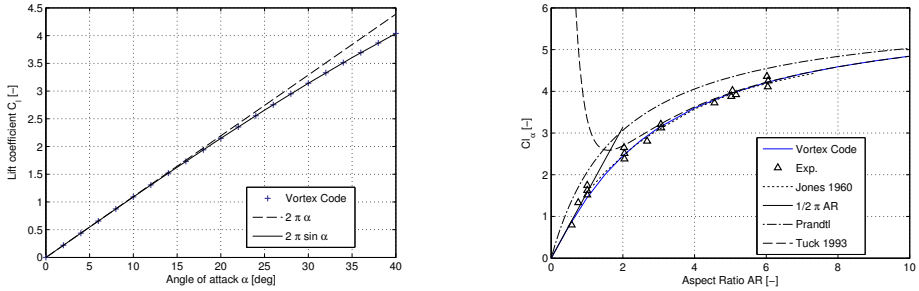

Figure 10.3: Validation of lifting surface representation for a flat plate. Lift coefficient for a (left) very large aspect ratio and (right) various aspect ratios

lifting surface implementation is shown in figure 10.4, where $k^2 = (a^2 - b^2)/a^2$, with a and b the two semi-axes of the ellipse.

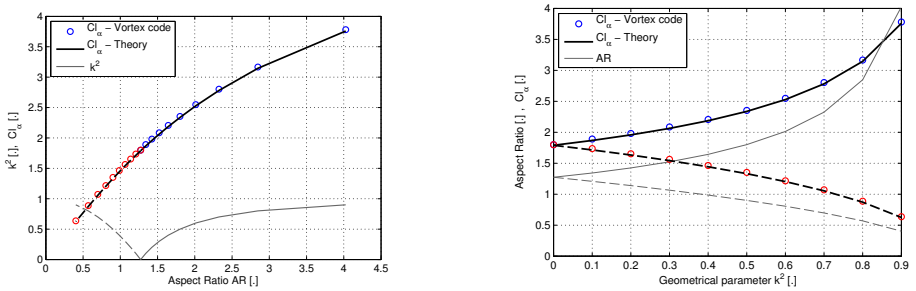

Figure 10.4: Validation of the lifting surface representation using an elliptical wing. For a same value of k two aspect ratios are possible (marked with two different colors).

Trapezoidal wing The trapezoidal wing was also used as a validation case and can be found in previous work of the author [20]. Existing relations used for validation can be found in [15] and [3].

Linearized squared flat plate In [99, p. 124], Kerwin presents results for the lift coefficient of a flat plate with 7 digits accuracy. The results obtained using the current vortex code are given in table 10.1 with 8 digits accuracy. The round off at 7 digits matches exactly the results from Kerwin. The exact configuration presented by Kerwin needs to be applied: M spanwise and N chordwise panels with an identical panelling configuration as the one used by Kerwin; the last vortex ring control points needs to be at the trailing edge (TE); the infinite wake needs to be along the flat plate and not along U_0; the KJ force needs to be computed even for the last vortex ring (the one just before the TE), since the last filament do not have 0 intensity; no core or exit conditions should be applied in the induced velocity functions.

10.4 Thick bodies

Airfoil - Doublet representation The representation of an airfoil using constant strength doublet was validated using the van de Vooren and Kármán-Trefftz airfoils [96]. A wing with a

Table 10.1: Convergence of vortex lattice calculation for a squared foil with aspect ratio 1.0. Tabulated values of $dC_l/d\alpha$ obtained with 8 digits accuracy.

M/N	4	8	16	32	64	128
4	1.4587018	1.4592853	1.4593515	1.4593570	1.4593572	1.4593572
8	1.4592630	1.4600102	1.4600966	1.4601047	1.4601057	1.4601058
16	1.4593061	1.4600848	1.4601958	1.4602086	1.4602098	1.4602099
32	1.4593089	1.4600909	1.4602065	1.4602223	1.4602241	1.4602243
64	1.4593089	1.4600915	1.4602074	1.4602238	1.4602260	1.4602263
128	1.4593089	1.4600915	1.4602075	1.4602239	1.4602262	1.4602265

large aspect ratio is used to validate the 3D version of the code against the 2D version. Results for the van de Vooren airfoil are shown in figure 10.5. The slight differences observed are of the

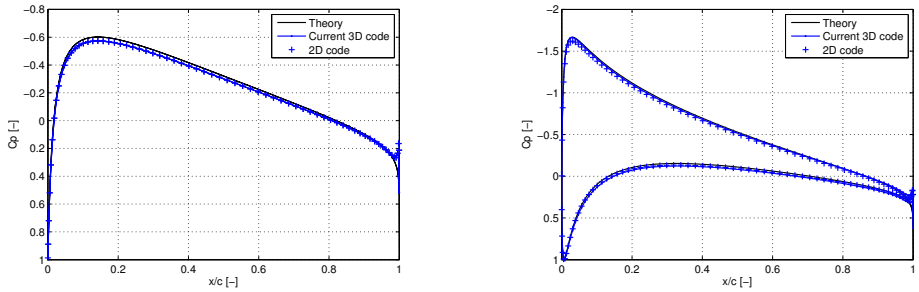

Figure 10.5: Pressure distribution for the the van de Vooren airfoil at (left) 0 and (right) 5 degrees angle of attack

same order of magnitude as the one shown in the book of Katz and Plotkin. The overshoot at the trailing edge is found in doublet formulations. Better results are obtained in with a combination of sources and doublets.

Sphere - Source representation Validation of the quad source panels is done using the inviscid flow about a sphere. The corresponding theory can be found in [229]. The pressure distribution on the sphere is illustrated and compared to the theory in figure 10.6.

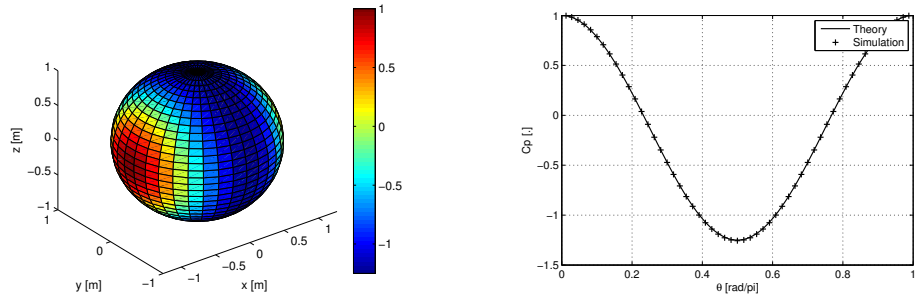

Figure 10.6: Validation of the quad source panels representation using the inviscid flow about a sphere.

10.5 Unit-tests

A number of unit-tests are run regularly to ensure consistency of results between each revision of the code and test the different library interfaces. At the time of writing about 32 unit-tests are present. A short description of some of the most important unit-tests is given below. Results from some of these tests corresponds to the ones shown in the previous sections.
- Elementary flows: Validation of the induced and gradient velocity functions (*chipmunk* level)
- Parallel/Sequential: Evaluate the relative norm between the velocities and gradients obtained with the parallel and sequential implementations (*ze mouffette* and *raccoon* levels) .
- Flow past a sphere
- Flow around an analytical vortex ring and cylinders (both at *ze mouffette* and *raccoon* levels)
- Elliptic wing with lifting-line formulation: both with wake time-stepping or an infinite wake panel
- Geometry interpolation based on thick profile geometries.
- Rectangular plate lift coefficient for different aspect ratios
- Pressure distribution over 6 different airfoils
- Diffusion of a 2D Lamb-Oseen vortex
- Check that the conversion to particle and remeshing do not affect the loads on a wing
- Check that the proper shear profile is retrieved using vortex particles and a surface map (see Chapter 14)

10.6 Further validation

Furher validation cases are presented in a separate document [21]: Numerical experiments related to the accuracy of vortex methods were reproduced to validate the vortex code; The implementation of the current PSE diffusion scheme implementation was done by considering the diffusion of the Lamb-Oseen vortex.
More validation cases can also be found in a previous work of the author [20], with in particular: unsteady flat plate simulations, comparisons with other vortex codes and various applications to wind turbine simulations in uniform and yawed inflow. All these validation cases were not run again for this new implementation since the results are expected to be identical.
Future work will focus on the grid-based vortex particle formulation, using in particular Hill's vortex solution and vortex rings instabilities (see e.g. Cocle et al. [45]) for validation. Comparison of results from the oscillating wing performed by Conway and Tezok may be considered [50]. The next chapter will present examples of validation cases applied to wind energy which were run using the current implementation.

Chapter 11

Examples of wind energy validation cases

This chapter presents contents given in the following articles: 'Validation of vortex code viscous models using lidar wake measurements and CFD' **[30]** and 'Aeroelastic large eddy simulations using vortex methods: un-frozen turbulent and sheared inflow' **[31]** . The chapter also consists of unpublished content.

Prologue The current chapter presents results obtained from the current vortex code compared to BEM, CFD and measurement results. Vortex segment simulations are performed using Configuration 2-1 and particle simulations using Configuration 3 (see section 9.3). The CFD computations presented were performed using the in-house *EllipSys3D* flow solver developed by Michelsen and Sørensen [139, 197]. The Actuator-Disk (AD) version of the code is described in [140]. The Actuator-Line (AL) version of the code is described in [196].

11.1 Comparison with BEM and Actuator-Line simulations

BEM codes, Actuator-line CFD and lifting-line vortex codes can easily be compared to each other since they all represent the blade as a line and the same airfoil data can be used.

Uniform inflow Simulations for the Mexico rotor [179] at $U_0 = 15$m/s, $\Omega = 424.46$ RPM, $-2.3°$ pitch were performed using all codes. Comparison of the AL code with measurements was done by Shen et al. [187] and is not done here. Results are shown in figure 11.1. The Mexico rotor is known to have drastic changes of airfoil characteristics along the span responsible for the trailing of strong vortices between two family of airfoils. The AL simulations were performed using a resolution of 60 points along the span, whereas the other simulations used 40 points. The method of interpolation of profiles may be different in the AL-CFD and the two other methods. This could explain why the vortex code does not reveal a variation of loading as drastic as the CFD. In general, the three codes are in good agreement.

Yawed inflow AL and vortex code results for yawed conditions are illustrated in figure 5.2 for the mid-span of the blade. The two codes agree to a high degree in this situation. Closer to the blade root, the agreement between the AL and the vortex code was reduced **[22]**. The differences in the core next to the root may be due to the absence of viscous diffusion of the root vortex in the vortex code. This remark is only speculative and needs further investigation.

11.2 Wakes and flow field for uniform inflows

A model of the three-bladed stall regulated Nordtank 500kW turbine is used ([78]: $D = 2R = 41$m, $\Omega = 27.1$ RPM) with a tilt angle of $0°$ and with $U_0 = 7.5$m/s, $C_T = 0.75$ and $\lambda = 7.7$.

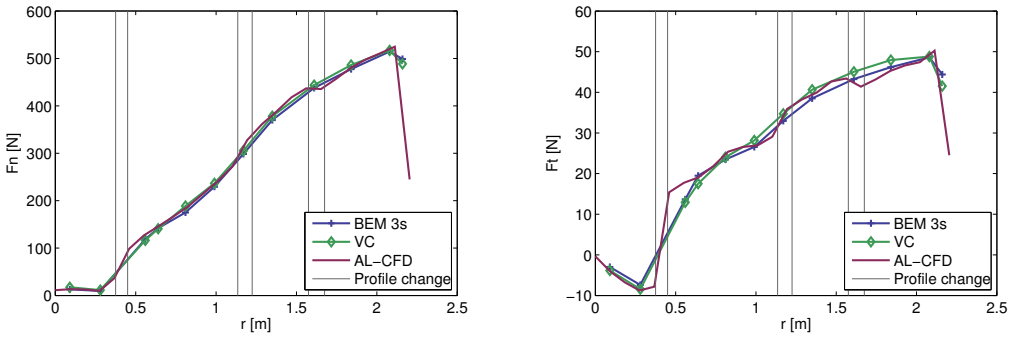

Figure 11.1: Normal (left) and tangential (right) forces for the Mexico rotor in uniform inflow as obtained with three "lifting-line"-based codes that use the same tabulated airfoil coefficients.

AD simulation and segment wake A qualitative comparison of AD and lifting-line vortex wake results is presented here [30]. Both codes use the same profile data. A uniform inflow of 7.5m/s without shear and turbulence is used. Details of the simulation setup for both codes are found in [30]. Mean velocity contours are displayed in figure 11.2 to provide an overview of the flow as simulated by both tools. The two codes reveal the same flow qualitative features. Differences are yet expected since the CFD-AD distributes the blades loads on a disk. A high velocity core, in the inner region of the wake is observed for the vortex code. The deterioration of results of the vortex code is seen in the far-wake due to Lagrangian distortion and the absence of redistribution. A more detailed comparison of the wake deficits will follow in the next section.

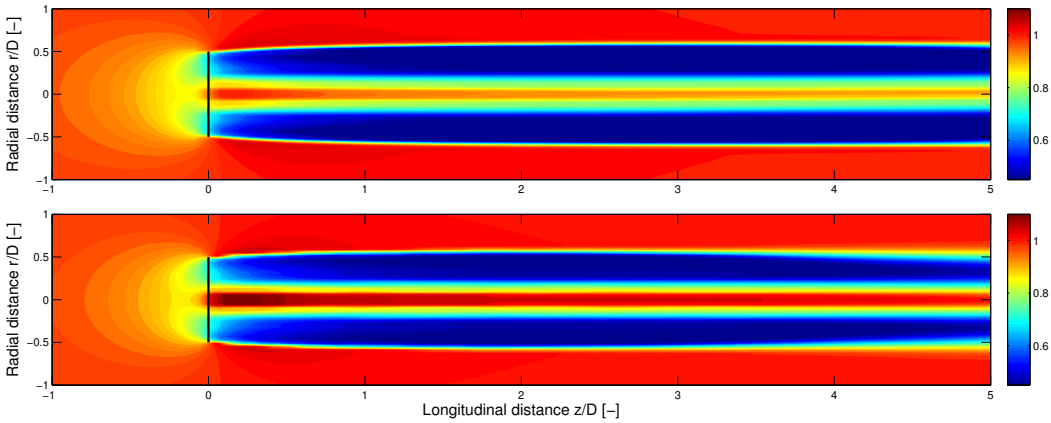

Figure 11.2: Mean dimensionless velocity contour simulated by AD-CFD (top) and the vortex code (bottom) [31].

Particle wake simulation The particle wake formulation was validated against the segment wake formulation in [31]. The circulation along the span of the wind turbine blade for a simulation with a vortex segment wake and with a particle wake is shown in the right of figure 11.3. The agreement between the two cases validates the implementation of the particle wake method.

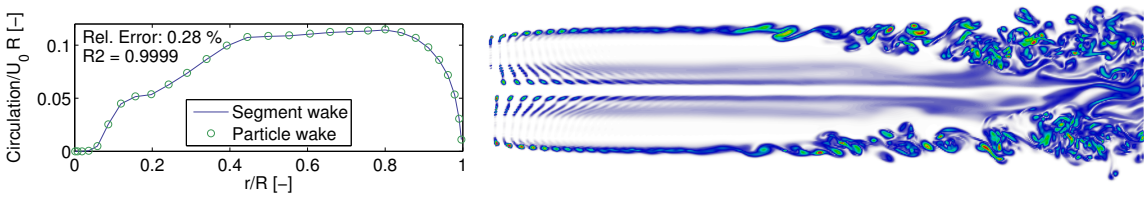

Figure 11.3: Left: Circulation along the blade at the end of the simulation using a vortex segment wake or a particle wake. Right: vorticity values obtained from the particle simulation for a wake extending from to 0 to 6D [31].

11.3 Effect of Viscosity - Comparison with AD

The Nordtank turbine is used again to assess the effect of wake viscosity. The AD and vortex codes are run for two values of the kinematic viscosity: the standard air viscosity ($\overline{\nu} = 1$) and a value 1000 times higher ($\overline{\nu} = 1000$). The profile data are assumed independent of the Reynolds number for ease of comparison. The Reynolds number based on the rotor diameter for the normal and high viscosity are respectively $\mathrm{Re}_D = 19 \times 10^6$ and $\mathrm{Re}_D = 19 \times 10^3$. Velocity deficits obtained from CFD and different vortex-code simulations are compared in figure 11.4. A previous study revealed that wake

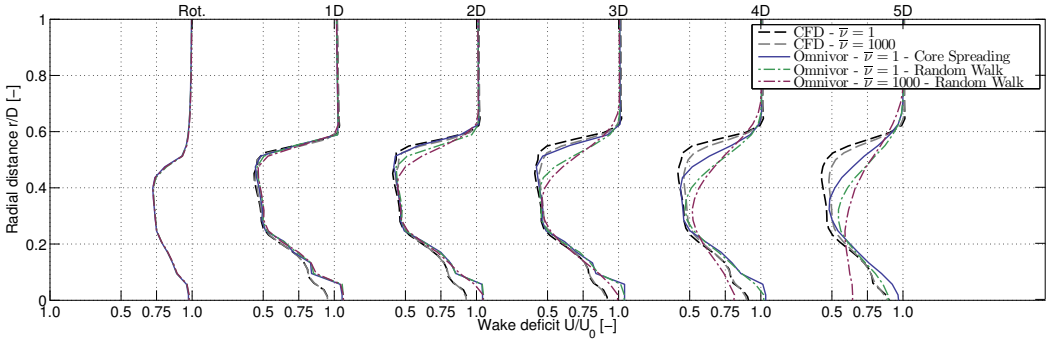

Figure 11.4: Wake deficits for AD and vortex codes at two viscosity values. Two different viscous models are represented for the vortex code: the core spreading model ($\delta = 1$, $t_0 = 0.1$) and the random-walk model ($\epsilon = 0.5h$) (see notations in [30]). The core-spreading case with $\overline{\nu} = 1000$ is not represented since close to the case $\overline{\nu} = 1$.

deficits were slightly independent of viscosity for Reynolds number Re_D higher than 50×10^3 [140]. At the current Reynolds number, $\mathrm{Re}_D = 19 \times 10^3$, the viscous effects are seen to slightly decrease the wake deficit. This trend is observed by both codes but in different proportions. The vortex code and CFD tool correlates to a large degree in the near-wake and up to three diameters downstream for the low viscosity case. A clear smoothing and reduction of the deficit occurs in the far-wake of the vortex simulations. These effects can be attributed to the Lagrangian distortion and the absence of re-sampling in this case. A consistent description of viscosity from near-wake to far-wake is expected to improve the accuracy of vortex methods. Yet, the effect of the wake viscosity and the choice of viscous model are not seen to have an influence on the rotor axial induction. This is of course only true for a proper choice of the viscous models parameters. These were obtained using a parametric study and by trying to respect the overlap condition of vortex cores necessary for the satisfaction of the convergence properties of vortex methods (see e.g. Beale and Majda [13]). The core-spreading method has been widely used for low-order vortex filament simulation and it

can be seen that it is indeed well tuned. The random-walk method applied to the vortex filaments appears to overestimate the viscous diffusion. Neither of the methods are expected to be physically accurate, partly because the viscous reconnection of two segments is not accounted for. Vortex particle methods offer greater advantages in this prospect.

11.4 Effect of Turbulence - Comparison with Lidar and AD

Lidar measurement data [166, 119, 120] of the wake of the Nordtank turbine are used for comparison with $U_0 = 7.5$m/s and $C_T = 0.75$. The lidar measurements are averaged over approximately 18 hours of data selected for a bin of wind speeds between 7 and 8 m/s. Comparison with the measurements are obtained for both AD-CFD and the vortex code by performing an average over 6 simulations, each of length 10 min. The measured mean-shear corresponds to a power-law coefficient of 0.18 and the measured mean turbulence-intensity is of 0.13. These values are used to model the inflow for both codes. Each 10-min simulation is using a different turbulent box generated according to the Mann model [130, 131]. The simulation setup is similar to the one of section 11.2 and is detailed in **[30]**. The vorticity associated with the turbulence is not accounted for in the vortex code simulation: the turbulent velocity field has an influence of the vortex elements but the vortex elements do not have an influence on the turbulence vorticity. This case is referred to as *external turbulence*. The fully-coupled case is the topic of Chapter 13.

A simplistic nacelle model using of ellipsoidal body made of source panels and the generation of vortex particles corresponding to the vorticity flux necessary to ensure the no-slip condition was implemented in a fashion similar to that of Ploumhans et al. [160]. Wake deficits from measurements and simulations are compared in figure 11.5. Both simulation tools are in overall agreement with the measurements. The asymmetry of the wake due to the presence of shear and tilt is well captured by the codes. The correlation between the two codes is greatest for the downstream distances 2D and 3D. The lack of wake expansion from the vortex code at $1D$ was seen to be reduced by using more span-wise elements and lower time steps. The differences with the measurements observed at $x = 1D$ is due to the quality of this specific measurement point. Later campaigns confirmed the onset of the double hump shape seen in the simulations [121], so such a variation is physically correct.

The lower wake deficits obtained by the measurements in the far wake is likely to be due to differences in atmospheric stability between the measurements and the simulations, the former being more unstable in average. The measurements were averaged over 18h of data under different atmospheric stability conditions [121]. Deficits are expected to be lower in unstable conditions.

11.5 Conclusions

This chapter presented different applications of the vortex code implementation to specific wind turbine simulations.

Simple comparisons of loads at the rotor from BEM, AL-CFD and vortex code showed excellent agreement for the uniform inflow case. AL-CFD and vortex code results agreed to a high degree in yawed configuration expect near the blade root. Since the AL code has been extensively used and validated, the agreement between the two codes demonstrates the possibility of the vortex code to be used as a predictive tool.

The vortex segment wake formulation was mainly used in this chapter. It was shown that the particle wake simulation is consistent with vortex segment wake results.

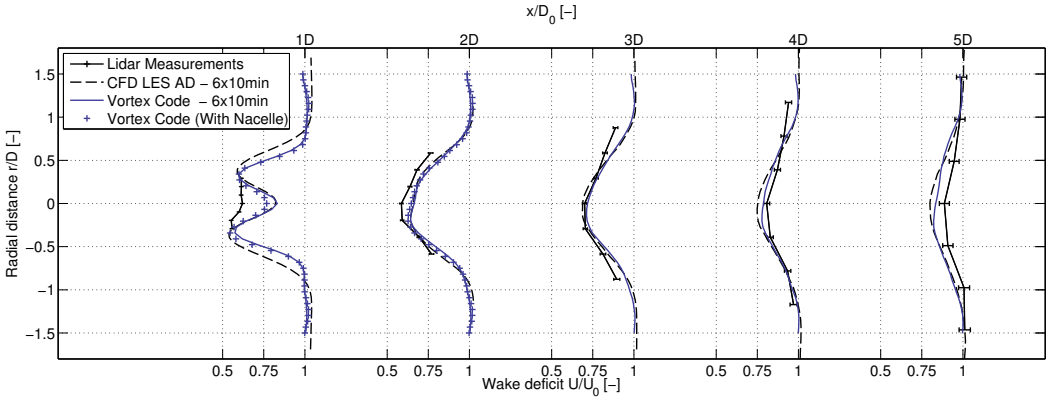

Figure 11.5: Normalized wake deficit for an average wind speed of 7.5 m/s, measured by the nacelle-mounted Lidar and compared with actuator-disk and vortex code simulations. The absence of double-hump shape at 1D is a measurement error. The influence of the Nacelle slightly increases the wake deficit.

A part of the results presented came from a study that was motivated by the consideration that a better modelling of the wake by vortex methods should imply better performance evaluation at the rotor plane. The improvement considered was the modelling of viscosity in the wake. It appeared that such viscous effects were not significant for the range of Reynolds numbers used in wind energy. Validation of the models for other applications will then be considered in the future.
For both turbulent and laminar simulations, the vortex code showed a coherent modelling of the near-wake up to three diameters downstream. Further downstream, divergence of results between CFD and the vortex code was observed.
Using external turbulence flow fields and sheared inflow appeared sufficient to obtain results in agreement with both CFD and lidar measurements. Investigation of turbulence and shear within vortex methods is the topic of Part V.

Part V

Vortex methods for complex inflow and aero-elastic simulations

12 Reconstruction of a velocity field using vortex particles. 77
12.1 *Introduction*
12.2 *Simple velocity reconstruction using vortex particles*
12.3 *Associated errors and discussions*
12.4 *Example of velocity reconstruction for a turbulent field*
12.5 *Conclusions*
13 Effect of wind turbines on the turbulent inflow 83
13.1 *Introduction*
13.2 *Contributions and key results*
13.3 *Conclusions*
14 Aeroelastic simulation of a wind turbine under turbulent and sheared conditions 89
14.1 *Introduction*
14.2 *Contributions and key-results*
14.3 *Conclusions*

Chapter 12

Reconstruction of a velocity field using vortex particles

This chapter presents contents given in the following articles: 'Impact of a wind turbine on turbulence: un-freezing the turbulence by means of a simple vortex particle approach' **[25]** and 'Aeroelastic large eddy simulations using vortex methods: un-frozen turbulent and sheared inflow' **[31]**

12.1 Introduction

The possibility to reproduce a given input velocity field using vortex particles is investigated. This operation will be referred to as "velocity reconstruction". A direct and simple approach is chosen to perform such operation. The errors inherent to the method, but also linked to these approximations are discussed. The problem is applied to a turbulent velocity field in an unbounded domain.

12.2 Simple velocity reconstruction using vortex particles

Particle approximation The particle approximation combines a mathematical and a physical approach. For the mathematical approach, the vorticity field $\boldsymbol{\omega}(x,t)$ is projected onto a set of base functions $f_p(\boldsymbol{x})$ and the component p of this projection is written $\boldsymbol{\alpha}_p(t)$, to give:

$$\boldsymbol{\omega}(\boldsymbol{x},t) \approx \sum_p f_p(\boldsymbol{x})\,\boldsymbol{\alpha}_p(t) \tag{12.1}$$

Each base function is further associated with a given point in space $\boldsymbol{x}_p$ and a local volume V_p is attributed around each point such that the sum of all volume forms the total support of $\boldsymbol{\omega}$. Choosing $f_p(\boldsymbol{x}) = \delta(\boldsymbol{x} - \boldsymbol{x_p})$ leads to a simple nodal point approximation of the vorticity field and the components are obtained as $\boldsymbol{\alpha}_p = \int_{V_p} \boldsymbol{\omega}\, dV$. The physical approach consists in splitting the domain into finite material volumes $\mathcal{V}_p$ representing a "particle". The mean position of the material volume gives the position of the particle $\boldsymbol{x}_p = \int_{\mathcal{V}_p} \boldsymbol{x}\, dV$. The particles carry an integral value of $\boldsymbol{\omega}$, noted $\boldsymbol{\alpha}_p = \int_{\mathcal{V}_p} \boldsymbol{\omega}\, dV$ which is referred to as the particle strength. The strength and volume being known, a particle-vorticity value $\boldsymbol{\omega}_p$ can be defined as $\boldsymbol{\omega}_p \overset{\wedge}{=} \boldsymbol{\alpha}_p/\mathcal{V}_p$, which is in general different from $\boldsymbol{\omega}(\boldsymbol{x}_p)$. The particle approximation consists in writing the vorticity field as a sum of particle strengths $\boldsymbol{\alpha}_p \overset{\wedge}{=} \int_{V_p} \boldsymbol{\omega}\, dV$ weighted by a local function ζ, usually chosen radially symmetric, as:

$$\boldsymbol{\omega}(\boldsymbol{x},t) \approx \boldsymbol{\omega}_\alpha(\boldsymbol{x},t) = \sum_p \zeta(|\boldsymbol{x} - \boldsymbol{x}_p|)\,\boldsymbol{\alpha}_p(t) \tag{12.2}$$

Choosing $\zeta \equiv \delta$ leads to the singular vortex particle method, whereas a proper choice of ζ leads to a regularization of the method which possess better convergence properties [221]. In the present study a second order exponential function is used for ζ ([217]).

Velocity reconstruction approach For most physical applications, a velocity field $\boldsymbol{u}$ can be written according to the following Helmholtz decomposition: $\boldsymbol{u} = \boldsymbol{u}_\infty + \boldsymbol{u}_\omega + \boldsymbol{u}_\phi$ where $\operatorname{curl} \boldsymbol{u}_\infty = \operatorname{div} \boldsymbol{u}_\infty = 0$, $\operatorname{curl} \boldsymbol{u}_\omega = 0$ and $\operatorname{curl} \boldsymbol{u}_\phi = 0$ (see [167]). For incompressible flows $\boldsymbol{u}_\phi$ accounts for boundary conditions. In absence of boundaries and for a flow occupying the entire space $\boldsymbol{u}_\phi = 0$. If the domain is truncated for numerical reasons then $\boldsymbol{u}_\phi \neq 0$ and this term represents the effect of the omitted outer domain. The divergent free component is written $\boldsymbol{u}_\omega = \operatorname{rot} \boldsymbol{\psi}$, with the gauge $\operatorname{div} \boldsymbol{\psi} = 0$. In an unbounded space, if the vorticity field is known, the formula $\boldsymbol{\omega} = \operatorname{curl} \boldsymbol{u}$ leads to $\Delta \boldsymbol{\psi} = -\boldsymbol{\omega}$ which is partially inverted using the Biot-Savart law:

$$\boldsymbol{u}_\omega(\boldsymbol{x}) = \int_V \boldsymbol{K}(\boldsymbol{x} - \boldsymbol{x'}) \boldsymbol{\omega}(\boldsymbol{x'})\, dV(\boldsymbol{x'}) \;\approx \boldsymbol{u}_\alpha(\boldsymbol{x}) = \sum_p \boldsymbol{K}_\alpha(\boldsymbol{x} - \boldsymbol{x}_p) \boldsymbol{\alpha}_p \;, \qquad \boldsymbol{K}(\boldsymbol{r}) = -\frac{[\boldsymbol{r}\times]}{4\pi\, r^3} \quad (12.3)$$

using the notations of [84], and where $\boldsymbol{K}_\alpha = \boldsymbol{K} * \zeta$ is the Biot-Savart kernel resulting from the particle approximation. In the presence of boundaries, surface terms are added to satisfy the boundary conditions.

In this chapter a Simplistic Velocity Reconstruction Approach (SVRA) for incompressible flow is chosen. It consists in only using $\boldsymbol{u}_\alpha$ to represent $\boldsymbol{u} - \boldsymbol{u}_\infty$. For a given velocity field $\boldsymbol{u}_{\text{in}}$ the procedure, further called SVRA, is as follows: Compute the rotational of the input field $\boldsymbol{\omega}_{\text{in}} = \operatorname{curl}(\boldsymbol{u}_{\text{in}})$, perform the particle approximation $\boldsymbol{\omega}_{\alpha,\text{in}}$ and obtain the velocity field $\boldsymbol{u}_{\alpha,\text{out}}$ using equation (12.3). Obviously, the component $\boldsymbol{u}_\phi$ and $\boldsymbol{u}_\infty$ are not accounted for: By taking the rotational of the velocity field, the divergent-free part $\boldsymbol{u}_\phi + \boldsymbol{u}_\infty$ is lost since the divergence and the rotational are orthogonal operators. Errors are further introduced from the particle approximation and the numerical implementation of the method, as discussed below.

12.3 Associated errors and discussions

Wrong input - divergence of the velocity field If the input field $\boldsymbol{u}_{\text{in}}$ is not divergence free, then a divergence-free field $\boldsymbol{u}_{\text{out}}$ can be obtained as $\boldsymbol{u}_{\text{out}} = \boldsymbol{u}_{\text{in}} - \boldsymbol{u}_\varphi$, where $\boldsymbol{u}_\varphi = -\nabla\varphi$. Developing the divergence free condition of $\boldsymbol{u}_{\text{out}}$ leads to the Poisson equation $\Delta\varphi = -\operatorname{div} \boldsymbol{u}_{\text{in}}$ which is easily solved using a Poisson solver (with proper boundary conditions). This approach is used in incompressible CFD solvers inserting synthetic turbulence as body forces [103, 205]. It was observed by the current author that the divergence-free operation introduced a smoothing of the velocity field and a cut-off of high frequencies. This step can be skipped here since the SVRA automatically implies that the output velocity field is divergence-free even if the input field is not. Indeed $\boldsymbol{u}_{\alpha,\text{out}} = \operatorname{curl} \boldsymbol{\psi}$ and is thus divergence free[1].

Model error: No handling of the finite support of vorticity In a numerical implementation, the support of vorticity has to be restricted to a given domain[2]. The contribution of the external domain may be accounted for by means of a Neumann to Dirichlet map which ensures the continuity of tangential and normal velocity at the interface S. The velocity field inside the computational domain is $\boldsymbol{u} = \boldsymbol{u}_\infty + \boldsymbol{u}_\omega + \boldsymbol{u}_{\text{ext}}$, where $\boldsymbol{u}_\omega$ is the solution of the homogeneous problem in unbounded

[1] The particle vorticity field $\boldsymbol{\omega}_{\alpha,\text{in}}$ generating the divergent free velocity field $\boldsymbol{u}_{\alpha,\text{out}}$ may not be divergent free and thus not the "true" vorticity field corresponding to $\boldsymbol{u}_{\alpha,\text{out}}$. This is a problem inherent to particle methods and various methods have been implemented to correct the vorticity field every few time-steps to account for it [220]. This justifies the approach of Backaert et al. [4] who input directly the particles obtained from $\boldsymbol{\omega}_{\text{in}}$ into the domain. One can also compute the rotational of the solution $\boldsymbol{\omega}_{\text{out}} = \operatorname{curl}(\boldsymbol{u}_{\alpha,\text{out}})$ and perform the particle approximation again $\boldsymbol{\omega}_{\alpha,\text{out}}$.

[2] In case the input field is periodic, several options are available: 1. Using mirror techniques, a method well adapted to tree-codes [45, 224] but yet approximate since the number of periodic images is finite; 2. Using a grid-based Poisson solver and apply periodic boundary conditions 3. Using vortex particles periodic in a half plane based on Euler-MacLaurin formulae.

space, i.e. equation (12.3), and where $\boldsymbol{u}_{\text{ext}}$ is the surface integral solution of $\nabla^2\boldsymbol{u} = \operatorname{curl}\boldsymbol{\omega}$ that satisfies the mapping with the external domain [154]:

$$\boldsymbol{u}_{\text{ext}}(\boldsymbol{x}) = \int_S \left[u_n(\boldsymbol{x'})\boldsymbol{K}(\boldsymbol{x}-\boldsymbol{x'}) + \boldsymbol{u}_t \times \boldsymbol{K}(\boldsymbol{x}-\boldsymbol{x'})\right] dS(\boldsymbol{x'}) \ , \qquad \boldsymbol{K}(\boldsymbol{r}) = \frac{\boldsymbol{r}}{4\pi\, r^3} \tag{12.4}$$

where, u_n is the component of the input field normal to dS such that $u_n = \boldsymbol{u}\cdot\boldsymbol{n}$, with $\boldsymbol{n}$ pointing towards the interior of the domain, and $\boldsymbol{u}_\tau = -\boldsymbol{u}\times\boldsymbol{n}$. The omission of $\boldsymbol{u}_{\text{ext}}$ in the SVRA is a source of error. Since $K \propto \frac{1}{r^2}$ is involved in $\boldsymbol{u}_{\text{ext}}$, the error decreases further away from the boundary. The inclusion of $\boldsymbol{u}_{\text{ext}}$ in a time-marching simulation is non trivial since the turbulent field evolves and decays. Furthermore, a dedicated tree-algorithm method would be required for an efficient estimation of the surface integral from equation (12.4).
The approach chosen in this study consists in using a computational domain large enough. The input velocity field is further "clipped" so that it continuously reaches zero on the domain boundary. This implies that the vorticity field also smoothly drops to zero. This is necessary in order to avoid any "broken" vortex lines on the boundary that would artificially generate strong vortices and gradually expand to reconnect to the main support [4]. The clipping function is obtained from a smooth approximation of the Heavyside function as:

$$c(x) = \left[1 + \exp\left(\frac{k(1-2x)}{(x(x-1)}\right)\right]^{-1} \qquad x \in]0,1[\tag{12.5}$$

The value $k = 1$ was used and the extent was restricted to five grid cells.

Differentiation error The computation $\boldsymbol{\omega}_{\text{in}} = \operatorname{curl}\boldsymbol{u}_{\text{in}}$ involves a discretization error associated with the order of the differentiation scheme used and the grid resolution of the input velocity field. For the results presented in this thesis, fourth order central differences were used to determine the vorticity with fourth order single-sided stencils on the domain boundaries.

Regularization error The function ζ is in general chosen as a smooth approximation of the δ-Dirac function and taken as function of a parameter σ [221]. The regularization of the method improves the convergence property of the method, but it also prevents drastic variations of the velocity field. Low-order ζ function, or high value of the smooth parameter σ will smoothen the peaks of the output velocity signals compared to the input. In the current study a second order smooth function with a smooth parameter satisfying the overlapping condition was used to ensure the quality of the vortex particle time simulation [12].

Particle distribution and discretization error In the evaluation of equation (12.3), the particles can be seen as quadrature points and there is thus a quadrature error associated to the integral evaluation. The discretization error is minimal when the particles are disposed on a regular lattice [13]. The error related to the quadrature in the Biot-Savart evaluation is here quantified using a 2D sinusoidal input field:

$$\forall\ (x,y) \in \mathbb{R}\times[-\frac{\lambda}{2},\frac{\lambda}{2}], \qquad u = \sin(ky), \qquad v = 0, \qquad \omega_z = -k\cos(ky), \qquad \operatorname{div}\boldsymbol{u} = 0 \tag{12.6}$$

where $\lambda = 2\pi/k$ corresponds to the wave number k. ω_z is projected onto periodic point vortices [105] which x-period is taken as their y-spacing h. A study of the discretization error for different number of points per period $n = \lambda/h$ is shown in figure 12.1(left). The analysis reveals that the error is second order with respect to h, similar to a linear interpolation error. In order to reconstruct a sinusoid of wave number k with a precision of 2%, around 10 particles per wave length are required. Said differently, for a given grid spacing h, the method cuts-off wave-lengths smaller than $10h$. This is illustrated in figure 12.1(right) using a superposition of random sinusoids $\boldsymbol{u} = \sum_i a_i \sin(k_i y)\boldsymbol{e}_x$. This cut-off is relevant for the choice of the minimum scale, or maximum frequency, the method

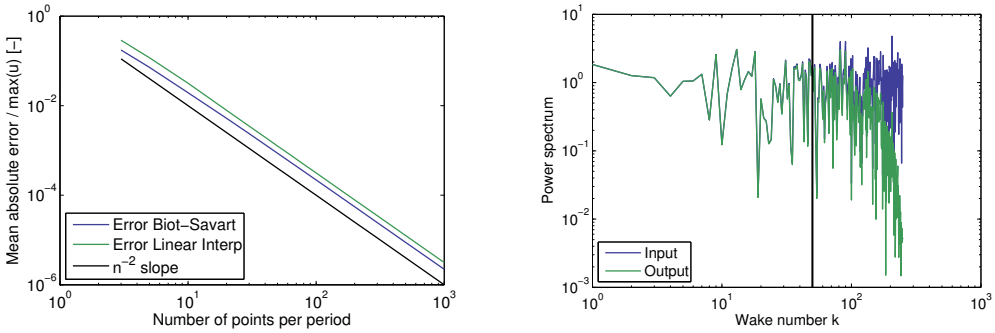

Figure 12.1: Reconstruction of sinusoidal signals in 2D using periodic point vortices. Left: Discretization error in the reconstruction of one sinusoid together with linear interpolation error. Right: Power spectra for a superposition of sinusoids before and after the reconstruction. The approximate cut-off $k_{\text{cut}} = 2\pi/10h$ is marked by a vertical line.

can physically represent.

Oversampling of the velocity or the vorticity can be considered to alleviate the cut-off problem. Oversampling indeed improves the agreement between the input and output field (see figure 12.2(right)). Nevertheless, matching to a given frequency resolution by oversampling the data on one hand and accepting that the method cuts-off around a given frequency on the other, are two different views of the same problem.

12.4 Example of velocity reconstruction for a turbulent field

The SVRA is here applied to the reconstruction of a turbulent velocity field generated using the Mann model [130]. In figure 12.2 a comparison is carried out in terms of velocity signals and spectra at the center of the computational domain. The input turbulent field is an isotropic field of dimensions $10D \times 3D \times 3D$. Three different resolutions were tested. The resolution labeled 1 has dimensions $256 \times 64 \times 64$ while resolutions 2 and 3 are obtained from resolution 1 by successive refinements by a factor 2 in each direction. There is good agreement in the low frequency range while at higher frequencies the velocity spectra obtained with SVRA are seen to loose energy (figure 12.2-right). This deviation is linked to the spatial resolution of the method. For $U_0 = 10\text{m/s}$, $D = 41\text{m}$, $h = 10D/511$, the configuration 2 leads to an estimated cut-off frequency of $f_{\text{cut}} \approx U_0/10h = 1.2Hz$. Increasing the number of particles by a factor of 2^3 increases the estimated cut-off frequency by a factor 2. Cut-off values are indicated by vertical lines in the figure. The mean relative error on the velocity in the plane is 4% for all three velocity components. The error was observed to be larger for the longitudinal component, the component for which the dimension of the domain is largest. The effect of oversampling of either the input velocity or the vorticity field is also shown in the figure. Figure 12.3 shows contours of $|u|$ on a slice of the domain along side with the corresponding relative error (with respect to the maximum amplitude). The mean relative error over the entire slice is 5% while the maximum error is as high as 25%. By excluding a buffer zone along the boundary, in the restricted domain defined by the dashed line, the mean and maximum errors drop to 3.5% and 16% respectively. Consequently, a reconstruction of high quality can be obtained within a certain domain by sufficiently extending the original turbulence box. Clipping was applied, thus the contribution from equation (12.4) is zero but the velocity field is altered and is not ensured to satisfy the continuity equation in this area. If no clipping was applied, the error due to the omission

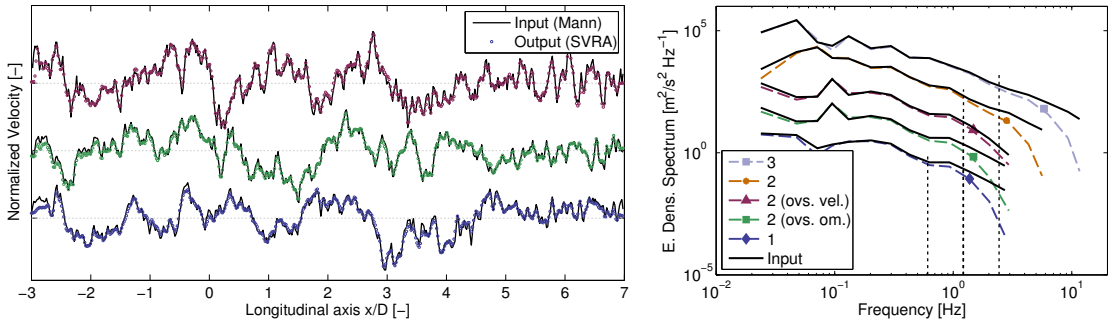

Figure 12.2: Comparison of the input velocity field with the one obtained by the SVRA. (right) Velocity components u, v, w (from bottom to top) for resolution 2, normalized by their maxima. - (left) Spectra of v obtained for different resolutions and oversampling (ovs) methods . Oversampled spectra are cut at the maximum physical frequency value. Oversampling the vorticity (ovs. om.) is seen to be less beneficial than oversampling the input velocity (ovs. vel.).

of $\boldsymbol{u}_{\text{ext}}$ was observed to be larger. The error within the reduced domain is mainly due to the cut-off of the method and the order of the regularization kernel. The mean relative error on the turbulence intensity is 6% in the reduced domain and 3.5% along the centerline of the domain. Lower standard deviations are obtained with the SVRA due to the cut-off of the method at high-frequencies.

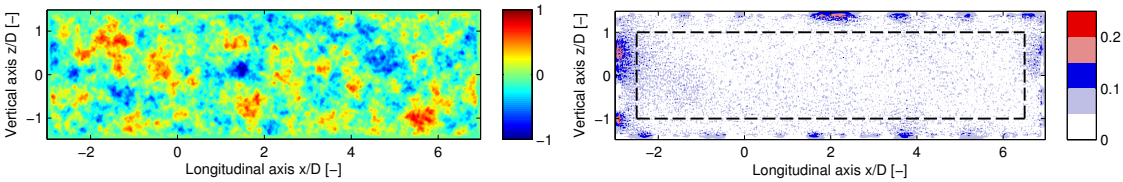

Figure 12.3: Comparison of input turbulent field with the field obtained using the SVRA: (left) field from SVRA - (right) Relative error (from 0 to 25%). .

12.5 Conclusions

The reconstruction of a velocity field using a vortex particle representation was investigated. The main sources of error that were associated with this representation were presented. If a finite support of vorticity is used to represent an infinite unbounded fluid, a surface term should be accounted for to supplement this representation. The use of a domain large enough can justify the omission of this surface term. The cut-off of the frequency content as function of the grid resolution was highlighted. The possibility to use this simplistic approach to represent a turbulent field using particles appears satisfactory for an engineering implementation of turbulence. The use of this representation for time marching turbulent simulations of wind turbines will be the topic of the next chapter.

Chapter 13

Effect of wind turbines on the turbulent inflow

This chapter is based on the following publication: 'Impact of a wind turbine on turbulence: un-freezing the turbulence using a simple vortex particle approach' **[25]**.

Prologue The simplified vortex particle representation of a turbulent field presented in Chapter 12 is applied in order to address the following questions: Does a wind turbine affect the statistics of atmospheric turbulence? Should this imply a change in the way turbulence boxes are used in wind turbine aero-elastic simulations? Is the error involved in neglecting the influence of the wake and the wind turbine on inflow turbulence acceptable in an engineering context?

13.1 Introduction

The impact of turbulence on a wind turbine has always been a first priority topic due to its relevance to safety and design amelioration as indicated by the numerous articles published (e.g. [89, 102]). The current chapter takes the opposite approach and investigates the impact of a wind turbine on turbulence, a topic which has recently received interest [190].

Proper reproduction of the atmospheric conditions is crucial to achieve realistic simulations of wind turbines. The assessment of fatigue and the simulation of extreme events are related to the turbulent velocity fluctuations contained in the inflow received by the wind turbine. Standard tools use synthetic turbulence models [101] to generate turbulent fields prior to the simulations. Examples of models are the ones developed by Kaimal [95], Mann [130, 131] and Veers [215]. In standard BEM based design tools, the information from the generated turbulent field is contained in a so called "turbulence box". The turbulence box is convected with the mean wind speed at hub height under the assumption of Taylor's frozen hypothesis [201]. The frozen external field is fed into the simulation and the turbulent velocity fluctuations are added to the mean wind flow characteristics [109]. This will be defined as a one-way interaction process: The turbulence affects the turbine and its wake, but the turbine does not influence the turbulence. Bossanyi [19] suggested an approach to "un-freeze" inflow turbulence by letting the turbulent field evolve from one turbulence box to another relying on the model of Kristensen [106]. Yet, this approach does no address the full interaction.

The generated turbulent fields are also used in higher fidelity CFD tools. The fields are then included as body forces in a plane upstream of the turbine [103, 205]. The interaction with the turbine is then a two-ways process: The turbulence affects the turbine and vice-versa. A review on the simulation of turbulence by means of vortex methods is given by Yokota [224]. On the application side, Rasmussen et al. [164] inserted vortex particles at the inlet of the computational domain in order to investigate 2D bridge aerodynamics under turbulent conditions. A similar approach was used by Chatelain et al. [42], and Backaert et al. [4] who simulated wind turbine

aerodynamics in 3D, and by Sale et al. who analyzed marine turbines [171]. These works showed that vortex methods are indeed suitable for analyzing inflow turbulence.

13.2 Contributions and key results

Contributions The current study of the impact of a wind turbine on turbulence is believed to be the first of its kind. A crude account of the small scales is done by limiting the amount of vorticity stretching.

Problem definition The two-ways interaction of a wind turbine operating in an unbounded domain with turbulence generated at a "mask" far upstream is considered. The turbulence is represented by vortex particles. A sketch of the lay-out is shown in figure 13.1. The problem is considered in the context of incompressible flows (Ma ≈ 0.2) and the flow equations are given by equation (9.1). The problem is simplified by neglecting the viscous term (Re $\approx [10^5 - 10^7]$). Still the turbulent nature of the underlying flow calls for some account of viscous effects to balance the production of vorticity from the stretching term (see [201, 10]). A crude way to prevent the blow-up of the flow in inviscid simulations is suggested by limiting the amount of stretching (a 2% bound between time-steps is used) and using remeshing to introduce numerical diffusion. The vortex code formulation used for the handling of the wind turbine and the turbulent particles corresponds to Configuration 3-turb (section 9.3). A critical discussion on the limitations of the method can be found in **[25]**.
The SVRA described in Chapter 12 is used to obtain particles based on an input turbulence box generated using Mann's model (forced stratified turbulence could also be used [58]). The approach used by Chatelain et al. [42] is applied to insert turbulent particles at each time-step at the inlet of the domain. The computational domain used in the present study has dimensions $10D \times 5D \times 5D$ and is shown in figure 13.1. The turbulence box has dimensions $64D \times 2.5D \times 2.5D$, discretized into $4096 \times 64 \times 64$ cells. The lateral extent is smaller than the computational domain so as to accommodate any possible growth of the turbulence support. The turbulence was generated as isotropic, using a length scale $L = 30$m and a spectral parameter $\alpha\epsilon^{2/3} = 1.0$ so as to reproduce conditions observed in the measurement campaign of section 11.4. Around 3 million particles are present in the computational domain at each time step. Particles exiting the outlet of the domain are discarded even though other alternatives exist [217, 30]. Simulations of 10min are performed with a time step of 0.15s. During the simulation, the turbulence box is run around 4 times in the domain.

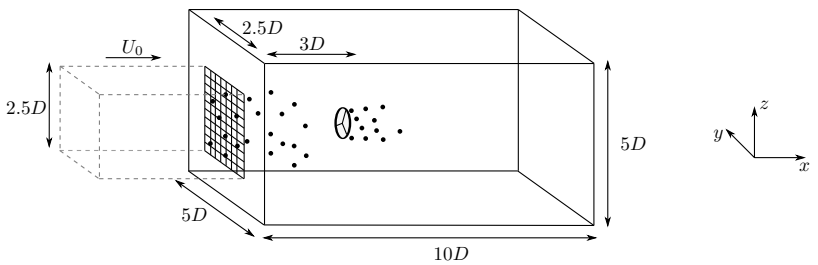

Figure 13.1: Sketch and computational setup. Turbulent vortex particles generated by a "turbulent mask" (represented by a grid), are inserted at each time step. The turbine is located at $x = 0$ and the mask at $x = -3D$.

Time evolution of the turbulent flow field in the absence of a wind turbine In the absence of shear and in the presence of viscous forces the decay of turbulence kinetic energy (TKE, also noted k_t) behind a mask is expected [141, 207]. This is the case in the current study and it was observed that the TKE was linearly decreasing as the particles evolve away from their insertion point. This is consistent with isotropic turbulence theory [201, 56, 10]. Energy density spectra (S) obtained for 10min simulations are shown in figure 13.2. In the "frozen" simulation the particles convects with the free-stream only, whereas they are convected and stretched by the local flow field in the "unfrozen" case. As mentioned in section 12.4 a cut-off is expected, here estimated at 0.5Hz. This explains the differences found in high frequencies between the "Mann" input spectrum and the reconstructed "frozen" spectrum. The shape of the "frozen" and "unfrozen" spectra shown in

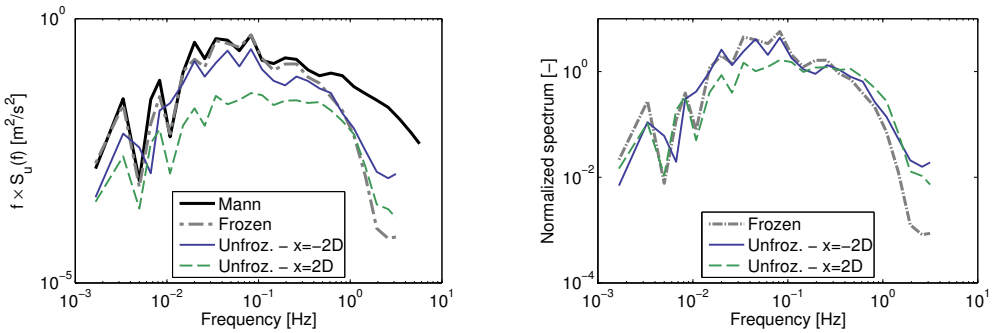

Figure 13.2: Energy density spectra of u obtained at the center line of the domain. Unfrozen turbulence is shown after the turbulence has evolved over a distance of 1 and 5 diameters ($x = -2D$ and $x = 2D$ respectively). The turbulence is decaying in the absence of a driving force such as a shear. Left: spectra normalized by their integral values. A slight shift towards higher frequencies is observed.

figure 13.2 are in good correlation over the low frequency range. The global loss of kinetic energy is seen by comparing the unfrozen spectra at two different distances downstream. The relative comparison of spectra in the right of figure 13.2 shows that the energy distribution tends to shift towards higher frequencies. This can be interpreted as a positive cascade towards the "Kaimal" spectrum [95] in a way similar to the observations found in CFD simulations [205]. The apparition of more energy at high frequencies is likely to be the manifestation of the creation of smaller scales due to vortex stretching [52] and specific LES-treatment such as the "hairpin" removal technique should be used to handle these scales [44].
Simulations without the stretching term (in a 2D fashion) were also performed. Significantly less diffusion was found at lower frequencies whereas at higher frequencies the fluctuations were decaying further and further away from the mask. A negative cascade is indeed expected to occur in 2D [135].

Influence of the wind turbine on the inflow turbulence The turbine and operating conditions were presented in section 11.4. Simulations were performed in the presence of this turbine and the two-way interaction was accounted for. The presence of the turbine was not seen to significantly affect the TKE upstream of the turbine (see **[25]**). By modeling all flow contributions with vortex particles, it is possible to split the flow field depending on the origin of the particles: turbulence vorticity, bound vorticity, and wake vorticity. This decomposition leads to the results of figure 13.3-left where the influence of the wake and turbulence vorticity at an upstream position $x = -0.2R$ is considered. The curve labelled "(all)" refers to the complete flow field while that labelled "(turbulence)" only contains the separate contribution of the turbulence vorticity. It is clear that the peaks at $3p$ and $6p$ are due to the presence of the rotor and its wake. Apart from that, their effect

on other frequencies is insignificant. This result shows that the wind turbine and its wake have

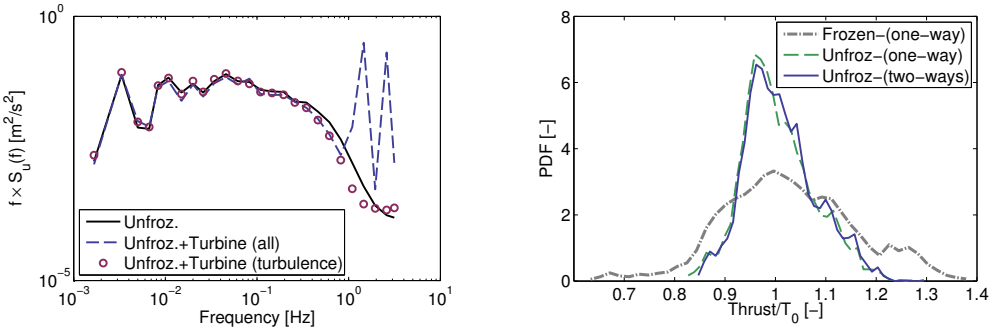

Figure 13.3: (left:) Two-way interaction of the wind turbine with turbulence. Spectra upstream of the turbine at $x = -0.2R$ and at the radial position $r = 0.7R$. The spectrum of the velocity induced by the turbulent particles is labelled "(turbulence)". (right:) Statistics of the rotor thrust from wind turbine simulations using frozen and unfrozen turbulence and for one-way and two-way interactions.

little impact on the turbulence. A careful view reveals that the "Unfrozen+turbine(turbulence)" result contains more energy at low frequencies and less energy at high ones than in the "Unfrozen" result.

Three different simulations were run in order to investigate the effect on the integrated rotor loads. The results are presented in the right of figure 13.3. In all sets the influence of the turbulence vortex particles on the wake and turbine is accounted for. The converse interaction is only accounted for in the "Unfrozen-(two-way)" set. In the "(one-way)" sets, the wake and turbine do not influence the turbulence. By comparing the two unfrozen sets of results it is reconfirmed that the effect of the wind turbine on turbulence is negligible and that in its turn the effect of turbulence on the wind turbine loads will not be affected.

Application to wake deficits The above focused on the turbine-turbulence interaction upstream of the turbine and on the turbine itself. The effect downstream of the turbine is here investigated in a qualitative way. The simulation and measurements from section 11.4 are used. In figure 13.4 the curves labelled "Frozen and Ext." refer to results reported in a previous study ([30] and section 11.4), where velocities from frozen turbulence-boxes were applied as an "external free-stream" to the vortex code (one-way interaction). Results labeled "Unfrozen" were obtained using vortex particle turbulence (two-way interaction), where the turbulence intensity was adjusted such as to obtain the same turbulence intensity as in the frozen turbulence box at the rotor location. The close agreement between the two vortex code simulations suggests that inclusion of the wake-turbulence interaction is of second order when studying averaged wake statistics. Furthermore, Taylor's frozen hypothesis also appears to be sufficient for such studies. It is indeed expected that the wake is mainly driven by the large turbulence scales, which were seen to be barely affected by the turbine. The decay of kinetic energy introduced by the lack of turbulence driving-force does not seem to affect the wake deficits. The agreement between the CFD-LES and vortex code results reveals that the absence of proper LES modelling in the vortex code is a fair approximation for such study. The comparison shows good qualitative agreement with the measurements. The differences observed were justified in section 11.4.

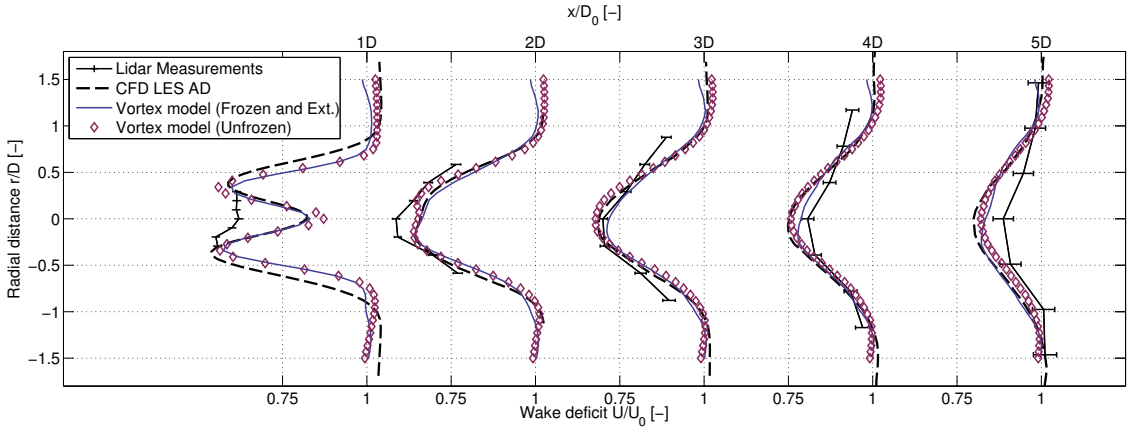

Figure 13.4: Normalized wake deficits obtained from (1h) computations and (18h) measurements. Computations were made using 6×10min with different turbulent boxes of statistics matching the measurements conditions.

13.3 Conclusions

With respect to the questions raised in the prologue out of the results presented, the following conclusions can be drawn:

1. To a first approximation, the presence of the wind turbine does not affect the turbulence spectrum significantly.

2. A closer look at the results revealed a slight decrease of energy in the lower scales of turbulence (high frequencies), which in turn implied a slight reduction of the turbine load fluctuations. Further investigations are nevertheless required to conclude whether this effect is systematic and if the statistics of turbulence boxes should be altered to account for this effect at the rotor.

3. The use of Taylor's frozen hypothesis (one-way interaction) in vortex methods appeared adequate in studying the wake statistics over large time periods. Furthermore, small differences were found between the one-way and two-way interaction results for the wake analysis performed. The extra cost of using the computationally expensive two-way method does not appear justifiable for such a study.

Future work should address the physical modelling of the small scales and the interaction between the turbulence and the turbine linked to the elasticity of the blade. A great challenge also lays in the possibility to include shear in the method. This is the topic of the next chapter.

Chapter 14

Aeroelastic simulation of a wind turbine under turbulent and sheared conditions

This chapter is based on the following publication: 'Aeroelastic large eddy simulations using vortex methods: un-frozen turbulent and sheared inflow' [**31**]

Prologue The simulation of turbulence introduced in Chapter 13 is extended by adding a sheared inflow modelled using vortex particles. The method is then applied for aeroelastic simulations.

14.1 Introduction

Conventional aeroelastic codes use BEM methods to determine the induced velocities and the aerodynamic loads at the blade. Aeroelastic simulations have also been performed using higher order aerodynamic tools such as vortex methods [168] and traditional CFD [83], at a successively increasing computational cost. The methods have been applied to steady inflow conditions. The current study is conducted by performing aeroelastic LES of wind turbines using vortex methods and by further examining the inclusion of shear in the method.

14.2 Contributions and key-results

Contributions A model of shear using vortex methods is established. Aero-elastic simulations under sheared and turbulence inflow is performed for the first time using a vortex code.

Problem definition and computational setup A wind turbine operating under sheared and turbulent inflow is considered. The shear and the turbulence are assumed to be given at a distance upstream of the turbine, while the process responsible for their generation is not modelled. The insertion of turbulence is identical to what was done in Chapter 13. A sketch of the layout and the computational domain is shown in figure 14.1. The problem is studied in the context of incompressible flows (here Ma ≈ 0.2. Equation (9.1) is solved using the vortex particle method, and the lifting line formulation (Configuration 3, in section 9.3). Viscosity is grid filtering is applied as in Chapter 13.
The computational domain, D_{in}, used in the present study has dimensions $8D \times 3D \times 3D$ as shown in figure 14.1. The three-bladed Nordtank 500kW stall regulated wind turbine located at one of DTU Wind Energy's test sites is modelled. The turbine diameter is $D = 2R = 41$m and it rotates at the constant speed $\Omega = \dot{\theta} = 27.1$ RPM. The free-stream velocity is chosen as $U_0 = 7.5\text{m.s}^{-1}$ and the tip-speed ratio is then $\lambda = 7.7$. The shear is assumed linear of slope $du_s/dz = 0.079\text{s}^{-1}$ so that the free-stream velocity at the blade tip varies between 6 and 9m.s^{-1}. In the baseline low resolution case, the domain consists of a grid of $256 \times 96 \times 96$ cells resulting in 2.4M particles. Re-meshing

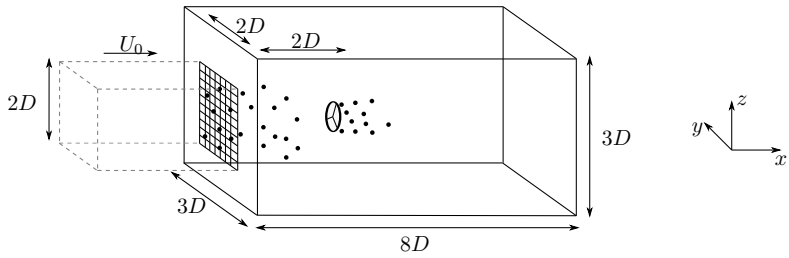

Figure 14.1: Sketch and computational setup. Turbulent vortex particles generated by a "turbulence mask" (represented by a grid), are inserted at each time step. The wind turbine wake is modeled with vortex particles. The domain is filled with particles (not shown) representing the shear vorticity which are also inserted at each time step.

is performed every 10 time steps. The time step chosen is $dt = 0.086$s ($d\theta = 14°$), while the total simulation time is 300s.

Representation of shear A uniform shear profile $\boldsymbol{u}_s = u_s(z)\boldsymbol{e}_x$ is associated to a vorticity profile $\boldsymbol{\omega}_s = \frac{du_s}{dz}\boldsymbol{e}_z$ and the gradient of the velocity field is $[\boldsymbol{\nabla u}_s] = \frac{du_s}{dz}\,\boldsymbol{e}_y \otimes \boldsymbol{e}_z$. In all vortex methods wind turbine simulations known to the author[1], the wind shear is included as part of the "free-stream" $\boldsymbol{U}_0$ [127, 73]. In vortex particle simulations, the term $[\boldsymbol{\nabla u}_s]$ should be added to the gradient $[\boldsymbol{\nabla u}_\omega]$ in order to include the deformations due to the shear. It is the approach chosen for instance in the vortex code GENUVP [217]. In such case, the shear deforms the free vorticity, but the free-vorticity does not deform the shear vorticity and thus equation (9.1) is not fully solved. This approach will be further referred to as a "frozen shear".
The full "unfrozen" situation is here considered. The shear vorticity contained within the computational domain is interpolated onto vortex particles. Since the shear vorticity has an infinite support, the external map from equation (12.4) is used to account for the velocity $\boldsymbol{u}_{\text{ext}}$ and gradient $[\boldsymbol{\nabla u}_{\text{ext}}]$ due to the vorticity outside of the computational domain. In a time-stepping simulation, the "shear" vortex particles convecting outside of the domain at the outlet are discarded whereas new particles are inserted at the inlet. The particles are inserted on a regular grid of spacing h in the $y-z$ plane of the inlet. The validation of the whole procedure is shown in figure 14.2 for a step shear and a linear shear. The contribution of the external map from equation (12.4) is crucial to reconstruct the exact shear and allow long term simulations with the proper deformation of the vortex particles. The surface map integral is computed using point sources and point vortices which result in loss of accuracy close to the boundary D_{in}. Small instabilities were observed at the end of the computational domain due to this point-wise approximation. The rest of the domain is not seen to be significantly affected by these instabilities as seen in figure 14.2. The use of piecewise constant surface panels and the account of the principal value of the integral at the surface itself will increase the accuracy.

Combination of shear and turbulence It was seen in Chapter 13 that the "unfrozen" turbulence tend to loose energy progressively as the eddies evolve away from the mask where they had been generated. The inclusion of shear is expected to sustain the turbulence. Shear and turbulence particles are here inserted. When combining shear and turbulence, the velocities on the boundary ∂D_{in} will not be exactly the ones from the undisturbed shear. This is clear at the inlet and outlet of the turbulence but also on all other boundaries due to the induced velocities of the turbulence

[1] And the coauthors of the paper [26].

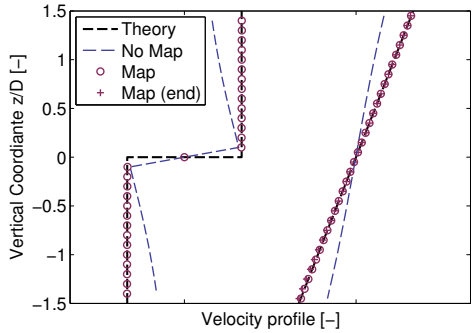

Figure 14.2: Modelling of shear using vortex particles. Velocity profiles obtained at the center of the domain for a step shear and a linear shear. The inclusion of the surface map from equation (12.4) is important. The curved labelled "(end)" is extracted at the end of the simulation. The shear is seen to be conserved with time despite the numerical error that could be introduced by the re-meshing, numerical stretching and convection.

vortex particles on ∂D_{in} and due to the interaction between the shear and turbulence particles which may affect the strength of the shear particles. The difference between the unsteady velocity at the boundary and the steady state shear velocities are expected to be of second order and they are here omitted for simplicity. Since meandering occurs, some shear particles might exit the domain on one side of the domain and holes may be created on the other side. Shear vortex particles are also inserted on the sides of the domain when such holes are detected. At the inlet, the shear particles are inserted as described in section 14.2: More shear vorticity is inserted where the wind velocity is higher. This approach is not followed for the turbulence as the turbulent particles are inserted with the free-stream. Further, the turbulence box used to generate the vortex particles is isotropic and it does not account for an inherent shear. The influence of these two limitations will be investigated in the future.
The evolution of the turbulence intensity across the domain is shown in figure 14.3 for different cases. All simulations corresponds to "unfrozen turbulence". It is observed in the figure that the frozen shear does not significantly affect the turbulence kinetic energy which is seen to decay in the same proportion as the non-sheared case. On the other hand, the account for the full interaction is seen to reduce the decay and a trend towards a stabilisation of the turbulent kinetic energy can be foreseen. Analysis of the velocity profiles revealed that the shear slope was reduced when the full interaction was allowed. The turbulence extracts energy from the shear and tends to homogenize the profile. Troldborg et al. performed CFD simulations with prescribed linear shear and insertion of turbulence in an upstream plane of the domain [207]. In one of their test cases, the boundary condition consisted in artificially prescribing the velocity on the lower and higher boundary. This situation can be linked to the one used here where the surface map is assumed constant. The authors observed that the inclusion of shear was sustaining turbulence and constant statistical properties of turbulence were obtained [207]. The current results are not as pronounced but the difference between the uniform and sheared inflow cases follow the same trends as their results.

Combination of shear and wind turbine Simulations of the Nordtank wind turbine are here presented for cases of frozen and unfrozen shear. Vorticity contours for the two cases are shown in figure 14.4. The wake shape shown in the top of figure 14.4 is consistent with vortex segments simulations performed without the inclusion of the shear vorticity [73]. In the current study, it is seen that the interaction between shear vorticity and the turbine has an important impact on the

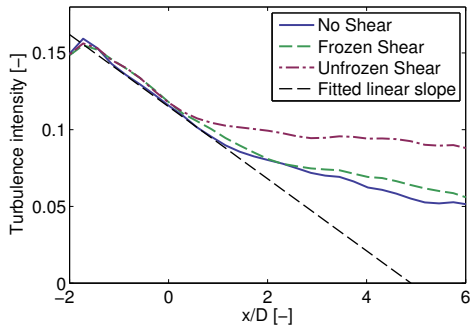

Figure 14.3: Evolution of the turbulence intensity with the distance from the turbulence insertion point. Accounting for the interaction between the shear and turbulence ("unfrozen shear") is seen to increase the turbulence intensity.

wake shape. The wake does not have such a significant upward motion when the full interaction is included. This result is consistent with CFD simulations [228]. The cancellation of the longitudinal vorticity of the wake induced by the shear and the longitudinal vorticity of the shear induced by the wake is likely to be the source of this result. It can be proven using a simple vortex model (see Chapter 7, i.e. [67]). For the current simulation, the omission of this interaction leads to an overestimation of 4% of the power and 1% of the thrust.

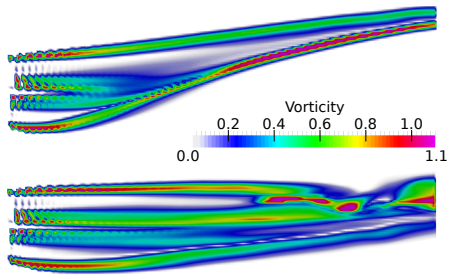

Figure 14.4: Vorticity contours in the wake of the turbine ($x \in [0D, 6D]$) for the case of frozen (top) and unfrozen (bottom) shear. For ease of comparison, the upstream shear vorticity $\boldsymbol{\omega_s} = du_s/dz\boldsymbol{e}_y$ was removed to the local vorticity in the lower plot. The ground effect is not included in either plots. The interaction between the shear vorticity and the turbine has an important impact on the wake shape and a moderate impact on loads.

Aeroelastic LES of wind turbine with shear and turbulence A proof of concept of the applicability of the different models to aero-elastic wind turbine simulations is presented here using the *HAWC2* and *OmniVor* tools. Turbulent simulations with different modelling of shear are run. The simulation time for the full unfrozen case, was 7h30 with 160 CPUs using the tree-code algorithm. A total of 1h was spent in the iterative interaction with the structural code. Many future optimizations of the code are yet possible since new bottlenecks appeared in this study. Further speed up will be obtainable by using the Poisson solver and by optimizing the re-meshing procedure (accounting for 30min here). Results are shown in figure 14.5. The vertical lines corresponds to values obtained using the BEM aerodynamic module of *HAWC2* without turbulence. Both the BEM

and vortex code predicts a reduction of loads and power when shear is present for the simulated operational conditions. Unfreezing the shear is seen to reduce the power mean value but increases its standard deviation. Little impact is seen on the flap-wise moment. Further investigations will be the topic of future work.

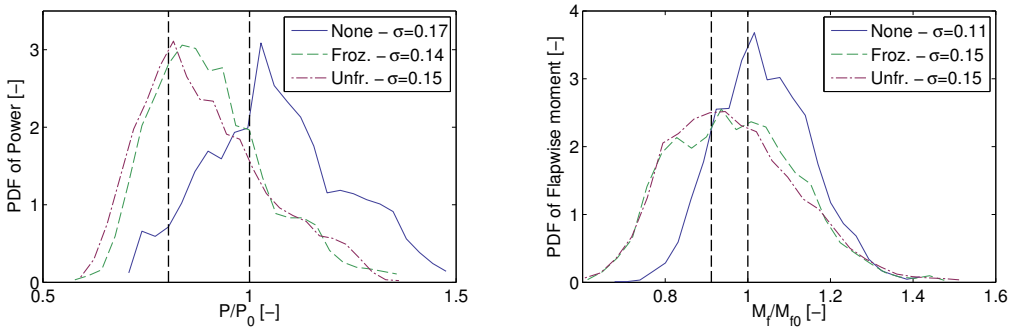

Figure 14.5: Probability density functions of power and flap-wise moments for turbulent aeroelastic simulations perform using the vortex code coupled with *HAWC2* under different shear conditions: no shear, frozen shear, unfrozen shear. The turbulence intensity is TI = 12% (see figure 14.3 at $x = 0$). Vertical lines represent BEM value for TI = 0%, $P_0 = 148$kW, $M_{f,0} = 1.36$kNm. Unfreezing the shear is seen to reduce the power but has little influence on the flapwise moment.

14.3 Conclusions

Vortex particle methods were applied to turbulence, shear, a wind turbine and the combinations of these cases. A Neumann to Dirichlet map was used to account for the vorticity outside of the domain in the modelling of shear. The interaction of the shear and turbulence vorticity was seen to avoid the decay of turbulent kinetic energy. If shear is present but the interaction is not a two-way interaction, the decay occurs. The interaction of the shear and the wind turbine vorticity appeared of importance both for the wake shape and the loads. The possibility to perform aero-elastic simulations of wind turbine under sheared and turbulent conditions was demonstrated. Future work should address the possibility to include unsteady boundary conditions in the method, more consistent SGS models, and further investigate the different interactions of vorticity.

Part VI

Final remarks and Bibliography

Conclusion 97
References 102

Conclusion

Simple vortex models and numerical vortex methods were used to investigate specific aerodynamic problems relevant to wind turbines. A general purpose vortex code was implemented and coupled to an aero-servo-elastic solver in order to perform aeroelastic simulations. The conclusions from the different studies were presented in each chapter.

1. Right cylindrical vortex wake model - Infinite number of blades

The main vortex model investigated was the cylindrical vortex wake model of an infinitely-bladed rotor as introduced by Joukowski in 1912.
- The elementary system of a rotor of constant spanwise circulation was further studied in this thesis for the finite and infinite tip-speed ratio cases. The model is equivalent to 1D momentum theory in the infinite tip-speed ratio case. The advantage of the vortex model lays in the possibility to obtain the velocity in the entire domain, in particular upstream of the rotor.
- A rotor model of radially varying circulation was constructed using a superposition of such elementary systems. If arbitrary circulation values are given to the different vortex cylinders, the kinematic jump-condition across the vortex sheets is in general not satisfied. By consideration of the kinematics across the vortex sheets in the far wake, the condition required to form a consistent vortex system was obtained for the finite and infinite tip-speed ratio cases.
- It was seen that the superposition of cylindrical models leads to the radial independence of annuli in the infinite tip-speed ratio case. Consequently, the model is identical to that of a BEM algorithm provided the three following conditions: the number of blade is infinite, the drag contribution is not accounted for in the determination of the BEM induced velocities, and the loading is azimuthally constant. The fact that the drag contribution should be omitted goes along the line of other authors' work.
- In the finite tip-speed ratio case, the independence of annuli does no longer hold and the analysis showed the importance of the thrust contribution induced by the wake rotation. This contribution is omitted in most BEM implementation or implemented in a different way than the one obtained in the current study.
- An example of implementation of the cylindrical vortex wake model to unsteady inflow was shown and proved to give consistent results with measurements and existing dynamic inflow models. The model can be used for further tuning of dynamic inflow models, or for analysis requiring the knowledge of the unsteady velocity field in a part of the domain different than the rotor disk.
- Application of the cylindrical model to a step-shear inflow in the infinite tip-speed ratio case showed that 1D momentum theory is valid in a local sense, i.e. using the local "free-stream" velocity. The model did not predict any cross-shear deflection of the wake.

Future work
- A way to include wake expansion in the cylindrical wake model should be found

- A way to relax the assumption of azimuthally constant circulation should be found. The work of Drees [60] may be relevant, it was nevertheless not available to the author. The use of indicial [14, 124, 158] functions could be considered.
- Concerning the pressure drop due to wake rotation the following should be addressed: provide the details of a BEM implementation, perform comparison between Actuator disk and vortex cylinder results, investigate whether a possible performance gain can be obtained.
- Velocity fields from Actuator disk simulations should be compared with the fields from a superposition of cylinders.
- The validity of the shear model using numerical vortex methods should be investigated.

2. Helical vortex wake model

The helical vortex wake model by Joukowski was used to investigate tip-losses and optimal circulation theory (in Appendix D).
- A tip-loss factor based on the analytical formulae of semi-infinite helical vortex was devised. The new formulation is more representative of the wake geometry than the one derived by Prandtl. The results are consistent with Glauert's formulation of Prandtl's tip-loss factor, but Glauert's formulation was seen to imply more tip-losses.
- The analytical wake expansion model from Theodorsen (based on Goldstein's circulation) was applied to the wind energy case. The effect of wake expansion on tip-losses was investigated using numerical analysis. It revealed that tip-losses are reduced due to wake expansion. This implies that further overestimation of tip-losses is expected when using Glauert's formulation.
- The analysis revealed that wake deformation had limited impact on tip-losses.
- As part of this study, a BEM-like helical vortex wake code was implemented. The determination of the pitch angle based on the velocity triangle was not seen sufficient for high thrust cases. It is recommended instead to determine the helical pitch of each trailed filaments according to the pitch relationship found in the cylindrical case.

Future work
- High-quality flow and loads measurements at the tip of a rotor are required to validate the gain in performance of the new tip-loss factor compared to Glauert's formulation. Such measurements are usually challenging. The use of CFD data can also be considered. The complex performance of the airfoil in the tip-region will unfortunately add a lot to the uncertainty of the results. Means of abolishing the angle of attack could help the study.
- Further applications of the helical vortex wake code should be considered.
- The derivation of approximate closed-form formulae for the velocity field induced by a semi-infinite helical filaments in the vicinity of the rotor plane would be of interest. In particular, the formulation could be used coupled with beam theory to perform analytical aero-elastic gradient optimization.

3. Skewed cylindrical wake model - Yaw conditions

Coleman and his co-authors used a skewed cylindrical model to investigate yawed rotor of infinite tip-speed ratio. The model forms the basis of current BEM yaw models.
- The skewed cylindrical wake model was further investigated under the condition of finite tip-speed ratio. The induced velocities in the entire domain from the different vorticity components were derived using semi-analytical formulae. The semi-analytical method is appealing in terms of computational time compared to actuator disk CFD. The analysis focused first on a single cylinder. For even faster evaluations, empirical relations were derived on the rotor disk.

- By comparison of the induced velocities in the skewed and right cylinder case, it was possible to derive corrections to be applied in a BEM algorithm. This effectively extends the current BEM yaw model to the case of finite tip-speed ratio. The new yaw model showed better agreement in average with vortex code simulations. The analysis revealed that further gain could be obtained if a superposition of cylinders was used.
- The extension of the BEM yaw model to a superposition of cylinders was partially presented. The model benefits from the determination of the pitch angle of each cylinder obtained in the analysis of the superposition of right cylinders. The model further requires the determination of empirical formulae in the entire rotor plane and not only in the rotor disk. Empirical formulae for the main component, namely the tangential vorticity, were provided.

Future work
- Empirical formulae outside of the rotor disk should be derived for the longitudinal vorticity.
- The BEM implementation of the yaw model using a superposition of skewed cylinders should be finalized and validated against measurements and simulations.
- Velocity fields obtained using the superposition of cylinders should be compared to Actuator disk simulations.

4. Implementation of a vortex code for aero-elastic simulations

- A multi-purpose vortex code, *OMNIVOR*, was implemented as part of this study and coupled to the aero-servo elastic code *HAWC2*.
- The code was validated against measurements, CFD simulations and analytical results.

Recommendations
- Low-order vortex segments methods are simple to implement. The benefit of using such methods for steady simulations does not appear justified since the obtained results were in high-agreements with BEM simulations. The method is nevertheless of relevance for cases that challenge the underlying BEM assumptions: unsteady inflow, yaw, winglets, swept blades, etc. The methods was not used to its fullest yet on these applications. To the author's opinion, the motives to chose such methods are: 1. the ease of implementation, 2. the possibility to separate the effects from different vorticity sources: trailed, shed, bound, turbulence, wake, shear, etc.
- The difficulty of implementation of high-order vortex particle methods is not so far from the one of the vortex segment method. The apparent difficulty might come from the large amount of mathematical results and historical methods presented in the literature and reference books, which can be discouraging at first. The two complications that appear in particles methods are: 1. the need to compute the velocity gradient/deformation tensor, 2. the need to correct the fact that the vorticity field is not divergence free. The first point is easily implemented. The second is difficult to account for in grid-free simulations, but a redistribution procedure can moderate the error. Apart from these two points, particles offer more options than vortex segments methods and can reach high-order accuracy. The inherent (and important) problem of Lagrangian distortion is easily solved by remeshing. Viscous diffusion can be accurately accounted for in grid-free and grid-based formulations. Acceleration techniques such as multipole expansions are simple to implement. The author would recommend implementing a low-order particle method at first. Then consider a tree-code implementation. Tree-based algorithm are of high relevance to vortex methods since they can be used in many applications: induced velocity evaluation, boundary elements/panels evaluations, surface integrals evaluations in Poisson solvers, etc. Extending the method to grid-based vortex methods could then be considered to obtain scalable computational times and benefit

from all the grid-based tools available to make the computation accurate and extensible to complex flows (viscous flows, LES, compressible flows).
- The modelling of bodies and boundary layers is possible in many ways using vortex methods. Yet, it is the author's opinion that Eulerian methods are more adapted to such problems. The use of an Eulerian code around bodies coupled to a Lagrangian vortex code is believed to be a formulation that takes the best from both worlds. Such coupling was successfully achieved in 2D and 3D compressible flows by Papadakis and Voutsinas at NTUA [155].

Future work
- The low-order vortex segment formulation should be used further to investigate the BEM-challenging topics: unsteady inflow, yaw, winglets, swept blades, etc.
- The low-order vortex code could be used in optimization framework such as OpenMDAO.
- Specific aero-elastic simulations should be run using the vortex code. In particular, results should be compared with the different in-house aerodynamic models which are coupled to *HAWC2*: BEM, full rotor CFD, Actuator disk CFD and near-wake models. Simple validation cases using an oscillating blade at standstill can be considered.
- The high-order particle method was implemented in a late stage of this study and would require more validation and code polishing.
- Results from the high-order particle methods should be compared to actuator-line CFD, with and without LES models.
- A coupling between an Eulerian code and the current code could be considered in view of better accounting for bodies and boundary layers.

5. Investigation of complex inflows

The implemented vortex code was applied to wind turbines in complex inflows. This step required a preliminary study on the possibility to reconstruct a given velocity field using vortex particles.
- The different sources of errors that could result from the application of a vortex particle approach to reconstruct a velocity field were considered. The spatial discretization is an unavoidable source of error. Different methods to account for an infinite support of vorticity were mentioned. A surface integral corresponding to the Neumann to Dirichlet map can allow the computational domain to be finite. With no such account, clipping the vorticity support results in an important source of error. The error is yet limited to a buffer layer near the boundary of the domain. Consequently, a reconstruction of high quality can be obtained within a certain domain by sufficiently extending the vorticity support.
- The velocity reconstruction method was applied to a turbulent field. The study investigated the influence of a wind turbine on the upstream turbulence. The contribution from the wind turbine and its wake was not seen to significantly influence the statistical properties of turbulence upstream of the turbine. The study also revealed that the full account of turbulence in vortex methods was not justified to a first approximation for the study of wind turbine aerodynamics and wake dynamics. Using external and frozen turbulence boxes appeared satisfactory.
- The modelling of shear using vortex particle methods was possible by consideration of a constant Neumann to Dirichlet map. It was possible to reproduce any wind shear profile and sustain it in a time-stepping simulation. The interaction of the shear and turbulence vorticity was seen to avoid the decay of turbulent kinetic energy. If shear is present but the interaction is not a two-way interaction, the decay occurs. The interaction of the shear and the wind turbine vorticity appeared of importance both for the wake shape and the loads.
- The possibility to perform aero-elastic simulations of a wind turbine with shear and turbulence using a pure vortex particle formulation was demoustrated.

Future work
- Aeroelastic simulations in complex inflows should be compared with simulations from CFD solvers and measurements.
- The account of the Neumamn to Dirichlet map in a time-stepping simulation should be addressed. The map should be updated at each time step if the flow field external to the domain is varying. Furthermore, a proper account of the flux through the domain surface should be done: Changes within the computational domain will affect the velocity field at the boundary. Simplified assumptions and compromises can be used in a first investigation stage.
- A proper account of shear in vortex methods is challenging. The questions raised can be partially solved if the unsteady Neumann to Dirichlet map mentioned above is properly handled. Another approach would consist in accounting for the boundary layer responsible for the shear. This can be achieved using an Eulerian or Lagrangian solver. In both cases, the longitudinal extent of the computational domain will reach drastic proportions in order for the boundary layer to be fully developed when it reaches the wind turbine.

6. Final words

Clearly the current work only scratched the surface of the innovations possible using vortex-based methods. Both low-order and high-order numerical vortex methods can contribute to the research of wind turbine aerodynamics and aeroelasticity in the future. The author particularly like the "idealization" procedure mentioned in the introduction, and the possibility to decompose the effects from different vorticity sources. These approaches were seen to offer great potential and it is hoped that this study will inspire further work.

Bibliography

[1] Akhmetov, D. G. *Vortex rings*. Springer, 2009. ISBN 3642050158, 9783642050152.

[2] Anderson, C. R. A method of local corrections for computing the velocity field due to a distribution of vortex blobs. *Journal of Computational Physics*, 62(1):111–123, 1986.

[3] Anderson, J. *Fundamentals of aerodynamics - Third Edition*. Mc Graw Hill, 2001.

[4] Backaert, S., Chatelain, P., Winckelmans, G., and Visscher, I. D. Vortex particle-mesh simulations of atmospheric turbulence effects on wind turbine blade loading and wake dynamics. In Hölling, M., Peinke, J., and Ivanell, S., editors, *Wind Energy - Impact of Turbulence*, volume 2 of *Research Topics in Wind Energy*, pages 135–140. Springer Berlin Heidelberg, 2014. ISBN 978-3-642-54695-2. doi: 10.1007/978-3-642-54696-9_20. URL `http://dx.doi.org/10.1007/978-3-642-54696-9_20`.

[5] Bak, C., Johansen, J., and Andersen, P. Three-dimensional corrections of airfoil characteristics based on pressure distributions. *European Wind Energy Conference & Exhibition - Athens, Greece*, 2006.

[6] Balls, G., and Colella, P. A finite difference domain decomposition method using local corrections for the solution of poisson's equation. *Journal Of Computational Physics*, 180(1): 25–53, 2002. ISSN 00219991, 10902716. doi: 10.1006/jcph.2002.7068.

[7] Barba, L. A. *Vortex Method for computing high-Reynolds number flows : Increased accuracy with a fully mesh-less formulation*. PhD thesis, California Institute of technology, 2004.

[8] Bashforth, F., and Adams, J. *An Attempt to Test the Theories of Capillary Action by Comparing the Theoretical and Measured Forms of Drops of Fluid, with an Explanation of the Method of Integration Employed in Constructing the Tables which Give the Theoretical Forms of Such Drops*. Cambridge Univestiy Press, 1883.

[9] Batchelor, G. K. *An introduction to fluid dynamics*. Cambridge University Press, 1967.

[10] Batchelor, G. K., and Townsend, A. A. Decay of vorticity in isotropic turbulence. *Proceedings of the Royal Society of London A: Mathematical, Physical and Engineering Sciences*, 190(1023):534–550, 1947. ISSN 0080-4630. doi: 10.1098/rspa.1947.0095.

[11] Beale, J. T., and Majda, A. Rates of convergence for viscous splitting of the navier-stokes equations. *Mathematics of Computation*, 37:243–259, 1981.

[12] Beale, J. T., and Majda, A. High Order Accurate Vortex Methods with Explicit Velocity Kernels. *Journal of Computational Physics*, 208:188–208, 1985.

[13] Beale, J. T., and Majda, A. Vortex Methods . I : Convergence in Three Dimensions. *Mathematics of Computation*, 39(159):1–27, 2011.

[14] Beddoes, T. S. A near wake dynamic model. *proc. of the AHS national specialist meeting on aerodynamics and aeroacoustics*, 1987.

[15] Bertin, J., and Cummings, R. *Aerodynamics for engineers - 5th Edition*. Pearson Prentice Hall, 2009.

[16] Betz, A. Schraubenpropeller mit geringstem energieverlust - mit einem zusatz von L. Prandtl. *Göttinger Klassiker der Strömungsmechanik Bd. 3*, pages p68–88, 1919. (in German).

[17] Birkhoff, G. Helmholtz and taylor instability. In *Proc. Symp. Appl. Math.*, pages 55–76. Amer. Math. Soc., 1962.

[18] Bisplinghoff, R., Ashley, H., and Halfman, R. *Aeroelasticity*. Dover Books on Aeronautical Engineering Series. Dover Publications, 1996. ISBN 9780486691893.

[19] Bossanyi, E. Un-freezing the turbulence: application to lidar-assisted wind turbine control. *IET Renewable Power Generation*, 7(4):321–329, 2013. ISSN 17521424, 17521416. doi: 10.1049/iet-rpg.2012.0260.

[20] Branlard, E. Wind turbine tip-loss corrections: Review, implementation and investigation of new models. Master's thesis, Risø-DTU, Siemens Energy Inc. (available at DTU's library), September 2011.

[21] Branlard, E. Vortex theory and vortex methods for wind energy. Annex to PhD thesis, 2015. (Avaible upon request).

[22] Branlard, E., and Gaunaa, M. Development of new tip-loss corrections based on vortex theory and vortex methods. *Journal of Physics: Conference Series (Online)*, 555:1–8, 2014. ISSN 1742-6596. doi: 10.1088/1742-6596/555/1/012012.

[23] Branlard, E., and Gaunaa, M. Cylindrical vortex wake model: right cylinder. *Wind Energy*, 524(1):1–15 (Online), 2014. ISSN 10954244, 10991824. doi: 10.1002/we.1800.

[24] Branlard, E., and Gaunaa, M. Cylindrical vortex wake model: skewed cylinder, application to yawed or tilted rotors. *Wind Energy*, page (Online), 2015. ISSN 1099-1824. doi: 10.1002/we.1838.

[25] Branlard, E., and Gaunaa, M. Impact of a wind turbine on turbulence: un-freezing the turbulence by means of a simple vortex particle approach, 2015. (Submitted to the Journal of Wind Engineering and Industrial Aerodynamics, currently under review).

[26] Branlard, E., and Gaunaa, M. Superposition of vortex cylinders for steady and unsteady simulation of rotors of finite tip-speed ratio, 2015.

[27] Branlard, E., Dixon, K., and Gaunaa, M. An improved tip-loss correction based on vortex code results. In *Proceedings*. EWEA - The European Wind Energy Association, 2012.

[28] Branlard, E., Dixon, K., and Gaunaa, M. Vortex methods to answer the need for improved understanding and modelling of tip-loss factors. *IET Renewable Power Generation*, 7(4):311–320, 2013. ISSN 1752-1416.

[29] Branlard, E., Gaunaa, M., and Machefaux, E. Investigation of a new model accounting for rotors of finite tip-speed ratio in yaw or tilt. *Journal of Physics: Conference Series (Online)*, 524(1):1–11, 2014. ISSN 1742-6596. doi: 10.1088/1742-6596/524/1/012124.

[30] Branlard, E., Machefaux, E., Gaunaa, M., Brandenborg Sørensen, H., and Troldborg, N. Validation of vortex code viscous models using lidar wake measurements and CFD. In *Proceedings*. EWEA - The European Wind Energy Association, 2014.

[31] Branlard, E., Papadakis, G., Gaunaa, M., Winckelmans, G., and Larsen, T. J. Aeroelastic large eddy simulations using vortex methods: unfrozen turbulent and sheared inflow. *Journal of Physics: Conference Series (Online)*, 625, 2015. ISSN 1742-6596. doi: 10.1088/1742-6596/625/1/012019.

[32] Branlard, E., Pedersen, A., Mann, J., Angelou, N., Fischer, A., Mikkelsen, T., Harris, M., Slinger, C., and Montes, B. Retrieving wind statistics from average spectrum of continuous-wave lidar. *Atmospheric Measurement Techniques*, 6(1):1943–1977, 2013. ISSN 1867-8610.

[33] Breslin, J. P., and Andersen, P. *Hydrodynamics of Ship Propellers*. Cambridge University Press, 1993.

[34] Burton, T., Sharpe, D., Jenkins, N., and Bossanyi, E. *Wind Energy Handbook*. J. Wiley & Sons, New-York, N.Y., first edition, 2002. ISBN 9780471489979. doi: 10.1002/0470846062. URL `http://dx.doi.org/10.1002/0470846062`.

[35] Burton, T., Sharpe, D., Jenkins, N., and Bossanyi, E. *Wind Energy Handbook, New-York, N.Y.* J. Wiley & Sons, second edition, 2011. ISBN 9780470699751.

[36] Butcher, J. *Numerical Methods for Ordinary Differential Equations, Second Edition*. Jogn Wiley & Sons, 2008.

[37] Callaghan, E. E., and Maslen, S. H. The magnetic field of a finite solenoid. Technical report, NASA technical note D-456, Lewis Research Center, Cleveland, Ohio, 1960.

[38] Castles, W., and De Leeuw, J. H. The normal component of the induced velocity in the vicinity of a lifting rotor and some examples of its application. Technical report, NACA Report No. 1184, Giorgia Institure of Technology, Atlanta, 1954.

[39] Castles, W., and Durham, H. L. Distribution of normal component of induced velocity in lateral plane of a lifting rotor. Technical report, NACA TN-3841, 1956.

[40] Chaney, K., and Eggers, A. J. Expanding wake induction effects on thrust distribution on a rotor disc. *Wind Energy*, 5:213–226, 2002.

[41] Chaney, K., Eggers, A. J., Moriarty, P. J., and Holley, W. E. Skewed wake induction effects on thrust distribution on small wind turbine rotors. *J. Sol. Energy Eng.*, 123(4):290–295, 2001. doi: 10.1115/1.1410109.

[42] Chatelain, P., Backaert, S., Winckelmans, G., and Kern, S. Large eddy simulation of wind turbine wakes. *Flow Turbulence And Combustion*, 91(3):587–605, 2013. ISSN 13866184, 15731987. doi: 10.1007/s10494-013-9474-8.

[43] Chorin, A. J. Numerical study of slightly viscous flow. *Journal of Fluid Mechanics*, 57: 785–796, 1973.

[44] Chorin, A. J. Hairpin removal in vortex interactions. *Journal of Computational Physics*, 87(2):496, 1990. ISSN 00219991, 10902716.

[45] Cocle, R., Winckelmans, G., and Daeninck, G. Combining the vortex-in-cell and parallel fast multipole methods for efficient domain decomposition simulations. *Journal of Computational Physics*, 227(4):2263–2292, 2008. ISSN 00219991, 10902716.

[46] Coleman, R. P., Feingold, A. M., and Stempin, C. W. Evaluation of the induced-velocity field of an idealized helicopter rotor. *NACA ARR No. L5E10*, pages 1–28, 1945.

[47] Conway, J. T. Exact actuator disk solutions for non-uniform heavy loading and slipstream contraction. *Journal Of Fluid Mechanics*, 365:235–267, 1998. ISSN 00221120, 14697645.

[48] Conway, J. T. Application of an exact nonlinear actuator disk theory to wind turbines. In *Proceedings of ICNPAA, Melbourne Florida*, 2002.

[49] Conway, J. T. Analytical solutions for the general non-axisymmetric linearized actuator disk. In *Proceedings of AIAA Orlando*, 2003.

[50] Conway, J. T., and Tezok, F. Unsteady three-dimensional vortex sheet panel solutions for oscillating wings. In *Third International Conference On Nonlinear Problems in Aviation and Aerospace*, 2000.

[51] Conway, J. T. Analytical solutions for the actuator disk with variable radial distribution of load. *Journal of Fluid Mechanics*, 297:327–355, 1995. ISSN 00221120, 14697645.

[52] Cottet, G.-H., and Koumoutsakos, P. *Vortex methods: theory and practice*. Cambridge University Press, 2000.

[53] Cottet, G., Michaux, B., Ossia, S., and VanderLinden, G. A comparison of spectral and vortex methods in three-dimensional incompressible flows. *Journal Of Computational Physics*, 175(2):702–712, 2002. ISSN 00219991, 10902716, 01617389. doi: 10.1006/jcph.2001.6963.

[54] Crawford, C. *Advanced engineering models for wind turbines with application to the design of a coning rotor concept*. PhD thesis, Trinity College, Department of Engineering, University of Cambridge, 2006.

[55] Daeninck, G. *Developments in hybrid approaches: Vortex method with known separation location Vortex method with near-wall Eulerian solver RANS-LES coupling*. PhD thesis, Université catholique de Louvain, Faculté des sciences appliiquées, 2006.

[56] de Kármán, T., and Howarth, L. On the statistical theory of isotropic turbulence. *Proceedings of The Royal Society of London Series A-Mathematical And Physical Sciences*, 164(917):192–215, 1937.

[57] de Vaal, J. B., Hansen, M. O. L., and Moan, T. Validation of a vortex ring wake model suited for aeroelastic simulations of floating wind turbines. *Journal of Physics: Conference Series*, 555(1):012025, 2014. URL `http://stacks.iop.org/1742-6596/555/i=1/a=012025`.

[58] De Visscher, I., Bricteux, L., and Winckelmans, G. Aircraft vortices in stably stratified and weakly turbulent atmospheres: Simulation and modeling. *AIAA Journal*, 51(3):551–566, 2013. ISSN 00011452, 1533385x. doi: 10.2514/1.J051742.

[59] De Vries, O. Fluid dynamic aspects of wind energy conversion. *AGARD report, Brussels, Belgium*, AG-243:1–50, 1979.

[60] Drees, M. A theory of airflow through rotors and its application to some helicopter problems. *Journal of the Helicopter Association of Great Britain*, 3(2):79–104, 1949.

[61] Drzewiecki, S. Méthode pour la détermination des éléments mécaniques des propulseurs hélicoïdaux. *Bulletin de l'Association Technique Maritime No. 3 - Session de 1892*, pages p11–31, 1893. (in French).

[62] Egolf, A., and Landgrebe, A. J. Helicopter rotor wake geometry and its influence in forward flight. Technical report, NASA CR-3726, 1983.

[63] Euler, L. *Institutionum Calculi Intergralis - Volume 1-3*. Impenfis Academiae Imperialis Scientiarum, 1792.

[64] Foelsch, K. Magnefeld und indukticität einer zylindrischen spule. *Archiv für Elektrotechnik*, 30(3):139–157, 1936.

[65] Frandsen, S., Barthelmie, R., Pryor, S., Rathmann, O., Larsen, S., Højstrup, J., and Thøgersen, M. Analytical modelling of wind speed deficit in large offshore wind farms. *Wind Energy*, 9(1–2):39–53, 2006.

[66] Gaunaa, M., Sørensen, N., and Døssing, M. Prediction of steady aerodynamic performance of rotors with winglets using simple prescribed ake methods. *AIAA Aerospace Sciences Meeting*, 543, 2011.

[67] Gaunaa, M., Troldborg, N., and Branlard, E. Modelling the influence of wind shear using a simple vortex rotor model, 2015. (To appear in *Wind Energy*).

[68] George, M. F. On the velocity induced by a vortex elliptic cylinder. *Journal of Ship Research*, 24(1):1–7, 1980.

[69] Gibson, I. S. Velocity induced by a semi-infinite vortex cylinder - with extension to short solenoid. *Royal aeronautical soc.*, 78(762):262–268, 1974. ISSN 0001-9240.

[70] Glauert, H. A general theory of the autogyro. Technical report, NACA Reports and Memoranda No. 111, 1926.

[71] Glauert, H. *Airplane propellers, Division L*, volume 4. Julius Springer, Berlin, W.F. Durand (ed) edition, 1935.

[72] Goldstein, S. On the vortex theory of screw propellers. Technical report, St. John's College, Cambridge, January 1929.

[73] Grasso, F. Ground and Wind Shear Effects in Aerodynamic Calculations. Technical Report ECN-E–10-016, Energy research center of the Netherlands (ECN), 2010.

[74] Greengard, L., and Rokhlin, V. A fast algorithm for particle simulations. *Journal of computational physics*, 73(2):325–348, 1987. ISSN 00219991, 10902716.

[75] Guntur, S., Troldborg, N., and Gaunaa, M. Application of engineering models to predict wake deflection due to a tilted wind turbine. In *EWEC, Copenhagen*, 2012.

[76] Gupta, S., and Leishman, J. Comparison of momentum and vortex methods for the aerodynamic analysis of wind turbines. *43rd AIAA Aerospace Scieces and Exhibit*, 2005.

[77] Haans, W. *Wind turbine aerodynamics in yaw - unravelling the measured rotor wake*. PhD thesis, DU Wind - Delft University of Technology, 2011.

[78] Hansen, K. *Description of Nordtank 500/41 at RisøNational Laboratories*. Risø, 2003.

[79] Hansen, M. O. L. *Aerodynamics of Wind Turbines - Second Edition*. Earthscan, London, Sterling, VA, 2008. ISBN 978-1-84407-438-9.

[80] Hansen, M. O. L., Sørensen, J. N., Voutsinas, S., Sørensen, N., and Madsen, H. A. State of the art in wind turbine aerodynamics and aeroelasticity. *Progress in Aerospace Sciences*, 42:285–330, 2006. doi: 10.1016/j.paerosci.2006.10.002.

[81] Hardin, J. C. The velocity field induced by a helical vortex filament. *Phys. Fluids*, 25: 1949–1952, 1982. doi: 10.1063/1.863684.

[82] Harman, C. R. PROPX: Definitions, Derivations, and data Flow. Technical report, Oregon State University, Corvallis, 1994.

[83] Heinz, J. C. *Partitioned Fluid-Structure Interaction for Full rotor computations using CFD*. PhD thesis, Technical University of Denmark, 2013.

[84] Hejlesen, M. N., Rasmussen, J. T., Chatelain, P., and Walther, J.-H. A high order solver for the unbounded poisson equation. *Journal of Computational Physics*, 252:458–467, 2013. ISSN 00219991, 10902716. doi: 10.1016/j.jcp.2013.05.050.

[85] Hess, J. L., and Smith, A. M. O. Calculation of non-lifting potential flow about arbitrary three-dimensional bodies. Technical report, Douglas Aircraft Division, Report No. E.S. 40622, AD0282255, 1962.

[86] Heyson, H., and Katzoff, S. Normal component of induced velocity field in the vicinity of a lifting rotor with a nonuniform disk loading. Technical report, NACA TN-3690, Langley Aeronautical Laboratory, Langley Field, 1956.

[87] Heyson, H., and Katzoff, S. Induced velocities near a lifting rotor with nonuniform disk loading. Technical report, NACA report 1319, 1957.

[88] Hill, M. J. M. *On a spherical vortex*. the Royal Society, 1894.

[89] Hölling, M., Peinke, J., and Ivanell, S., editors. *Wind Energy - Impact of Turbulence*, volume 2 of *Research Topics in Wind Energy*. Springer Berlin Heidelberg, 2014. ISBN 978-3-642-54695-2. doi: 10.1007/978-3-642-54696-9_20. URL `http://dx.doi.org/10.1007/978-3-642-54696-9_20`.

[90] International Standard IEC. *IEC 61400-12 Power performance measurements of electricity producing wind turbines*. International Electrotechnical Commission, Geneva, 2005. ISBN 2831883334.

[91] Jiménez, A., Crespo, A., and Migoya, E. Application of a LES technique to characterize the wake deflection of a wind turbine in yaw. *Wind Energy*, 13(6):559–572, 2010. ISSN 1099-1824. doi: 10.1002/we.380. URL `http://dx.doi.org/10.1002/we.380`.

[92] Johnson, W. *Helicopter theory, Second edition*. Dover books on physics. Dover Publications, Mineola, N.Y., 1994. ISBN 9780486682303.

[93] Johnson, W. *Rotorcraft aeromechanics*. Cambridge University Press, Cambridge, 2013. ISBN 1107357780, 9781107028074, 9781107357785.

[94] Joukowski, N. E. Vortex theory of screw propeller, I. *Trudy Otdeleniya Fizicheskikh Nauk Obshchestva Lubitelei Estestvoznaniya*, 16(1):1–31, 1912. (in Russian). French translation in: Théorie tourbillonnaire de l'hélice propulsive. Gauthier-Villars: Paris, 1929; 1: 1-47.

[95] Kaimal, J. C., Izumi, Y., Wyngaard, J. C., and Cote, R. Spectral characteristics of surface-layer turbulence. *Quarterly Journal Of The Royal Meteorological Society*, 98(417): 563–589, 1972. ISSN 00359009, 1477870x.

[96] Katz, J., and Plotkin, A. *Low-Speed Aerodynamics, 2nd Edition*. Cambridge Aerospace Series(No. 13). Cambridge University Press, February 2001. ISBN 9780521665520.

[97] Kawada, S. Induced velocities of helical vortices. *Journal of Aeronautical Sciences*, 3, 1936.

[98] Kerwin, J. The solution of propeller lifting surface problems by vortex lattice methods. Technical report, Massachusetts Institute of Technology, 1961.

[99] Kerwin, J. Lecture notes hydrofoil and propellers. Technical report, M.I.T., 2000.

[100] Kida, T. A theoretical treatment of lifting surface theory of an elliptic wing. *ZAMM*, 60: p645–651, 1980.

[101] Kleinhans, D., Friedrich, R., Schaffarczyk, A. P., and Peinke, J. Synthetic turbulence models for wind turbine applications. *Progress In Turbulence III*, 131:111–114, 2010. ISSN 09308989.

[102] Kleinhans, D., Friedrich, R., Schaffarczyk, A. P., and Peinke, J. *Progress In Turbulence III*, volume 131. SPRINGER-VERLAG BERLIN, 2010. ISBN 9783642022241.

[103] Kondo, K., Murakami, S., and Mochida, A. Generation of velocity fluctuations for inflow boundary condition of LES. *Journal of Wind Engineering and Industrial Aerodynamics*, 67&68:51–64, 1997.

[104] Kramer, K. The induced efficiency of optimum propellers having a finite number of blades. Technical report, NACA - TM - 884, 1939.

[105] Krasny, R. Desingularization of periodic vortex sheet roll-up. *Journal of Computational Physics*, 65:292–313, 1986.

[106] Kristensen, L. On longitudinal spectral coherence. *Boundary-Layer Meteorology*, 16(3): 145–153, 1979. ISSN 00068314, 15731472. doi: 10.1007/BF03335363.

[107] Kutta, W. Beitrag zur näherungsweisen integration totaler differentialgleichungen. *Zeitschr. für Math. u. Phys.*, 46:453, 1901.

[108] Lamb, H. *Hydrodynamics*. Cambridge University Press, Sixth Edition, 1932.

[109] Larsen, G. C., Madsen, H. A., Thomsen, K., and Larsen, T. J. Wake meandering. *Wind Energy*, 11(4):377–395, 2008. ISSN 10991824, 10954244. doi: 10.1002/we.267.

[110] Larsen, T. J., and Hansen, A. M. *HAWC2 - User manual*. DTU-Risø-R-1597, 2007.

[111] Larsen, T. J., and Hansen, A. M. *HAWC2 - User manual*. DTU-Risø-R-1597, 2007.

[112] Larsen, T. J., Madsen, H. A., Larsen, G. C., and Hansen, K. S. Validation of the dynamic wake meander model for loads and power production in the egmond aan zee wind farm. *Wind Energy*, 16(4):605–624, 2013. ISSN 10954244, 10991824. doi: 10.1002/we.1563.

[113] Leishman, J. G. *Principles of Helicopter Aerodynamics - Second Edition*. Cambridge Aerospace Series(No. 12). Cambridge University Press, april 2006. ISBN 9780521858601.

[114] Leishman, J. G., and Beddoes, T. A semi-empirical model for dynamic stall. *Journal of the American Helicopter Society*, 34(3):p3–17, 1989.

[115] Lerbs, H. W. Moderately loaded propellers with a finite number of blades and an arbitrary distribution of circulation. *Transactions of the Society of Naval Architects and Marine Engineer*, 60:73–117, 1952.

[116] Lewis, R. I. *Vortex Element Methods for Fluid Dynamic Analysis of Engineering Systems*. Cambridge University Press, 1991. ISBN 9780511529542. URL `http://dx.doi.org/10.1017/CBO9780511529542`. Cambridge Books Online.

[117] Lindenburg, C. Investigation into rotor blade aerodynamics. Technical Report ECN-C-03-025, ECN, 2003.

[118] Lissaman, P. Energy effectiveness of arbitrary arrays of wind turbines. *Journal of Energy*, 3(6):323–328, 1979.

[119] Machefaux, E., Larsen, G. C., Troldborg, N., and Rettenmeier, A. Single Wake Meandering, Advection and Expansion - an analysis using an adapted Pulse Lidar and CFD LES-ACL simulations. In *Scientific proceedings*, pages 50–55. EWEC 2013 Vienna, 2013.

[120] Machefaux, E., Larsen, G. C., Troldborg, N., Gaunnaa, M., and Rettenmeier, A. Empirical modelling of single wake advection and expansion using full scale pulsed lidar based measurements. *In review - Journal of Wind Energy*, 2014.

[121] Machefaux, E., Larsen, G., Koblitz, T., Troldborg, N., Kelly, M., Chougule, A., Hansen, K., and Rodrigo, J. Experimental and numerical study of the atmospheric stability impact on wind turbine wake. *Wind Energy*, 2015. Submitted to the journal Wind Energy in December 2014.

[122] Madsen, H., Mikkelsen, R., Øye, S., Bak, C., and Johansen, J. A detailed investigation of the blade element momentum (bem) model based on analytical and numerical results and proposal for modifications of the bem model. *Journal of Physics: Conference Series 75*, 2007.

[123] Madsen, H., Bak, C., Døssing, M., Mikkelsen, R., and Øye, S. Validation and modification of the blade element momentum theory based on comparisons with actuator disc simulations. *Wind Energy*, 13:p373–389, 2010.

[124] Madsen, H. A., and Rasmussen, F. A near wake model for trailing vorticity compared with the blade element momentum theory. *Wind Energy*, 7:325–341, 2004.

[125] Madsen, H. A cfd analysis of the actuator disc flow compared with momentum theory results. *10th IEA Meeting, Edingburg*, 1995.

[126] Madsen, H., Mikkelsen, R., Johansen, J., Bak, C., Øye, S., and Sørensen, N. Inboard rotor/blade aerodynamics and its influence on blade design. Technical Report Riso-R-1559 - Chapter 3, Risø Laboratory for Sustainable Energy, Roskilde, 2005.

[127] Madsen, H., Riziotis, V., , Zahle, F., Hansen, M., Snel, H., Grasso, F., Larsen, T., Politis, E., and Rasmussen, F. Blade element momentum modeling of inflow with shear in comparison with advanced model results. *Wind Energy*, 15:63–81, 2012.

[128] Madsen Aagaard, H., Mikkelsen, R., Sørensen, N., Hansen, M., Øye, S., and Johansen, J. *Influence of wind shear on rotor aerodynamics, power and loads*, pages 101–116. Risoe-R-1611. Forskningscenter Risoe., 2007. ISBN 978-87-550-3610-9.

[129] Mangler, K. W., and Squire, H. B. The induced velocity field of a rotor. Technical report, Aeronautical Research Council - R.&M. No. 2642, 1950.

[130] Mann, J. The spatial structure of neutral atmospheric surface-layer turbulence. *Journal of Fluid Mechanics*, 273:p141–168, 1994.

[131] Mann, J. Wind field simulation. *Prob. Engng. Mech.*, 13(4):p269–282, 1998.

[132] Manolas, D., Riziotis, V., and Voutsinas, S. Assessment of 3d aerodynamic effects on the behaviour of floating wind turbines. *Journal of Physics: Conference Series*, 555(1): 012067, 2014. ISSN 17426596, 17426588. doi: 10.1088/1742-6596/555/1/012067.

[133] Manwell, J., McGowan, J., and Rogers, A. *Wind Energy Explained*. J. Wiley and Sons, LTD, August 2003.

[134] McWilliam, M. K., Lawton, S., S.Cline, and Crawford, C. A corrected blade element momentum method for simulating wind turbines in yawed flow. *Proceedings of 49th AIAA Meeting, Orlando*, pages 1–10, 2011.

[135] McWilliams, J. C. The emergence of isolated coherent vortices in turbulent-flow. *Journal Of Fluid Mechanics*, 146(SEP):21–43, 1984. ISSN 00221120, 14697645.

[136] Mercier, P. Fast vortex method for large scale wind energy simulations. Technical report, Institut Supérieur de l'Aéronautique et de l'Espace, 2014.

[137] Micallef, D., Ferreira, C., Sant, T., and van Bussel, G. An Analytical Model of Wake Deflection Due to Shear Flow. *3rd Conference on The science of making Torque from Wind, Crete, Greece*, pages 337–347, 2010.

[138] Michelsen, J. A. *Basis3D - a Platform for Development of Multiblock PDE Solvers*. PhD thesis, Technical University of Denmark (DTU) - Deparment of Fluid Mechanics, 1992.

[139] Michelsen, J. A. *Block Structured Multigrid Solution of 2D and 3D elliptic PDE's*. AFM 94-05 - Department of Fluid Mechanics, Technical University of Denmark, 1994.

[140] Mikkelsen, R. F. *Actuator Disc Methods Applied to Wind Turbines*. PhD thesis, DTU-MEK, 2004.

[141] Monin, A. S., and Yaglom, A. M. *Statistical fluid mechanics mechanics of turbulence. vol. 1*. MIT press, Cambridge, 1971. ISBN 978-0-262-13062-2.

[142] Mukherjee, R., and Gopalarathnam, A. An iterative decambering approach for post-stall prediction of wing characteristics using section data. In *AIAA 2003-1097*, 2003.

[143] Müller, K. F. Berechnung des induktivität von spulen. *Archiv für Elektrotechnik*, 17(5): 336–353, 1926.

[144] Munk, M. *The minimum induced drag of aerofoils.* NACA report No. 121, 1923.

[145] Okulov, V. L. The velocity induced by vortex filaments with cylindrical and conic supporting surface. *Russian Journal of Engineering Thermophysics*, 5:63–75, 1995.

[146] Okulov, V. L., Sørensen, J. N., and Wood, D. H. The rotor theories by professor joukowsky: Vortex theories. *Progress in Aerospace Sciences*, 73(0):19 – 46, 2015. ISSN 0376-0421. doi: http://dx.doi.org/10.1016/j.paerosci.2014.10.002.

[147] Okulov, V. Limit cases for rotor theories with Betz optimization. *Journal of Physics: Conference Series (Online)*, 524(1):1–7, 2014. ISSN 1742-6596. doi: 10.1088/1742-6596/524/1/012129.

[148] Okulov, V., and Sørensen, J. Instability of a vortex wake behind wind turbines. *Doklady Physics*, 49:p772–777, 2004.

[149] Okulov, V., and Sørensen, J. Optimum operating regimes for the ideal wind turbine. *Journal of Physics - Conference series 75*, 75, 2007. doi: 10.1088/1742-6596/75/1/012009.

[150] Okulov, V., and Sørensen, J. An ideal wind turbine with a finite number of blades. *Doklady Physics*, 53:p337–342, 2008.

[151] Okulov, V., and Sørensen, J. Maximum efficiency of wind turbine rotors using Joukowsky and Betz approaches. *Journal of Fluid Mechanics*, 649:497–508, 2010. ISSN 00221120, 14697645. doi: 10.1017/S0022112010000509.

[152] Øye, S. A simple vortex model of a turbine rotor. In *Proc. of the third IEA Symposium on the Aerodynamics of Wind Turbines, ETSU, Harwell*, pages 4.1–1.15, 1990.

[153] Øye, S. Induced velocities for rotors in yaw - an extension of the blade element momentum method. *Sixth IEA Symposium on the Aerodynamics of Wind Turbines, ECN, Petten*, pages 1–5, 1992.

[154] Papadakis, G., and Voutsinas, S. G. In view of accelerating CFD simulations through coupling with vortex particle approximations. *Journal of Physics: Conference Series*, 524(1): 012126, 2014. ISSN 17426588, 17426596. doi: 10.1088/1742-6596/524/1/012126.

[155] Papadakis, G. *Development of a hybrid compressible vortex particle method and application to external problems including helicopter flows.* PhD thesis, National Technical University of Athens, 2014.

[156] Pascal, L. Mexico project data analysis. Master's thesis, ISAE-Supaero - ECN Wind Memo-09-010, 2008.

[157] Peirce, B. *A Short table of integrals.* Ginn & Company, Boston, U.S.A., Revised edition, 1899.

[158] Pirrung, G. R., Hansen, M. H., and Madsen, H. A. Improvement of a near wake model for trailing vorticity. In *Proceedings of the science of making torque from wind, Oldenburg*, 2012.

[159] Pitt, D. M., and Peters, D. A. Theoretical prediction of dynamic-inflow derivatives. *Vertica*, 5:21–34, 1981.

[160] Ploumhans, P., Daeninck, G., and Winckelmans, G. Simulation of Three-Dimensional Bluff-Body Flows Using the Vortex Particle and Boundary Element Methods. *Systems Engineering*, (i):117–131, 2004.

[161] Prandtl, L. Appendix to Betz's article: Schraubenpropeller mit geringstem energieverlust - mit einem zusatz von L. Prandtl. *Göttinger Klassiker der Strömungsmechanik Bd. 3*, pages p89–92, 1919. (in German).

[162] Prandtl, L. *Applications of modern hydrodynamics to aeronautics.* NACA report No. 116, 1921.

[163] Protheroe, R., and Koks, D. The transient magnetic field outside an infinite solenoid. *American Journal Of Physics*, 64(11):1389–1393, 1996. ISSN 00029505, 19432909, 00029595.

[164] Rasmussen, J. T., Hejlesen, M. M., Larsen, A., and Walther, J.-H. Discrete vortex method simulations of the aerodynamic admittance in bridge aerodynamics. *Journal of Wind Engineering and Industrial Aerodynamics*, 98(12):754–766, 2010. ISSN 18728197, 01676105. doi: 10.1016/j.jweia.2010.06.011.

[165] Rathmann, O., Barthelmie, R., and Frandsen, S. Turbine wake model for wind resource software. *Proceedings of EWEC*, 2006.

[166] Rettenmeier, A., Bischoff, O., Schlipf, D., Anger, J., Hofsäss, M., Cheng, P., Wagner, R., Courtney, M., and Mann, J. Turbulence and wind speed investigations using a nacelle-based lidar scanner and a met mast. *Presentation Proceedings of EWEA 2012 conference, Copenhagen*, 2012.

[167] Richardson, S. M., and Cornish, A. R. H. Solution of three dimensional incompressible flow problems. *Journal of Fluid Mechanics*, 82:pp. 309–319, 1977. doi: 10.1017/S0022112077000688.

[168] Riziotis, V. A., Manolas, D. I., and Voutsinas, S. G. Free-wake aeroelastic modelling of swept rotor blades. *European Wind Energy Conference and Exhibition 2011, EWEC 2011*, 2011.

[169] Runge, C. Ueber die numerische auflösung von differentialgleichungen. *Math. Ann.*, 46: 167–178, 1895.

[170] Saffman, P. *Vortex Dynamics.* Cambridge University Press, 1992.

[171] Sale, D., Aliseda, A., and Lic, Y. Simulation of hydrokinetic turbines in turbulent flow using vortex particle methods. In *Proceedings of the 2nd Marine Energy Technology Symposium: METS2014-April 15-18, 2014, Seattle, WA*, 2014.

[172] Salmon, J. K., Warren, M., and Winckelmans, G. Fast parallel tree codes for gravitational and fluid dynamical n-body problems. *Intl. J. Supercomput. Appl. High Perf. Comp.*, 8(2):192–142, 1994.

[173] Sankar, L. Computational studies of horizontal axis wind turbines - annual status report 2000-2001. Technical report, NREL - Georgia institute of technology, 2001.

[174] Sant, T. *Improving BEM-based aerodynamics models in Wind turbine design codes.* PhD thesis, DU Wind - Delft University of Technology, 2007.

[175] Sarpkaya, T. Computational methods with vortices - the 1988 freeman scholar lecture. *Journal of fluids engineering-transactions of the asme*, 111(1):5–52, 1989. ISSN 00982202, 1528901x.

[176] Sbalzarini, I. F., Walther, J. H., Bergdorf, M., Hieber, S. E., Kotsalis, E. M., and Koumoutsakos, P. PPM - A highly efficient parallel particle - mesh library for the simulation of continuum systems. *Journal of Computational Physics*, 215:566–588, 2006. doi: 10.1016/j.jcp.2005.11.017.

[177] Schaffarczyk, A. P., and Conway, J. T. Application of nonlinear actuator disk theory to wind turbines. In *14th Symposium IEA Joing Action on Aerodynamics of Wind Turbines, NREL, Boulder, Colorado*, 2000.

[178] Schaffarczyk, A. P., and Conway, J. T. Comparison of a nonlinear actuator disk theory with numerical integration including viscous effects. *Canadian Aeronautics and Space Journal, Can Aeronaut Space J*, 46(4):209–215, 2000. ISSN 00082821.

[179] Schepers, J. G., Boorsma, K., and et al. Final report of IEA Task 29, Mexnext (Phase 1): Analysis of Mexico wind tunnel measurementsc. Technical report, IEA Wind - ECN, 2012.

[180] Schepers, J. *An Engineering Model for Yawed Conditions, Developed on the Basis of Wind Tunnel Measurements*. ECN-RX-98-057. Netherlands Energy Research Foundation ECN, Petten, 1998.

[181] Schepers, J., and Snel, H. Model Experiments in Controlled Conditions. Technical report, ECN - ECN-E–07-042, 2007.

[182] Schepers, J., Boorsma, K., and Munduate, X. Final results from mexnext-i: "analysis of detailed aerodynamic measurements on a 4.5 m diameter rotor placed in the large german dutch wind tunnel dnw". In *The Science of Making Torque from the Wind, Oldenburg*, 2012.

[183] Sezer-Uzol, N., and Uzol, O. Effect of steady and transient wind shear on the wake structure and performance of a horizontal axis wind turbine rotor. *Wind Energy*, 16:1–17, 2013.

[184] Sharpe, D. A general momentum theory applied to an energy-extracting actuator disc. *Wind Energy*, 7(3):177–188, 2004. ISSN 10954244, 10991824. doi: 10.1002/we.118.

[185] Shen, W. Z., Mikkelsen, R., Sørensen, J. N., and Bak, C. Tip loss corrections for wind turbine computations. *Wind Energy*, 8:p457–475, 2005.

[186] Shen, W. Z., Sørensen, J. N., and Yang, H. Actuator line/navier-stokes computations for flows past the yawed mexico rotor. *Proceedings of the Wake Conference*, 2011.

[187] Shen, W. Z., Zhu, W. J., and Sorensen, J. N. Actuator line/navier-stokes computations for the mexico rotor: comparison with detailed measurements. *Wind Energy*, 15(5):811–825, 2012. ISSN 10954244, 10991824. doi: 10.1002/we.510.

[188] Shen, X., Zhu, X., and Du, Z. Wind turbine aerodynamics and loads control in wind shear flow. *Energy*, 36:1424–1434, 2011.

[189] Shepers, J. G., Barthelmie, R. J., and Politis, E. S. Upwind wp8: Deliverable d8.5, wake reducing concepts, 2010.

[190] Simley, E., Pao, L. Y., Gebraad, P., and Churchfield, M. Investigation of the impact of the upstream induction zone on lidar measurement accuracy for wind turbine control applications using large-eddy simulation. *Journal of Physics: Conference Series*, 524 (1):012003, 2014. ISSN 17426588, 17426596. doi: 10.1088/1742-6596/524/1/012003.

[191] Snel, H., and Schepers, J. G. Joint investigation of dynamic inflow effects and implementation of an engineering method. Technical report, ECN-C–94-107, Energy Research Centre of the Netherlands, Petten, 1995.

[192] Sørensen, J. N. 2.08 - aerodynamic analysis of wind turbines. In Sayigh, A., editor, *Comprehensive Renewable Energy*, pages 225 – 241. Elsevier, Oxford, 2012. ISBN 978-0-08-087873-7. doi: http://dx.doi.org/10.1016/B978-0-08-087872-0.00209-2.

[193] Sørensen, J. N., and van Kuik, G. A. M. General momentum theory for wind turbines at low tip speed ratios. *Wind Energy*, 14(7):821–839, 2011. ISSN 10991824, 10954244. doi: 10.1002/we.423.

[194] Sørensen, J. N., Naumov, I. V., and Okulov, V. Multiple helical modes of vortex breakdown. *Journal of Fluid Mechanics*, 683:430–441, 2011. ISSN 00221120, 14697645. doi: 10.1017/jfm.2011.308.

[195] Sørensen, J. N., Dag, K. O., and Ramos-Garcia, N. A new tip correction based on the decambering approach. *Journal of Physics: Conference Series*, 524(1):012097, 2014. ISSN 17426588, 17426596. doi: 10.1088/1742-6596/524/1/012097.

[196] Sørensen, J., and Shen, W. Numerical modelling of wind turbine wakes. *Journal of Fluids Engineering*, 124(2):393–399, 2002. ISSN 0098-2202. doi: 10.1115/1.1471361.

[197] Sørensen, N. N. *General Purpose Flow Solver Applied to Flow over Hills*. PhD thesis, Risø National Laboratory., 1995.

[198] Sørensen, N. N., Bechmann, A., Réthoré, P. E., and Zahle, F. Near wake reynolds-averaged navier-stokes predictions of the wake behind the mexico rotor in axial and yawed flow conditions. *Wind Energy*, 17(1):75–86, 2014. ISSN 10954244, 10991824. doi: 10.1002/we.1559.

[199] Spalart, P. R., Leonard, A., and Baganoff, D. Numerical simulation of separated flows. Technical report, PhD Thesis, also NASA Technical Memorandum 84328, 1983.

[200] Stepniewski, W., and Keys, C. *Rotary-Wings Aerodynamics*. Dover Publication, 1984.

[201] Taylor, G. I. The spectrum of turbulence. *Proceedings of The Royal Society of London Series A-Mathematical And Physical Sciences*, 164(A919):0476–0490, 1938. ISSN 00804630.

[202] Theodorsen, T. The theory of propellers i-iv. Technical report, NACA reports 775-778, 1944.

[203] Theodorsen, T. *Theory of propellers*. McGraw-Hill publications in aeronautical science. McGraw-Hill Book Company, New-York, 1948.

[204] Tibery, C., and Wrench, J. Tables of Goldstein factor. Technical report, Applied mathematics laboratory - Department of the navy - report 1534, 1964.

[205] Troldborg, N., Sorensen, J. N., and Mikkelsen, R. Actuator line simulation of wake of wind turbine operating in turbulent inflow. *Science Of Making Torque From Wind*, 75(1): –, 2007. ISSN 17426596, 17426588. doi: 10.1088/1742-6596/75/1/012063.

[206] Troldborg, N., Gaunaa, M., and Guntur, S. Modelling the influence of yaw using a simple vortex rotor model. In *EWEC, Copenhagen*, pages 1–5, 2012.

[207] Troldborg, N., Sørensen, J. N., Mikkelsen, R. F., and Sørensen, N. N. A simple atmospheric boundary layer model applied to large eddy simulations of wind turbine wakes. *Wind Energy*, 17(4):657–669, 2014. ISSN 10991824, 10954244. doi: 10.1002/we.1608.

[208] Tuck, E. Some accurate solutions of the lifting surface integral equation. *J. Austral. Math. Soc. Ser. B*, 35:p127–144, 1993.

[209] Uzol, O. Free-wake calculations of wind turbine wake-rotor interactions: The effect of vortex filament core size, expansion and stretching on performance prediction. In *Science of making torque from the wind - Oldenburg*, 2012.

[210] Van Bussel, G. J. W. The use of the asymptotic acceleration potential method for horizontal axis windturbine rotor aerodynamics. *Journal of Wind Engineering and Industrial Aerodynamics*, 39:161–172, 1992.

[211] van Garrel, A. Development of a wind turbine aerodynamics simulation module. Technical Report ECN-C–03-079, ECN, 2003.

[212] van Kuik, G. A. M. The ideal wake of an ideal actuator disc. In *Proceedings of the Wake Conference, Visby*, pages 127–132, 2011.

[213] van Kuik, G. A. M. On the generation of vorticity by force fields in rotor- and actuator flows. *Renewable Energy*, 70:124–128, 2014. URL `http://dx.doi.org/10.1016/j.renene.2014.02.056`.

[214] van Kuik, G. An inconsistency in the actuator disc momentum theory. *Wind Energy*, 7(1): 9–19, 2004. ISSN 10954244, 10991824. doi: 10.1002/we.104.

[215] Veers, P. Three-dimensional wind simulation. *American Society of Mechanical Engineers, Solar Energy Division (Publication) SED*, 7:23–31, 1988.

[216] Voutsinas, S., and Bergeles, G. Numerical calculation of singular integrals appearing in three-dimensional potential flow problems. *Applied Mathematical Modelling*, 14(12):618–629, 1990. ISSN 0307904x, 18728480.

[217] Voutsinas, S. G. Vortex methods in aeronautics: how to make things work. *International Journal of Computational Fluid Dynamics*, 2006.

[218] Wald, Q. R. The aerodynamics of propellers. *Progress in Aerospace Science*, 42:85–128, 2006. doi: 10.1016/j.paerosci.2006.04.001.

[219] Wilson, R., and Lissaman, P. Applied aerodynamics of wind power machines. Technical report, Oregon State University, Corvallis, May 1974.

[220] Winckelmans, G. S. *Encyclopedia of computational mechanics - Volume 1. Chapter 5: Vortex Methods*, chapter 5. J. Wiley & Sons, New-York, N.Y., 2004. ISBN 0470846992, 9780470846995.

[221] Winckelmans, G. S., and Leonard, A. Contributions to vortex particle methods for the computation of 3-dimensional incompressible unsteady flows. *Journal Of Computational Physics*, 109(2):247–273, 1993. ISSN 00219991, 10902716. doi: 10.1006/jcph.1993.1216.

[222] Winckelmans, G., Cocle, R., Dufresne, L., and Capart, R. Vortex methods and their application to trailing wake vortex simulations. *C. R. Physique*, 6:467–486, 2005. doi: 10.1016/j.crhy.2005.05.001.

[223] Wrench, J. W. The calculation of propeller induction factors. *Reprint of Applied Mathematics Laboratory Tecnical Report 13*, 1957.

[224] Yokota, R., and Obi, S. Vortex methods for the simulation of turbulent flows: review. *Journal of Fluid Science and Technology*, 6(1):14–29, 2011. ISSN 18805558.

[225] Yokota, R., Sheel, T. K., and Obi, S. Calculation of isotropic turbulence using a pure lagrangian vortex method. *Journal Of Computational Physics*, 226(2):1589–1606, 2007. ISSN 10902716, 00219991. doi: 10.1016/j.jcp.2007.06.003.

[226] Zahle, F., and Sørensen, N. Navier-Stokes rotor flow simulations with dynamic inflow. *Torque Conference,Crete, Greece*, 2010.

[227] Zahle, F., Bak, C., Sørensen, N. N., Guntur, S., and Troldborg, N. Comprehensive Aerodynamic Analysis of a 10 MW Wind Turbine Rotor Using 3D CFD. *Proceedings of 32nd ASME Wind Energy Symposium, National Harbor, Maryland*, pages 1–14, 2014.

[228] Zahle, F., and Sørensen, N. Rotor aerodynamics in atmospheric shear flow. *EWEC 2008 Conference Proceedings*, pages 120–124, 2008.

[229] Zahm, A. F. Flow and drag formulas for simple quadrics. Technical report, NACA Report No. 253, 1979.

Part VII

Appendices

A Vortex cylinders and vortex disk 123
- A.1 *Right cylinder of tangential vorticity with arbitrary cross section*
- A.2 *Right vortex cylinder of tangential vorticity - Circular cross section*
- A.3 *Vortex cylinder of longitudinal vorticity*
- A.4 *Bound vortex disk*
- A.5 *Skewed vortex cylinders*

B Helical vortex filaments 147
- B.1 *Exact expressions for infinite helical vortex filaments*
- B.2 *Approximate expressions for infinite helical filaments*
- B.3 *Expressions for semi-infinite helices evaluated on the lifting line*
- B.4 *Notations introduced for approximate formulae*
- B.5 *Summation of several helices - Link between Okulov's relation and Wrench's relation*

C Kutta-Joukowski theorem applied to a rotor with straight lifting lines 151
- C.1 *Vortex actuator disk*
- C.2 *Kutta-Joukowski theorem for a rotor made of straight lifting lines*

D Vortex theory for rotors: Helical wake, optimal circulation, tip-losses and wake expansion . 157
- D.1 *Introduction*
- D.2 *From optimal distribution of circulation to a modern interpretation of tip-losses*
- D.3 *Vortex representation of the wake*
- D.4 *Relation between far wake and near wake parameters*
- D.5 *Analytical and numerical wake models*
- D.6 *Analysis of tip-loss using vortex methods and vortex theory*
- D.7 *Conclusions*
- D.8 *Complements*

E Right cylindrical vortex model applied to wind energy - Complements 181
- E.1 *Introduction notes*
- E.2 *Elementary cylindrical system*
- E.3 *Superposition of cylindrical vortex models for rotor modelling*
- E.4 *System closure under assumption of large tip-speed ratio*
- E.5 *System closure for finite tip-speed ratio*
- E.6 *Superposition of cylindrical vortex systems with wrong closure*
- E.7 *Algorithm for system closure*

F Application of the helical and cylindrical models - comparison with Actuator disk 189
- F.1 *Cylindrical model with wake rotation*
- F.2 *Helical model*

APPENDICES

Appendix A

Vortex cylinders and vortex disk

A.1 Right cylinder of tangential vorticity with arbitrary cross section

A right cylinder of tangential vorticity γ_t of arbitrary cross-section extending along the z-axis from z_1 and z_2 is considered. The cylinder volume is delimited by the surfaces S_1 at $z = z_1$, S_2 at $z = z_2$ and S_c in between. S_c is the only support of vorticity.

A.1.1 Velocity in terms of solid angle

Introduction The velocity induced by a vortex loop of constant intensity $\gamma_t dz'$ is given in the book of Saffman [170] as:

$$d\boldsymbol{u}(\boldsymbol{x}) = \frac{\gamma_t dz'}{4\pi} \nabla\Omega(\boldsymbol{x}, z') \tag{A.1}$$

where $\Omega(\boldsymbol{x}, z')$ is the solid angle of the vortex loop centered on z' as seen from the point $\boldsymbol{x}$ and where the gradient is taken at $\boldsymbol{x}$. Since all the vortex loops of the cylinder have the same shape and radii, the solid angle is a function of $z' - z$, and will be further written: $\Omega(x, y, z' - z)$. The convention $\Omega > 0$ when $z' > z$ is adopted and the gradient $\partial\Omega/\partial z > 0$ with z' fixed. The total velocity is obtained by integration

$$\boldsymbol{u}(\boldsymbol{x}) = \frac{\gamma_t}{4\pi} \int_{z_1}^{z_2} \nabla\Omega(x, y, z' - z)\, dz' \tag{A.2}$$

Considering only the axial component, the integrand is $\frac{\partial\Omega}{\partial z}\, dz'$. Introducing the change of variable $\zeta = z' - z$:

$$u_z(\boldsymbol{x}) = \frac{\gamma_t}{4\pi} \int_{z_1}^{z_2} \frac{\partial\Omega}{\partial z}(x, y, z' - z)\, dz' = \frac{\gamma_t}{4\pi} \int_{\zeta_1}^{\zeta_2} \frac{\partial\zeta}{\partial z} \frac{\partial\Omega}{\partial\zeta}(x, y, \zeta)\, d\zeta = -\frac{\gamma_t}{4\pi} \int_{\zeta_1}^{\zeta_2} d\Omega(x, y, \zeta) \tag{A.3}$$

Care should be used when integrating the solid angle since it is discontinuous at $\zeta = 0$ when the point of evaluation is within the cylinder cross section. Also the same sign convention should be used for each elementary angle $d\Omega$. The dependency with respect to x and y is dropped in the following.

Outside of the cylinder If $\boldsymbol{x}$ is not contained within the cylinder, then the solid angle is continuous and:

$$u_z(\boldsymbol{x}) = \frac{\gamma_t}{4\pi} \left[\Omega_z(\zeta_1) - \Omega_z(\zeta_2)\right] \tag{A.4}$$

Above the subscript z has been added to specity that the normal to S_i has been taken as $\boldsymbol{e}_z$ for the evaluation of both solid angle. Since the control point is outside of the cylinder, the solid angle of the closed surface $S_1 \cup S_c \cup S_2$ is zero:

$$\Omega_{\text{tot}} = \Omega_{-z}(\zeta_1) + \Omega_{\text{c}}(\zeta_1, \zeta_2) + \Omega_z(\zeta_2) = 0 \tag{A.5}$$

where Ω_c is the solid angle subtented by the cylinder surface S_c. Since S_1 is contained in a plane normal to e_z, $\Omega_{-z}(\zeta_1) = -\Omega_z(\zeta_1)$, and thus:

$$u_z(\boldsymbol{x}) = \frac{\gamma_t}{4\pi}\Omega_c(x, y, \zeta_1, \zeta_2) \tag{A.6}$$

Inside the cylinder The solid angle experiences a discontinuity at $\zeta = 0$. The cylinder is split into three cylinders by dividing the original cylinder at $\zeta = \pm\epsilon$, with $\epsilon > 0$. For the two cylinders such that $|\zeta| > \epsilon$, the control point is outside of the cylinders and the induced velocity is readily obtained using either equation (A.4) or equation (A.6). The cylinder delimited by $\zeta = \pm\epsilon$ is now considered. Within this interval $d\Omega$ is discontinuous, but the discontinuity is finite and the integral can be carried on. Since $d\Omega$ is odd the integral is 0. The total velocity field is then, using equation (A.4):

$$u_z(\boldsymbol{x}) = \frac{\gamma_t}{4\pi}\lim_{\epsilon\to 0^+}\left[\Omega_z(\zeta_1) - \Omega_z(-\epsilon) + \Omega_z(\epsilon) - \Omega_z(\zeta_2)\right] = \frac{\gamma_t}{4\pi}\left[\Omega_z(\zeta_1) - \Omega_z(\zeta_2) + 2\lim_{\epsilon\to 0^+}\Omega_z(\epsilon)\right] \tag{A.7}$$

where $\Omega_z(-\epsilon) = -\Omega_z(\epsilon)$ has been used since Ω is odd. Given the convention chosen that $\Omega > 0$ for $\zeta > 0$, the limit is 2π and the velocity is:

$$u_z(\boldsymbol{x}) = \frac{\gamma_t}{4\pi}\left[\Omega_z(\zeta_1) - \Omega_z(\zeta_2) + 4\pi\right] \tag{A.8}$$

Alternatively equation (A.4) can be used using the solid angle of the two cylinder surfaces such that $|\zeta| > \epsilon$ to give:

$$u_z(\boldsymbol{x}) = \frac{\gamma_t}{4\pi}\lim_{\epsilon\to 0^+}\left[\Omega_c(\zeta_1, -\epsilon) + \Omega_c(\epsilon, \zeta_2)\right] = \frac{\gamma_t}{4\pi}\Omega_c(\zeta_1, \zeta_2) \tag{A.9}$$

General expression By comparison of equation (A.6) and equation (A.9) the follwoing expression is obtained for the velocity induced by the cylinder of arbitrary cross section:

$$u_z(\boldsymbol{x}) = \frac{\gamma_t}{4\pi}\Omega_c(x, y, \zeta_1, \zeta_2) \tag{A.10}$$

where Ω_c is the solid angle of the surface of the cylinder. The above formula can also be used for points on the boundary of the cylinder.

A.1.2 Infinite and semi-infinite cylinders of arbitrary cross sections

Infinite cylinder The velociy inside the cylinder is constant, equal to the vortex sheet strength γ_t, and is 0 outside of the cylinder. This is direclty obtained from the results of section A.1.1 with $\Omega_z(\zeta_1) = \Omega_z(\zeta_2) = 0$, or by considerating that the surface S_c is equivalent to a closed surface for the determination of Ω_c.
This result was proved by the author using simple considerations in **[67]**, but is also bound in the book of Batchelor [9, p. 98].

Semi-infinite cylinder The velociy for $\zeta \to +\infty$ is the same as the infinite cylinder. The velociy for $\zeta \to -\infty$ is 0 since the solid angle decreases with the distance. For $\zeta = 0$, the velocity is 0 outside of the cylinder and $\gamma_t/2$ inside the cylinder since for these two cases $\Omega_c = 0$ and $\Omega_c = 2\pi$.

A.2 Right vortex cylinder of tangential vorticity - Circular cross section

Part of the results presented in this section were published in **[23]**, **[26]**.

The right vortex cylinder with tangential vorticity is not only a classical fluid-dynamic but also magnetostatic problem. The model of a rotor using a semi-infinite vortex cylinder was introduced in 1912 by Joukowski [94]. Joukowski presented analytical results using direct integration of the Biot-Savart equation. The results were not explicitly written in elliptic integral. The author nevertheless mentioned this possibility In 1926, Müller [143] derived analytical formulae for the magnetic field of a finite solenoid based on the mutual inductance of two circular rings. Foelsch also discussed the topic in 1936 [64]. In 1960, Callaghan and Maslen [37] presented formulae based on the derivation of the vector potential. Their work can be applied in fluid-dynamics to obtain the velocity field induced by the tangential vorticity of a right vortex cylinder. In 1974, analytical formulae were also derived by Gibson [69], following a different approach than the previous authors. His results are based on a general Lemma and the use of integration by parts. The current author used direct integration to express the induced velocity field from a finite and semi-infinite cylinder. Results are summarized in **[23]** but more details are given below.

A.2.1 Solenoid - Finite cylinder

Introduction A finite vortex cylinder of circular cross section is considered. Notations are presented in figure A.1. The cylinder has a radius r_0 and extends along the z axis between the coordinates z_1 and z_2 so that its total length is $L = z_2 - z_1$. The vorticity is solely in the tangential direction and reduces to the vortex sheet forming the surface of the cylinder of equation $r = r_0$. No vorticity is assumed to be present in the inlet $z = z_1$ and outlet $z = z_2$ planes of the cylinder. Using the δ-Dirac function and the Π-gate function, this can be formalized as:

$$\boldsymbol{\omega}(\boldsymbol{x}) = \gamma_t \, \Pi_{[z_1,z_2]}(z) \, \delta(r - r_0) \, \boldsymbol{e}_\theta \tag{A.11}$$

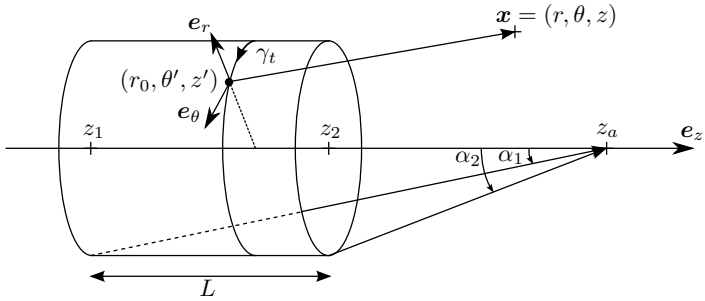

Figure A.1: Polar coordinate system used for vortex cylinder.

The Biot-Savart law writes in terms of vector potential:

$$\boldsymbol{\psi}(\boldsymbol{x}) = \frac{1}{4\pi} \int_V \frac{\boldsymbol{\omega}(\boldsymbol{x'})}{\|\boldsymbol{x} - \boldsymbol{x'}\|} r_0 d\theta' dr' dz' = \frac{\gamma_t}{4\pi} \int_V \frac{\Pi_{[z_1,z_2]}(z')\delta(r' - r_0)\boldsymbol{e}_\theta(\theta')}{\|\boldsymbol{x} - \boldsymbol{x'}\|} r_0 d\theta' dr' dz' \tag{A.12}$$

$$= \frac{\gamma_t r_0}{4\pi} \int_{z_1}^{z_2} \int_0^{2\pi} \frac{\boldsymbol{e}_\theta(\theta')}{[r^2 + r_0^2 - 2rr_0\cos(\theta' - \theta) + (z - z')^2]^{\frac{1}{2}}} d\theta' dz \tag{A.13}$$

In term of velocity $\boldsymbol{u} = \nabla \times \boldsymbol{\psi}$, the Biot-Savart law writes:

$$\boldsymbol{u}(\boldsymbol{x}) = \frac{-\gamma_t}{4\pi} \int_{z_1}^{z_2} \int_0^{2\pi} \frac{(\boldsymbol{x} - \boldsymbol{x'}) \times \boldsymbol{e}_\theta(\theta')}{\|\boldsymbol{x} - \boldsymbol{x'}\|^3} r_0 d\theta' dz' \tag{A.14}$$

$$= \frac{\gamma_t r_0}{4\pi} \int_{z_1}^{z_2} \int_0^{2\pi} \frac{(z - z')\boldsymbol{e}_r(\theta') - [r\cos(\theta' - \theta) - r_0]\,\boldsymbol{e}_z}{[r^2 + r_0^2 - 2rr_0\cos(\theta' - \theta) + (z - z')^2]^{\frac{3}{2}}} d\theta' dz' \tag{A.15}$$

In these formulae, one recognizes the vortex rings formulae integrated over z. As a result of this, it is known that the integration over θ can be done analytically. Yet, analytical formulae may be obtained if the integration over z is done first.

Simplifications (axi-symmetry) Similar simplifications to the ones introduced for the vortex rings are applied. From azimuthal symmetry it will be assumed that the control point is located in the plane $x-z$, and thus $\theta = 0$. Then, $\boldsymbol{e}_r$ may be replaced by $\cos\theta \boldsymbol{e}_x$ and $\boldsymbol{e}_\theta(\theta')$ by $\cos\theta' \boldsymbol{e}_y$.

Velocity on axis On the ring axis, $r = 0$ and $\theta = 0$, the radial velocity is 0 by symmetry and the Biot-Savart law equation (A.15) reduces to:

$$u_z(0,0,z) = \frac{\gamma_t r_0^2}{4\pi} \int_{z_1}^{z_2} \int_0^{2\pi} \frac{1}{\left[r_0^2 + (z-z')^2\right]^{\frac{3}{2}}} d\theta dz' = -\frac{\gamma_t}{2} \left[\frac{\zeta}{\sqrt{r_0^2+\zeta^2}} \right]_{z-z_1}^{z-z_2}$$
$$= \frac{\gamma_t}{2} \left(\cos\alpha_1 - \cos\alpha_2\right) \tag{A.16}$$

where α is the half-angle of the cone formed by a point on the axis and a ring on the cylinder as sketched in figure A.1.

Velocity on axis - Using solid angle Equation (A.16) may also be found by integration of the solid angle formula [170].. The cylinder may be seen as a superposition of infinitesimal vortex rings. Considering such a ring at position z', then the solid angle of this ring viewed by the control point on the axis is the one of a cone

$$\Omega = 2\pi \int_{\cos\alpha}^{1} d\cos\theta = 2\pi(1-\cos\alpha) \tag{A.17}$$

where α is the cone half angle as illustrated in figure A.1, such that:

$$\cos\alpha = \frac{z-z'}{\sqrt{(z-z')^2 + r_0^2}} \tag{A.18}$$

For an infinitesimal distance dz', the ring intensity is $\gamma_t dz'$. The elementary velocity induced by this ring is:

$$\boldsymbol{du}(0,0,z) = \frac{-\gamma_t dz'}{4\pi} \nabla\Omega = \frac{-\gamma_t dz'}{4\pi} \frac{\partial\Omega}{\partial z} \boldsymbol{e}_z \tag{A.19}$$

By integration along the cylinder axis, introducing the change of variable $\zeta = z - z'$, and eventually using equation (A.17):

$$u_z(0,0,z) = \frac{-\gamma_t}{4\pi} \int_{z_1}^{z_2} \frac{\partial\Omega}{\partial z} dz' = \frac{\gamma_t}{4\pi} \int_{\zeta_1}^{\zeta_2} \frac{\partial\Omega}{\partial\zeta} \frac{\partial\zeta}{\partial z} d\zeta = \frac{\gamma_t}{4\pi} \left[\Omega(\zeta_2) - \Omega(\zeta_1)\right] \tag{A.20}$$
$$= \frac{\gamma_t}{2} \left[\cos\alpha_1 - \cos\alpha_2\right] \tag{A.21}$$

which confirms equation (A.16).

General equation - Vector potential - Work of Callaghan and Maslen and extension The axi-symmetry simplifications mentioned previously are used. Primes are dropped for the integration variable θ'. The vector potential equation (A.13) reduces to is tangential component and

may be further manipulated as follow [37]:

$$\psi_\theta(\boldsymbol{x}) = \frac{\gamma_t r_0}{2\pi}\int_{z_1}^{z_2}\int_0^\pi \frac{\cos\theta}{\left[r^2+r_0^2+(z-z')^2-2rr_0\cos\theta\right]^{\frac{1}{2}}}d\theta dz' \qquad \text{(even function of } \theta\text{)}$$

$$= -\frac{\gamma_t r_0}{2\pi}\int_0^\pi\int_{\zeta_1}^{\zeta_2} \frac{\cos\theta}{\left[r^2+r_0^2+\zeta^2-2rr_0\cos\theta\right]^{\frac{1}{2}}}d\zeta d\theta \qquad (\zeta = z-z') \tag{A.22}$$

$$= -\frac{\gamma_t r_0}{2\pi}\int_0^\pi \cos\theta\Big[\ln\left(\zeta+\sqrt{\zeta^2+C(\theta)}\right)\Big]_{\zeta_1}^{\zeta_2}d\theta \qquad (\zeta \text{ integration}) \tag{A.23}$$

where for the last step $\frac{\partial}{\partial\zeta}\ln\left(\zeta+\sqrt{\zeta^2+C(\theta)}\right) = [\zeta+C(\theta)]^{-1/2}$ has been used with $C(\theta) = r^2+r_0^2-2rr_0\cos\theta$. Equation (A.23) may be rearranged by integrating by part over θ:

$$\psi_\theta(\boldsymbol{x}) = -\frac{\gamma_t r_0}{2\pi}\left[\int_0^\pi \cos\theta\ln\left(\zeta+\sqrt{\zeta^2+C(\theta)}\right)d\theta\right]_{\zeta_1}^{\zeta_2} \qquad \text{(rearranging limits)} \tag{A.24}$$

$$= -\frac{\gamma_t r_0}{2\pi}\left[\Big[\sin\theta\ln\left(\zeta+\sqrt{\zeta^2+C(\theta)}\right)\Big]_0^\pi - \int_0^\pi \frac{rr_0\sin^2\theta}{\sqrt{\zeta^2+C(\theta)}\left(\zeta+\sqrt{\zeta^2+C(\theta)}\right)}d\theta\right]_{\zeta_1}^{\zeta_2}$$

The first term is zero due to the values taken by $\sin\theta$. The second term may be further reduced by multiplying by $\frac{\sqrt{\zeta^2+C(\theta)}-\zeta}{\sqrt{\zeta^2+C(\theta)}-\zeta}$, to give:

$$\psi_\theta(\boldsymbol{x}) = \frac{\gamma_t r_0^2 r}{2\pi}\left[\int_0^\pi \frac{\sin^2\theta\left(\sqrt{\zeta^2+C(\theta)}-\zeta\right)}{\sqrt{\zeta^2+C(\theta)}\,C(\theta)}d\theta\right]_{\zeta_1}^{\zeta_2} \tag{A.25}$$

$$= \frac{\gamma_t r_0^2 r}{2\pi}\left\{\left[\int_0^\pi \frac{\sin^2\theta}{C(\theta)}d\theta\right]_{\zeta_1}^{\zeta_2} - \left[\int_0^\pi \frac{\zeta\sin^2\theta}{\sqrt{\zeta^2+C(\theta)}\,C(\theta)}d\theta\right]_{\zeta_1}^{\zeta_2}\right\} \qquad \text{(expanding numerator)}$$

$$= -\frac{\gamma_t r_0^2 r}{2\pi}\left[\int_0^\pi \frac{\zeta\sin^2\theta}{\sqrt{\zeta^2+C(\theta)}\,C(\theta)}d\theta\right]_{\zeta_1}^{\zeta_2} \qquad (\text{since } [\text{cst}]_{\zeta_1}^{\zeta_2}=0) \tag{A.26}$$

Callaghan stops his calculation here, but the expression found for A_θ may be extended further into elliptic integrals. This is done by introducing $\phi = \theta/2$ and $m_0 = m(\zeta=0)$,

$$\psi_\theta(\boldsymbol{x}) = -\frac{\gamma_t r_0^2 r}{2\pi}\left[\zeta\int_0^\pi \frac{\sin^2\theta}{\sqrt{\zeta^2+r^2+r_0^2-2rr_0\cos\theta)}(r^2+r_0^2-2rr_0\cos\theta)}d\theta\right]_{\zeta_1}^{\zeta_2} \tag{A.27}$$

$$= -\frac{\gamma_t r_0^2 r}{2\pi}\left[2\zeta\frac{\sqrt{m}}{2\sqrt{r_0 r}}\frac{m_0}{4r_0 r}\int_0^{\pi/2}\frac{\sin^2(2\phi)}{\sqrt{1-m\cos^2\phi}(1-m_0\cos^2\phi)}d\phi\right]_{\zeta_1}^{\zeta_2} \tag{A.28}$$

and using $\sin^2(2\phi) = 4(\cos^2\phi-\cos^4\phi)$):

$$\psi_\theta(\boldsymbol{x}) = -\frac{\gamma_t r_0^2 r}{2\pi}\frac{m_0}{(r_0 r)^{3/2}}\left[\zeta\sqrt{m}\int_0^{\pi/2}\frac{\cos^2\phi-\cos^4\phi}{\sqrt{1-m\cos^2\phi}(1-m_0\cos^2\phi)}d\phi\right]_{\zeta_1}^{\zeta_2}$$

$$= -\frac{\gamma_t}{2\pi}\sqrt{\frac{r_0}{r}}m_0\Big[\zeta\sqrt{m}(I_1-I_2)\Big]_{\zeta_1}^{\zeta_2} \tag{A.29}$$

The first integral, noted I_1, is expressed by using the following manipulation of the numerator $\cos^2\phi = \frac{1}{m_0}(m_0\cos^2\theta - 1 + 1)$:

$$I_1 = \int_0^{\pi/2} \frac{\cos^2\phi}{\sqrt{1-m\cos^2\phi}(1-m_0\cos^2\phi)}d\phi = \frac{1}{m_0}\left[\Pi(m_0,m) - K(m)\right] \tag{A.30}$$

For the second integral, the idea is first to transform $\cos^4$ to make the product $(1-m_0\cos^2\phi)(1+m_0\cos^2\phi)$ appear. Usual $-1+1$ operations are successively used:

$$\begin{aligned}
I_2 &= \int_0^{\pi/2} \frac{\cos^4\phi}{\sqrt{1-m\cos^2\phi}(1-m_0\cos^2\phi)}d\phi \\
&= \frac{1}{m_0^2}\int_0^{\pi/2} \frac{m_0^2\cos^4\phi - 1 + 1}{\sqrt{1-m\cos^2\phi}(1-m_0\cos^2\phi)}d\phi \\
&= \frac{1}{m_0^2}\left[\int_0^{\pi/2} \frac{-(1+m_0\cos^2\phi)}{\sqrt{1-m\cos^2\phi}}d\phi + \Pi(m_0,m)\right] \\
&= \frac{1}{m_0^2}\left[-K(m) - \frac{m_0}{m}\int_0^{\pi/2} \frac{m\cos^2\phi - 1 + 1}{\sqrt{1-m\cos^2\phi}}d\phi + \Pi(m_0,m)\right] \\
&= \frac{1}{m_0^2}\left[-K(m) - \frac{m_0}{m}\left(K(m) - E(m)\right) + \Pi(m_0,m)\right]
\end{aligned} \tag{A.31}$$

Inserting the values of I_1 and I_2 into equation (A.29), gives the following final form for the vector potential:

$$\psi_\theta(\boldsymbol{x}) = -\frac{\gamma_t}{2\pi}\sqrt{\frac{r_0}{r}}\frac{1}{m_0}\left[\zeta\sqrt{m}\left(\left(1-m_0+\frac{m_0}{m}\right)K(m) - \frac{m_0}{m}E(m) + (m_0-1)\Pi(m_0,m)\right)\right]_{\zeta_1}^{\zeta_2} \tag{A.32}$$

where it is recalled that $m = m(\zeta)$, $m_0 = m(0)$ and this equation may be expressed with the variable k since $m = k^2$.

General equation - Velocity from direct derivation of vector potential The general velocity equations for the finite cylinder may be obtained by derivation of the vector potential as:

$$u_r = -\frac{\partial\psi_\theta}{\partial z} \tag{A.33}$$

$$u_z = \frac{1}{r}\frac{\partial\left(r\psi_\theta\right)}{\partial r} = \frac{1}{\rho}\psi_\theta + \frac{\partial\psi_\theta}{\partial r} \tag{A.34}$$

For this purpose, one may take the integrated form with elliptic functions equation (A.32) and use the derivatives formulae of the elliptic functions to eventually obtain:

$$u_r(r,z) = \frac{\gamma_t}{2\pi}\sqrt{\frac{r_0}{r}}\left[\frac{2-k^2}{k}K\left(k(\zeta)^2\right) - \frac{2}{k}E\left(k(\zeta)^2\right)\right]_{\zeta_1=z-z_1}^{\zeta_2=z-z_2} \tag{A.35}$$

$$u_z(r,z) = -\frac{\gamma_t}{4\pi\sqrt{rr_0}}\left[\zeta k(\zeta)\left(K\left(k(\zeta)^2\right) + \frac{r_0-r}{r_0+r}\Pi\left(k(0)^2|k(\zeta)^2\right)\right)\right]_{\zeta_1=z-z_1}^{\zeta_2=z-z_2} \tag{A.36}$$

with

$$m(\zeta) = k(\zeta)^2 = \frac{4rr_0}{\zeta^2 + (r+r_0)^2} \tag{A.37}$$

The velocity field induced by a finite vortex cylinder is illustrated in figure A.2.

General equation - Velocity from indirect derivation of vector potential The approach chosen by Callaghan [37] consisted in using the integral forms of the vector potential. This approach is less direct but less tedious than having to derive the elliptic integrals as in the previous paragraph.

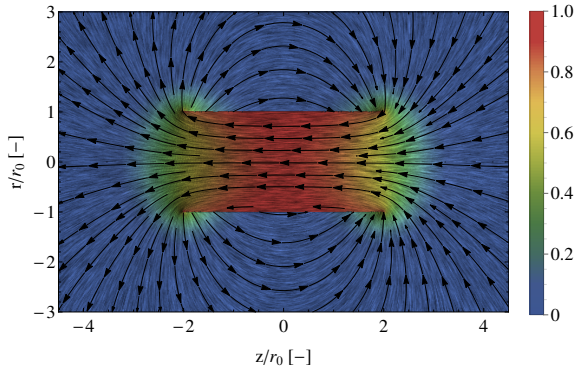

Figure A.2: Streamlines and velocity field induced by a finite vortex cylinder illustrated using Line Integral Convolution(LIC) flow visualization. The Cylinder is contained within the planes $|z/r_0| \leq 2$ and $|r| = r_0$. The vortex intensity is $\gamma_t = -1$.

For the radial component, the integral form equation (A.22) is used and combined to derivation properties of integrals,

$$\frac{d}{dz}\int_{z_1}^{z_2} f(z)dz = \big[f(z)\big]_{z_1}^{z_2} \tag{A.38}$$

gives directly:

$$u_r(r,z) = -\frac{d\psi_\theta}{dz} = -\frac{d\psi_\theta}{d\zeta}\frac{d\zeta}{dz} = -\frac{d\psi_\theta}{d\zeta} = \frac{\gamma_t r_0}{2\pi}\left[\int_0^\pi \frac{\cos\theta}{\left[r^2 + r_0^2 + \zeta^2 - 2rr_0\cos\theta\right]^{\frac{1}{2}}}d\theta\right]_{\zeta_1}^{\zeta_2} \tag{A.39}$$

The above equation may be expressed in the form of elliptic integrals without difficulty. Equation (A.35) is readily obtained with this method, and we can further observe that:

$$u_r(r,z) = \left[\psi_{\theta,\mathrm{Ring}}(r,z')\right]_{z-z_1}^{z-z_2} \tag{A.40}$$

For the derivation of the longitudinal component, one may evaluate first $\partial\psi_\theta/\partial r$ using the integral form of equation (A.24):

$$\frac{\partial\psi_\theta}{\partial r} = -\frac{\gamma_t r_0}{2\pi}\left[\int_0^\pi \cos\theta\frac{\partial}{\partial r}\ln\left(\zeta + \sqrt{\zeta^2 + C(\theta)}\right)d\theta\right]_{\zeta_1}^{\zeta_2} \tag{A.41}$$

$$= -\frac{\gamma_t r_0}{2\pi}\left[\int_0^\pi \cos\theta\frac{r - r_0\cos\theta}{\sqrt{\zeta^2 + C(\theta)}(\zeta + \sqrt{\zeta^2 + C(\theta)})}d\theta\right]_{\zeta_1}^{\zeta_2} \tag{A.42}$$

The steps steps used from equation (A.25) to equation (A.26) are applied to the above integral to eventually give:

$$\frac{\partial\psi_\theta}{\partial r} = \frac{\gamma_t r_0}{2\pi}\left[\int_0^\pi \zeta\cos\theta\frac{r - r_0\cos\theta}{\sqrt{\zeta^2 + C(\theta)}\,C(\theta))}d\theta\right]_{\zeta_1}^{\zeta_2} \tag{A.43}$$

Using equation (A.43) and equation (A.26) one obtains:

$$u_z = \frac{1}{\rho}\psi_\theta + \frac{\partial\psi_\theta}{\partial \boldsymbol{r}} = \frac{\gamma_t r_0}{2\pi}\left[\int_0^\pi \frac{\zeta(r\cos\theta - r_0)}{\sqrt{\zeta^2 + C(\theta)}\,C(\theta)}d\theta\right]_{\zeta_1}^{\zeta_2} \tag{A.44}$$

The same steps as the one used for equation (A.27) are applied:

$$u_z = \frac{\gamma_t r_0}{\pi}\left[\zeta\int_0^{\pi/2}\frac{(r\cos(2\phi)-r_0)}{\sqrt{\zeta^2+C(2\phi)}\,C(2\phi)}d\phi\right]_{\zeta_1}^{\zeta_2} \quad (\phi=\theta/2)$$

$$= \frac{\gamma_t r_0}{\pi}\left[\zeta\frac{\sqrt{m}}{2\sqrt{rr_0}}\frac{m_0}{4rr_0}\int_0^{\pi/2}\frac{2r\cos^2\phi-(r+r_0)}{\sqrt{1-m\cos^2\phi}(1-m_0\cos^2\phi)}d\phi\right]_{\zeta_1}^{\zeta_2} \tag{A.45}$$

$$= \frac{\gamma_t r_0}{\pi}\frac{1}{2\sqrt{rr_0}}\frac{m_0}{4rr_0}\left[\zeta\sqrt{m}\big(2rI_1-(r+r_0)\Pi(m_0,m)\big)\right]_{\zeta_1}^{\zeta_2} \tag{A.46}$$

$$= \frac{\gamma_t r_0}{\pi}\frac{1}{2\sqrt{rr_0}}\frac{m_0}{4rr_0}\left[\zeta\sqrt{m}\frac{2r}{m_0}\left(\Pi(m_0,m)-K(m)-\frac{m_0}{2r}(r+r_0)\Pi(m_0,m)\right)\right]_{\zeta_1}^{\zeta_2} \tag{A.47}$$

$$= -\frac{\gamma_t}{4\pi}\frac{1}{\sqrt{rr_0}}\left[\zeta\sqrt{m}\left(K(m)+\left(\frac{m_0}{2r}(r+r_0)-1\right)\Pi(m_0,m)\right)\right]_{\zeta_1}^{\zeta_2} \tag{A.48}$$

and equation (A.36) is readily obtained.

General equation - Velocity from Biot-Savart law - Indefinite form [23] Instead of using the vector potential, the Biot-Savart law from equation (A.15) may be integrated directly. In this perspective, the indefinite integral over z in equation (A.15) will be determined below. From the axi-symmetry of the flow it may be assumed without loss of generality that the control point lays in the x axis, i.e. $\theta=0$, and that the radial component of the field may be seen as the x-component. We will write $\boldsymbol{e}_\rho$ this fake Cartesian representation of the radial component, which is such that $\boldsymbol{e}_\theta(\theta')=\cos\theta'\boldsymbol{e}_\rho$. Using these assumptions equation (A.15) becomes:

$$\boldsymbol{u}^{z'}(\boldsymbol{x}) = \frac{\gamma_t r_0}{4\pi}\int_0^{2\pi}\int_{z'}\frac{(z-z')\cos\theta'\boldsymbol{e}_\rho-[r\cos(\theta')-r_0]\,\boldsymbol{e}_z}{[r^2+r_0^2-2rr_0\cos(\theta')+(z-z')^2]^{\frac{3}{2}}}dz'd\theta' \tag{A.49}$$

The notation $C(\theta)=r^2+r_0^2-2rr_0\cos(\theta)$ is introduced and the change of variable $\zeta=z-z'$ is applied with $d\zeta=-dz'$. Noting that the integrand over θ' is periodic and an even function the integration limit may be reduced to obtain:

$$\boldsymbol{u}^{\zeta}(\boldsymbol{x}) = -\frac{\gamma_t r_0}{2\pi}\int_0^{\pi}\int_{\zeta}\frac{\zeta\cos\theta'\boldsymbol{e}_\rho-[r\cos(\theta')-r_0]\,\boldsymbol{e}_z}{[C(\theta')+\zeta^2]^{\frac{3}{2}}}d\zeta d\theta' \tag{A.50}$$

The integrals over ζ are straightforward using the following relations:

$$\int\frac{d\zeta}{(C+\zeta^2)^{\frac{3}{2}}}=\frac{\zeta}{C\sqrt{C+\zeta^2}}, \qquad \int\frac{\zeta d\zeta}{(C+\zeta^2)^{\frac{3}{2}}}=\frac{-1}{\sqrt{C+\zeta^2}} \tag{A.51}$$

So that equation (A.50) becomes

$$\boldsymbol{u}^{\zeta}(\boldsymbol{x}) = \frac{\gamma_t r_0}{2\pi}\int_0^{\pi}\frac{\cos\theta'}{\sqrt{C(\theta')+\zeta^2}}\boldsymbol{e}_\rho+\frac{[r\cos(\theta')-r_0]}{C(\theta)\sqrt{C(\theta')+\zeta^2}}\boldsymbol{e}_z d\theta' \tag{A.52}$$

The presence of square root of cosine terms evoke elliptic integrals. As a result of this the change of variable $\phi=\theta/2$ is introduced, so that $\cos\theta=\cos(2\phi)=2\cos^2\phi-1$:

$$\boldsymbol{u}^{\zeta}(\boldsymbol{x}) = \frac{\gamma_t r_0}{\pi}\int_0^{\pi/2}\frac{2\cos^2\phi-1}{\sqrt{C(2\phi)+\zeta^2}}\boldsymbol{e}_\rho+\frac{\big[2r\cos^2\phi-(r_0+r)\big]}{C(2\phi)\sqrt{C(2\phi)+\zeta^2}}\boldsymbol{e}_z d\phi \tag{A.53}$$

Developing the expression $C(2\phi)=(r_0+r)^2-2rr_0\cos^2\phi$, the parameter for the elliptic integral is readily determined and defined as:

$$m(\zeta)=k(\zeta)^2=\frac{4rr_0}{(r_0+r)^2+\zeta^2} \tag{A.54}$$

The components of the integral are now treated separately. The radial component is successively reduced by factorizing the elliptical parameter then noting that $2\cos^2\phi=\frac{2}{m}(m\cos^2\phi-1+1-\frac{m}{2})$

and using the definition of the complete elliptic integrals of the first and second kind noted K and E respectively. The steps are as follow:

$$u_r^\zeta(\boldsymbol{x}) = \frac{\gamma_t r_0}{\pi}\frac{\sqrt{m}}{2\sqrt{rr_0}}\int_0^{\pi/2}\frac{2\cos^2\phi - 1}{\sqrt{1-m\cos^2\phi}}d\phi \tag{A.55}$$

$$= \frac{\gamma_t r_0}{\pi}\frac{\sqrt{m}}{2\sqrt{rr_0}}\left[-\frac{2}{m}E(m) + \frac{2}{m}\left(1-\frac{m}{2}\right)K(m)\right] \tag{A.56}$$

$$= \frac{\gamma_t}{2\pi}\sqrt{\frac{r_0}{r}}\left[\frac{2-k^2}{k}K(k^2) - \frac{2}{k}E(k^2)\right] \tag{A.57}$$

The parameter m or k is used indifferently, and the dependence of these parameters with respect to ζ has been dropped to shorten notations. For the longitudinal component the factorization of the elliptic parameters leads to

$$u_z^\zeta(\boldsymbol{x}) = \frac{\gamma_t r_0}{\pi}\zeta\frac{\sqrt{m}}{2\sqrt{rr_0}}\frac{m_0}{4rr_0}\int_0^{\pi/2}\frac{2r\cos^2\phi - (r+r_0)}{\sqrt{1-m\cos^2\phi}(1-m_0\cos^2\phi)}d\phi \tag{A.58}$$

where the notation $m_0 = m(0)$ is used. By definition of the elliptic integral of the third kind Π, the above equation writes:

$$u_z^\zeta(\boldsymbol{x}) = \frac{\gamma_t r_0}{\pi}\frac{1}{2\sqrt{rr_0}}\frac{m_0}{4rr_0}\left[\zeta\sqrt{m}\big(2rI_1 - (r+r_0)\Pi(m_0,m)\big)\right] \tag{A.59}$$

where I_1 has been introduced since it is an integral that needs further development. Using $\cos^2\phi = \frac{1}{m_0}(m_0\cos^2\phi - 1 + 1)$ and the definitions of elliptic integrals the following expression is obtained for I_1:

$$I_1 = \int_0^{\pi/2}\frac{\cos^2\phi}{\sqrt{1-m\cos^2\phi}(1-m_0\cos^2\phi)}d\phi = \frac{1}{m_0}\left(\Pi(m_0,m) - K(m)\right) \tag{A.60}$$

Inserting equation (A.60) in equation (A.59) leads to:

$$u_z^\zeta(\boldsymbol{x}) = \frac{\gamma_t r_0}{\pi}\frac{1}{2\sqrt{rr_0}}\frac{m_0}{4rr_0}\left[\zeta\sqrt{m}\frac{2r}{m_0}\left(\Pi(m_0,m) - K(m) - \frac{m_0}{2r}(r+r_0)\Pi(m_0,m)\right)\right] \tag{A.61}$$

$$= -\frac{\gamma_t}{4\pi}\frac{1}{\sqrt{rr_0}}\left[\zeta\sqrt{m}\left(K(m) + \left(\frac{m_0}{2r}(r+r_0) - 1\right)\Pi(m_0,m)\right)\right] \tag{A.62}$$

$$= -\frac{\gamma_t}{4\pi}\frac{1}{\sqrt{rr_0}}\left[\zeta k\left(K(k^2) + \frac{r_0-r}{r_0+r}\Pi(k_0^2,k^2)\right)\right] \tag{A.63}$$

General equation - Velocity from Biot-Savart law - Finite cylinder [23] The indefinite integral forms obtained in equation (A.57) and equation (A.63) may be used on a known interval. Assuming a cylinder extends from z_1 to z_2 then the induced velocities are simply:

$$u_{\mathrm{sol,r}}(\boldsymbol{x}) = \frac{\gamma_t}{2\pi}\sqrt{\frac{r_0}{r}}\left[\frac{2-k^2}{k}K(k^2) - \frac{2}{k}E(k^2)\right]_{\zeta_1=z-z_1}^{\zeta_2=z-z2} \tag{A.64}$$

$$u_{\mathrm{sol,z}}(\boldsymbol{x}) = -\frac{\gamma_t}{4\pi}\frac{1}{\sqrt{rr_0}}\left[\zeta k\left(K(k^2) + \frac{r_0-r}{r_0+r}\Pi(k_0^2,k^2)\right)\right]_{\zeta_1=z-z_1}^{\zeta_2=z-z2} \tag{A.65}$$

A regularization of these equations is given in section A.2.3.

A.2.2 Semi-infinite cylinder

Results for the semi-infinite cylinder derive directly from the results of the finite cylinder. Results from this section were published in [23].

Introduction and notations An infinite vortex cylinder of circular cross section is considered. Notations are presented in figure A.3. The cylinder has a radius r_0 and extends along the z axis between the coordinates $z = 0$ and $z = +\infty$.

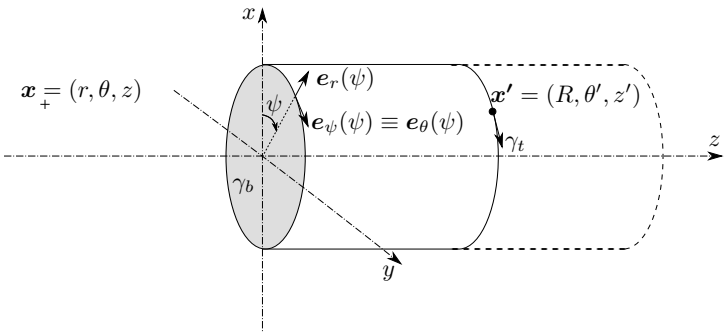

Figure A.3: Polar coordinate system used for infinite vortex cylinder.

The Biot-Savat law for the vector potential and velocity is given by equation (A.13) and equation (A.15) using $z_1 = 0$ and $z_2 \to +\infty$.

Induced velocity field The induced velocity field for the semi-infinite cylinder is obtained with $z_1 = 0$ and $z_2 \to +\infty$. For the r component the limit when z_2 tends to $+\infty$ is zero. For the z component the limit as $z_2 \to +\infty$ has different value for radii lower or greater than r_0. The bracket notation could have been used as in equation (B.7), but the same result may be obtained by using an absolute value expression. The results from these calculation leads to:

$$u_{r,\mathrm{cyl}}(r,z) = -\frac{\gamma_t}{2\pi}\sqrt{\frac{r_0}{r}}\left[\frac{2-k^2}{k}K\left(k(z)^2\right) - \frac{2}{k}E\left(k(z)^2\right)\right] \tag{A.66}$$

$$u_{z,\mathrm{cyl}}(r,z) = \frac{\gamma_t}{2}\left[\frac{r_0 - r + |r-r_0|}{2|r-r_0|} + \frac{zk(z)}{2\pi\sqrt{rr_0}}\left(K\left(k(z)^2\right) + \frac{r_0-r}{r_0+r}\Pi\left(k(0)^2|k(z)^2\right)\right)\right] \tag{A.67}$$

where

$$k^2(z) = m(z) = \frac{4rr_0}{(r_0+r)^2+z^2} \tag{A.68}$$

and the dependency in r was omitted to shorten notations. The velocity field induced by a semi-infinite vortex cylinder is illustrated in figure A.4.

Flow near the axis and on the axis The velocity field near the axis is obtained via a Taylor series of the formulae:

$$u_{r,t}(r \ll r_0, z) = -\frac{\gamma_t}{4}\frac{rr_0^2}{\left(r_0^2+z^2\right)^{3/2}} + O(r^{5/2}), \quad u_{z,t}(r \ll r_0, z) = \frac{\gamma_t}{2}\left[1 + \frac{z}{\sqrt{r_0^2+z^2}}\right] + O(r). \tag{A.69}$$

The axial induction exactly on the axis can be directly obtained by simple application of equation (A.16) (integration of the Biot-Savart law) or equation (A.21) (gradient of the solid angle, as e.g. Stepniewski and Keys [200, p. 155], van Kuik [212]).

Axial induction: analysis of the different terms involved equation (A.67) consists of the sum of three terms. The contribution of the different terms involved is shown in figure A.5. Absolute values are used in this equation to conveniently write in mathematical form the discontinuity of the first term at $r = r_0$. This first term is the only one that remains when $z = 0$. As $z \to +\infty$,

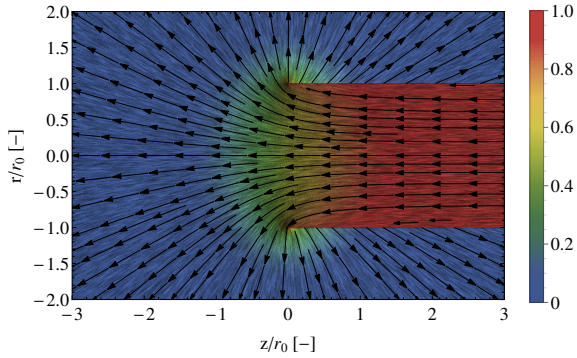

Figure A.4: Streamlines and velocity field induced by a vortex cylinder illustrated using Line Integral Convolution(LIC) flow visualization. The plane of observation interesects the ring at $z = 0$ and $|r| = r_0$. The vortex intensity is $\gamma_t = -1$.

the sum of the two terms involving elliptical integrals tends to $\gamma_t/2$ for $r < r_0$ and tends to 0 for $r > r_0$. Both the elliptic integral of the third kind and the absolute value term have discontinuities at $r = r_0$. The term involving the elliptic integral K is always continuous. When $z < 0$, the sum of all three terms is such that the solution is continuous with respect to r and tends to zero as $z \to -\infty$. On the other hand, for $z > 0$, the axial velocity is discontinuous with a jump of value equal to $-\gamma_t$ between the upper and inner part of the vortex cylinder. This jump is half for $z = 0$. For all values of z the axial induction is always highest for $r < r_0$ than for $r \geq r_0$. Axial velocity contours and streamlines are shown in figure A.6.

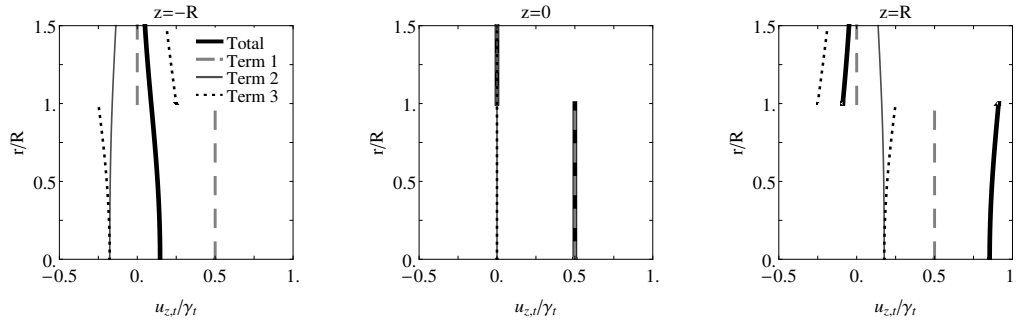

Figure A.5: Contribution of the different terms of equation (A.67) to the total axial induction at three different axial positions.

Axial induction at particular locations The axial induced velocity is seen to be constant in the rotor plane by inserting $z = 0$ in equation (A.67) and is also constant in the far-wake by evaluation of the limit of the elliptic integrals. The values at these locations are:

$$u_{z,t}(r, 0) = \left\{ \begin{matrix} 0 \\ \frac{\gamma_t}{2} \end{matrix} \right\} \tag{A.70}$$

$$u_{z,t}(r, z \to +\infty) = \left\{ \begin{matrix} 0 \\ \gamma_t \end{matrix} \right\} \tag{A.71}$$

where the upper value of the bracket correspond to $r > r_0$ and the lower value to $r < r_0$. The velocity at the vortex sheet is the average of the value on the upper and lower bracket value [69]. This is true for all positive values of z. Noting that the third term of equation (A.67) is antisymmetric around $r = r_0$, the axial induction on the cylinder itself reduces to:

$$u_{z,t}(r = r_0, z > 0) = \frac{\gamma_t}{4} + \frac{\gamma_t}{2}\frac{zk(z)}{2\pi\sqrt{rr_0}}K\left(k^2(z)\right)), \tag{A.72}$$

As previously mentioned, the vortex sheet induces across it a velocity jump in the axial direction of intensity $-\gamma_t$ between the velocities in the outer and the inner part. This jump is exactly half on the leading edge of the cylinder.

Note on the radial induction The radial velocity is an even function of the variable z, i.e. $u_{r,t}(-z) = u_{r,t}(z)$. It is continuous in the entire domain except at the cylinder's leading edge. In the far wake, the radial velocities tends to zero and the flow is purely in the axial direction. In particular, equation (A.66) can be evaluated at the rotor for $r < r_0$. It can also be evaluated on the cylinder itself where it is seen to be non-zero. This means that there is flow going through the cylinder (see discussion by Lewis [116, p. 168] about the leakage through the wall of the semi-infinite cylinder near the free-end side). This is indeed required to satisfy continuity since the cross-sectional area of the cylinder remains constant while the axial velocity varies by a factor 2. The flow thus tends to move the vortex sheet towards a more realistic shape. The converged vortex system, when the vortex sheet is allowed to expand and the convection velocity varies along the wake, has an axial induction that corresponds well with the one from the tangential vorticity cylinder of constant strength [152].

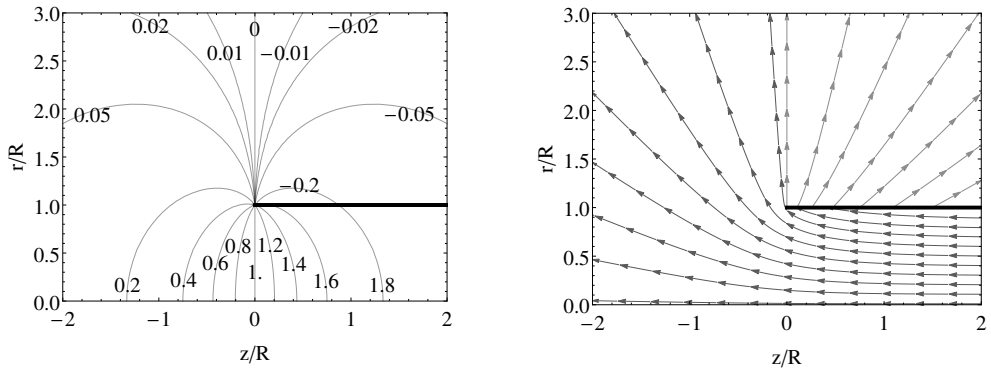

Figure A.6: Semi infinite vortex cylinder velocities. Axial velocity contour plot normalized by $2r_0/\gamma_t$ (left). Streamlines for $\gamma_t = -1$ m/s reveals the strong singularity at the cylinder rim and the radial flow through the cylinder surface (right).

A.2.3 Regularization of the cylinder's equations

A simple regularization of the cylinder's equation consists in introducing a cut off length ϵ in the denominator of the elliptic parameter k, namely:

$$m_\epsilon(\zeta) = k_\epsilon^2(\zeta) = \frac{4rr_0}{(r + r_0)^2 + \zeta^2 + \epsilon^2} \tag{A.73}$$

The singularity mainly concerns the radial component of the velocity, so it may be chosen to regularize only this component. The regularized expression of k can be used for the indefinite form of the radial component (equation (8.2)) but also in the definite form of the radial component of the

semi-infinite cylinder (equation (A.66)). The longitudinal component do not present a singularity, but a discontinuity at $r = r_0$ when $z >= 0$. The regularization presented above will remove the discontinuity. For this, the parameter $k(0)$ should also be replaced by $k_\epsilon(0)$ in both the indefinite and definite forms: equation (A.65) and equation (A.67). For the latter equation, $u_{z,\text{cyl}}$,the limit needs to be evaluated again which will affect the first term as follow:

$$\frac{\gamma_t}{2}\left[\frac{1}{2}\left(1+\frac{r_0-r}{(r_0+r)\sqrt{1-k_\epsilon(0)^2}}\right)+\frac{zk_\epsilon(z)}{2\pi\sqrt{rr_0}}\left(K\left(k_\epsilon(z)^2\right)+\frac{r_0-r}{r_0+r}\Pi\left(k_\epsilon(0)^2|k_\epsilon(z)^2\right)\right)\right]$$

Developing the first term:

$$\frac{\gamma_t}{2}\left[\frac{1}{2}\left(1+\frac{(r_0-r)\sqrt{1+\epsilon^2/(r_0+r)^2}}{\sqrt{(r_0-r)^2+\epsilon^2}}\right)+\frac{zk_\epsilon(z)}{2\pi\sqrt{rr_0}}\left(K\left(k_\epsilon(z)^2\right)+\frac{r_0-r}{r_0+r}\Pi\left(k_\epsilon(0)^2|k_\epsilon(z)^2\right)\right)\right]$$

It is seen that when $\epsilon = 0$ the non regularized form (equation (A.67)) is retrieved.

A.3 Vortex cylinder of longitudinal vorticity

The result presented in this section were published in [23].

A.3.1 Introduction

A semi-infinite vortex cylinder of circular cross-section is considered. Notations are presented in figure A.7. The cylinder has a radius R and extends along the z-axis between the coordinates $z_1 = 0$ and $z_2 \to +\infty$. The vorticity is assumed to be solely in the longitudinal direction. It reduces to the vortex sheet forming the surface of the cylinder so that at a point $\boldsymbol{x} = (r, \psi, z)$ the vorticity is: $\boldsymbol{\omega}(\boldsymbol{x}) = \gamma_z \, \Pi_{[z_1,z_2[}(z) \, \delta(r-R) \, \boldsymbol{e}_z$.

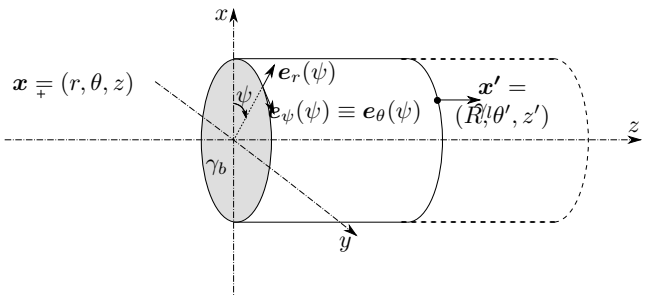

Figure A.7: Vortex cylinder of longitudinal vorticity and coordinate system.

A.3.2 Properties

The longitudinal vorticity component of the cylinder will induce a tangential velocity component only. For an infinite cylinder this velocity would be 0 within the cylinder and equal to $\Gamma_{\text{tot}}/2\pi r$ outside of the cylinder. This result can be obtained from the definition of the circulation and the axi-symmetry of the flow. Γ_{tot} may be expressed in terms of γ_l as $\Gamma_{\text{tot}}\boldsymbol{e}_z = \boldsymbol{\gamma}_l 2\pi R$. The tangential velocity outside of the infinite cylinder is then $\gamma_l R/r$. The result from the infinite cylinder is valid for the far-wake of the semi-infinite cylinder, i.e. for $z \to +\infty$. By geometrical consideration, the induced velocity from the semi-infinite cylinder on the rotor plane is half the far-wake value:

$$u_{\psi,l}(r,0) = \left\{\begin{array}{c}\frac{\gamma_l R}{2r}\\ 0\end{array}\right\}, \qquad u_{\psi,l}(r, z\to+\infty) = \left\{\begin{array}{c}\frac{\gamma_l R}{r}\\ 0\end{array}\right\}, \tag{A.74}$$

where the upper value of the bracket correspond to $r > R$ and the lower value to $r < R$. The velocity at the vortex sheet is the average of the value on the upper and lower bracket value. The vortex sheet induces across it a velocity jump in the tangential direction of intensity γ_l between the outer and inner part of the cylinder. This jump is half on the leading edge of the cylinder. These results may be verified from the full analytical expression derived in section A.3.3.

A.3.3 Derivation by direct integration

The Biot-Savart law in term of velocity writes:

$$\boldsymbol{u}(\boldsymbol{x}) = \frac{\gamma_z R}{4\pi} \int_{z_1}^{z_2} \int_0^{2\pi} \frac{r\boldsymbol{e}_\theta(\psi) - R\boldsymbol{e}_\theta(\theta')}{\left[r^2 + R^2 + (z-z')^2 - 2rR\cos(\theta'-\psi)\right]^{\frac{3}{2}}} d\theta' dz'. \tag{A.75}$$

Using the axi-symmetry of the problem only the tangential component remains:

$$u_\theta(\boldsymbol{x}) = \frac{\gamma_z R}{4\pi} \int_{z_1}^{z_2} \int_0^{2\pi} \frac{r - R\cos\theta'}{\left[r^2 + R^2 + (z-z')^2 - 2rR\cos\theta'\right]^{\frac{3}{2}}} d\theta' dz'. \tag{A.76}$$

The integration over z can be readily done and would lead to an integrated form that would match the one of a semi-infinite filament and only the integral over θ would need to be computed. Yet, this step may be skipped by using the following analogy. The form taken by equation (A.76) directly recalls the one found in the study of the solenoid (see equation (A.50)). The same integration steps may be followed to eventually lead to the indefinite form:

$$u_\theta(\boldsymbol{x}) = -\frac{\gamma_z}{4\pi} \frac{1}{\sqrt{rR}} \frac{R}{r} \left[\zeta k \left(K(k^2) - \frac{R-r}{R+r} \Pi(k_0^2, k^2) \right) \right]_{\zeta_1 = z - z_1}^{\zeta_2 = z - z2}. \tag{A.77}$$

Using $z_1 = 0$ and the limit as $z_2 \to +\infty$ the tangential velocity component induced by the system of trailed vorticity is obtained as:

$$u_\theta(r,z) = \frac{\gamma_z}{2} \frac{R}{r} \left[\frac{r - R + |R-r|}{2|R-r|} + \frac{zk(z)}{2\pi\sqrt{rR}} \left(K\left(k^2(z)\right) - \frac{R-r}{R+r} \Pi\left(k^2(0), k^2(z)\right) \right) \right], \tag{A.78}$$

where the function k is defined in equation (A.68).

$$k^2(z) = \frac{4rR}{(r+R)^2 + z^2} \tag{A.79}$$

The result is consistent with the one found by Gibson[1] [69] though the procedure leading to it is different.

A.3.4 Derivation using semi-infinite vortex lines

It is possible to obtain the result presented in section A.3.3 by using a continuous distribution of semi-infinite vortex lines. The induced velocity for a semi-infinite vortex line is given in [23].

The variation of the azimuthal velocity computed with equation (A.78) with the axial position is shown in figure A.8. The factor two between the far-wake and the rotor plane velocities can be seen on the figure. As expected from equation (A.78), the velocity tends to 0 for all regions far from the cylinder edge and is anti-symmetric with respect to z for $r < R$.

A.4 Bound vortex disk

The result presented in this section were published in **[23]**.

[1] In his article, the value V_C has been mistyped and should read $V_C = 1/(2r)$.

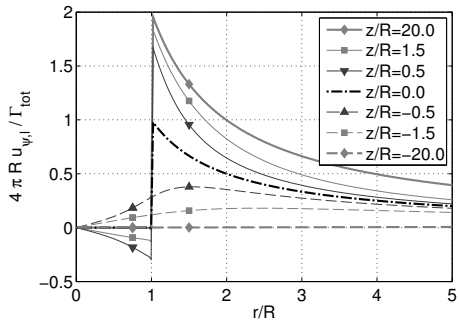

Figure A.8: Tangential velocity induced by the longitudinal part of the tip vortices. Velocities at the rotor plane are half the ones in the far-wake plane. On these planes, the velocity is 0 for $r < R$, and equal to $\Gamma_{\text{tot}}/4\pi r$ and $\Gamma_{\text{tot}}/2\pi r$ for $r > R$. The velocity tends to 0 for all regions far from the cylinder edge and is anti-symmetric with respect to z for $r < R$.

Introduction The circular vortex disk illustrated in figure A.9 is considered. The disk of radius R is normal to the z-axis and its origin is located at $z = z_0$. The vorticity is assumed to be purely in the radial direction. Axi-symmetry in the vortex distribution is further assumed and as a result of this the induction will be purely tangential. The cross-product in the Biot-Savart law implies that the bound vortex disk induces only velocity in the tangential direction. This velocity is zero on the z-axis given the axi-symmetry of the problem. The induced velocity from the disk is also zero on the rotor plane. The vorticity field at a point $\boldsymbol{x} = (r, \theta, z)$ is $\boldsymbol{\omega}(\boldsymbol{x}) = \gamma_b(r)\, \Pi_{[0,R]}(r)\, \delta(z - z_0)\, \boldsymbol{e}_r(\theta)$, where γ_b is given by:

$$\boldsymbol{\gamma}_b(r) = \frac{\Gamma_{\text{tot}}}{2\pi r}\, \boldsymbol{e}_r \tag{A.80}$$

The Biot-Savart law writes:

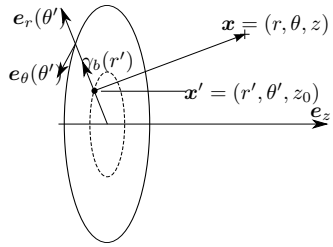

Figure A.9: Polar coordinate system used for the computation of the bound vortex disk induction.

$$\boldsymbol{u}(\boldsymbol{x}) = \frac{1}{4\pi} \int_V \frac{\boldsymbol{\omega}(\boldsymbol{x'}) \times (\boldsymbol{x} - \boldsymbol{x'})}{|\boldsymbol{x} - \boldsymbol{x'}|^3} r'\, dr'\, d\theta'\, dz' \tag{A.81}$$

$$= -\frac{1}{4\pi} \int_0^{2\pi} \int_0^R \gamma_b(r') \frac{(z - z_0)\boldsymbol{e}_\theta(\theta') - r \sin(\theta - \theta')\boldsymbol{e}_z}{\left[r^2 + r'^2 + (z - z_0)^2 - 2rr' \cos(\theta - \theta')\right]^{\frac{3}{2}}} r' dr' d\theta' \tag{A.82}$$

$$= -\frac{\Gamma_{\text{tot}}}{4\pi^2} \int_0^{\pi} \int_0^R \frac{(z - z_0)\boldsymbol{e}_\theta(\theta')}{\left[r^2 + r'^2 + (z - z_0)^2 - 2rr' \cos(\theta - \theta')\right]^{\frac{3}{2}}} dr' d\theta' \tag{A.83}$$

The z-component vanishes since the integrand is an odd, 2π-periodic function. From the axi-symmetry of the problem, θ will be assumed to be zero and $\boldsymbol{e}_\theta(\theta')$ replaced by $\cos\theta' \boldsymbol{e}_t$ where $\boldsymbol{e}_t = \boldsymbol{e}_\theta(0)$. z_0 will further be chosen as zero.

Indefinite form of the Biot-Savart law Since the vorticity tends to infinity as $r \to 0$, a singular behavior is expected at this point. The indefinite form of the Biot-Savart integral in r', written $u_\theta^{r'}$, is thus sought first. Using the simplifications discussed in the previous paragraph, the integration over r' of equation (A.82) is readily obtained to give:

$$u_\theta^{r'}(\boldsymbol{x}) = -\frac{\Gamma_{\text{tot}}}{4\pi^2}\int_0^\pi \int_{r'} z\cos\theta' \frac{1}{\left[r^2 + r'^2 + z^2 - 2rr'\cos\theta'\right]^{\frac{3}{2}}}\, dr'\, d\theta' \tag{A.84}$$

$$= -\frac{z\Gamma_{\text{tot}}}{4\pi^2}\int_0^\pi \cos\theta' \frac{r' - r\cos\theta'}{(r^2 + z^2 - r^2\cos^2\theta')\sqrt{r^2 + r'^2 + z^2 - 2rr'\cos\theta'}}\, d\theta'. \tag{A.85}$$

The first term in the denominator may be expanded into a product as:

$$r^2 + z^2 - r^2\cos^2\theta' = \left(\sqrt{r^2+z^2} + \cos\theta'\right)\left(\sqrt{r^2+z^2} - \cos\theta'\right). \tag{A.86}$$

Using this expansion, the form of equation (A.85) recalls the definition of the elliptic integral of the third kind. To reveal this similarity in form the change of variable $\phi = \theta/2$ is introduced. The integration interval is reduced to $[0, \pi/2]$ and squared cosine terms appear since $\cos(2\phi) = 2\cos^2\phi - 1$. It leads to:

$$u_\theta^{r'}(\boldsymbol{x}) = -\frac{z\Gamma_{\text{tot}}}{2\pi^2}\int_0^{\pi/2} \frac{r'\cos(2\phi) - r\cos(2\phi)^2}{(r^2 + z^2 - r^2\cos(2\phi)^2)\sqrt{(r+r')^2 + z^2 - 4rr'\cos^2\phi}}\, d\phi \tag{A.87}$$

$$= \frac{z\Gamma_{\text{tot}}}{2\pi^2}\frac{\sqrt{m}}{2\sqrt{rr'}}\frac{n_1}{2r}\frac{n_2}{2r}\int_0^{\pi/2} \frac{r'\left(2\cos^2\phi - 1\right) - r\left(2\cos^2\phi - 1\right)^2}{(1 - n_1\cos^2\phi)(1 - n_2\cos^2\phi)\sqrt{1 - m\cos^2\phi}}\, d\phi, \tag{A.88}$$

where the following parameters have been introduced to recall elliptic integral forms:

$$m = \frac{4rr'}{(r+r')^2 + z^2}, \quad n_1 = \frac{2r}{r + \sqrt{r^2+z^2}}, \quad n_2 = \frac{2r}{r - \sqrt{r^2+z^2}}. \tag{A.89}$$

Three integrals are introduced for their subsequent use:

$$I_3 = \int_0^{\pi/2} \frac{2\cos^2\phi - 1}{d_1 d_2 d_s}\, d\phi, \quad I_4 = \int_0^{\pi/2} \frac{4(\cos^4\phi - \cos^2\phi) - 1}{d_1 d_2 d_s}\, d\phi, \quad I_5 = \int_0^{\pi/2} \frac{1}{d_1 d_2 d_s}\, d\phi,$$

with $d_1 = 1 - n_1\cos^2\phi$, $d_2 = 1 - n_2\cos^2\phi$ and $d_s = \sqrt{1 - m\cos^2\phi}$. With these notations, Equation (A.88) becomes

$$u_\theta^{r'}(\boldsymbol{x}) = -\frac{z\Gamma_{\text{tot}}}{2\pi^2}\frac{\sqrt{m}}{2\sqrt{rr'}}\frac{1}{z^2}\left[r' I_3 - r I_4\right], \tag{A.90}$$

where the relation $n_1 n_2 = -4r^2/z^2$ has been used to simplify the expression. The integrals are solved by decomposing them into partial fractions to reveal expressions of the elliptic integral of the third kind. The integral I_3 may be reduced my manipulation of its numerator as follow: $2\cos^2\phi - 1 = \left(n_1\cos^2\phi - 1 + 1\right)/n_1 + \left(n_2\cos^2\phi - 1 + 1\right)/n_2 - 1$ and and further noting that $1/n_1 + 1/n_2 = 1$. Alternatively it is possible to proceed to identification on the coefficient a and b that are such that the integrand of I_3 is split as: $a/(d_1 d_s) + b/(d_2 d_s)$. The identification leads to $a = (n_2 - 2)/(n_1 - n_2) = -1/n_1$ and $b = (2 - n_1)/(n_1 - n_2) = -1/n_2$ and the expression of I_3 is readily obtained as:

$$I_3 = -\frac{1}{n_1}\Pi(n_2, m) - \frac{1}{n_2}\Pi(n_1, m). \tag{A.91}$$

The integral I_4 is now to be evaluated. Given the relation between n_1 and n_2 mentioned above, it is observed that:

$$(1 - n_1\cos^2\phi)(1 - n_2\cos^2\phi) = 1 + n_1 n_2(\cos^4\phi - \cos^2\phi). \tag{A.92}$$

Isolating the term $(\cos^4\phi - \cos^2\phi)$ and inserting it into the definition of I_4 leads to:

$$I_4 = \frac{4}{n_1 n_2}\int_0^{\pi/2} \frac{1}{\sqrt{1 - m\cos^2\phi}}\, d\phi + \left(1 - \frac{4}{n_1 n_2}\right) I_5 = \frac{-z^2}{r^2}K(m) + \frac{r^2 + z^2}{r^2} I_5. \tag{A.93}$$

The integrand of I_5 is split into two fractions as was done previously and the identification of the coefficients leads to $a = -n_2/(n_1 - n_2)$ and $b = n_1/(n_1 - n_2)$. This decomposition gives the following expression for I_5:

$$I_5 = \frac{1}{n_1 - n_2} \left[n_1 \Pi(n_1, m) - n_2 \Pi(n_2, m) \right]. \tag{A.94}$$

The indefinite integral expression equation (A.90) may now be developed using equation (A.91), (A.93) and (A.94):

$$u_\theta^{r'}(\boldsymbol{x}) = -\frac{\Gamma_{\text{tot}}}{4\pi^2 z} \sqrt{\frac{r}{r'}} \frac{z^2}{r^2} \sqrt{m} \left[K(m) + T_1 \, \Pi(n_1, m) - T_2 \, \Pi(n_2, m) \right], \tag{A.95}$$

with T_1 and T_2 given in equation (A.99) if R is replaced by r'.

Definite form of the Biot-Savart law The definite form of the Biot-Savart integral is readily obtained from equation (A.95) to give the influence of the bound vorticity disk as: $u_{\theta,b}(\boldsymbol{x}) = u_\theta^R(\boldsymbol{x}) - \lim_{r' \to 0} u_\theta^{r'}(\boldsymbol{x})$. The evaluation of the limit gives:

$$\lim_{r' \to 0} u_\theta^{r'}(\boldsymbol{x}) = \frac{\Gamma_{\text{tot}}}{4\pi r} \left[\frac{|z|}{z} - \frac{z}{\sqrt{r^2 + z^2}} \right]. \tag{A.96}$$

The total velocity field induced by the bound vortex disk is then:

$$u_{\theta,b}(\boldsymbol{x}) = \frac{\Gamma_{\text{tot}}}{4\pi} \left\{ \frac{1}{r} \left[\frac{z}{\sqrt{r^2 + z^2}} - \frac{|z|}{z} \right] - \frac{1}{\pi z} \sqrt{\frac{r}{R}} \frac{z^2}{r^2} \sqrt{m} \left[K(m) + T_1 \, \Pi(n_1, m) - T_2 \, \Pi(n_2, m) \right] \right\} \tag{A.97}$$

with

$$T_1 = \frac{\left(\sqrt{r^2 + z^2} - r \right)(r + R) - z^2}{2z^2} \tag{A.98}$$

$$T_2 = \frac{\left(\sqrt{r^2 + z^2} + r \right)\left(\sqrt{r^2 + z^2} + R \right)}{2z^2} \tag{A.99}$$

and

$$m = \frac{4rR}{(r + R)^2 + z^2}, \quad n_1 = \frac{2r}{r + \sqrt{r^2 + z^2}}, \quad n_2 = \frac{2r}{r - \sqrt{r^2 + z^2}} \tag{A.100}$$

An alternate form of equation (A.97) can be obtained using the definition of circulation and the induced velocities from the root-vortex and the longitudinal tip-vorticity (see **[23]**, section A.3).

Properties The disk generates a jump of velocity across it as:

$$\boldsymbol{u}_b(r, 0^+) - \boldsymbol{u}_b(r, 0^-) = \boldsymbol{\gamma}_b \times \boldsymbol{n}, \tag{A.101}$$

where the normal to the disk $\boldsymbol{n}$ is taken along the vector $\boldsymbol{e}_z$. From equation (A.80) and equation (A.101) it is clear that the velocity jump is purely tangential. This result is expected since the velocity is solely in the tangential direction. Observing that the velocity field is anti-symmetric with respect to z, equation (A.101) leads to

$$u_{\psi,b}(r, 0^-) = -u_{\psi,b}(r, 0^+) = \left\{ \begin{matrix} 0 \\ \frac{\Gamma_{\text{tot}}}{4\pi r} \end{matrix} \right\}. \tag{A.102}$$

The above result may also be obtained by a careful evaluation of the limit of equation (A.97) as z tends to zero. The induced velocity field at different axial position downstream of the rotor disk is plotted in figure A.10. Far from the disk the induced velocity tends to zero.

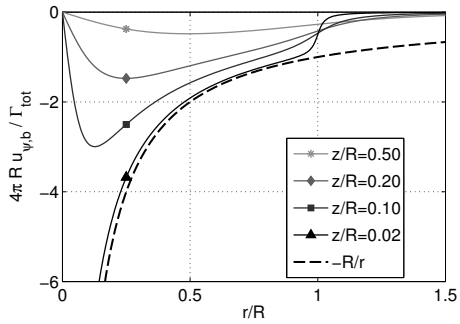

Figure A.10: Tangential velocity induced by the bound vortex disk at different axial positions downstream of the disk in the wind turbine convention. From anti-symmetry with respect to z, the velocity field is zero at $z = 0$ and is opposite upstream of the disk.

A.5 Skewed vortex cylinders

A.5.1 Skewed cylinder of tangential vorticity - Semi-numerical integration

The application of the Biot-savart law in this study takes the following dimensionless form:

$$I = C \int_0^{2\pi} \int_0^{+\infty} \frac{a' + b'z'}{(a + bz' + cz'^2)^{3/2}} dz' d\theta \tag{A.103}$$

$$= C \int_0^{2\pi} \left[\frac{-2\left[2\left(ab'^2 - a'bb' + ca'^2\right) + \left(bb' - 2a'c\right)\left(a' + b'z'\right)\right]}{b'(4ac - b^2)\sqrt{a + bz' + cz'^2}} \right]_0^{+\infty} d\theta \tag{A.104}$$

where the indefinite integral in z' can be found in the book of Peirce [157, p. 28]. The definite integral written $I_{z'}$ is evaluated through the limit as z' tends to infinity to lead equation (A.106). The last form of equation (A.106) corresponds to the one presented by Castles and Durham [39]. To facilitate the comparison, notations from this reference are compared to the ones of this document in table A.1.

$$I_{z'} = \frac{1}{\sqrt{c}} + \frac{2(2ab' - a'b)}{\sqrt{a}\,(4ac - b^2)} + \frac{4c(a' - a) + b(b - 2b')}{\sqrt{c}\,(4ac - b^2)} \tag{A.105}$$

$$= \frac{2\,(a'\sqrt{c} + b'\sqrt{a})}{\sqrt{ac}\,(2\sqrt{ac} + b)} = \frac{1}{\sqrt{c}} \frac{a' + \frac{b'}{\sqrt{c}}\sqrt{a}}{\sqrt{a}\left(\sqrt{a} + \frac{b}{2\sqrt{c}}\right)} \tag{A.106}$$

This result was applied to obtain the induction of the tangential vorticity given in equation (4.2) after making sure that the integral over z had no physical dimension. The velocity induced at any point by the tangential vorticity is obtained by numerical integration over θ. As a control point approaches the vortex cylinder the integral becomes singular and the result from numerical integration will depend on the number of quadrature points. In the cases tried, a number of quadrature points of 600 gave a relative error lower than 0.05% when compared to the value obtained with 10000 points. Examples of adaptive or semi-analytical treatment of the singularity can be found in the work of Voutsinas and Bergeles for similar integrals [216]. For simplicity, the integrals can also be regularized by adding a small positive constant in the denominator. In the current study, no specific treatment of the singularity was done since sufficient accuracy was obtained for the control points of interest. The control points were taken such that $|\tilde{r} - 1| < 0.01$ and a fixed number of 600 quadrature points was used.

Table A.1: Table of equivalence between notations used in Castles and Durham article [39] and the current document.

Current	a'	b'	a	b	c	$-b/2\sqrt{c}$	$b/\sqrt{c}$
Castles and Durham	A	a	C	b	c	D	B

A.5.2 Skewed vortex cylinder - Extension of the work of Castles and Durham

A point on the skewed cylinder surface S will be written in Cartesian coordinates $\boldsymbol{x'} = (R\cos\theta' + mz', R\sin\theta', z')$ with $m = \tan\chi$. The evaluation of the Biot-Savart law at a control point of Cartesian coordinates $\boldsymbol{x} = (r\cos\psi, r\sin\psi, z)$ writes:

$$\begin{aligned}\boldsymbol{u}(\boldsymbol{x}) &= \int_S \frac{\boldsymbol{\gamma_t}(\boldsymbol{x'})\times(\boldsymbol{x}-\boldsymbol{x'})}{4\pi|\boldsymbol{x}-\boldsymbol{x'}|^3} R d\theta' dl' \\ &= \frac{\gamma_t}{4\pi}\int_0^{2\pi}\int_0^{+\infty} \frac{(z-z')\boldsymbol{e}_r(\theta') + (R - r\cos(\theta'-\psi) + mz'\cos\theta')\boldsymbol{e}_z}{|\boldsymbol{x}-\boldsymbol{x'}|^3} R d\theta' dl'\end{aligned}$$

where the infinitesimal length along the skewed wake dl' is $\sqrt{1+m^2}dz'$ and with:

$$|\boldsymbol{x}-\boldsymbol{x'}|^2 = R^2 + r^2 + z^2 - 2rR\cos(\theta'-\psi) + (2mR\cos\theta' - 2z - 2rm\cos\psi)z' + (1+m^2)z'^2 \quad \text{(A.107)}$$

The coefficients introduced in section A.5.1 are directly obtained by identification for the Cartesian variables (x, y, z) and by projection for (r, ψ). They are given in eqs. (4.2)-(4.3) with $C = \left\{\frac{\gamma_t}{4\pi}\sqrt{c}\right\}$.

$$\{a,\ b,\ c\} = \left\{R^2 + r^2 + z^2 - 2rR\cos(\theta'-\psi),\ 2mR\cos\theta' - 2mr\cos\psi - 2z,\ 1+m^2\right\}$$

$$\{a'_x,\ b'_x\} = R\{z\cos\theta',\ -\cos\theta'\} \qquad \{a'_z,\ b'_z\} = R\{R - r\cos(\theta'-\psi),\ m\cos\theta'\}. \quad \text{(A.108)}$$

$$\{a'_y,\ b'_y\} = R\{z\sin\theta',\ -\sin\theta'\} \quad \text{(A.109)}$$

Further, using the polar coordinates at the control point the azimuthal and radial velocities are immediately obtained by expressing $\boldsymbol{e}_\psi$ and $\boldsymbol{e}_\psi$ and using the above coefficients:

$$\{a'_\psi,\ b'_\psi\} = R\{z\sin(\theta'-\psi),\ -\sin(\theta'-\psi)\}, \quad \{a'_r,\ b'_r\} = R\{z\cos(\theta'-\psi),\ -\cos(\theta'-\psi)\}, \quad \text{(A.110)}$$

be directly applicable the integral over z should have no physical dimension. This is why the variable R has to be present in the coefficients a' and b' and not be associated with the variable C. Equivalently, all length may be made dimensionless by division by R. This choice would give relations identical to equation (A.108)-(A.110) for $R = 1$ and the variables r, z being dimensionless. The application of equation (A.106) leads to

$$u_{\bullet,t}(r,\psi,z) = \frac{\gamma_t}{4\pi}\int_0^{2\pi} \frac{2\left(a'_\bullet\sqrt{c} + b'_\bullet\sqrt{a}\right)}{\sqrt{a}\left(2\sqrt{ac}+b\right)} d\theta' = \frac{\gamma_t}{4\pi}\int_0^{2\pi} \frac{a'_\bullet + \frac{b'_\bullet}{\sqrt{c}}\sqrt{a}}{\sqrt{a}\left(\sqrt{a}+\frac{b}{2\sqrt{c}}\right)} d\theta' \quad \text{(A.111)}$$

where the symbol $\bullet$ stands indifferently for x, y, z, ψ or r. It should be noted that a simplification of the factor $\sqrt{c}$ was performed in equation (A.111). The rearrangement leading to the second form of equation (A.111) is done for ease of comparison with the work of Castles and Durham [39].

A.5.3 Skewed vortex cylinder - Longitudinal axis - Work of Coleman et al.

The axial velocity from the Biot-Savart law applied to a control point on the fore-aft diameter is directly obtained from results of the previous section by $\psi = \psi_0 = 0$ and $z = 0$:

$$u_{z,t}(r,\psi_0) = \frac{\gamma_t}{4\pi}\int_0^{2\pi}\int_0^{+\infty} \frac{[(R - r\cos\theta' + mz'\cos\theta')\boldsymbol{e}_z]\ \ R\sqrt{1+m^2}d\theta' dz'}{[R^2 + r^2 - 2rR\cos\theta' + (2mR\cos\theta' - 2rm)z' + (1+m^2)z'^2]^{\frac{3}{2}}} \tag{A.112}$$

Identification with the results from section A.5.1 gives $c = 1 + m^2$, $C = \frac{\gamma_t}{4\pi}\sqrt{c}$,

$$\{a, b\} = \left\{R^2 + r^2 - 2rR\cos\theta', 2mR\cos\theta' - 2mr\right\}$$
$$\{a', b'\} = R\left\{R - r\cos\theta', m\cos\theta'\right\}$$

The difference in coordinate systems implies that θ' and χ (and thus m) have opposite signs compared to the original article [46]. Integration of equation (A.106)(left) with respect to θ' is done term by term. The first term is constant and integrates directly to $\gamma_t/2$. The second term is shown to be zero from symmetry. If the third term is left in integral form this leads to:

$$u_{z,t}(r,\psi_0) = \gamma_t\Big[\frac{1}{2} + \frac{m\sqrt{1+m^2}\tilde{r}}{2\pi}\int_0^{\pi} \frac{\sin^2\theta'\ d\theta'}{\sqrt{1+\tilde{r}^2 - 2\tilde{r}\cos\theta'}\left(1+\tilde{r}^2 - 2\tilde{r}\cos\theta' + m^2\sin^2\theta'\right)}\Big] \tag{A.113}$$

where the notation $\tilde{r} = r/R$ is introduced since dimensionless quantities are required to apply results of section A.5.1. Coleman et al. split the integral into two partial fractions corresponding to term 3 and 4 of equation (B5) of their article [46]. The first fraction leads to an elliptic integral of the first kind while the other leads to two elliptic integrals of the third kind and two of the first kind, but the two latter cancel out. Details will be provided in the following paragraph where alternative forms are provided. The axial induced velocity on the fore-aft diameter $\psi = 0$ is:

$$\begin{aligned} u_{z,t}(r,\psi_0) = \frac{\gamma_t}{2}\Big[1 &+ \frac{2\tilde{r}\sqrt{1+m^2}}{m\pi}K\left(\tilde{r}^2\right) \\ &- \frac{\tilde{r}(\tilde{r}+1)}{4m\pi\sqrt{m^2+\tilde{r}^2}}\left[\left(b_1 + j^2\right)\Pi\left(-b_1, j^2\right) + \left(b_2 - j^2\right)\Pi\left(b_2, j^2\right)\right]\Big] \end{aligned} \tag{A.114}$$

with

$$k^2 = \left(\frac{1-\tilde{r}}{1+\tilde{r}}\right)^2, \quad j^2 = 1 - k^2, \quad m_\pm = \frac{\sqrt{1+m^2} \pm \sqrt{\tilde{r}^2+m^2}}{1+\tilde{r}}, \quad b_1 = m_+^2 - 1, \quad b_2 = 1 - m_-^2$$

Alternative forms Assuming the the following form for $u_{z,t}$:

$$u_{z,t}(r,\psi,\chi) = u_{z,0}\left[1 + K_{z,t}(r,\chi)\cos\psi\right] \tag{A.115}$$

the identification with equation (A.113) for $\psi = 0$ leads to

$$K_{z,t} = \frac{\tilde{r}m\sqrt{1+m^2}}{\pi}\int_0^{\pi} \frac{\sin^2\theta'}{\sqrt{1+\tilde{r}^2 - 2\tilde{r}\cos\theta'}\left(1+\tilde{r}^2 - 2\tilde{r}\cos\theta' + m^2\sin^2\theta'\right)}d\theta' \tag{A.116}$$

Coleman et al. split the integral into two partial fractions:

$$K_{z,t} = \frac{-\tilde{r}\sqrt{1+m^2}}{\pi m}\int_0^{\pi} \frac{-1}{\sqrt{1+\tilde{r}^2 - 2\tilde{r}\cos\theta}} + \frac{\sqrt{1+\tilde{r}^2 - 2\tilde{r}\cos\theta}}{1+r^2 - 2r\cos\theta + m^2\sin^2\theta}d\theta \tag{A.117}$$

Which gives:

$$K_{z,t} = \frac{2\tilde{r}\sqrt{1+m^2}}{m\pi}K\left(\tilde{r}^2\right) - \frac{\tilde{r}(\tilde{r}+1)}{2m\pi\sqrt{m^2+\tilde{r}^2}}\left[\left(b_1 + j^2\right)\Pi\left(-b_1, j^2\right) + \left(b_2 - j^2\right)\Pi\left(b_2, j^2\right)\right] \tag{A.118}$$

The integral form of the equation may be preferred since the two elliptic terms involved are two large numbers of opposite sign which can pose numerical difficulties [34]. Introducing the change of variable $\phi = \theta/2$ into equation (A.116) and noting that $\left(\tilde{r} - \cos(2\phi)\right)^2\cos^2\chi + \sin^2(2\phi) =$

$\frac{1}{1+m^2}\left(1+\tilde{r}^2-2\tilde{r}\cos(2\phi)+m^2\sin^2(2\phi)\right)$ then the following alternative form is found:

$$K_{z,t}=\frac{2\tilde{r}\sin\chi}{\pi}\int_0^{\pi/2}\frac{\sin^2(2\phi)}{\sqrt{(1+\tilde{r})^2-4\tilde{r}\cos^2\phi}\left[\left(\tilde{r}-\cos(2\phi)\right)^2\cos^2\chi+\sin^2(2\phi)\right]}d\phi \tag{A.119}$$

The change of variable $\epsilon=\pi/2-\phi$ will transform the integral of equation (A.119) into the same integral as the one presented in reference the book by Burton et al. [34]. The flow expansion function F_t may be defined as:

$$F_t(\tilde{r},\chi)=\frac{K_{z,t}(\tilde{r},\chi)}{2\tan\frac{\chi}{2}}=\frac{K_{\xi,t}(\tilde{r},\chi)}{\sec^2\left(\frac{\chi}{2}\right)} \tag{A.120}$$

The comparison with [34] is possible using this. In the first edition typographical errors are found. In the second edition an approximate formula is provided. From the definition of the flow expansion given here, equation (A.115) writes:

$$u_{z,t}(r,\psi,\chi)=u_{z,0}\left[1+2F_t(\tilde{r},\chi)\tan\frac{\chi}{2}\cos\psi\right] \tag{A.121}$$

It is observed that the flow expansion varies only slightly with χ so the dependency with respect to this variable may be dropped [34]. Øye [153] suggested the following fit to the function F_t:

$$F_t(\tilde{r})\approx 0.5\left(\tilde{r}+0.4\tilde{r}^3+0.4\tilde{r}^5\right) \tag{A.122}$$

A.5.4 Infinite skewed cylinder with longitudinal vorticity

The velocity field induced by an infinite cylinder of elliptic cross-section is considered. The vorticity along the cylinder is not constant and is distributed according to the skewed vortex model presented in **[24]**. Using a symmetry analysis similar to the one of Katsoff [87] with rotation of the system by an angle π with respect to each of the Cartesian axis shows that: u_x is an even function of y and an odd function of x, while u_y is an odd function of x and an even function of y. Further, the investigation of two vortex points on the ellipse symmetric with respect to x or with respect to y shows that $u_x=0$ for $\psi=\pi/2$ and $u_y=0$ for $\psi=0$. The velocity field is 0 on both axis from the same symmetry result. It will be proven below that the velocity field is actually zero everywhere inside the ellipse. Two proofs are given.

Stream function analysis in elliptic coordinate system The vortex system may be seen as a continuous distribution of 2D vortex points distributed along an ellipse $\{a\cos\theta, b\sin\theta\}$. It is assumed that the ellipse lays in the $(x-y)$-plane and $a>b$. The intensity of each vortex point is written $\Gamma=R\gamma_l d\theta$. A vortex point located at a point $\boldsymbol{x'}$ induces a velocity field $d\boldsymbol{u}(\boldsymbol{x})=\frac{\Gamma}{2\pi|\boldsymbol{x}-\boldsymbol{x'}|}\boldsymbol{e}_\perp$ where $e_\perp$ is the unitary vector orthogonal to $(\boldsymbol{x}-\boldsymbol{x'})$ which in 2D is: $\boldsymbol{e}_z\times(\boldsymbol{x}-\boldsymbol{x'})/|\boldsymbol{x}-\boldsymbol{x'}|$. The vorticity of a single point vortex is $d\boldsymbol{\omega}=\mathrm{curl}\,(d\boldsymbol{u})=\boldsymbol{e}_z\Gamma\delta(\boldsymbol{x}-\boldsymbol{x'})$. The full velocity field can be obtained from the knowledge of the stream function. The stream function in two dimensions is related to the vorticity vector from the Poisson's equation: $\Delta\psi=-\omega_z\equiv-\boldsymbol{\omega}\cdot\boldsymbol{e}_z$. Given the geometry of the problem, an elliptic coordinate system is introduced with coordinates $(\mu,\ \theta)$ as $x=c\cosh\mu\cos\theta$ and $y=c\sinh\mu\sin\theta$. The considered ellipse corresponds to a fixed value $\mu=\mu_0$ with $a=c\sinh\mu_0$ and $b=c\sinh\mu_0$. The total vorticity is obtained upon integration of $d\boldsymbol{\omega}$ over the ellipse:

$$\begin{aligned}\boldsymbol{\omega}=\mathrm{curl}\,\boldsymbol{u}&=R\gamma_l\int_0^{2\pi}\delta(\boldsymbol{x}-\boldsymbol{x'}(\theta'))d\theta'\,\boldsymbol{e}_z\\&=R\gamma_l\int_0^{2\pi}\delta(x-a\cos\theta')\delta(y-b\sin\theta')d\theta'\,\boldsymbol{e}_z\end{aligned} \tag{A.123}$$

The determinant of the Jacobian related to the change to elliptical variables, written D, is such that the elementary area in the plane is: $dA=dxdy=Dd\mu\,d\theta$, where $D=c^2(\cosh^2\mu+\cos^2\theta)$.

Thus, Equation (A.123) writes in elliptical variables:

$$\boldsymbol{\omega} = R\gamma_l \int_0^{2\pi} D^{-1}\delta(\mu-\mu_0)\delta(\theta-\theta')d\theta'\,\boldsymbol{e}_z = R\gamma_l D^{-1}\delta(\mu-\mu_0)\,\boldsymbol{e}_z \tag{A.124}$$

Using equation (A.124), Poisson's equation in (μ,θ) variables is:

$$D^{-1}\left(\frac{\partial^2\psi}{\partial\mu^2}+\frac{\partial^2\psi}{\partial\theta^2}\right) = -R\gamma_l D^{-1}\delta(\mu-\mu_0). \tag{A.125}$$

The common factor on both side is strictly positive and can be simplified. Since the source term is purely a function of μ, the method of integration by separation of variable is reduced to find a solution depending only μ, i.e. $\frac{\partial^2\psi}{\partial\mu^2} = -R\gamma_l\delta(\mu-\mu_0)$ for which a solution compatible with $\boldsymbol{u}(\mathbf{0}) = \mathbf{0}$ is: $\psi = -R\gamma_l H(\mu-\mu_0)\cdot(\mu-\mu_0)$, where $H(x)$ is the Heaviside function. The stream function is constant and equal to zero within the ellipse, which implies the same for the velocity field. Further, this result shows that outside of the ellipse the streamlines are confocal ellipses. The full velocity field can be determined analytically by computing the partial derivatives of the stream function.

Contribution from points on the same line - Viewing angle A geometrical approach is presented here to show that the induced velocity inside the circle and the ellipse are zero. The case of the circle is considered first. The elementary velocity induced by two infinitesimal curved segments of the circle at a control point P are considered. The elementary segments dl_A and dl_B are centered respectively around point A and B such that APB forms a straight segment (see left of figure A.11). The angle from which both paired segment are viewed from P is $d\beta$. Since the vorticity

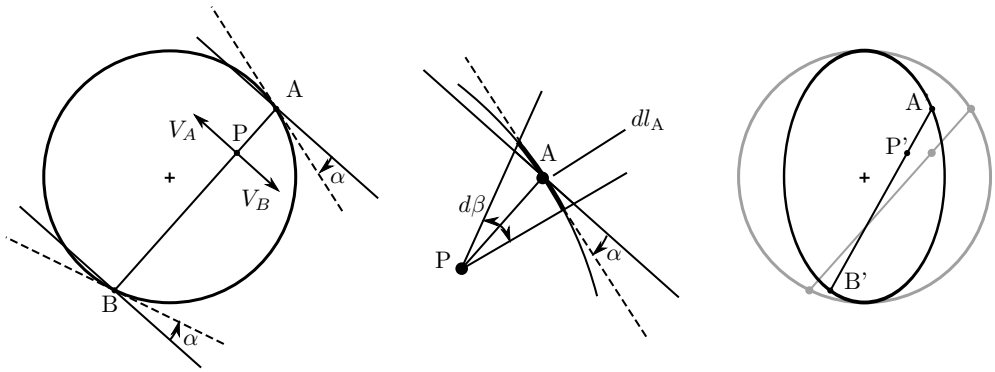

Figure A.11: Notations used for the integration of paired elementary length viewed from the same angle at a given control point..

is constant along z, the induced velocities from the two segments will be in opposite direction. It is yet to be proven that these intensities have the same magnitudes. The total velocity at P is obtained upon integration over all pairs of such elementary segments. The total velocity is thus obtained upon integration of β from 0 to π.

The angle formed by the normal to AB and the tangent of the circle is the same for both points and written α. Using figure A.11(middle), the length of each segment is obtained as:

$$dl_\mathrm{A}\cos\alpha = \mathrm{PA}\,d\beta, \qquad dl_\mathrm{B}\cos\alpha = \mathrm{PB}\,d\beta \tag{A.126}$$

where PA and PB refer to the length of the segments. The vortex strength of each segment is γdl_A and γdl_B. From the Biot-Savart law, the norm of the velocities induced by each elementary

segment is:

$$dV_{\mathrm{A}} = \frac{\gamma dl_{\mathrm{A}}}{2\pi \mathrm{PA}} = \frac{\gamma d\beta}{2\pi \cos\alpha} \tag{A.127}$$

$$dV_{\mathrm{B}} = \frac{\gamma dl_{\mathrm{B}}}{2\pi \mathrm{PB}} = \frac{\gamma d\beta}{2\pi \cos\alpha} \tag{A.128}$$

Since the velocities have opposite directions their contribution is zero and this will apply to all pairs of segments upon integration over β. This shows that the induced velocities inside the circle are zero.

By definition of the problem, the vorticity distribution along the ellipse is such that:

$$\gamma_e dl_e = \gamma dl_c \tag{A.129}$$

where the subscript e refer to the ellipse and c to the circle. Without loss of generality it is assumed that the ellipse is obtained from the circle by the simple transformation displayed in figure A.11(right) and prime notations are used for the transformed points. A pair of elementary segments along the ellipse corresponds to a pair of elementary segment on the circle. First, from equation (A.129), the total vorticity of corresponding segments is the same: $\gamma_{\mathrm{A'}} dl_{\mathrm{A'}} = \gamma dl_{\mathrm{A}}$ and $\gamma_{\mathrm{B'}} dl_{\mathrm{B'}} = \gamma dl_{\mathrm{B}}$. Second, the length are affected by the same constant c by the transformation, so that: P'A' = cPA and P'B' = cPB. Third, since the vorticity is in the z direction, the induced velocities by both elementary ellipse segments will have opposite direction. Last, the magnitude of these velocities are from the Biot-Savart law:

$$dV_{\mathrm{A'}} = \frac{\gamma_{\mathrm{A'}} dl_{\mathrm{A'}}}{2\pi \mathrm{P'A'}} = \frac{\gamma dl_{\mathrm{A}}}{2\pi c \mathrm{PA}} = \frac{\gamma d\beta}{2\pi c \cos\alpha} \tag{A.130}$$

$$dV_{\mathrm{B'}} = \frac{\gamma_{\mathrm{B'}} dl_{\mathrm{B'}}}{2\pi \mathrm{P'B'}} = \frac{\gamma dl_{\mathrm{B}}}{2\pi c \mathrm{PB}} = \frac{\gamma d\beta}{2\pi c \cos\alpha} \tag{A.131}$$

The norm of the velocities are equal which implies that the vectorial sum is zero and this consequently true for all pair of ellipse segments. It results that the velocity field is zero inside the ellipse.

Appendix B

Helical vortex filaments

References The potential correponding to a system of B equally-spaced infinite helical filaments was derived by Kawada in 1936 [97]. Lerbs [115] introduced an approximate expression in 1952. Later, in 1957, Wrench [223] added a correction term to reduce the error of the approximation done by Lerbs. Different relation are also found in the work of Kerwin [98, p. 12] who refer to the work of Betz and Strcheletsky. The formulae have also been derived more recently by Okulov, as given for instance in [146].

Note on the stability of Joukowski helical model In the work of Okulov and Sørensen [151] the stability of helical vortex systems is studied. It is shown that the far wake described by the helical model of Joukowski is unconditionally unstable for all pitch values.

Conventions The induced velocity of infinite and semi-infinite helices are discussed in this section. The canonical helix is regular, it has a pitch $h = 2\pi l$, it surrounds the z axis and has the radius r_0. The difference between left-handed and right handed relations will be made by introducing a sign parameter with value $s = -1$ for left-handed helix and $s = 1$ for right-handed helix. From the symmetry and periodicity of helices a relevant position parameter is $\chi = \theta - sz/l$. The induced velocity for a system of B identical helices equally spaced azimuthally will also be considered.

Semi-infinite helix and rotor terminology In applications to rotors, semi-infinite helices are used and the induced velocities are evaluated in the "half-plane", corresponding to the rotor-plane. Each of the B semi-infinite helix is trailed from a rotor blade. The rotor-blade will be referred to as the line from which the helix is issued, or "lifting-line". For a wind turbine rotating in the clockwise direction, the trailed helix will be left-handed. The helix from the first blade is defined by the following congruence $\chi \equiv 0 \pmod{2\pi}$, and on the lifting line one has simply $\chi = 0$. Results from Lerbs and Wrench which are expressed at the lifting line ($\chi = 0$) are slightly simpler than the one presented by Okulov.
From the second result of section D.3.2, the induced velocities at the lifting line are computed as half the velocities induced by an infinite helix. For distinction, results for infinite helix are written using a over-tilde notation.

Tangential velocity The tangential induction is directly related to axial induction with the following formula:

$$u_\theta = u_0 - s u_z \frac{l}{r} \quad \text{or} \quad \tilde{u}_\theta = \tilde{u}_0 - s \tilde{u}_z \frac{l}{r} \tag{B.1}$$

Where u_0 is the velocity induced by a root vortex line representing the vortex system, i.e.:

$$\tilde{u}_0 = \frac{B\Gamma_t}{2\pi r} \quad \text{(for } B \text{ infinite helices, or in the far wake of semi-infinite helices)} \tag{B.2}$$

$$u_0 = \frac{B\Gamma_t}{4\pi r} \quad \text{(for } B \text{ semi-infinite helices evaluated at the rotor-plane)} \tag{B.3}$$

B.1 Exact expressions for infinite helical vortex filaments

One infinite helical filament Exact analytical formulae for the velocity field induced by an infinite helical vortex filament is found e.g. in Hardin [81](1982) in terms of modified Bessel functions:

$$\begin{matrix}\text{for } r < r_0 \\ \text{for } r_0 > r\end{matrix}, \quad s\,\tilde{u}_z(r,\chi) = \frac{\Gamma_t}{2\pi l}\begin{Bmatrix}1\\0\end{Bmatrix} - \frac{\Gamma_t r_0}{\pi l^2}\sum_{n=1}^{\infty} n \begin{Bmatrix} I_n\left(\frac{nr}{l}\right)\cdot K_n'\left(\frac{nr_0}{l}\right) \\ K_n\left(\frac{nr}{l}\right)\cdot I_n'\left(\frac{nr_0}{l}\right)\end{Bmatrix}\cos(n\chi) \tag{B.4}$$

$$\tilde{u}_r(r,\chi) = \frac{\Gamma_t r_0}{\pi l^2}\sum_{n=1}^{\infty} n \begin{Bmatrix} I_n'\left(\frac{nr}{l}\right)\cdot K_n'\left(\frac{nr_0}{l}\right) \\ K_n'\left(\frac{nr}{l}\right)\cdot I_n'\left(\frac{nr_0}{l}\right)\end{Bmatrix}\sin(n\chi) \tag{B.5}$$

$$\tilde{u}_\theta(r,\chi) = \frac{\Gamma_t}{2\pi r} \qquad -u_z\frac{l}{r} \tag{B.6}$$

In the above the upper value of the bracket should be used for radial positions such that $r < r_0$. The first term corresponds to the first term of the series, i.e. $n = 0$ while the second term result from the folding of the negative and positive series index.

B.2 Approximate expressions for infinite helical filaments

The approximate expressions for several filaments can be attributed to the work of Lerbs [115] and Wrench [223] eventhough the authors presented results at $\chi = 0$ in their references. General formulae are presented by Okulov for one filament. The link between the two is investigated in section B.5. The value of the functions C and the different notation used are mare explicit in section B.4. The induced velocities for one ($B = 1$) or B helical filaments are given by:

$$s\tilde{u}_z(r,\chi) = \frac{B\Gamma_t}{2\pi l}\begin{Bmatrix}1\\0\end{Bmatrix} + \frac{B\Gamma_t}{2\pi l}C_{0z}\Big[\operatorname{Re}\left[\pm F_B\right] + \frac{1}{B}C_{1z,\bullet}\operatorname{Re}\left[\log\left(1+F_B\right)\right]\Big] \tag{B.7}$$

$$\tilde{u}_r(r,\chi) = -\frac{B\Gamma_t}{2\pi r}C_{0r}\Big[\operatorname{Im}\left[\ F_B\right] \pm \frac{1}{B}C_{1r}\operatorname{Im}\left[\log(1+F_B)\right]\Big] \tag{B.8}$$

where

$$F_B = \frac{1}{e^{\mp B\xi - iB\chi} - 1} \tag{B.9}$$

and where the sign notation $\pm$ or $\mp$ follow the same stacking layout than the brackets notation: the upper value should be used when $r < r_0$. The expression of Lerbs or Wrench are obtained depending on the definition of the constant C_{1z} used (see section B.4).

B.3 Expressions for semi-infinite helices evaluated on the lifting line

The expressions for semi-infinite helical filaments evaluated on the lifting line are directly obtained from the results of section B.1 and section B.2 by division by 2 and evaluation at $\chi = 0$.

Exact expression for several semi-infinite evaluated on the lifting line The axial velocity induced by B semi-infinite helical filaments on the lifting line($\chi = 0$) can be derived from this potential. It can also be obtained from equation (B.4)-(B.6), by summing the contribution of B helical filaments and dividing the contribution by two. This leads to:

$$\begin{matrix}\text{for } r < r_0 \\ \text{for } r_0 > r\end{matrix}, \quad s\,u_z(r) = \frac{B\Gamma_t}{4\pi l}\begin{Bmatrix}1\\0\end{Bmatrix} - \frac{B^2\Gamma_t r_0}{2\pi l^2}\sum_{n=1}^{\infty} n \begin{Bmatrix} I_{nB}\left(\frac{Bnr}{l}\right)\cdot K_{nB}'\left(\frac{Bnr_0}{l}\right) \\ K_{nB}\left(\frac{Bnr}{l}\right)\cdot I_{nB}'\left(\frac{Bnr_0}{l}\right)\end{Bmatrix} \tag{B.10}$$

Approximate expression for several semi-infinite evaluated on the lifting line The expression from Lerbs and Wrench given at the lifting line ($\chi = 0$) are:

$$s\,u_z(r) = \frac{B\Gamma_t}{4\pi l}\begin{Bmatrix}1\\0\end{Bmatrix} + \frac{B\Gamma_t}{4\pi l}C_{0z}\left[\frac{\pm 1}{e^{\mp B\xi}-1} + \frac{1}{B}C_{1z}\log\left(1+\frac{1}{e^{\mp B\xi}-1}\right)\right] \tag{B.11}$$

(B.12)

The value of the functions C are developed in equation (B.15)-(B.13).

B.4 Notations introduced for approximate formulae

The different notations introduced for the derivation of approximate formulae are given below. The variable ξ is used in all simplified expressions, it is defined in an exponential form as follows:

$$e^{\xi} = \frac{r}{r_0}\frac{\left(l+\sqrt{l^2+r_0^2}\right)}{\left(l+\sqrt{l^2+r^2}\right)}\frac{\exp\left(\sqrt{l^2+r^2}/l\right)}{\exp\left(\sqrt{l^2+r_0^2}/l\right)} \tag{B.13}$$

The attention is drawn on the required factor $1/l$ in equation (B.13) if comparison is to be done with other references. From the exponential notation, the following relations holds and will be convenient to compare expressions in the literature:

$$e^{-\xi} = \frac{1}{e^{\xi}}, \qquad \log\left(1+\frac{1}{e^{\mp\xi}-1}\right) = -\log\left(1-e^{\pm\xi}\right) \tag{B.14}$$

The variables C_{0z} and C_{0r} are used in all approximate relations:

$$C_{0z} = \left(\frac{l^2+r_0^2}{l^2+r^2}\right)^{\frac{1}{4}}, \qquad C_{0r} = \frac{1}{l}\left[(l^2+r_0^2)(l^2+r^2)\right]^{\frac{1}{4}} \tag{B.15}$$

The variables with the index 1 are different between the expression of Lerbs and Wrench:

$$C_{1z} = \frac{l}{2}\frac{r_0^2}{(l^2+r_0^2)^{\frac{3}{2}}} \quad \text{(Lerbs)} \tag{B.16}$$

$$C_{1z} = \frac{l}{24}\left[\frac{9r_0^2+2l^2}{(l^2+r_0^2)^{\frac{3}{2}}} + \frac{3r^2-2l^2}{(l^2+r^2)^{\frac{3}{2}}}\right] \quad \text{(Wrench)} \tag{B.17}$$

$$C_{1r} = \frac{l}{24}\left[\frac{9r_0^2+2l^2}{(l^2+r_0^2)^{\frac{3}{2}}} + \frac{-9r^2-2l^2}{(l^2+r^2)^{\frac{3}{2}}}\right] \tag{B.18}$$

For comparison between the different expressions in the litterature it is good to note the relations given by equation (B.19) and (B.14) :

$$\frac{y}{y_0}\frac{\left(\sqrt{1+y_0^2}+1\right)}{\left(\sqrt{1+y^2}+1\right)} = \frac{y_0}{y}\frac{\left(\sqrt{1+y^2}-1\right)}{\left(\sqrt{1+y_0^2}-1\right)} = \left[\frac{\left(\sqrt{1+y^2}-1\right)\left(\sqrt{1+y_0^2}+1\right)}{\left(\sqrt{1+y^2}+1\right)\left(\sqrt{1+y_0^2}-1\right)}\right]^{\frac{1}{2}} \tag{B.19}$$

B.5 Summation of several helices - Link between Okulov's relation and Wrench's relation

Within a more general context, Okulov [145] derived approximate expression for the velocity field induced by one infinite helical filament at any location contrary to the work of Lerbs and Wrench which are specified on the lifting line only. In this paragraph the consistency between Okulov's and Wrench's relation is briefly shown, the motivation for this is threefold. First, it is not obvious that the sum over B helices of the approximate velocity field for one helix is equal to the approximation of the summed velocity field from B helices. Superposition of the Biot-Savart law is obvious, but

not if approximations are done. Second, some of the elements of demonstration can be useful in other context where summation over different blades are required (see e.g. [33, p . 212]). Last, the process of linking Okulov's and Wrench relation is an interesting exercise that helps revealing typographical errors that can be found in other references. Okulov's approximate relation for the velocity field induced by an infinite vortex filament is:

$$s\,\overline{u}_{z,\mathrm{Ok}}(r,\chi) = \frac{\Gamma_t}{2\pi l}\begin{Bmatrix}1\\0\end{Bmatrix} + \frac{\Gamma_t}{2\pi l} C_{0z}\,\mathrm{Re}\left[\frac{\pm e^{i\chi}}{e^{\mp\xi}-e^{i\chi}} - C_{1z,\mathrm{Wr}}\log\left(1-e^{\pm\xi+i\chi}\right)\right] \tag{B.20}$$

Below are presented the elements of the demonstration that show that Wrench's expressions can be obtained by summation of Okulov's approximate solution for one infinite vortex filament. Each of the B helical filaments is defined by $\chi_k = \frac{2k\pi}{B}$. The e^{χ_k} are roots of unity, and hence are roots of the polynomial $P_B(Z) = Z^B - 1 = \prod(Z - e^{i\chi_k})$. The first relation required for the demonstration is the following:

$$\sum_k \frac{e^{i\chi_k}}{Z - e^{i\chi_k}} = \sum_k \frac{e^{i\chi_k}\prod_{j\neq k}(Z-e^{i\chi_j})}{Z^B-1} = \frac{B}{Z^B-1} \tag{B.21}$$

To derive the second equality one can for instance notice that the numerator is a polynomial of degree $B-1$ in Z which has the same value on B different points, the $e^{i\chi_k}$. This value is found to be B by expressing the derivative of P_B on one of the root of unity. It follows that the numerator is the constant polynomial whose value is B. Another general relation required for the demonstration is readily obtained from the properties of the roots of unity:

$$\sum_k \log\left(1-Ze^{i\chi_k}\right) = \log\left(\prod_k\left(1-Ze^{i\chi_k}\right)\right) = \log\left(1-Z^B\right) = -\log\left(1+\frac{1}{Z^{-B}-1}\right) \tag{B.22}$$

Using equation (B.21) and (B.22) the consistency between Okulov's and Wrench's relation is easily shown and the typographical errors revealed.

Appendix C

Kutta-Joukowski theorem applied to a rotor with straight lifting lines

The current chapter presents the different formulae resulting from the application of the Kutta-Joukowski theorem to a wind turbine. The chapter mainly presents formulae without justifications. The actuator-disk case is treated in a separate section first. The case of rotors with finite number of straight lifting lines is treated next. The vortex actuator disk results are then obtained again as a limiting case of a rotor with an infinite number of straight lifting lines.

Notations A rotor with B blades is considered with each blade modelled with a straight lifting line (no coning or sweep). The circulation along each blade is $\Gamma_B(r)$, at the radial position r. $\boldsymbol{e}_\theta$ is positive around the axis z and defines the rotation of the turbine with clockwise convention. At a radial position r, the velocity normal and tangential to the lifting line are written without loss of generality $U_n = U_0(1-a_B)$ and $U_t = \Omega r(1+a'_B)$, where U_0 is the free stream velocity, Ω the rotor rotational speed, a the axial induction and a' the tangential induction. The subscript B is used to highlight the difference with the average induction factor. For an axisymmetric actuator disk, no distinction is to be made between the induction on a blade or the azimuthally averaged induction. The subscript "KJ" is used for Kutta-Joukowski relations, as opposed to the subscript "MT" and "BT" that used for momentum theory and Blade element momentum theory.

C.1 Vortex actuator disk

Actuator disk and velocity triangle The loads on the rotor are assumed to act solely on a disk surface. Axisymmetry of the loads, and conversely of the flow, is assumed. The coordinate system illustrated in figure 2.1 is adopted.

Kutta-Joukowski analysis (or Blade Element Theory without drag) The Kutta-Joukowski (KJ) relation and the velocity triangle on the rotor disk provides the local thrust $dT_{\mathrm{KJ}}(r)$, torque $dQ_{\mathrm{KJ}}(r)$, and power $dP_{\mathrm{KJ}}(r)$, which dimensionless coefficients are:

$$C_{t,\mathrm{KJ}}(r) \equiv \frac{dT_{\mathrm{KJ}}(r)}{\frac{1}{2}\rho U_0^2 2\pi r dr} = k(r)(1+a'(r)), \quad C_{q,\mathrm{KJ}}(r) \equiv \frac{dQ_{\mathrm{KJ}}(r)}{\frac{1}{2}\rho U_0^2 r 2\pi r dr} = \frac{\Gamma(r)}{\pi r U_0}(1-a(r)) \tag{C.1}$$

$$C_{p,\mathrm{KJ}}(r) \equiv \lambda_r C_{q,\mathrm{KJ}}(r) = k(r)(1-a(r)) \tag{C.2}$$

where

$$k(r) = \frac{\Omega\Gamma(r)}{\pi U_0^2}, \qquad \lambda_r \equiv \frac{\Omega r}{U_0} \tag{C.3}$$

and $\Gamma(r)$ is the rotor circulation. In the absence of drag, the coefficients obtained from this KJ-analysis are identical to the ones that would be obtained using the Blade Element Theory (BET) as introduced by Drzewiecki [61] (see e.g. [79]). This is further detailed in section C.2.1.

C.2 Kutta-Joukowski theorem for a rotor made of straight lifting lines

C.2.1 Kutta-Joukowski and velocity triangle - Local relations

The application of the Kutta-Joukowski theorem leads to:

$$\boldsymbol{U}_{\text{rel}} = U_n \boldsymbol{e}_z - U_t \boldsymbol{e}_\theta \tag{C.4}$$

$$\boldsymbol{\Gamma}_B = \Gamma_B \boldsymbol{e}_r \tag{C.5}$$

$$\boldsymbol{L} = \rho \boldsymbol{U}_{\text{rel}} \times \Gamma_B = \rho \Gamma_B \left(U_n \boldsymbol{e}_\theta + U_t \boldsymbol{e}_z \right) \tag{C.6}$$

$$\|\boldsymbol{L}\| = \rho \Gamma_B U_{\text{rel}} \tag{C.7}$$

$$C_l = \frac{\|\boldsymbol{L}\| dr}{\frac{1}{2}\rho U_{\text{rel}}^2 c dr} = \frac{2\Gamma_B}{c U_{\text{rel}}} \qquad \Rightarrow \quad \Gamma_B = \frac{1}{2} c U_{\text{rel}} C_l \tag{C.8}$$

$$dT_{\text{KJ}} = B\rho\Gamma_B U_t dr \quad \left(= \frac{1}{2}\rho (B c dr) U_{\text{rel}} U_t C_l \quad = dT_{\text{BT},L} \right) \tag{C.9}$$

$$dQ_{\text{KJ}} = B\rho\Gamma_B U_n r dr \quad \left(= \frac{1}{2}\rho (B c dr) r U_{\text{rel}} U_n C_l = dQ_{\text{BT},L} \right) \tag{C.10}$$

The expression in parenthesis in the last two equations shows the compatibility between the blade element theory result without drag and the Kutta-Joukowski formulation. Such compatibility is expected since a blade element analysis has been made when applying the Kutta-Joukowski relation on a elementary airfoil of span dr. Eventually, the local coefficients can be found from the above relation:

$$C_{t,\text{KJ}} \triangleq \frac{dT_{\text{KJ}}}{\frac{1}{2}\rho U_0^2 2\pi r dr} = \frac{B\Gamma_B U_t}{\pi r U_0^2} = \frac{B\Gamma_B \lambda (1 + a'_B)}{\pi R U_0} \qquad [\text{ - }] \tag{C.11}$$

$$C_{q,\text{KJ}} \triangleq \frac{dQ_{\text{KJ}}}{\frac{1}{2}\rho U_0^2 r 2\pi r dr} = \frac{B\Gamma_B U_n}{\pi r U_0^2} = \frac{B\Gamma_B (1 - a_B)}{\pi r U_0} \qquad [\text{ - }] \tag{C.12}$$

$$C_{p,\text{KJ}} \triangleq \frac{dP_{\text{KJ}}}{\frac{1}{2}\rho U_0^3 2\pi r dr} = \frac{B\Gamma_B \Omega U_n}{\pi U_0^3} = \frac{B\Gamma_B \lambda (1 - a_B)}{\pi R U_0} \qquad [\text{ - }] \tag{C.13}$$

Conversely the circulation along the blade can be obtained from the coefficients:

$$\Gamma_B = \frac{\pi R U_0}{B\lambda(1 + a'_B)} C_{t,\text{KJ}} \qquad [\text{ m}^2/\text{s }] \tag{C.14}$$

$$\Gamma_B = \frac{\pi r U_0}{B(1 - a_B)} C_{q,\text{KJ}} \qquad [\text{ m}^2/\text{s }] \tag{C.15}$$

$$\Gamma_B = \frac{\pi R U_0}{B\lambda(1 - a_B)} C_{p,\text{KJ}} \qquad [\text{ m}^2/\text{s }] \tag{C.16}$$

The ratios between the torque and thrust are:

$$\frac{dQ_{\text{KJ}}}{dT_{\text{KJ}}} = \frac{r U_n}{U_t} = \frac{(1 - a_B) R}{(1 + a'_B)\lambda} \qquad \text{and,} \qquad \frac{C_{q,\text{KJ}}}{C_{t,\text{KJ}}} = \frac{(1 - a_B)}{(1 + a'_B)\lambda_r} = \tan\phi \tag{C.17}$$

C.2.2 From local to rotor factors

From the local results of section C.2.1, the rotor parameters can be obtained by integration. The rotor coefficients are:

$$C_{T,\mathrm{KJ}} = \frac{2}{R^2}\int_0^R rC_{t,\mathrm{KJ}}dr = \frac{B\lambda}{\frac{1}{2}\pi R^3 U_0}\int_0^R \Gamma_B(1+a'_B)rdr \qquad [\text{ - }] \tag{C.18}$$

$$C_{Q,\mathrm{KJ}} = \frac{2}{R^3}\int_0^R r^2C_{q,\mathrm{KJ}}dr = \frac{B}{\frac{1}{2}\pi R^3 U_0}\int_0^R \Gamma_B(1-a_B)rdr \qquad [\text{ - }] \tag{C.19}$$

$$C_{P,\mathrm{KJ}} = \frac{2}{R^2}\int_0^R rC_{p,\mathrm{KJ}}dr = \frac{B\lambda}{\frac{1}{2}\pi R^3 U_0}\int_0^R \Gamma_B(1-a_B)rdr \qquad [\text{ - }] \tag{C.20}$$

are the corresponding rotor loads:

$$T_{\mathrm{KJ}} = B\rho\int_0^R \Gamma_B\Omega r(1+a'_B)dr \qquad [\text{ N }] \tag{C.21}$$

$$Q_{\mathrm{KJ}} = B\rho\int_0^R \Gamma_B U_0(1-a_B)rdr \qquad [\text{ Nm }] \tag{C.22}$$

$$P_{\mathrm{KJ}} = B\rho\Omega\int_0^R \Gamma_B U_0(1-a_B)rdr \qquad [\text{ W }] \tag{C.23}$$

The relations above can also be presented using an integration over λ_r.

C.2.3 Application for infinite number of blades

Results for an actuator disk are presented in section C.1. There are here obtained as a limiting case of the case presented in section C.2.1. The limit of infinite number of blades implies:

$$\Gamma_\infty = \lim_{B\to\infty} B\,\Gamma_B \tag{C.24}$$

$$Bc \xrightarrow[B\to\infty]{} 2\pi r \tag{C.25}$$

$$a_B \xrightarrow[B\to\infty]{} a \tag{C.26}$$

Combining the two first expressions, it is possible to use finite number of blades analysis in a non rigorous way to go directly to infinite number of blades by using the following relations:

$$B = \frac{2\pi}{\delta\theta} \tag{C.27}$$

$$\Gamma_B = \Gamma_\infty\frac{\delta\theta}{2\pi} \tag{C.28}$$

These equations smear out the discretization over the entire disc.

The definition of lift and C_l becomes unphysical for infinite number of blades, it should be taken with care.

$$C_l = \frac{\|\boldsymbol{L}\|dr}{\frac{1}{2}\rho U_{\mathrm{rel}}^2 cdr} = \frac{2\Gamma_B}{cU_{\mathrm{rel}}} \qquad \Rightarrow \qquad \Gamma_B = \frac{1}{2}cU_{\mathrm{rel}}C_l \tag{C.29}$$

$$dT_{\mathrm{KJ}} = \rho B\Gamma_B U_t dr \xrightarrow[B\to\infty]{} dT_{\mathrm{KJ},\infty} = \rho\Gamma_\infty U_t dr \qquad [\text{ N }] \tag{C.30}$$

$$dQ_{\mathrm{KJ}} = \rho B\Gamma_B U_n r dr \xrightarrow[B\to\infty]{} dQ_{\mathrm{KJ},\infty} = \rho\Gamma_\infty U_n r dr \qquad [\text{ Nm }] \tag{C.31}$$

$$dP_{\mathrm{KJ}} = \rho B\Gamma_B U_n\Omega r dr \xrightarrow[B\to\infty]{} dP_{\mathrm{KJ},\infty} = \rho\Gamma_\infty U_n\Omega r dr \qquad [\text{ Nm/s }] \tag{C.32}$$

The dimensionless coefficients are then:

$$C_{t\mathrm{KJ},\infty} \triangleq \frac{dT_{\mathrm{KJ},\infty}}{\frac{1}{2}\rho U_0^2 2\pi r dr} = \frac{\Gamma_\infty U_t}{\pi r U_0^2} = \frac{\Gamma_\infty \lambda(1+a'_B)}{\pi R U_0} \quad [\text{ - }] \tag{C.33}$$

$$C_{q\mathrm{KJ},\infty} \triangleq \frac{dQ_{\mathrm{KJ},\infty}}{\frac{1}{2}\rho U_0^2 r 2\pi r dr} = \frac{\Gamma_\infty U_n}{\pi r U_0^2} = \frac{\Gamma_\infty (1-a_B)}{\pi r U_0} \quad [\text{ - }] \tag{C.34}$$

$$C_{p\mathrm{KJ},\infty} \triangleq \frac{dP_{\mathrm{KJ},\infty}}{\frac{1}{2}\rho U_0^3 2\pi r dr} = \frac{\Gamma_\infty \Omega U_n}{\pi U_0^3} = \frac{\Gamma_\infty \lambda(1-a_B)}{\pi R U_0} \quad [\text{ - }] \tag{C.35}$$

And these expressions can be used to express the circulation as:

$$\Gamma_\infty = \frac{\pi R U_0}{\lambda(1+a'_B)} C_{t\mathrm{KJ},\infty} \quad [\text{ m}^2/\text{s }] \tag{C.36}$$

$$\Gamma_\infty = \frac{\pi r U_0}{(1-a_B)} C_{q\mathrm{KJ},\infty} \quad [\text{ m}^2/\text{s }] \tag{C.37}$$

$$\Gamma_\infty = \frac{\pi R U_0}{\lambda(1-a_B)} C_{p\mathrm{KJ},\infty} \quad [\text{ m}^2/\text{s }] \tag{C.38}$$

The ratios between the torque and thrust are:

$$\frac{dQ_{\mathrm{KJ},\infty}}{dT_{\mathrm{KJ},\infty}} = \frac{rU_n}{U_t} = \frac{(1-a_B)R}{(1+a'_B)\lambda} \quad \text{and,} \quad \frac{C_{q\mathrm{KJ},\infty}}{C_{t\mathrm{KJ},\infty}} = \frac{(1-a_B)}{(1+a'_B)\lambda_r} \tag{C.39}$$

The same results can be obtained using a discrete number of blades analysis together with the smearing relations equation (C.27) and (C.28). It is interesting to detail a little, the different way of seeing the loading though it doesn't bring additional information to the above analysis. The total force in an annulus, if concentrated on B blade is

$$dT = Bk_n dr \tag{C.40}$$

where k_n is a linear force in [N/m], homogeneous with convention used in this document for the lift term L. In this case k_n is equal to $\rho\Gamma_B U_t$ from the Kutta-Joukowski relation. Which can be averaged as a pressure term (surface force in [N/m2]) over an annulus as:

$$p_n(r) = \frac{dT}{2\pi r dr} = B\frac{k_n}{2\pi r} \quad \Rightarrow \quad Bk_n = 2\pi r p_n \tag{C.41}$$

$$p_n(r) = \frac{2\pi}{\delta\theta}\frac{\rho\Gamma_B U_t}{2\pi r} = \frac{2\pi}{\delta\theta}\frac{\rho\Gamma_\infty \delta\theta U_t}{2\pi\cdot 2\pi r} = \frac{\rho\Gamma_\infty U_t}{2\pi r} \tag{C.42}$$

The local thrust coefficient can be found by dividing this pressure force by the dynamic pressure $\frac{1}{2}\rho U_0^2$:

$$C_t = \frac{p_n}{\frac{1}{2}\rho U_0^2} = \frac{\Gamma_\infty U_t}{U_0^2 \pi r} \tag{C.43}$$

C.2.4 BET without drag and Joukowski - Finite and infinite number of blades

It has been seen in section C.2.1 that the BET without drag and the KJ formulation are compatible since they are both based on 2D blade element analysis. To go from one formulation to the other one uses the following relation:

$$\Gamma_B = \frac{1}{2} c U_{\mathrm{rel}} C_l \tag{C.44}$$

If a meaning can be given to the lift coefficient with an infinite number of blade, then an expression for the circulation can be found by multiplying the above relation by B and going to the limit:

$$\Gamma_B = \frac{1}{2} c U_{\mathrm{rel}} C_l \quad \xrightarrow[B\to\infty]{} \Gamma_\infty = \pi r U_{\mathrm{rel}} C_l \tag{C.45}$$

C.2.5 Specific cases with High λ

High λ Assuming high λ, or more precisely $a' << 1$, then, $\boldsymbol{U}_t \approx \Omega r = \lambda_r U_0$ and the Kutta-Joukowski formulation writes:

$$dT_{\mathrm{KJ}}(r) \approx B\rho\Gamma_B(r)\boldsymbol{U}_0\lambda_r dr \quad \left(= \frac{1}{2}\rho(Bcdr)U_{\mathrm{rel}}U_0\lambda_r C_l\right) \tag{C.46}$$

$$C_{t\mathrm{KJ}}(r) \approx \frac{B\lambda\Gamma_B(r)}{\pi R U_0} \quad \Rightarrow \quad \Gamma_B(r) \approx \frac{\pi R\boldsymbol{U}_0}{\lambda} C_{t\mathrm{KJ}}(r) \tag{C.47}$$

$$T_{\mathrm{KJ}} \approx B\rho \int_0^R \Gamma_B(r)\Omega r dr \tag{C.48}$$

For high λ : constant circulation along the blade is equivalent to constant local thrust coefficient that is $C_T = C_t$. The case of constant circulation will be presented in a separate paragraph below. For high λ the pitch of the wake helix should for to zero.

High λ - Infinite number of blades

$$dT_{\mathrm{KJ},\infty}(r) \approx \rho\Gamma_\infty(r)\boldsymbol{U}_0\lambda_r dr \quad \left(= \frac{1}{2}\rho(2\pi r dr)U_{\mathrm{rel}}U_0\lambda_r C_l\right) \tag{C.49}$$

$$C_{t\mathrm{KJ},\infty}(r) \approx \frac{\lambda\Gamma_\infty(r)}{\pi R U_0} \quad \Rightarrow \quad \Gamma_\infty(r) \approx \frac{\pi R\boldsymbol{U}_0}{\lambda} C_{t\mathrm{KJ},\infty}(r) \tag{C.50}$$

$$T_{\mathrm{KJ},\infty} \approx B\rho \int_0^R \Gamma_\infty(r)\Omega r dr \tag{C.51}$$

High λ - Constant circulation along the blade

$$dT_{\mathrm{KJ}}(r) \approx B\rho\Gamma_B\boldsymbol{U}_0\lambda_r dr \quad \left(= \frac{1}{2}\rho(Bcdr)U_{\mathrm{rel}}U_0\lambda_r C_l\right) \tag{C.52}$$

$$C_{t\mathrm{KJ}} \approx \frac{B\lambda\Gamma_B}{\pi R U_0} \quad \Rightarrow \quad \Gamma_B \approx \frac{\pi R\boldsymbol{U}_0}{B\lambda} C_{t\mathrm{KJ}} \tag{C.53}$$

$$T_{\mathrm{KJ}} \approx B\frac{1}{2}\rho R^2\Gamma_B\Omega \tag{C.54}$$

$$C_T = C_t \tag{C.55}$$

High λ - Constant circulation and infinite number of baldes

$$dT_{\mathrm{KJ},\infty}(r) \approx \rho\Gamma_\infty\boldsymbol{U}_0\lambda_r dr \quad \left(= \frac{1}{2}\rho(2\pi r dr)U_{\mathrm{rel}}U_0\lambda_r C_l\right) \tag{C.56}$$

$$C_{t\mathrm{KJ},\infty} \approx \frac{\lambda\Gamma_\infty}{\pi R U_0} \quad \Rightarrow \quad \Gamma_\infty \approx \frac{\pi R\boldsymbol{U}_0}{\lambda} C_{t\mathrm{KJ},\infty} \tag{C.57}$$

$$T_{\mathrm{KJ},\infty} \approx \frac{1}{2}\rho R^2\Gamma_\infty\Omega \tag{C.58}$$

$$C_T = C_t \tag{C.59}$$

Appendix D

Vortex theory for rotors: Helical wake, optimal circulation, tip-losses and wake expansion

The current chapter presents applications of vortex theory to rotors. Vortex theory was in particular applied at the beginning of the 19^{th} century to study optimal rotors and tip-losses. The historical developments are presented here and complemented by recent work of the author on the topic. In particular, the author investigated tip-losses using helical filaments model with and without expansion and wake roll-up. Part of these results were published in the two following references: **[28]**, **[22]**. The current chapter, focuses on the historical development and additional details and results from the author.

D.1 Introduction

D.1.1 Birth of the tip-loss factor

Tip-losses commonly refers to kinematic and/or dynamic differences between a two-dimensional and a three dimensional configuration of a lifting device. The main source of these differences for a wing of finite span or for a rotating device of finite number of blades is the circulation flow driven by the pressure equalization which arises at the tip of the lifting device. Prandtl used vortex theory analysis to assess the proportion of these losses for both a wing [162] and a propeller blade [161] at the beginning of the 20^{th} century. The latter study was introduced as a correction factor to be applied to Betz's optimal circulation [16] extending the applicability of Betz's result from an infinite to a finite number of blades. Prandtl's simplified model consider the axi-symmetric wake flow about a series of semi-infinite rigid lines. Glauert [71] suggested a modification to Prandtl's tip-loss factor for a convenient numerical implementation and it is his model which has been retained to this day in most BEM codes. It is worth mentioning that different variations of tip-loss factors are found in the literature: in [117, 173] empirical modifications are found, in [34, 79] the term "Prandtl's tip-loss factor" is used in Glauert's sense, and in [133] the result used is a special case (no tangential induction) of Glauert's factor. A review of the different expressions of the tip-loss factor is found in **[28, 20]**.

D.1.2 Tools provided by vortex theory

In collaboration with the German school, Goldstein [72] solved in 1929 the exact potential flow surrounding an ideal wake screw surface. The computational expense of his solution was removed thanks to the development of approximate solution of the flow field induced by equidistant infinite helical vortex filaments as done by Lerbs [115] in 1952 and further refined by Wrench [223] in

1957. In a similar way, Okulov [145] derived such approximate solution and used it to compute Goldstein's factor [150]. Design of propellers and wind turbines can be attempted using these helical solutions. Two shortcomings of the theoretical work of Betz, Prandtl and Goldstein are that they were undertaken as far-wake analysis and tacitly for light loading. In 1948, Theodorsen [203] presented an approach to extend the applicability of Goldstein's factor to heavy loading, relating far-wake and rotor parameters and deriving expressions for wake expansion/contraction. A different way to relate far-wake and near wake parameters was used by Okulov et al. [150] to comply with momentum theory results. In numerical applications, vortex theory gives rise to the development of different vortex codes which can described effects such as complex wake distortion contrary to analytical derivations.

D.1.3 Further studying tip losses

Recently, a free wake lifting-line code (see e.g. **[20]**, **[27]**) was used to derive tip-loss corrections accounting for wake expansion, roll-up and distortion, and applicable to a wide range of operation conditions contrary to Prandtl's tip-loss factor. The present study will make use of analytical vortex results to derive a new analytical tip-loss factor and various numerical counterparts and study the influence of wake expansion on tip-losses.

This study is organized in different sections that build up successively to ultimately enable the computation of tip-loss factors using analytical, semi-analytical and wake models. A large proportion of the chapter is dedicated to describe the tools and theory used. In a first time, the original definition of the tip-loss factor is presented together with different modern definitions that were thought and established within the context of vortex theory but are not restricted to it. Simple vortex filament analysis are presented since they helped establish the new analytical and numerical tip-loss factors derived in this study. The new analytical tip-loss factor relies an analytical approximate formulae which are presented in the third section of this chapter. The different wake models used to compute the tip-loss factor are described in a fourth section. Theodorsen's wake expansion being used by some prescribed wake models, relation between near-wake and far-wake parameters will be required and it will be the purpose of the fifth section to explain how they can be obtained. Last, analysis of the different tip-loss factors obtained with the different methods are performed.

D.2 From optimal distribution of circulation to a modern interpretation of tip-losses

Far wake analyses Far wake theories applies under the assumptions of inviscid and irrotational flow and they rely on the fact that there is a direct relation between the loading and hence the circulation at the lifting device and the momentum in the wake. All theoretical derivations concerning tip-losses are based on far wake considerations. The motivations for such analysis is that the flow is more complicated in the near wake due to the interaction with blades, boundary layers at the blade and separation effects. These effects dissipates and are thus no more present in the far wake. Moreover, the chord is left as a secondary consideration. The conceptual plane in the far wake perpendicular to the upstream velocity is called the Trefftz plane. By using a variational method on the velocity potential, Munk [144] derived the classical results of elliptical lift distribution which induces the minimum drag, results obtained earlier by Prandtl using a lifting line approach.

D.2.1 Far-wake analysis: the distribution of optimal circulation

In 1919, following an analogous far wake analysis to the one of Munk [144], Betz derived the optimum circulation distribution which minimizes the power losses for a propeller rotor with a *very large* number of blades [16]. To this end he calculated the thrust and power in the far wake and minimized the power for variations of the circulation. This yielded to the condition of the flow being locally perpendicular to the wake surface. The optimal circulation is obtained for this flow condition at any radial position by integrating the azimuthal velocity along a path surrounding the propeller axis. For this optimal condition the flow in the far-wake is the same *as if* the vortex surface formed by the trailing vortices was an impermeable rigid helix of constant pitch that translated downstream with a constant velocity w. In the propeller case, this velocity is oriented in the stream direction going away from the rotor, whereas for wind turbines, w is pointing towards the rotor. This analysis was performed under the assumption of lightly-loaded rotor. Betz referred to it as the "rigid-wake" condition but the flow itself does not follow a rigid rotation nor a rigid translation but has an axial and an azimuthal component. It should be noted that w is the apparent velocity of translation of the wake, an elementary wake surface at radius r would move at a velocity $w\cos\epsilon(r)$.

The assumption of infinite number of blades deserves a bit of attention regarding the definition of the circulation. If $\Gamma_B(r)$ designs the circulation around one blade at radius r, then the circulation for an infinite number of blade is

$$\Gamma_\infty(r) = \lim_{\substack{B\to\infty \\ \Gamma_B\to 0}} B\cdot\Gamma_B(r) \tag{D.1}$$

and the above limit is assumed to be finite. In the general case, the boundary conditions on the "rigid wake" writes [20]:

$$u_{z,w} = w\frac{V_t^2}{V_n^2+V_t^2} \tag{D.2}$$

$$u_{\theta,w} = w\frac{V_nV_t}{V_n^2+V_t^2} \tag{D.3}$$

Integrating the tangential velocity along a circle of radius r gives Betz's optimum circulation:

$$\Gamma_\infty(r) = \int_0^{2\pi} u_{\theta,w}rd\theta = 2\pi r u_{\theta,w} = 2\pi\frac{wV_n}{\Omega}\frac{V_t^2}{V_n^2+V_t^2} \tag{D.4}$$

Assuming this results apply for a rotor with B blades then the circulation of each blade is:

$$\Gamma_{\mathrm{Be}} = \frac{\Gamma_\infty}{B} = \frac{2\pi}{B}\frac{wV_n}{\Omega}\frac{V_t^2}{V_n^2+V_t^2} \tag{D.5}$$

which writes in dimensionless form:

$$C_{\Gamma_{\mathrm{Be}}} = \left(\frac{V_t}{\Omega r}\right)\frac{V_t^2}{V_n^2+V_t^2} \tag{D.6}$$

In the special and historical case of $V_t=\Omega r$ and $V_n=U_0$, i.e. using the simplified helix angle $\tan\epsilon = V_n/V_t = 1/\lambda_r$, the Betz circulation reduces to:

$$\Gamma_{\mathrm{Be},0} = \frac{2\pi}{B}\frac{wU_0}{\Omega}\frac{\lambda_r^2}{1+\lambda_r^2} \tag{D.7}$$

and in dimensionless form:

$$C_{\Gamma_{\mathrm{Be},0}} = \frac{\lambda_r^2}{1+\lambda_r^2} \tag{D.8}$$

More details can be found in [20]

D.2.2 Historical tip-loss factor

As a discussion following the work of Betz [161], Prandtl derived an approximate correction to account for rotors with finite number of blades. Figure D.1 is used in the following to illustrate the argumentation of Prandtl. In the case of the "rigid-wake" motion (a), which is the condition derived by Betz for optimal loading, the air going through the rotor's swept area stays within the boundary of the wake helix, there is no radial flow nor expansion of the wake. Outside the wake, the velocity is equal to the free-stream velocity. Neglecting the rotational component within the wake, this flow pattern can be approximated by straight vortex lines, infinitely close to each other in between which the air stays confined. One can assume that for an optimal propeller with finite number of blades, the wake can be approximated by straight lines further apart(c), in which case the flow will no longer stay confined between the lines. Prandtl considers that the proportion of which the flows varies from (c) to (b) is the same as from (d) to (a). Further, this proportion can be assumed to be a simple multiplicative factor. A detailed derivation and generalization of Prandtl's tip-loss factor can be found in **[20]**.

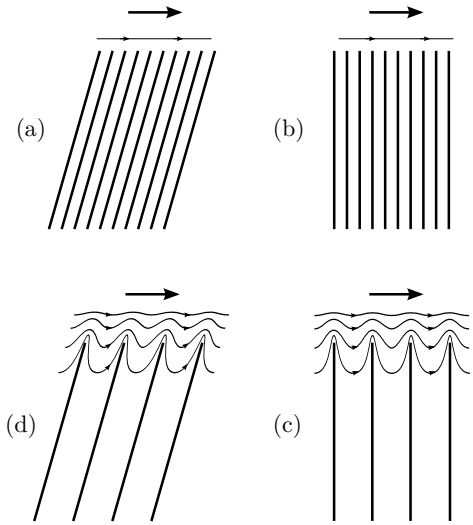

Figure D.1: Prandtl's interpretation of tip-losses. Betz's optimal rigid-wake for a very large number of blade(a) and Prandtl's interpretation for very large (b) and small (c) number of blades. Figure (d) is the representation of the flow pattern expected for a helical wake with finite number of blades

Prandtl's correction factor can be used to relate parameters from the optimal condition of Betz to a case where the number of blades is finite. The loss of loading between infinite number of blades and finite number of blades is referred as tip-losses and the correction factor called the tip-loss factor is usually noted F. In the derivation of the factor F, it is assumed that the velocity just outside the wake is the free-stream velocity (see **[20]**). This enforces that the factor F goes to zero at the tip of the wake. By multiplying the optimal circulation from Betz by this factor, the circulation will also go to zero at the tip. Nevertheless, the physical interpretation of Prandtl's tip-loss factor should not be pushed beyond the approximation context in which it was derived. The problem assumes axisymmetry and that the free stream velocity is reached at the tip of the wake, which is only the case paradoxically for infinite number of blades or infinite tip-speed ratios.
Prandtl's tip-loss factor and the many variations found in the litterature as listed in **[20]** can be written in the form:

$$F_{\mathrm{Pr}} = \frac{2}{\pi} \operatorname{acos} \exp\left[-f\right] \tag{D.9}$$

where f is a factor that would generally tends toward zero at the tip of the blade. Prandtl introduced this factor to compute the circulation on the blade Γ_B as function of the optimal circulation of Betz Γ_∞. In this context, a definition of tip-loss factor could be:

$$F_\Gamma = \frac{\Gamma_B}{\Gamma_\infty} \tag{D.10}$$

From this definition, it is then possible to compute Goldstein's tip-loss factor, by using Goldstein's circulation solution as Γ_B. A complement on the computation of Goldstein's factor are found in section D.8.2 and in [20]. Figure D.2 illustrates the different circulation functions and tip-loss functions from the work of Betz, Prandtl and Goldstein for different tip-speed ratios.

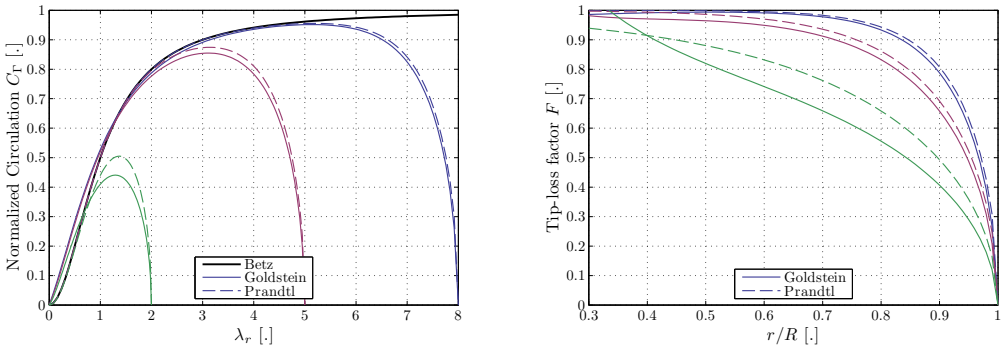

Figure D.2: Comparison between Betz, Prandtl and Goldstein theory for a three bladed rotor. (a) Normalized Circulation - (b) Tip-loss factor. The colors represent the different values of tip speed ratio taken: 2,5 and 8. The computation of Goldstein's factor is done using Okulov's method. The link used between the tip-speed ratio and the helical pitch is: $h = 2\pi R/\lambda$.

D.2.3 Modern definitions of the tip-loss factors

Let us assume that the entire flow field is known for a given rotor with B blades at a given operating condition. Such flow field can be obtained with vortex methods or other computational fluid dynamics methods. It will be further assumed that the flow field is also known in the case of a very large number of blades. The configuration with very large number of blades, considered as an infinite number of blades, does not present any tip-losses since the rotor can be modelled as an actuator disk. A tip-loss factor can thus be derived as the ratio between the induced velocity found on a blade for the case of an infinite number of blades, to the equivalent value found for a finite number of blades. Such ratio can be computed for both the axial and tangential velocities or similarly for their corresponding induction factors a and a', leading to the definition of the two following tip-loss factors:

$$F_a = \frac{a_\infty}{a_B} \tag{D.11}$$

$$F_{a'} = \frac{a'_\infty}{a'_B} \tag{D.12}$$

In the above, the ∞-subscript refers to the case of an infinite number of blades. This definition will be referred to as the natural definition of the tip-loss factor. As used in some BEM codes implementations, the tip-loss factor can also represent the proportion in which the axial induction

at the blades differs from the momentum theory value. The momentum value is sometimes seen as a average value over an annulus. From this perspective another definition of tip-losses can be established as e.g. in [185]. This tip-loss factor will be referred to as the planar tip-loss factor and will be defined as the ratio between the average induction in a circular annulus to the one on the blade, namely:

$$F_{\langle a \rangle} = \frac{\langle a \rangle_\theta}{a_B} \tag{D.13}$$

$$F_{\langle a' \rangle} = \frac{\langle a' \rangle_\theta}{a'_B} \tag{D.14}$$

In the above, the brackets refer to the azimuthal average in an annulus defined between the radii r and $r + dr$:

$$\langle \bullet \rangle_\theta = \frac{1}{2\pi} \int_0^{2\pi} \bullet \, r d\theta \tag{D.15}$$

D.3 Vortex representation of the wake

D.3.1 Classical wing theory applied to rotors

In the case of a non-optimal rotor, Betz's condition of an helical wake of constant pitch does not hold. A classical results of vortex wing theory in application of Helmotz theorem is that changes in bound circulation along the blade will result in vorticity being trailed in the wake. Unless the circulation is constant along the span, a continuous sheet of vorticity is trailed behind the blade. The strength per unit of length of the trailed vorticity is directly equal to the opposite of the bound circulation's gradient which writes:

$$\Gamma_t(r) = -\frac{\partial \Gamma(r)}{\partial r} dr \qquad [\ \mathrm{m}^2/\mathrm{s}\ ] \tag{D.16}$$

As a result of this, the strength of the vortex sheet increases towards the wing extremities where the circulation gradient is expected to be the highest. These higher intensities of trailed vorticity at the tip will induce a roll-up of the wake into a concentrated tip-vortex. Prandtl neglected this roll-up to develop his lifting-line theory where the wing was modelled as a superposition of horseshoe vortices laying on the wing and expending towards infinity. Extending Prandtl's lifting line theory from wings to rotors consists in using horseshoe vortices that are prescribed to follow an helical path. In the following, both prescribed and free wake analysis will be performed to study tip-losses. The problem of solving the flow for a given rotor is non-linear since the wake geometry depends on the induced velocities which are generated by the wake. For free-wake methods this problem is solved by time-convergence, while in prescribed wake methods a relation has to be found between the flow at the rotor and the wake geometry and an iterative algorithm should be used. Such relation will be presented in appropriate sections.

D.3.2 Vortex filament analysis leading to preliminary considerations

By using a vortex filaments analysis of the wake, three important results can be obtained in light of the study of tip-losses. While the second result is used extensively in vortex theory, the first and third results are established and used for the first time to the authors' knowledge. It will be seen in section B.1 that convenient approximate analytical solutions for infinite helical filaments exist. Nevertheless, by applying Prandtl's lifting line theory to rotors the wake would be made of semi-infinite helices and not infinite helices. The second and third result below help relating analytical relations for infinite and semi-infinite helices.

First result: equality between the natural and planar tip-loss factor In the case of an axi-symmetric wake and by assuming that the wake shape is the same for any number of blades, the natural tip-loss factor and the planar tip-loss factors are the same. These assumptions are satisfied in particular in the case of a non-expanding wake consisting in different trailed helices. This result can easily be proven analytically but is similarly obtained by a simple reasoning. Figure 3.1 illustrates the following. Let us consider the case of one blade with circulation Γ and its corresponding case of B blades, which by conservation of circulation will each have the circulation Γ/B. The system of trailed vortices between the two cases will also have a factor $1/B$ between their intensities. Now let us consider an elementary trailed vortex filament belonging to the wake of the single bladed case and the B corresponding elements from the B bladed case which are actually obtained from the former by B successive rotation of angle $2\pi/B$ around the rotor axis. It is easily seen that the sum of the contribution of the B azimuthal elements with intensity scaled by $1/B$ on one control point on the blade is equal to the average contribution from one element with full intensity on B different azimuthal positions. This demonstration is easily extended to an infinite number of blades and azimuthal control points by using integrals instead of summations and limits instead of direct circulation intensity.

Second result: Infinite and semi-infinite helical filaments By considering an infinite helix, any plane perpendicular to it would slice the helix in two semi-infinite helices. The induced velocities generated by the two semi-helices are the same on the radial line supporting the helix in the slicing plane but also symmetric with respect to that line. As a result of this the induced velocities on the radial line supporting the semi-infinite helix are half the one obtained with an infinite helix.

Third result: Infinite and semi-infinite helical filaments - average value The azimuthal average of the induced velocities on a plane perpendicular to the helix axis and from which a semi-infinite helix is emitted is half the value found for an infinite helix. This is found from a similar analysis as the previous paragraph due to the symmetry of the induced velocities with respect to the radial line supporting the helix. This result can also be derived more formally by considering for instance two elementary elements at equal distance to the slicing plane and use the parity of the induced velocity function in the longitudinal coordinate and its 2π-periodicity without actually making explicit the induced velocity function.

D.4 Relation between far wake and near wake parameters

Since most vortex theory results are obtained using far-wake analysis, the problem of relating far-wake parameters to near-wake parameters has to be solved. If such relation is known the computation of the Goldstein's circulation that corresponds to a given operating condition of a rotor could be computed. This circulation could then be prescribed to the rotor for further studies. Historical developments from Prandtl and Goldstein for low-loading and small expansion used the simple relation $\bar{l} = 1/\lambda$ to defined the pitch of the wake screw surface, while the wake displacement velocity w remains a parameter that is expected to vary with the thrust coefficient. Theodorsen [203] extended Goldstein's analysis for high loading and wake expansion. Theodorsen's system of equations is recursive and requires iterations to determine the far-wake parameters. By use of charts, table and rule of thumbs the expenses was circumvented by Theodorsen. The iterative procedure required to solve Theodorsen's set of equation will be made explicit in section D.4.2, while the different approach suggested by Okulov and Sørensen will be presented in section D.4.1. In the strict sense, both methods only applies for the condition of a rotor with ideal load distribution. In such case, according to Theodorsen, the far wake can be modelled as helical vortex sheets that

translates without deformation. Outside of this frame of validity, and in particular for high loading, the mathematical model of helical sheet becomes inadequate and the far-wake parameters abstruse. Nevertheless, since far-wake parameters will be solely used in this study to compute Theodorsen's far-wake expansion, deviations from the range of validity can be granted within the context of this study.

D.4.1 Extension of the work of Okulov and Sørensen for non-optimal condition

In a first article [149], Okulov and Sørensen presented rotor parameters as function of the far wake helix dimensionless pitch $\bar{l}$. Indeed, for a given value of $\bar{l}$, Goldstein's factor is known and they derived an optimal value for $\overline{w}$ that leads to the optimal power coefficient. In a following article [150] the authors assumed the equality between the far wake and near wake pitch of the wake helix, and from that derived the link between the tip-speed ratio λ, the far-wake dimensionless pitch $\bar{l}$ and the dimensionless helix velocity $\overline{w}$ as follows:

$$\lambda = \frac{1}{\bar{l}}\left(1 - \frac{\overline{w}}{2}\right) \tag{D.17}$$

Though the context of applicability is strictly the optimal operational regime, one can use the same assumption than the authors and derive an iterative procedure to compute the far-wake parameters corresponding to a given operation condition $(\lambda_d, C_{T,d})$. The procedure is as follow:

1. Guess an initial value for $\overline{w}$ using for instance the following semi-empirical relation inspired by 1D momentum theory:
$$\overline{w} = 0.6\ (1 - \sqrt{1 - C_{T,d}}) \tag{D.18}$$
2. Compute $\bar{l}$ using equation (D.17)
3. Compute Goldstein's factor for the given value of $\bar{l}$ and number of blades, using for instance Okulov's method [149].
4. Compute the two integral I_1 and I_3. I_1 is referred to as the mass coefficient and will also be further written κ.
$$I_1 = 2\int_0^1 G(x, \bar{l}, B) x dx = \kappa \tag{D.19}$$
$$I_3 = 2\int_0^1 G(x, \bar{l}, B) \frac{x^3}{\bar{l}^2 + x^2} dx \tag{D.20}$$
5. Eventually compute the thrust coefficient as:
$$C_T = 2\overline{w}\left(I_1 - \frac{\overline{w}}{2} I_3\right) \tag{D.21}$$
6. Repeat step 2 till convergence between the value C_T and the design value $C_{T,d}$.

At the end of the iterative process the far-wake parameters $(\overline{w}, \bar{l})$ corresponding to the operating condition (λ, C_T) are known. Examples of the relation between such parameters obtained with this iterative procedure are found in table D.1.

D.4.2 Iterative application of Theodorsen's theory

Theodorsen's results are function of the far wake parameters $(\bar{l}, \overline{w})$ but also of the thrust coefficient in the far wake c_t. If these three parameters are known, the complete set of equations

Table D.1: Far wake parameters obtained using the current iterative procedure

Case	$\mathbf{C_T}$	λ	$\mathbf{1/\bar{l}}$	$\overline{\mathbf{w}}$
1	0.8	12	17.4	0.62
2	0.8	9	13.4	0.65
3	0.7	9	12.2	0.53
4	0.7	8	11.0	0.54
5	0.7	7	9.7	0.56
6	0.7	6	8.5	0.58
7	0.6	7	9.1	0.45
8	0.3	5	5.6	0.23
9	0.1	3	3.2	0.10

from Theodorsen's work, including wake expansion can be computed. For his design methodology, Theodorsen's uses a rule of thumb to determine the thrust coefficient in the far wake. He further justifies his approximation by the balancing effect between expansion and drag losses. For further precision, and since no rule of thumb is mentioned for wind turbines, a doubly-iterative procedure has been implemented for this study. This procedure differs from Wald's procedure which uses a different wake expansion formulation, and, as formulated in [218], does not make explicit the iterative process required for the rotor and far-wake thrust coefficient to be consistent with the wake expansion.
The operating condition of the rotating device, (C_T, λ) are assumed given. The iterative procedure to determine the far-wake parameters that corresponds to this operating point is as follow:

1. Guess the far wake radius as infinity using a momentum/mass conservation analysis using equation (D.36).

2. Compute far wake coefficients

$$c_{t,d} = C_T \frac{R^2}{R_w^2} \tag{D.22}$$

$$c_{p,d} = C_P \frac{R^2}{R_w^2} \tag{D.23}$$

3. Find the value of $\overline{w}$ that gives the proper far-wake thrust or power coefficient through an optimization process:

   (a) Guess an initial value for $\overline{w}$ either from previous step or from an semi-empirical result inspired by momentum-theory: $\overline{w} \approx 0.6(1 - \sqrt{1 - CT})$

   (b) Compute the dimensionless torsional parameter:

$$\bar{l} = \frac{1}{\lambda}(1 - \overline{w})\frac{R}{R_w} \tag{D.24}$$

   (c) For the couple of far wake parameters $(\bar{l}, \overline{w})$ compute the mass coefficient κ and the axial loss factor ϵ_z defined by:

$$\kappa = 2\int_0^1 G(x, \bar{l}, B)dx \tag{D.25}$$

$$\frac{\epsilon_z}{\kappa} = 1 + \frac{1}{2}\frac{\bar{l}}{\kappa}\frac{d\kappa}{d\bar{l}} \tag{D.26}$$

$$\epsilon_z = \frac{\epsilon_z}{\kappa}\kappa \tag{D.27}$$

Several operational points around the desired value of $\bar{l}$ can be used to determine the derivative involved.

(d) The far wake coefficients are obtained through:

$$c_t = 2\kappa\overline{w}\left(1+\overline{w}\left(\frac{1}{2}+\frac{\epsilon}{\kappa}\right)\right) \tag{D.28}$$

$$c_p = 2\kappa\overline{w}\left(1+\overline{w}\right)\left(1+\frac{\epsilon}{\kappa}\overline{w}\right) \tag{D.29}$$

(e) Go back to step (b) with a new value of $\overline{w}$ until the far wake coefficients reach the desired value $c_{t,d}$ or $c_{p,d}$.

4. The far wake parameters $(\bar{l}, \overline{w})$ being known, compute the expansion of the wake using equation (D.39) and (D.40).

5. The new value of R_w will now be used in step 2 till there is convergence on the far wake parameters.

After convergence, other variables from Theodorsen's work can be computed:

$$e = 2\kappa\overline{w}^2\left(\frac{1}{2}+\frac{\epsilon}{\kappa}\overline{w}\right) \tag{D.30}$$

$$\eta = \frac{1+\overline{w}\left(\frac{1}{2}+\frac{\epsilon}{\kappa}\right)}{(1+\overline{w})(1+\frac{\epsilon}{\kappa}\overline{w})} \tag{D.31}$$

$$a_0 = \frac{\frac{1}{2}\overline{w}+\frac{\epsilon}{\kappa}\overline{w}^2}{1+\overline{w}\left(\frac{1}{2}+\frac{\epsilon}{\kappa}\right)} \tag{D.32}$$

Results of application of Theodorsen's theory are shown in figure D.3 for various number of blades.

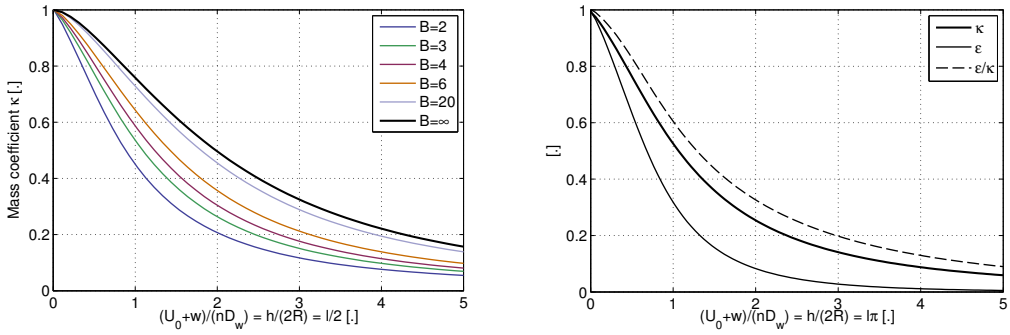

Figure D.3: Theodorsen theory. (a) Mass coefficient computed for different number of blades. (b) Loss estimate for $B = 3$

D.5 Analytical and numerical wake models

D.5.1 Introduction

Since in vortex theory and for a symmetric rotor, the velocity field at the rotor plane is entirely determined by the wake geometry, different wake models will give different tip-loss factors. This

section will focus on key aspects used by some of the prescribed wake models implemented for this study. A free wake lifting line code was also used in this study. The reader is referred to [20] and [28] for a description of this code and a its use to study tip-losses. Also, the aim of this study is not to derive an advanced prescribed wake model, but simply to assess the influence of different effects on tip-losses.

The simplest and fastest prescribed wake model implemented make use of the analytical expression presented in section B.1 and allow the calculation of natural and planar tip-losses in an analytical form. The wake consists of a series of semi-infinite helices trailed from the blade and whose pitches are different along the blade. The determination of the helix pitches is studied in section D.5.2. A numerical analog to this wake model has been implemented for validation but being more computationally expensive, its analytical counterpart will be always preferred. This numerical analog though can be slightly modified to account for wake expansion. In a very simple fashion, using the same helix pitches, an expansion factor as function of the downstream location can be applied to the trailed vortex filament. Different expansion factors are presented in section D.5.3, including the theoretical one from Theodorsen. The last kind of prescribed wake used, which also require numerical computation, is the one used by Gaunaa et al. [66] which will not be described in details here. Gaunaa's prescribed wake mode includes wake expansion and distortion with varying pitches along the wake and different convection velocities and rotational velocities of the vortex elements. This model has been established based on the results from free wake computations.

D.5.2 Pitch of the helix

Some of the prescribed wake models used, including the analytical one, require the prescription of the pitch of the trailed helix. The velocity triangle at the blade has been used in this study for the determination of the pitch angle. More complex alternatives are mentioned in section D.4.

Helix pitch based on near wake velocity triangle To understand the path followed by the trailed vorticity, one can consider a particle passing the blade at a given radial position r. At the blade the particle has the velocity $U_0(1-a)$ and $-\Omega r a'$ in the normal and tangential direction respectively. Immediately after the rotor, it is usually considered that the tangential induced velocity is then $2\Omega r a'$. The tangential direction is taken positive in the direction of the rotor's rotation. If the tangential induction was zero, then the particle trajectory in the wake would be a straight line normal to the rotor plane. When a' is different than zero, the particle will follow an helix oriented in the negative tangential direction with tangential velocity $2a'\Omega r$. The pitch of this helix will be rather important since a' is considerably smaller than a. Nevertheless, this helix does not correspond to the helix formed by the trailed vorticity. To form this helix one has to consider all the particles which have passed the position r of the blade at anterior times. Even though all these particles are travelling mainly longitudinally, joining these particles together would form an helix mainly due to the rotation of the blade. This helix is also opposite to the direction of the blade. Eventually, the direction taken by these joined particles entirely determines the pitch of the helix. The above discussion is illustrated in figure 3.3, and from this it is immediate that the components of the trailed vorticity can be decomposed as in [152]:

$$\gamma_z = \frac{\Gamma_t}{2\pi r} \tag{D.33}$$

$$\gamma_t = \frac{\Gamma_t}{2\pi r}\frac{U_0(1-a_B)}{\Omega r(1+2a'_B)} \tag{D.34}$$

The pitch of the helix is found to be

$$h = \frac{2\pi U_0(1-a)}{\Omega(1+2a')} \tag{D.35}$$

In theory, for the pitch angle to be determined solely by the velocity triangle at the rotor plane, the rotor should be assumed to operate at low-loading and in the absence of wake expansion. Under these assumptions the pitch of a trailed filament can be assumed to be constant along the wake and equation (D.35) can be used. In practice this relation will be assumed for different loading conditions since it will be used for relative comparisons between the case of expanding and non-expanding wakes. It is expected that the value of the pitch angle as given in the following paragraph would give improved results.

Velocity pitch based on far wake convection velocity In [26] (or Chapter 2) the wake helical pitch is determined by solving for the equilibrium condition of the far-wake convection velocities.

D.5.3 Wake Expansion

Different " vortex theory" models of wake expansion are presented here.

Simple Momentum theory / vortex cylinder model Using the conservation of mass flux at the disk and at the wake, i.e. $\rho U A = \rho U_w A_w$, the size of the far wake can be obtained using the 1D momentum theory/vortex cylinder result $a = \frac{1}{2}\left(1 - \sqrt{1 - C_T}\right)$ as:

$$\left(\frac{R_w}{R}\right)^2 = \frac{U}{U_w} = \frac{1-a}{1-2a} = \frac{1}{2}\left[\frac{1}{\sqrt{1-C_T}} + 1\right] \tag{D.36}$$

In the special case of $a = 1/3$, the two radii are related by $R_w = \sqrt{2}R$.

Cylinder analog expansion Using the velocity induced by a vortex cylinder on the rotor axis and using the conservation of mass, the radius of the wake can be determined at any downstream position. From equation (A.69), the velocity on the cylinder axis is:

$$u_z(r=0) = \frac{\gamma_t}{2}\left(1 + \frac{z}{\sqrt{R^2+z^2}}\right) \tag{D.37}$$

where by definition $\gamma_t = 2a$. Assuming the velocity is uniform throughout the wake and using the conservation of mass, the following expansion of the wake is obtained:

$$\left(\frac{R_w(\overline{z})}{R}\right)^2 = \frac{1-a}{1-a\left(1 + \frac{\overline{z}}{\sqrt{1+\overline{z}^2}}\right)} \tag{D.38}$$

Where a may be replaced by the 1D momentum theory/vortex cylinder result $a = \frac{1}{2}(1 - \sqrt{1-C_T})$. This cylindrical model converges towards the one from equation (D.36) when $z \to \infty$.

Theodorsen's wake expansion Using the Biot-Savart law, Theodoren derives the elementary radial velocity induced by a vortex segment at another point downstream, with a different radius. By integration of this expression over the entire wake he obtains the radial velocity at a given point. The helical relation $U_0 dt = l d\theta$ leads to another form of the radial velocity. Equating the two forms allows the integration of dr with respect to θ which Theodorsen used to find the wake expansion at any location downstream. Below, a sign convention parameter is used with $s = -1$ for wind turbines and $s = 1$ for propellers. Theodorsen's expansion formula is:

$$\frac{R_w(\overline{z})}{R} = 1 - s\frac{c_t}{\kappa}\frac{\overline{l}^3}{4}\int_X^{\overline{z}/\overline{l}}\int_\theta^\infty\int_0^1 \frac{G(x,\overline{l},B)}{B}\sum_{b=1}^{B} y_1(\theta, x, 2\pi b/B)dx d\theta d\theta \tag{D.39}$$

with $X = 0$ for wind turbines and $X = \infty$ for propellers and the function y_1 being defined as:

$$y_1(x,\theta,\tau) = \frac{\left(1 - 2x^2 + \bar{l}^2\theta^2 + x\cos(\tau+\theta)\right)}{\left(1 + x^2 + \bar{l}^2\theta^2 - 2x\cos(\tau+\theta)\right)^{\frac{5}{2}}}\left[\theta\cos(\tau+\theta) - \sin(\tau+\theta)\right] \tag{D.40}$$

The above equations are entirely determined by the knowledge of the dimensionless torsional parameter $\bar{l} = h/2\pi R$ and the thrust coefficient in the far wake c_t. The Goldstein factor is defined as $G = B\Gamma/hw$ and the double of it's first moment is referred to as the mass coefficient κ:

$$\kappa = 2\int_0^1 G(x,\bar{l},B)x\,dx \tag{D.41}$$

The determination of the far-wake parameters as function of the near-wake (λ, C_T) is described in section D.4. Illustration of different expansions obtained using Theodorsen's theory are plotted in figure 3.2. The curves for the different operating conditions follow a similar trend. Nevertheless, if plotted against each other small differences between the shapes can be found. In the range of operation of propellers even more differences in the wake shape would be seen [203, p. 81].

Comparison of wake expansions The two expansion models above are compared with the model used by the Prescribed wake model of Gaunaa [66]. For this latter model, the tip-vortex location is determined within a plane supporting the rotor axis by taking the maximum radial position of the vortex elements in the different intervals found. The comparison for different rotor configurations are plotted on figure D.4. The semi-empirical model from Gaunaa has been established using canonical free-wake simulations.

It should be noted that the expansion models presented here are near-wake expansion models, and

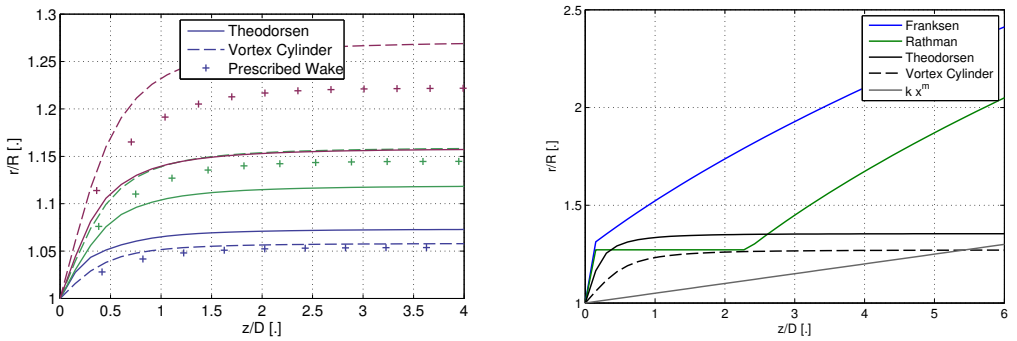

Figure D.4: Comparison of wake expansion. Left: theoretical expansion models compared with semi-empirical prescribed wake from Gaunaa for $C_T = \{0.35, 0.65, 0.8\}$ (from top to bottom). Right: Comparison of analytical models for $C_T = 0.8$.

thus differ from the one found in the literature like the one from Frandsen [65], Rathmann [165] or the kx^m-model [118] which try to account for wake meandering diffusion and mixing (shown in the right of figure D.4).

D.6 Analysis of tip-loss using vortex methods and vortex theory

D.6.1 Tools and Methodology

The tools available for this study as described in section D.5 consist in different numerical prescribed wake code, an analytical prescribed wake formulation, and a free wake code. With each of these methods the natural and planar tip-loss factor as defined in section D.1 can be computed. If no analytical expression is available, the case with "very large" number of blades is computed with 60 times more blades than the finite number of blade case. The equivalence between planar and natural tip-loss factors within the validity range from the first result of section D.3.2 has been verified as a validation case. For the analytical method, the natural tip-loss factor has a direct analytical expression which makes this method really convenient for computation of tip-losses without wake expansion. For numerical methods it is the opposite, the planar tip-loss factor is the fastest to be retrieved since the case with very-large number of blades is obviously expensive. Given the context of this study, the equivalence between the tip-loss factors is always satisfied and the definition giving the fastest computational time will be chosen accordingly.

New analytical tip-loss factor The formula of the new analytical tip-loss factor derived in this study is made explicit below. This tip-loss factor can be computed more easily using the natural definition but the planar definition could be used as well thanks to the third result from section D.3.2. At a given radial position, the tip-loss is the ratio between the total induced velocity from the helical vortex filaments of the infinitely bladed case to the induced velocity of the finite case:

$$F(r) = F_a(r) = \frac{\lim_{B_l \to \infty} \int_0^R u_{z,B_l}\left(r, r_0, h(r_0), \Gamma(r_0)/B_l\right) dr_0}{\int_0^R u_{z,B}\left(r, r_0, h(r_0), \Gamma(r_0)\right) dr_0} = \frac{\int_0^R \Gamma(r_0)/2h(r_0) dr_0}{\int_0^R u_{z,B}\left(r, r_0, h(r_0), \Gamma(r_0)\right) dr_0} \tag{D.42}$$

where $u_{z,B}$ is the sum of induced velocities from B helical filament emitted at radial position r whose expression is given in equation (B.7). For each radial position, the proper circulation Γ_t and helical pitch $h = 2\pi l$ as defined by equation (D.35) should be used. In practice the flow angle is known at finite positions and the integral is replaced by a summation. In the above, the limit was replaced based on the following result:

$$u_{z,\infty} = \lim_{B_l \to \infty} u_{z,B_l} = \frac{\Gamma_t}{2h} \begin{Bmatrix} 1 \\ 0 \end{Bmatrix} \tag{D.43}$$

using the same brackets convention as in section B.1.

Tip-losses outside BEM code For a given prescribed circulation a BEM code with prescribed circulation can be used to find values required to determine the pitch of the helices or setup Gaunaa's prescribed wake. The wake being set-up, the computation of the tip-loss factors are straightforward and the comparison between the results from the different model can be performed. Of main interest will be the effect of wake expansion by comparison between the two simple prescribed wake models using helices of constant pitch all along the wake.

Tip-losses within BEM code The simple prescribed wake models are not expected to perform as good as predictive tools for wind turbines at hight thrust coefficients. This drop of performance is mainly found in the amplitude of axial induction. Overall though, the local and global thrust and power coefficient are within satisfying range compared to usual BEM codes. Despite this

difference in amplitude, it was envisaged that the tip-loss factor, which is a ratio between axial inductions values, could be computed with enough accuracy by these prescribed wake models. As a result of this, each of the wake models implemented can be used within a BEM code to compute the tip-loss factor at each BEM iteration step. The computational expense of BEM is of course increased for the numerical wake methods, but barely noticeable when using the analytical wake model. Indeed in the later case, the definition of the natural tip-loss factor is purely analytical. To circumvent the computational expense of the numerical vortex codes computation within the BEM code, database-like solution can be implemented. This was done by the author in earlier work with free-wake codes [**27, 28**].

Quantification - Study cases In order to compare the different methods, two different circulation shapes will be prescribed to the various codes for different operating conditions. The two circulation curves are plotted in figure D.5. The first one corresponds to a case of higher loading towards the root of the blade. The curve is obtained with the following parameters $\{x_0 = 0.3, x_2 = 0.5, y_3 = 0.5, t_0 = 0.3\}$, corresponding to the coordinates of the Bézier points according to the parametrization developed in earlier work by the authors [**27, 28**]. The second circulation shape corresponds to the Goldstein circulation obtained for $\{C_T = 0.6, \lambda = 7\}$, which according to the methodology from section D.4 and its applied results from table D.1 corresponds to the far-wake values $\{1/\overline{l} = 9.1, \overline{w} = 0.45\}$. The two curve has been chosen for there difference and hence the expectation of different resulting tip-loss functions. Figure D.5 presents curves normalized

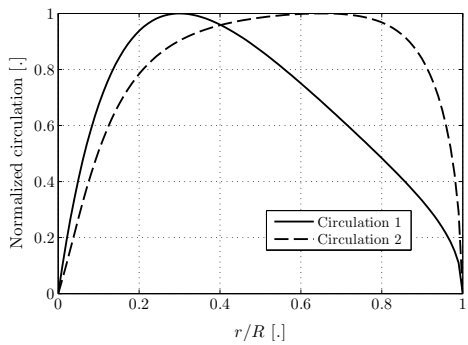

Figure D.5: Circulation shapes used for the study of tip-loss.

by their maxima. Simulations were run for the six sets of values $\{\lambda, C_T\}$ found in table D.2. For each set, the amplitude of the circulation shape that gives the design thrust coefficient is computed using a BEM code embedded in an optimization routine. The circulation with the right amplitude is then prescribed to the different codes.

Quantification - Measures To quantify the differences between the different tip-loss factors found by the different methods two measures are defined: the lost area A_F and the radius of 50% quantile related to the lost area r_{50}. The lost area is simply the difference between the area of the unit-square and the area below the tip-loss curve, when expressed in terms of dimensionless radius and without accounting for hub losses. A large loss area signifies large tip-losses and hence a large difference between finite and infinite number of blades. The value r_{50} corresponds to the radial value for which the lost area reaches 50% of its total value. It hence gives information on the shape of the curve. A high value of r_{50} signifies that the tip-loss factor drops abruptly at the tip.

It is expected that the proximity between the vortex sheets behind the rotor will have a large influence on the tip-losses. The closer the vortex sheets the closer to the infinite number blade configuration. It should be recalled that the main parameters in Prandtl's original definition of the tip-loss factor is the distance between the vortex sheets. A simple measure of the proximity of the sheets as function of the operational parameters (λ, C_T) can be defined using simple momentum analysis. The measure suggested is the distance between two successive vortex sheet assessed using the tip velocity triangle just behind the rotor, and by consideration of high tip speed ratio ($a' = 0$) and 1D momentum theory:

$$\overline{h}_B \triangleq \frac{h}{BR} = \frac{2\pi \tan\phi}{B} = \frac{2\pi}{B\lambda}(1-a) = \frac{\pi}{B\lambda}\sqrt{1-C_T} \tag{D.44}$$

The different values of $\overline{h}_B$ corresponding to the set of parameters used in this study are reported in table D.2. In most applications, the lost area will be an increasing function of $\overline{h}_B$. Nevertheless, it has been observed in this study that this sole parameter is not sufficient since it is only representative of the tip of the blade (similar to Prandtl's original theory). For this reason no bijection is to be expected between $\overline{h}_B$ and A_F in the general case, but for a constant parameter λ or C_T a near-linear relation is observed.

D.6.2 Results

The comparison of the two theoretical tip-loss factors are shown in figure D.6. The different codes

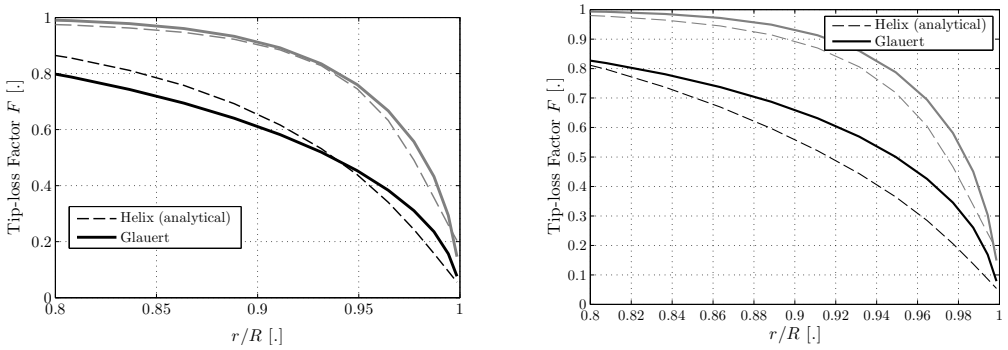

Figure D.6: Comparison of theoretical tip-loss factors. (left) Circulation 1 - (right) Circulation 2

have been run outside of a BEM code for the two circulation curves and six sets of rotor parameters presented in section D.6.1. For each case, the tip-loss factor has been computed together with the lost area parameter and reported in table D.2. For simplicity only four codes are used for comparison. The line entitled "BEM" refers to the tip-loss factor obtained in Glauert sense within a BEM code with prescribed circulation. The line entitled "Helix" corresponds to results from the simple analytical prescribed helical wake model. The line "Helix+Exp." stands for the simple prescribed wake model that uses Theodorsen's theory to compute the wake expansion. Last, the line "Free Wake" designs the tip-loss results obtained by the free wake lifting line vortex code.
From table D.2 several trends can be outlined. The most general ones being that all methods show the expected result that tip-losses are reduced with increasing tip-speed ratio and increasing C_T. This is observed with decreasing values of A_F for increasing values of λ or C_T. This trend can be explained by the increased proximity of the vortex sheets occurring with the increase of these parameters as seen by the measure $\overline{h}_B$. Comparisons between BEM code and free-wake code results follow the conclusions from a previous study [20]: the tip-loss factors obtained with

Table D.2: Lost Area A_F in percentage of the unit-square area computed for the six sets of operational parameters and the two circulation shapes.

	Circulation 1						Circulation 2					
λ	7.0	7.0	7.0	3.0	7.0	12.0	7.0	7.0	7.0	3.0	7.0	12.0
$\mathbf{C_T}$	0.2	0.5	0.7	0.6	0.6	0.6	0.2	0.5	0.7	0.6	0.6	0.6
$\mathbf{\bar{h}_B}$	0.13	0.10	0.08	0.20	0.09	0.06	0.13	0.10	0.08	0.20	0.09	0.06
BEM	6.2	5.8	5.5	11.1	5.6	3.5	6.1	5.4	4.8	10.2	5.1	3.1
Helix	5.9	6.0	6.2	9.7	6.1	4.3	7.3	6.7	6.2	11.2	6.4	4.3
Helix+TH. Exp.	5.3	4.3	3.8	6.0	4.0	2.8	6.9	5.6	4.8	9.5	5.2	3.4
Free Wake	3.6	3.1	2.6	7.1	2.8	1.7	5.4	4.5	3.8	8.2	4.2	2.4

Table D.3: 50 % radial quantile of the lost Area, r_{50} computed for the six sets of operational parameters and the two circulation shapes. Values closer to one corresponds to tip-loss factors that drops more abruptly towards the tip.

	Circulation 1						Circulation 2					
λ	7.0	7.0	7.0	3.0	7.0	12.0	7.0	7.0	7.0	3.0	7.0	12.0
$\mathbf{C_T}$	0.2	0.5	0.7	0.6	0.6	0.6	0.2	0.5	0.7	0.6	0.6	0.6
BEM	94.4	94.9	95.2	90.6	95.0	96.9	94.5	95.2	95.8	90.9	95.5	97.3
Helix	95.6	95.5	95.3	92.9	95.4	96.8	94.6	95.1	95.4	92.1	95.2	96.8
Helix+Th. Exp	95.9	96.3	96.5	95.3	96.5	97.3	94.6	95.1	95.4	92.4	95.2	96.7
Free Wake	96.6	96.7	96.7	93.4	96.8	97.8	94.7	95.3	95.6	92.8	95.5	96.7

Glauert's formulation often have a larger lost area and a lower r_{50} than the one obtained by the free-wake code. Yet, since the nature of the two codes are quite different, it is difficult to assess the reasons for these differences and the comparison can be quite abstruse. On the contrary, the comparison between the different vortex codes is justified and offers great potential. By looking at the three last lines of table D.2, it is observed that the lost area is always reduced when going from the simplest model to the more advanced free-wake model suggesting that both expansion and distortion of the wake tend to decrease the proportion of tip-losses. The sole effect of expansion on the tip-loss function is illustrated in figure 3.4b. In both cases illustrated the prescribed wake models with expansion show a lower lost area. Gaunaa's advanced prescribed wake models showed similar tip-loss functions as the simpler helical wake model with Theodorsen's wake expansion, showing coherence between the expansion models and suggesting that the expansion model is more influential than the distortion part of the model for the study of tip-losses. As mentioned earlier, the comparison between vortex methods and BEM tip-loss factor is not straightforward from their inherent differences in implementations. In the two plots from figure D.7a the influence of the circulation shape is illustrated. While there is a clear difference between free-wake results and BEM results for the first circulation shape, this difference is almost absent for the second circulation shape. Amongst vortex methods results though, the trends mentioned in the previous paragraph are visible in both cases. From the spread of results and the variation of the relative position of Glauert's tip-loss factor with different circulation functions, it is not obvious to assess whether the theoretical helix tip-loss factor derived in this study provides a better estimation of tip-losses.

D.6.3 Discussion

The results from the previous sections were obtained for six different set of values for the parameters (λ, C_T) and two different circulation shapes. These parameters have been selected to provide a

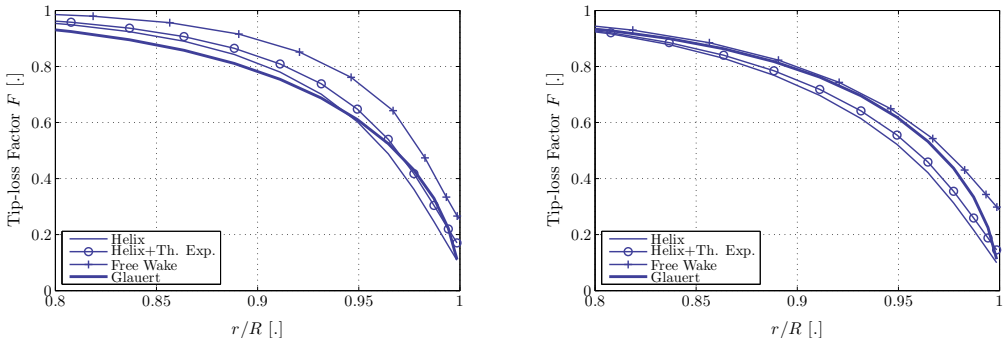

Figure D.7: Influence of the circulation shape and wake models on the tip-loss factor. (a) - Circulation 1 - (b) Circulation 2. Both simulation were run for $C_T = 0.2$ and $\lambda = 7$

representative set of wind turbine operation conditions. General trends could be extracted from this characteristics sets of simulation, nevertheless a more comprehensive study could support these conclusions. The comparisons between the different results from vortex methods are natural and justified, but it has been seen that the comparison between tip-loss factors from BEM and from vortex codes was not straightforward. From one circulation shape to the other no trends could be seen by comparing the tip-loss factor shape from the BEM code and from the vortex codes. But from the difference in formulation there is no obvious reason for a trend to actually be present. Since there is to this day no trustful reference for the assessment of tip-losses other than the tools presented in this study, the choice of one method against another is not possible. As a result of this, it can not be concluded if the new analytical tip-loss factor presented in this study is to be prevailed over Glauert's tip-loss factor.

The new analytical method presented in this article uses a helical wake made of different pitch angles, different circulation intensities and exact computation of induced velocities at the rotor to obtain the tip-loss factor. This is in contrast with Prandtl's tip-loss factor which was obtained for a non-helical wake and solely based on the distance between two vortex sheets. For this reason, the physical representation of the method presented in this study should be more advanced. In the absence of reference for validation no method can be said to prevail the other to this day. The new analytical formula for the tip-loss factor is only slightly more computational expensive than the original one so that BEM codes could be used similarly with this implementation.

When no analytical formula exists, vortex methods had to be used to study for instance the effect of wake expansion, effect not accounted for by the analytical tip-loss factors discussed in the previous paragraph. Numerical vortex methods methods always present two major shortcomings: their high computational time and the presence of singularity often dealt with by mollification of the vortex elements. When the prescribed wake methods are used within the BEM code implemented for this study, the BEM computational time is drastically increased since a call to the vortex routine is done at each iteration step from the BEM to compute a new tip-loss factor. The benefit of using such a upgraded BEM code compared to using directly a free-wake vortex code is then questionable. The second shortcoming is such methods is the presence of singularities. When studying tip-losses the knowledge of velocities close to the high-intensity tip-vortex is required. Such evaluation of velocity could depend on the choice of mollification. Nevertheless, a previous sensitivity analysis **[27]** revealed no clear impact on the computed tip-loss factor when several vortex core models were used. A dependence can be seen at the very tip (above 0.98% radius) and

if mollification parameters take non physical values.
Within this study a simple method to asses the influence of wake expansion on the tip-loss factor was implemented. Results from two similar prescribed wake were compared. For a given wake without expansion, a wake with expansion was built by multiplication of all the elements located at a given position downstream by the same factor. For a free wake configuration, the expansion would most certainly occur differently and have a different rate at different radial position. Despite simplicity of the model it was possible to capture the fact that expansion reduces tip-loss, results confirmed as well by free-wake simulations.

D.7 Conclusions

Distinctions and clarifications between different possible definitions of tip-losses have been presented in this article. By superposition of semi-infinite helical filaments whose pitch depends on the velocity triangle after the rotor, a tip-loss factor can be computed using analytical formulae. This method is physically more advanced than the one originally presented by Prandtl but in absence of a reference to compare the performance of the two, no method can be said to outperform the other. The expansion factor from Theodorsen has been successfully applied to wind energy for the first time and compared well with other models. Thanks to vortex methods the influence of wake expansion on the tip-loss factor has been studied. Despite the simplicity of the prescribed wake model it was possible to capture the fact that wake expansion reduces tip-loss and to confirm this result with free-wake simulations. Advanced development of numerical methods and accurate measurements of flow in the rotor plane will help reveal which of the methods assess best the phenomenon of tip-losses.

D.8 Complements

D.8.1 Optimal CP and CT

The validation of the tools used in the iterative procedure described in section D.4.1 is done first by using a non-iterative procedure. Following the approach of Okulov and Sørensen, the Optimal C_P and C_T are obtained using Goldstein's circulation function in combination with the near-wake/far-wake relation: $\bar{l} = \frac{1}{\lambda}(1 + \overline{w}/2)$. Results obtained are given in table D.4 and illustrated in figure D.8. The results are consistent with the ones given in [150].

D.8.2 Goldstein circulation and tip-loss factor

Goldstein Advised by Betz, Goldstein [72] derived the optimal circulation of a propeller under the same assumptions as Betz but for the case of finite number of blades. He assumed that Betz's result was still holding, namely that the optimal circulation distribution for a given thrust had a far-wake flow similar to the one of a rigid screw moving axially with a constant velocity. Goldstein took advantage of the periodicity of the flow between two screw surfaces to solve Poisson's equation which reduces to solving both the homogeneous and the inhomogeneous modified Bessel differential equations. Goldstein's made use of infinite series to solve these equations with the proper boundary conditions. Once the potential is known he determines the circulation at a given radial position, for a given tip-speed ratio by the jump of potential across the sheet at this radial position in the far wake. The velocity at any point of the far wake is obtained by differentiation of the potential ($\boldsymbol{V} = \operatorname{grad}\phi$). With the no-wake-expansion assumption, the velocities at the rotor are found to be

Table D.4: Optimal CP and CT obtained using Goldstein's circulation function, in combination with the near-wake/far-wake relation : $\bar{l} = \frac{1}{\lambda}(1 + \overline{w}/2)$.

λ	C_T	C_P	$1/\bar{l}$	$\overline{w}$	$\bar{l}$
1	0.37	0.22	1.7	0.83	0.575
2	0.57	0.36	3.2	0.74	0.312
3	0.67	0.43	4.7	0.71	0.214
4	0.72	0.47	6.1	0.70	0.163
5	0.76	0.50	7.6	0.69	0.131
6	0.78	0.51	9.1	0.68	0.110
7	0.80	0.53	10.6	0.68	0.094
8	0.81	0.53	12.1	0.68	0.083
9	0.82	0.54	13.6	0.68	0.074
10	0.83	0.55	15.1	0.67	0.066
11	0.83	0.55	16.6	0.67	0.060
12	0.84	0.56	18.1	0.67	0.055
13	0.84	0.56	19.6	0.67	0.051
14	0.84	0.56	21.1	0.67	0.047
15	0.85	0.56	22.6	0.67	0.044

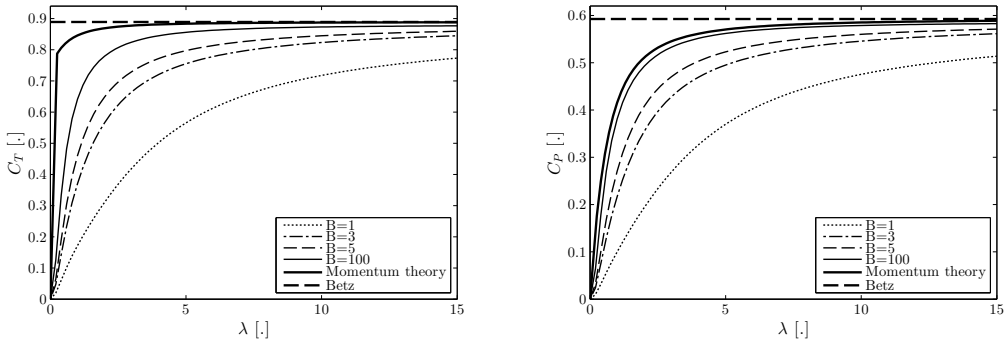

Figure D.8: Optimal thrust (left) and power coefficient (right) as obtained using the same procedure as Okulov et al. [150].

twice as much as the velocity in the far-wake and the flow-angle can be derived. The calculation of the thrust and torque follow with and without the presence of profile drag using the Kutta-Joukowski theorem. A guide to follow Goldstein's article can be found in **[20]**.
From Goldstein's optimal circulation, a tip-loss factor can be derived by dividing this circulation by the optimal circulation of Betz. The corresponding tip-loss factor is of the following form:

$$F_{\text{Go}} = \left(\frac{\lambda_r^2}{1+\lambda_r^2}\right)^{-1} \left[\frac{8}{\pi^2}\sum_{m=0}^{\infty}\frac{T_{1,\nu}(\nu\lambda_r)}{(2m+1)^2} + \frac{2}{\pi}\sum_{m=0}^{\infty} a_m \frac{I_\nu(\nu\lambda_r)}{I_\nu(\nu\lambda)}\right] \tag{D.45}$$

The work of Theodorsen In 1944, Theodorsen [202] presented a methodology for propeller design using Goldstein's factor. In his work though, he uses $V_n = U_0 + w$ for a generalization of Goldstein's theory, to remove the assumption of lightly-loaded rotor. Theodorsen uses the following notation for his derived "Goldstein" tip loss factor:

$$G(r) = \frac{\Gamma(r)}{hw} \tag{D.46}$$

By doing so, wake expansion [149] and highly loaded rotor can be studied using Goldstein's function. The question remains on finding the link between the screw pitch angle and the tip-speed ratio.

Computation of Goldstein's factor The computation of F_{Go} requires care but is not insuperable. Historical computation and tabulations include the work of Kramer in 1939 [104], Tibery and Wrench in 1964 [204]. Nevertheless, it has been observed that due do the slow convergence of the series, the computational time is quite important even for modern computers. In 1944, Theodorsen used the analogy with electromagnetism and used an experimental setup with different manufactured helical surfaces to measure Goldstein's factor.
Recently, the computation of this factor was carried out by modelling the wake-screw as the superposition of multiple single helical vortex filaments [149]. This method is fast, it presents no numerical issue and shows perfect agreement with tables from Tibery and Wrench [204]. A detailed description can be found in the appendix of **[20]**.

D.8.3 Summary of vortex theories - Far wake and near wake parameters

An attempt to summarize the different definitions and assumptions used in the literature as regard to the vortex theory of the rotor wake is presented in table D.5. The table is unfortunately not expected to be readable in the paper version of this document, but it should be the case using the numerical version. The author apologize if any theory was erroneously reproduced in this table.
The following variables are used in the table:

$$I_1 = 2\int_0^1 G(x,\bar{l},B)x dx = \kappa \tag{D.47}$$

$$I_{1W}(\overline{r}_h) = 2\int_0^1 G(x,\bar{l},B)\frac{x}{\bar{l}^2+x^2}\frac{x^2}{x^2+\frac{\overline{r}_h^2}{1-\overline{r}_h^2}}dx \tag{D.48}$$

$$I_3 = 2\int_0^1 G(x,\bar{l},B)\frac{x^3}{\bar{l}^2+x^2}dx \tag{D.49}$$

The function $\mathrm{r_w}(r,z)$ provides the radial position of the vortex filament at a downstream location z which was trailed at the radial position r at the rotor. The function $\overline{\mathrm{r}}_{\mathrm{w}}(\overline{r},\overline{z})$ provides the dimensionless radial position of the vortex filament at a downstream location $\overline{z}=z/R$ which was trailed at the radial position r/R at the rotor. The radial coordinate is made dimensionless with respect to the wake maximum radius at this location in harmony with Wald's work. Since such scaling can be a source of error, dimension quantities when dealing with radii should be preferred. If the second argument is dropped in the above function, the value refers to the far-wake value.

D.8.4 Other applications of vortex theory in the literature

The following section briefly refers to other applications in the literature without providing detailed information.

Actuator disk

- Momentum theory and vortex theory: from Sharpe 2004 [184], Wald 2006 [218], Conway 1995 and 1998 [51, 47]
- Conway 2003 [49](non axial, non axisymmetric)
- Work of Conway and Schaffarczyk, application to WT [48], [177, 178]
- Work of Sørensen and Van Kuik [193]

Table D.5: Summary of the different vortex theories of the rotor wake. For PDF view only.

	Definition	**General**	**Goldstein [72]**	**Okulov and Sørensen [150]**	**With Expansion**	**Wald/Th.[218]**
$\bar{l}_w$	$\tan\epsilon_w(R_W),\ \frac{h_w}{2\pi R_w}$	$\frac{U_0 \pm w}{\Omega_w R_w} = \frac{1}{\lambda}(1 \pm \overline{w})\frac{\Omega}{\Omega_w}\frac{R}{R_w}$	$\frac{1}{\lambda}$	$\frac{U_0 \pm w}{\Omega_w R} = \frac{1}{\lambda}(1 \pm \overline{w})\frac{\Omega}{\Omega_w}$	*idem*	$\frac{U_0 \pm w}{\Omega R_w} = \frac{1}{\lambda}(1 \pm \overline{w})\frac{R}{R_w}$ //$\lambda(Th)\lambda_2(W)$
$\bar{l}$	$\tan\epsilon(R),\ \frac{h}{2\pi R}$	[–]	$\frac{1}{\lambda}$	$\frac{U_0 \pm w/2}{\Omega R} = \frac{1}{\lambda}(1 \pm \overline{w}/2)$	*idem*	[–]
$\tan\epsilon_{w}$ $_{(geom.)}$	$\frac{dz}{rd\theta} \equiv \bar{l}_w\frac{R_w}{r} = \frac{\bar{l}_w}{\bar{r}_w}$	$\frac{U_0 \pm w}{\Omega_w r}$		$\frac{U_0 \pm w}{\Omega_w r}$	*idem*	$\frac{U_0 \pm w}{\Omega r}$
$\tan\epsilon_{w}$ $_{(tri.)}$	$\frac{U_{n_w}}{U_{t_w}}$	$\frac{U_0 \pm u_{z,w}}{\Omega_w r \mp u_{\theta,w}}$		$\frac{U_0 \pm u_{z,w}}{\Omega_w r \mp u_{\theta,w}}$	*idem*	$\frac{U_0 \pm u_{z,w}}{\Omega r \mp u_{\theta,w}}$
$\tan\epsilon$ $_{(geom.)}$	$\frac{dz}{rd\theta} \equiv \bar{l}\frac{R}{r} = \frac{\bar{l}}{\bar{r}}$	[–]		$\frac{U_0 \pm w/2}{\Omega r} = \frac{1}{\lambda_r}(1 \pm \overline{w}/2)$	*idem*	[–]
$\tan\phi$ $_{(tri.)}$	$\frac{U_n}{U_t}$	$\frac{U_0 \pm u_z}{\Omega r \mp u_\theta}$		$\frac{U_0 \pm u_z}{\Omega r \mp u_\theta}$	*idem*	$\frac{U_0 \pm u_z}{\Omega r \mp u_\theta}$
$\tan\phi$ $_{(tri.)}$	$\frac{U_n}{U_t}$	[–]	$\approx \frac{1}{\lambda_r}(1 \pm \overline{w}/2)$ //(5.20)	[–]	*idem*	$\bar{l}_w\frac{1 \pm \overline{w}/2}{1 \pm \overline{w}}\frac{R_w}{R} = \frac{1}{\lambda}(1 \pm \overline{w}/2)$ //$\lambda_p(Thp48)$
h_w	$2\pi r \tan\epsilon_w$	$\frac{2\pi U_0(1 \pm \overline{w})}{\Omega_w}$		$\frac{2\pi U_0(1 \pm \overline{w})}{\Omega_w}$	*idem*	$\frac{2\pi U_0(1 \pm \overline{w})}{\Omega}$
$\overline{h}_w$	$\frac{h_w}{R_w}$	$\frac{U_0(1 \pm \overline{w})}{\Omega_w R_w}$		$\frac{U_0(1 \pm \overline{w})}{\Omega_w R}$	*idem*	$\frac{U_0(1 \pm \overline{w})}{\Omega R_w}$
h	$2\pi r \tan\epsilon$	[–]		$\frac{2\pi U_0(1 \pm \overline{w}/2)}{\Omega}$	*idem*	[–]
$\overline{h}$	$\frac{h}{R}$	[–]		$\frac{U_0(1 \pm \overline{w}/2)}{\Omega R}$	*idem*	[–]
$B\Gamma_w(r)$	$G(\overline{r}_w)h_w w$	$2\pi\frac{U_0}{\Omega_w}w(1 \pm \overline{w})G$		$2\pi\frac{U_0}{\Omega_w}w(1 \pm \overline{w})G$	*idem*	$2\pi\frac{U_0}{\Omega}w(1 \pm \overline{w})G$
$B\Gamma_b(r)$	[–]	[–]		$G(r/R)\,h\,w = \begin{cases} B\Gamma_w\frac{h}{h_w}, & h \neq h_w \\ B\Gamma_w, & h = h_w \end{cases}$	*idem*	$B\Gamma_w(\mathrm{r}_w(r))$
$u_{z,w}$	$w\cos^2\epsilon_w \equiv \frac{w}{1+\tan^2\epsilon_w}$	$w\frac{1}{1+(\bar{l}_w/\overline{r}_w)^2}$ (arithmetic value)				
$u_{\theta,w}$	$w\cos\epsilon_w\sin\epsilon_w \equiv \frac{w\tan\epsilon_w}{1+\tan^2\epsilon_w}$	$w\frac{\bar{l}_w/\overline{r}_w}{1+(\bar{l}_w/\overline{r}_w)^2}$ (arithmetic value)				
$u_z(r)$	[–]	[–]		$\frac{1}{2}u_{z,w}(r)$	*idem*	$\frac{1}{2}u_{z,w}(\mathrm{r}_w(r))$
$u_\theta(r)$	[–]	[–]		$\frac{1}{2}u_{\theta,w}(r)$	*idem*	$\frac{1}{2}u_{\theta,w}(\mathrm{r}_w(r))\frac{\mathrm{r}_w(r)}{r}$ *(Wald)*
$\tan\phi$ $_{(tri.)}$	[–]	$\frac{\bar{l}_w^2 + \overline{r}_w^2(1 \pm \overline{w}/2)}{\lambda\bar{r}\bar{l}_w + \lambda\overline{r}\overline{r}_w^2 \mp \overline{r}_w\bar{l}_w\overline{w}/2}$	$\frac{1}{\lambda\overline{r}}\frac{1+\lambda^2\overline{r}^2(1 \pm \overline{w}/2)}{1+\lambda^2\overline{r}^2 \mp \overline{w}/2}$		*idem*	
$\tan\phi$ $_{(tri.Exp)}$	[–]		$\frac{1}{\lambda\overline{r}}\left[1 \pm \frac{\overline{w}}{2} \mp \frac{\overline{w}^2}{4\lambda^2\overline{r}^2+4}\right]$	$\frac{1}{\lambda\overline{r}}\left[1 \pm \frac{\overline{w}}{2}\left(1 + \frac{\Delta\Omega}{\Omega}\frac{1}{1+\lambda^2\overline{r}^2}\right)\right]$	*idem*	$\frac{1}{\lambda\overline{r}}\left[1 \pm \frac{\overline{w}}{2}\left(1 + \frac{\Delta R}{R}\frac{1}{1+\lambda^2\overline{r}^2}\right)\right]$
T $_{(bound)}$	$\int_{r_h}^{R}\rho B\Gamma_b(\Omega r \mp u_\theta)\,dr$			$\rho h w\int_0^R G(r/R)(\Omega r \mp u_\theta)\,dr$	$\rho h w\int_{r_h}^R G(\mathrm{r}_w(r)/R_w)(\Omega r \mp u_\theta)\,dr$	$\rho h_w w\int_{r_h}^R G(\mathrm{r}_w(r)/R_w)(\Omega r \mp u_\theta)\,dr$
P $_{(bound)}$	$\Omega\int_{r_h}^{R}\rho B\Gamma_b(U_0 \pm u_z)\,r\,dr$			$\rho h w\Omega\int_0^R G(r/R)(U_0 \pm u_z)\,r\,dr$	$\rho h w\Omega\int_{r_h}^R G(\mathrm{r}_w(r)/R_w)(U_0 \pm u_z)\,r\,dr$	$\rho h_w w\omega\int_{r_h}^{r} G(\mathrm{r}_w(r)/r_w)(u_0 \pm u_z)\,r\,dr$
C_T $_{(bound)}$	$\frac{T}{1/2\rho U_0^2\pi R^2}$		$2\overline{w}\left[\kappa \mp \frac{\overline{w}}{2}\frac{1}{\lambda^2}I_{1W}(0)\right]$	$2\overline{w}\left(1 \pm \frac{\overline{w}}{2}\right)\left[\kappa \mp \frac{\overline{w}}{2}\frac{\bar{l}_w}{\lambda}I_{1W}(0)\right]$	$2\overline{w}\left(1 \pm \frac{\overline{w}}{2}\right)\left[(1-\overline{r}_h^2)\kappa \mp \frac{\overline{w}}{2}\frac{\bar{l}_w}{\lambda}I_{1W}(\overline{r}_h)\right]$	$2\overline{w}(1 \pm \overline{w})\left[(1-\overline{r}_h^2)\kappa \mp \frac{\overline{w}}{2}\frac{\bar{l}_w}{\lambda}\frac{R_w}{R}I_{1W}(\overline{r}_h)\right]$
C_T $_{(bound.bis)}$				$2\overline{w}\left[\kappa \mp \frac{\overline{w}}{2}I_3\right]$		$2\overline{w}(1 \pm \overline{w})\left[(1-\overline{r}_h^2)\kappa \mp \frac{\overline{w}}{2}\frac{(1 \pm \overline{w})}{\lambda^2}I_{1W}(\overline{r}_h)\right]$
C_P $_{(bound)}$	$\frac{P}{1/2\rho U_0^3\pi R^2}$		$2\overline{w}\left[\kappa \pm \frac{\overline{w}}{2}I_3\right]$	$2\overline{w}\left(1 \pm \frac{\overline{w}}{2}\right)\left[\kappa \pm \frac{\overline{w}}{2}I_3\right]$	$2\overline{w}\left(1 \pm \frac{\overline{w}}{2}\right)(1-\overline{r}_h^2)\left[\kappa \pm \frac{\overline{w}}{2}I_3\right]$	$2\overline{w}(1 \pm \overline{w})(1-\overline{r}_h^2)\left[\kappa \pm \frac{\overline{w}}{2}I_3\right]$
T $_{(mom)}$	$\rho\int_{S_w}\left[\underbrace{(U_0 \pm u_{z,w})}_{U_w}\underbrace{u_{z,w}}_{U_w - U_0} + (p - p_0)\right]dS$				*idem*	$\rho\int_{S_w}\left[(U_0 \pm w)u_{z,w} + u_{z,w}^2 - u^2/2\right]dS$
T $_{(mom.bis.)}$					*idem*	$\rho\pi R_w^2\kappa w\left[(U_0 \pm w) + \frac{\epsilon}{\kappa}w - \frac{1}{2}w\right]$

- Discussion on the generation of vorticity: by van Kuik [213] Lewis [116, p. 214] (generation of vorticity in axi-symmetric flows)
- Sørensen chapter 2012 [192] Work of Joukowski detailed and revised by Okulov et al. 2015 [146]

Other topics

- Wake stability: Okulov et al. 2004 [148], Sørensen et al. 2011 [194]
- 3D decambering: "Weissinger lifting surface theory N.H. Van Dorn and J. De Young, J., A Comparison of Three Theoretical Methods of Calculating Span Load Distribution on

Swept Wings,NACA TN 1476, 1947", Ludweig and Ginzel theory [98], Mukherjee 2003 [142], Sørensen et al. 2014 [195]

- Application of vortex cylinder theory: Lewis [116, p. 170] uses two semi-infinite cylinders and panels to model a contraction, and also a contraction towards an annulus p.174 using an additional semi cylinder.
- Application of helical filaments: Lewis [116, p. 204 and p. 209] with discussion on helix angle

Appendix E

Right cylindrical vortex model applied to wind energy - Complements

The current chapter provides complements to Chapter 2. Some of its content were published in [23] and [26]. Further applications of vortex cylinder model for wind energy are found in [23] , [24] , [29] and [26]. Only the content related to the wake rotation are discussed here.

E.1 Introduction notes

Pressure drop due to wake rotation - introduction The pressure drop due to wake rotation can be obtained using the r-component of Euler's equation [123, 126], which, when the radial velocity component is neglected, writes $\frac{\partial p}{\partial r} = \rho \frac{u_\psi^2}{r}$. The pressure in the wake, just behind the rotor, can be obtained by integration with $u_\psi = -2\Omega r a'$ as: $p(R) - p(r) = \int_r^R \rho \frac{u_\psi^2}{r} dr$. In front of the rotor, the flow rotation is zero, so that the reference pressure due to rotation there is written p_0, with $p_0 = 0$, which is also the case at the disk rim, $p(R) = p_0$. The fluid will exert on an elementary disk area dA a force $dT_{\text{rot}} = (p_0 - p(r))dA$, positive along z. The local thrust coefficient associated to this force is:

$$C_{t,\text{rot}} \equiv \frac{dT_{\text{rot}}}{\frac{1}{2}\rho U_0^2 \, dA} = 2 \int_r^R \frac{u_\psi^2}{U_0^2} \frac{dr}{r} \tag{E.1}$$

E.2 Elementary cylindrical system

The elementary cylindrical system presented in Chapter 1 and Chapter 2 is considered.

System closure The pitch h of the helical wake corresponds to the longitudinal distance travelled by the wake vorticity in one helix rotation. Writing Δt the time spent during one helix rotation, V_z and V_ψ the axial and tangential convection velocity of the cylindrical vortex sheet, one obtains the distance run by the wake vorticity as $h = \Delta t \cdot V_z$ and $2\pi R = \Delta t(\Omega R - V_\psi)$. The same assumptions than Øye [152] are used to assess the convection velocity. The cylindrical vortex sheet is assumed to convect at a speed equal to the mean between the two far wake velocities surrounding the sheet:

$$V_z = \frac{1}{2}\left(U_0 + U_0 + \gamma_t\right) = U_0 + \frac{\gamma_t}{2}, \qquad V_\psi = \frac{1}{2}\left(0 + \frac{-\Gamma_{\text{tot}}}{2\pi R}\right) = -\frac{\Gamma_{\text{tot}}}{4\pi R}, \tag{E.2}$$

The helical wake pitch is then:

$$h = \Delta t \cdot V_z = \frac{2\pi}{\Omega(1 + a_c')}\left(U_0 + \frac{\gamma_t}{2}\right), \qquad \text{where} \quad a_c' \equiv \frac{\Gamma_{\text{tot}}}{4\pi\Omega R^2}. \tag{E.3}$$

Inserting the above expression of the pitch h into $\gamma_t = -\Gamma_{\text{tot}}/h$ leads to:

$$C = 4\frac{-\overline{\gamma}_t}{2}\left[1 - \left(-\frac{\overline{\gamma}_t}{2}\right)\right], \text{ with: } \quad C \equiv k(1 + a_c'), \quad k \equiv \frac{\Omega\Gamma_{\text{tot}}}{\pi U_0^2} \quad \text{and} \quad \overline{\gamma}_t \equiv \gamma_t / U_0 \tag{E.4}$$

A consistent vortex model is obtained by solving equation (E.4) for γ_t or h. This leads to:

$$\gamma_t = U_0\left[-1+\sqrt{1-C}\right], \qquad h = \frac{\pi R}{\lambda}\left[1+\sqrt{1-C}\right], \qquad V_z = \frac{U_0}{2}\left[1+\sqrt{1-C}\right] \tag{E.5}$$

where $\lambda = \Omega R/U_0$ and $C \in [0,1]$. The form of the solutions presented in this section are consistent with the ones presented in a previous work [23] for infinite tip-speed ratio (i.e. $a'_c = 0$ and thus $C = k$). The constrain $C \in [0;1]$ associated with equation (E.5) will be lifted in section 2.2.

Rotor variables Using equation (A.70) and equation (E.5), the axial and tangential inductions are:

$$a(r) \equiv -\frac{u_z(r,0)}{U_0} = \frac{-\gamma_t}{2U_0} = \frac{1}{2}\left(1-\sqrt{1-C}\right), \quad a'(r) \equiv \frac{-u_\psi(r,0)}{\Omega r} = \frac{\Gamma_{\text{tot}}}{4\pi\Omega r^2} \tag{E.6}$$

It is seen that the assumption of uniform circulation implies a constant axial induction on the rotor plane with this model. From the definition of equation (E.3) it is observed that the tangential convection induction a'_c is related to the tangential induction at the rim of the disk: $a'_c = a'(R)$. The left hand side of equation (E.6) can be rewritten $C = 4a(1-a) = k(1+a'_c)$ which gives an expression for the dimensionless circulation: $k = 4a(1-a)/(1+a'(R))$. Inserting the expression of k and $a'(r)$ into the general expressions of the KJ coefficients introduced in section C.1 gives:

$$C_{p,\text{KJ}} = k[1-a] = 4a[1-a]^2\frac{1}{1+a'(R)} \tag{E.7}$$

$$C_{t,\text{KJ}}(r) = k\left[1+a'(r)\right] = 4a[1-a]\frac{1+a'(r)}{1+a'(R)} = k+\left(\frac{k}{2}\right)^2\frac{1}{\lambda_r^2} = 4a[1-a]+\left(\frac{k}{2}\right)^2\left[\frac{1}{\lambda_r^2}-\frac{1}{\lambda^2}\right] \tag{E.8}$$

The above equations were derived by Øye [126]. It is seen that the constant C is equal to the local thrust coefficient at the rim of the disk: $C = C_{t,\text{KJ}}(R)$. For the current flow situation, with a and a' given by equation (E.6), a Stream-tube analysis as presented in [26], would give a constant thrust coefficient $C_{t,\text{ST}} = 4a[1-a] = C = C_{t,\text{KJ}}(R)$. On the contrary, the local thrust coefficient obtained in equation (E.8) is not constant but is increasing towards the root. It is pointed out that the case of constant rotor circulation leads to a singularity at $r = 0$ for the thrust coefficient and the tangential induction. Sørensen and Van Kuik [193] removed the singularity by inserting a smooth Rankine vortex at the root. In the current study, the singularity will be removed when using a superposition of cylinders by assuming that the circulation drops to zero at the root. The singularity vanishes when the tip-speed ratio tends to infinity. The power coefficient obtained with ST analysis is $C_{p,\text{ST}} = 4\lambda_r^2 a'(r)\left[1-a\right] = k[1-a]$, which is identical to the value found using the KJ analysis. The orthogonality of the induced velocity with the relative velocity (equation (2.1)) is only satisfied at the rim of the disk in the vortex model:

$$\frac{4a[1-a]}{\lambda_r^2} = \frac{k[1+a'_c]}{\lambda_r^2} = 4a'(r)[1+a'_c] \neq 4a'(r)[1+a'(r)] \tag{E.9}$$

Wake rotation The thrust coefficient associated with wake rotation, as given by equation (E.1) can be obtained using the definition of a' from equation (E.6), with $u_\psi = -2a'(r)\Omega r$:

$$C_{t,\text{rot}}(r) = 2\left(\frac{\Gamma}{2\pi U_0}\right)^2\int_r^R\frac{dr}{r^3} = \left(\frac{\Gamma}{2\pi U_0}\right)^2\left[\frac{1}{r^2}-\frac{1}{R^2}\right] = \left(\frac{k}{2}\right)^2\left[\frac{1}{\lambda_r^2}-\frac{1}{\lambda^2}\right] \tag{E.10}$$

Comparing equation (E.8) with equation (E.10), it is immediately seen that the thrust missing in the Stream-tube analysis is the thrust associated to the pressure drop due to the wake rotation, viz.:

$$C_{t,\text{KJ}}(r) = C_{t,\text{ST}} + C_{t,\text{rot}}(r) \tag{E.11}$$

This result is consistent with the careful momentum analysis performed by Sørensen and Van Kuik [193]. The power coefficient from equation (E.7) can also be written in term of $C_{t,\text{rot}}$, by

using $k = C_{t,\mathrm{KJ}}(r)/\left(1 + a'(r)\right)$ as:

$$C_{p,\mathrm{KJ}} = k\,[1-a] = \frac{C_{t,\mathrm{KJ}}(r)}{1+a'(r)}[1-a] = 4a[1-a]^2\frac{1}{1+a'(r)} + C_{t,\mathrm{rot}}(r)\frac{1-a}{1+a'(r)} \tag{E.12}$$

Equations (E.8) and (E.7) can be compared to the 1D momentum theory values, respectively: $4a[1-a]$ and $4a[1-a]^2$. The effect of wake rotation is then seen to increase the local thrust coefficient and reduce the local power coefficient as compared to the constant 1D case.

E.3 Superposition of cylindrical vortex models for rotor modelling

Introduction The assumption of constant circulation along the radius can be relaxed by using a superposition of elementary models with uniform circulation. The circulation is assumed to be piecewise continuous with the radius. Notations are introduced in figure E.1 (a) and (b). The i-th circulation change, occurring at $r = R_i$, is associated with an elementary vortex system extending from $R_0 = 0$ to R_i of intensity $\tilde{\Gamma}_i = \Gamma_i - \Gamma_{i+1}$. The last cylinder, indexed n, extends from 0 to R. For convenience the ghost index $n+1$ is introduced such that $\Gamma_{n+1} = 0$. The tangential vorticity of the cylinder i is

$$\gamma_i = \frac{\tilde{\Gamma}_i}{h_i} \tag{E.13}$$

where h_i is the local helical pitch to be determined to form a consistent vortex system.

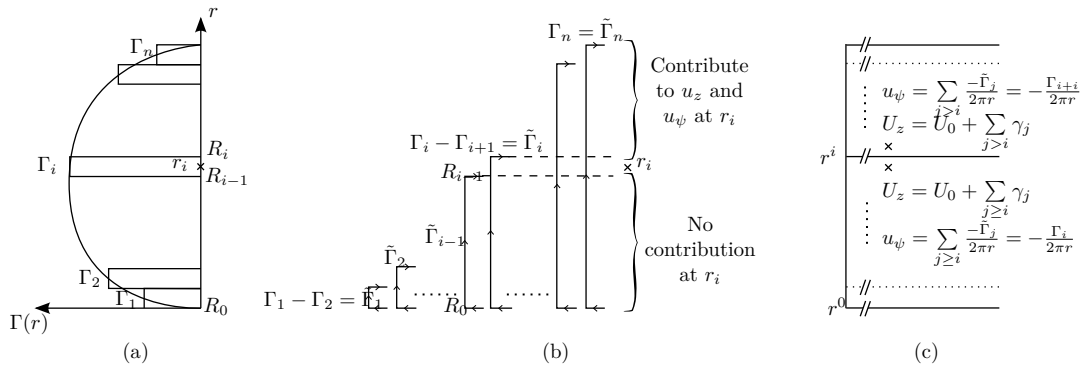

Figure E.1: Sketch and notations for the superposition of cylindrical models - Side view. (a) Discretization of the bound circulation along the rotor span. (b) Decomposition of the wake as a superposition of cylindrical models extending from R_0 to R_i and with intensities $\tilde{\Gamma}_i$. The cylinders all start at $z = 0$ but are represented spaced in this figure. (c) Velocities induced in the far-wake by the total system of cylindrical models on both side of cylinder i.

In the case of infinite tip-speed ratio, the superposition of vortex cylinder models gives similar results than 2D momentum theory. This link was mentioned by Glauert [71, p. 230] and was formally proved in a previous work by the authors **[23]**. The finite tip-speed ratio case is handled using the same approach as in **[23]**. For this reason, only the key steps are summarized in the following paragraph.

Inductions variables The axial and tangential inductions in the rotor plane for the superposition of cylinders are directly obtained from the properties of an elementary vortex cylinder introduced

in section E.2. For $R_{i-1} < r < R_i$ we obtain:

$$a_i = -\sum_{j=i}^{n} \frac{\gamma_j}{2U_0} \qquad , \qquad a_i'(r) = \sum_{j=1}^{n} \frac{\tilde{\Gamma}_j}{4\pi\Omega r^2} = \frac{\Gamma_i}{4\pi\Omega r^2} \tag{E.14}$$

It is immediately seen from equation (E.14) that the tangential induction is only a function of the circulation of the closest surrounding cylinder. The axial induction requires a more thorough analysis. Figure E.1c shows the velocities in the far wake which are twice the one at the rotor. The far wake axial induction is:

$$u_{z,\mathrm{FW}}(R_{i-1} < r < R_i) = \sum_{j=i}^{n} \gamma_j \tag{E.15}$$

Convection velocity Vortex sheet kinematics specify the intensity of a vortex sheet depending on the velocity jump across it. This condition is automatically satisfied by an isolated vortex cylinder and by the system of superposed cylinders. The difference arising when the systems are superposed lays in the convection velocity of the vortex sheets. An isolated cylinder is transported according to the surrounding free-stream velocity U_0 and its self induction $\gamma_t/2$ (see equation (E.2)). In the case of a cylinder contained within other cylinders, the surrounding free-stream "seen" by the cylinder is a function of the velocity induced by the containing cylinders. Using equation (E.15) and the fact that a vortex sheet convects as the mean of its surrounding velocities, the convection velocity in the far-wake of the cylinder i within the full vortex system is:

$$\begin{aligned} V_{c,i} &= \frac{1}{2}\left[U_0 + u_{z,\mathrm{FW}}\left(R_{i-1} < r < R_i\right) + U_0 + u_{z,\mathrm{FW}}\left(R_i < r < R_{i+1}\right)\right] \\ &= U_0 + \sum_{j=i+1}^{n} \gamma_j + \frac{\gamma_i}{2} = U_0\left(b_i + \frac{\overline{\gamma}_i}{2}\right) \end{aligned} \tag{E.16}$$

where the following notations are introduced:

$$\overline{\gamma} = \frac{\gamma}{U_0}, \qquad b_i = 1 + \sum_{j=i+1}^{n} \overline{\gamma}_j \tag{E.17}$$

The convection velocity is used to determined the pitch of the h_i introduced in equation (E.13).

E.4 System closure under assumption of large tip-speed ratio

In the general case relation equation (E.13) requires solving since the helix pitch depends on the induced velocities which in turn depend on the vorticity distribution. The following notations are introduced:

$$k_i = \frac{\Omega\Gamma_i}{\pi U_0^2}, \quad \tilde{k}_i = \frac{\Omega\tilde{\Gamma}_i}{\pi U_0^2} \tag{E.18}$$

In the absence of tangential induction in the wake (e.g. for high tip-speed ratio), it can be assumed that the helix pitch corresponds to the distance run by the vorticity within one rotor revolution:

$$h_i = \frac{2\pi}{\Omega} V_{c,i} \tag{E.19}$$

Under the same assumption, and considering one cylindrical vortex system of intensity $\tilde{\Gamma}_i$, the local and total thrust coefficients are equal and verify $C_T = C_t = \tilde{k}_i$. Introducing equation (E.19) and equation (E.16) into equation (E.13) gives:

$$\overline{\gamma}_i = \frac{-\tilde{\Gamma}}{U_0 h_i} = -\frac{\Gamma_i - \Gamma_{i+1}}{2\pi U_0 V_{c,i}} = -\frac{\Gamma_i - \Gamma_{i+1}}{2\pi U_0^2\left[b_i + \frac{\overline{\gamma}_i}{2}\right]} = -\frac{k_i - k_{i+1}}{2b_i + \overline{\gamma}_i}. \tag{E.20}$$

The above leads to the following system for γ_i

$$\overline{\gamma}_i^2 + 2b_i\gamma_i + (k_i - k_{i+1}) = 0, \tag{E.21}$$

for which a physical solution is

$$\overline{\gamma}_i = -b_i + \sqrt{b_i^2 - (k_i - k_{i+1})} \tag{E.22}$$

Using equation (E.22) and starting from $i = n$, it can proven by induction that:

$$\overline{\gamma}_n = -1 + \sqrt{1 - k_n}, \qquad \overline{\gamma}_i = -\sqrt{1 - k_{i+1}} + \sqrt{1 - k_i} \tag{E.23}$$

and thus:

$$b_n = 1 \qquad b_i = \sqrt{1 - k_{i+1}} \tag{E.24}$$

$$V_{c,n} = \frac{U_0}{2}(1 + \sqrt{1 - k_n}) \qquad V_{c,i} = U_0\left(b_i + \frac{\overline{\gamma}_i}{2}\right) = \frac{U_0}{2}(\sqrt{1 - k_{i+1}} + \sqrt{1 - k_i}) \tag{E.25}$$

$$h_n = \frac{\pi U_0}{\Omega}(1 + \sqrt{1 - k_n}) \qquad h_i = \frac{\pi U_0}{\Omega}(\sqrt{1 - k_{i+1}} + \sqrt{1 - k_i}) \tag{E.26}$$

Eventually, the induced velocity between two cylinders is:

$$u_z(r_{i-1} < r < r_i) = \sum_{j=i}^{n} \frac{\gamma_j}{2} = \frac{1}{2}\left(-1 + \sqrt{1 - k_i}\right) = \frac{\hat{\gamma}_i}{2} = -\frac{\Gamma_i}{2\hat{h}_i} \tag{E.27}$$

where the hat-notation refers to values obtained for an isolated cylinder of intensity Γ_i. For the isolated cylinder the convection velocity is solely influenced by the free-stream and its self induction and one has:

$$\hat{h}_i = \frac{\pi U_0}{\Omega}(1 + \sqrt{1 - k_i}), \qquad \hat{\gamma}_i = U_0(-1 + \sqrt{1 - k_i}) \tag{E.28}$$

Results from equation (E.27) reveals that between two vortex cylinders, the axial induced velocity is only influenced by the upper cylinder and the induction is equal to the one that would be obtained if the cylinder was isolated.

Closure with constant pitch If the kinematics condition is discarded, it can be assumed that each cylinder has the same helix pitch h. This erroneous assumption implies that equation (E.13) does not need to be solved. In this case, $\gamma_i = -\tilde{\Gamma}_i/h$ and the induced velocity between two cylinders given by equation (E.14) is:

$$u_z(r_{i-1} < r < r_i) = \sum_{j=i}^{n} \frac{\gamma_j}{2} = -\frac{\Gamma_i}{2h} \tag{E.29}$$

The independence of the axially induced velocities between the stream-tubes is also verified in this case. Nevertheless, the comparison of equation (E.29) and equation (E.27) shows surprising analogies between the two different approaches.

E.5 System closure for finite tip-speed ratio

Similar to section E.2, the total system is closed if the convection velocity of each cylinder is consistent with the definition of the different vortex cylinder strengths. The convection velocity of the cylinder i is defined as in equation (E.2) using the average velocity from both sides of the cylinder (see figure E.1c),

$$V_{\psi,i} = -\frac{\Gamma_i + \Gamma_{i+1}}{4\pi R_i}, \quad V_{z,i} = U_0\left(b_i + \frac{\overline{\gamma}_i}{2}\right), \qquad \text{with} \quad b_i \equiv 1 + \sum_{j=i+1}^{n} \overline{\gamma}_j, \quad b_n \equiv 1 \tag{E.30}$$

Similar to equation (E.3), the pitch associated with the cylinder i is:

$$h_i = \Delta t \cdot V_{z,i} = \frac{2\pi U_0}{\Omega\left(1+a'_{c,i}\right)}\left(b_i + \frac{\overline{\gamma}_i}{2}\right), \qquad a'_{c,i} \equiv \frac{\Gamma_i + \Gamma_{i+1}}{4\pi\Omega R_i^2}, \qquad a'_{c,n} \equiv \frac{\Gamma_n}{4\pi\Omega R^2} \tag{E.31}$$

Writing $\gamma_i = -\tilde{\Gamma}_i/h_i$, and using the pitch equation from equation (E.31), leads to the following system:

$$\overline{\gamma}_i^2 + 2b_i\overline{\gamma}_i + (k_i - k_{i+1})(1+a'_{c,i}) = 0 \qquad \text{with:} \qquad k_i \equiv \frac{\Omega\Gamma_i}{\pi U_0^2}, \qquad k_{n+1} \equiv 0. \tag{E.32}$$

The system is readily solved as:

$$\overline{\gamma}_i = -b_i + \sqrt{b_i^2 - (k_i - k_{i+1})(1+a'_{c,i})}, \qquad \text{if } \; b_i^2 - (k_i - k_{i+1})(1+a'_{c,i}) > 0 \tag{E.33}$$

In the case of infinite tip-speed ratio ($a'_{c,i} = 0$), a simplification occurs such that the tangential vorticity i only depends on the properties at $i+1$ and the independence of the annuli thus holds. It is seen that γ_i depends on the properties of all the surrounding systems from i to n. As a result of this the annuli-independence assumed in ST and BEM analysis does not hold. In section E.6, an erroneous system closure will be presented for which the annuli-independence holds.

Rotor variables From equation (E.14), and the definition of b_i (equation (E.30)) it is seen that $b_i = 1 - 2a_{i+1}$. The axial induction from equation (E.14) can then be written using equation (E.33):

$$a_i = -\frac{1}{2}\left[\overline{\gamma}_i + b_i - 1\right] = \frac{1}{2}\left[1 - \sqrt{1 - C_{t,i}(R_i) + C_{t,i+1}(R_i) - 4a_{i+1}(1-a_{i+1})}\right], \tag{E.34}$$

with

$$C_{t,i}(r) \equiv k_i\left(1 + \frac{k_i}{4\lambda_r^2}\right) \tag{E.35}$$

The function $C_{t,i}$ is defined for $R_{i-1} \leq r \leq R_i$. Defining the term $C_i = 4a_i(1-a_i)$ and using the expression from equation (E.34) gives:

$$C_i = 4a_i(1-a_i) = C_{t,i}(R_i) - C_{t,i+1}(R_i) + 4a_{i+1}(1-a_{i+1}) \tag{E.36}$$

Inserting C_i back into a_i gives:

$$a_i = \frac{1}{2} - \frac{1}{2}\sqrt{1 - C_{t,i}(R_i) + \left(\frac{k_{i+1}}{2}\right)^2\left[\frac{1}{\lambda_{R_i}^2} - \frac{1}{\lambda_{R_{i+1}}^2}\right] + C_{t,i+2}(R_i+1) - C_{i+2}}, \tag{E.37}$$

Using a proof by induction initialized for $i = n$ with the results of section E.2, it is shown that:

$$a_i = \frac{1}{2} - \frac{1}{2}\sqrt{1 - C_{t,i}(R_i) + C_{t,\mathrm{rot},i}} \;\; \text{with} \;\; C_{t,\mathrm{rot},i} = \sum_{j>=i+1}\left(\frac{k_j}{2}\right)^2\left[\frac{1}{\lambda_{R_{j-1}}^2} - \frac{1}{\lambda_{R_j}^2}\right] \tag{E.38}$$

From the result of the elementary system, the term $C_{t,\mathrm{rot},i}$ can be interpreted as the thrust coefficient of the force exerted on the disk by the wake rotation of the surrounding cylinders. Equation (E.38) can also be rewritten as:

$$C_{t,i}(R_i) = 4a_i(1-a_i) + C_{t,\mathrm{rot},i} \tag{E.39}$$

With equation (E.14) and equation (E.38), a'_i and a_i are known for a given distribution of k_i, and the thrust and power coefficients over the entire radius can be determined according to the KJ relation from equation (C.2):

$$C_{t,\mathrm{KJ}}(R_{i-1} < r < R_i) = k_i\left(1 + \frac{k_i}{4\lambda_r^2}\right), \quad C_{p,\mathrm{KJ}}(R_{i-1} < r < R_i) = k_i\left(1 - a_i\right) \tag{E.40}$$

A numerical implementation of the superposition of cylinders can easily be implemented using the above formulae.

E.6 Superposition of cylindrical vortex systems with wrong closure

Assuming that the variation in tangential inductions between two neighboring cylinders are small, equation (E.32) can be approximated as

$$\overline{\gamma}_i^2 + 2b_i\overline{\gamma}_i + C_i - C_{i+1} = 0 \qquad \text{with:} \qquad C_i \equiv k_i(1 + a'_{c,i}) \tag{E.41}$$

The system is similar to the one found for the case of infinite tip-speed ratio [23], but is obviously erroneous in the finite tip-speed ratio case. The resolution of the system using a proof by induction leads to:

$$\overline{\gamma}_i = -\sqrt{1 - C_{i+1}} + \sqrt{1 - C_i}, \qquad b_i = \sqrt{1 - C_{i+1}}, \qquad a_i(r) = -\sum_{j=i}^{n} \frac{\gamma_j}{2U_0} = \frac{1}{2}\left(1 - \sqrt{1 - C_i}\right) \tag{E.42}$$

It is shown in [26], that this system is similar to a BEM formulation. Indeed this system reveals the annuli independence which is assumed in ST analysis and can be exactly proven for the case of infinite tip-speed ratio [23].

$$aU_0 = -\frac{\Gamma_i}{2\hat{h}_i} \equiv \frac{\hat{\gamma}_i}{2} \equiv \hat{u}_{z,i} \tag{E.43}$$

$$a'(r) = -\sum_{j=1}^{n} \frac{\tilde{\Gamma}_j}{4\pi r} = -\frac{\Gamma_i}{4\pi r} \equiv \hat{u}_{\psi,i}(r) \tag{E.44}$$

where a and a' are dimensionless variables referred to as the axial and tangential coefficients respectively, and the hat-notation will be clarified in the following section.

E.7 Algorithm for system closure

The determination of the helical pitch of the superposition of vortex system requires a computation from the outer system to the inner one. The calculation is not iterative but purely incremental. The steps of the calculation are detailed below.

1. For $i = 1..n$ compute $a'_{c,i}$ from equation (E.31), $k_{c,i}$ from equation (E.32), and $C_{t,i}$ from equation (E.34):

$$a'_{c,i} = \frac{\Gamma_i + \Gamma_{i+1}}{4\pi\Omega R_i^2}, \quad a'_{c,n} = \frac{\Gamma_n}{4\pi\Omega R^2} \qquad k_i = \frac{\Gamma_i\Omega}{\pi U_0^2}, \quad C_{t,i} = k_i\left(1 + \frac{k_i}{4\lambda_{R_i}^2}\right)$$

2. Loop from the outer to the inner control points, $i = n..1$ to determine the intensities $\gamma_{t,i}$.

   - If $i = n$ the following initialization is required(from equation (E.30)):

$$b_n = 1, \quad \Delta C_{t,\mathrm{rot},n} = 0, \quad C_{t,\mathrm{rot},n} = 0 \tag{E.45}$$

   Otherwise for control points $i < n$:

$$b_i = 1 + \sum_{j=i+1}^{n} \overline{\gamma}_j \tag{E.46}$$

$$\Delta C_{t,\mathrm{rot},i+1} = \left(\frac{k_{i+1}}{2}\right)^2 \left[\frac{1}{\lambda_{R_i}^2} - \frac{1}{\lambda_{R_{i+1}}^2}\right] \tag{E.47}$$

$$C_{t,\mathrm{rot},n} = \sum_{j=i+1}^{n} \Delta C_{t,\mathrm{rot},j} \tag{E.48}$$

- The effective thrust coefficient is then computed:
$$C_{t,\text{eff},i} = C_{t,i} - C_{t,\text{rot},i} \tag{E.49}$$
- If $C_{t,\text{eff},i} > 4a_c(1-a_c)$, with $a_c \approx 0.34$, then apply Spera's high-thrust correction:
$$\overline{\gamma}_{t,i} = -b_i + 1 - 2\left[\frac{C_{t,\text{eff},i} - 4a_c^2}{4(1-2a_c)}\right] \tag{E.50}$$
Otherwise, use the solution from equation (E.33):
$$\overline{\gamma}_{t,i} = -b_i + \sqrt{b_i^2 - (k_i - k_{i+1})(1 + a'_{c,i})} \tag{E.51}$$

3. The values of γ_t being known, the convection velocities and the pitch can be computed for all i using equation (E.30) and equation (E.31):
$$V_{c,i} = U_0\left(b_i + \frac{\overline{\gamma}_{t,i}}{2}\right), \qquad h_i = \frac{2\pi}{\Omega(1+a'_{c,i})}V_{c,i} \tag{E.52}$$

Steps 1 and 3 can also be incorporated within the loop from $i = n..1$. They were isolated because they can be easily vectorized unlike the relations within the loop of Step 2.

Appendix F

Application of the helical and cylindrical models - comparison with Actuator disk

F.1 Cylindrical model with wake rotation

One rotor The superposition of cylindrical models with wake rotation introduced in Chapter 2 is here compared to Actuator disk simulations. The simulations results were extracted from the work of Madsen et al. [123]. A given thrust distribution along the span is prescribed for the AD simulations. The thrust is equal to 0.95 along most of the span and drops linearly to zero towards the root at $r/R = 0.11$ to avoid the singularity of the tangential induction. The prescribed thrust coefficients $C_{t,\mathrm{AD}}$ is shown in figure F.1a. The tip-speed ratio is $\lambda = 6$.
For the system of cylinders with a prescribed loading, the variable $k(r)$ can be determined either from the thrust relation equation (2.7) or the torque relation equation (2.9). The latter case is not as direct since it requires the axial induction, which in turn requires the thrust coefficient. Results using both approaches are shown in figure F.1b. A number of 150 cylinders along the span were used. The velocities at the disk obtained from the AD simulations and the superposition of vortex

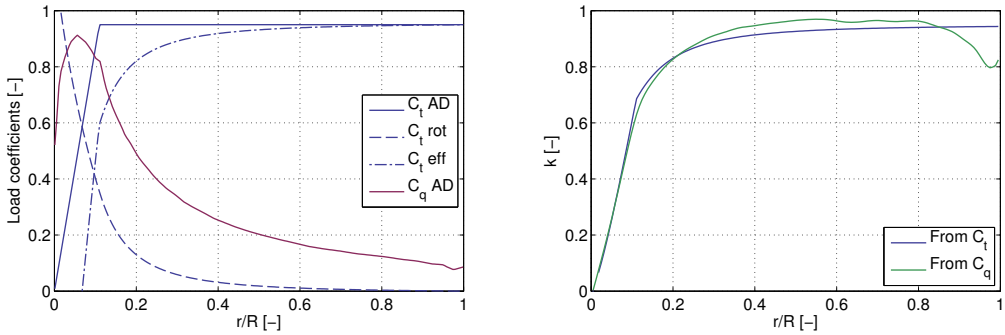

(a) (b)

Figure F.1: (a): Thrust and torque coefficients along the span. The thrust coefficient is presribed for the AD simulation and the vortex cylinder model. The thrust from wake rotation and the effective thrust coefficient as obtained from the cylindrical model are also plotted on the figure. (b): Factor k in the superposition of cylinders as obtained from C_t and C_q

cylinders (here labelled KJ) are compared to the one obtained using an "annuli-independent" Stream Tube (ST) theory. Results for the axial and tangential velocities are shown in figure F.2. Results from the cylindrical model are obtained using closed form analytical formulae. The agreement between the AD and the cylindrical model is strong for most of the rotor span. Differences of axial induction at the tip are observed most likely due to the wake expansion that is present in the AD

simulations but not accounted for by the cylindrical model. The plots show the importance of including the dependence between the different annuli, in particular, close to the root.

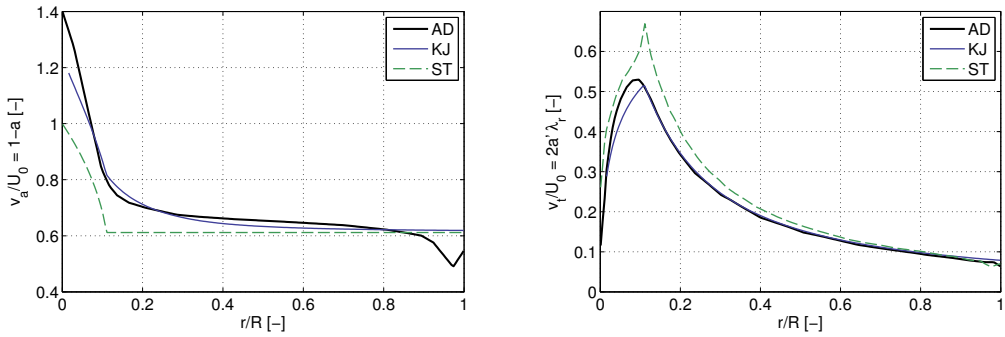

(a) (b)

Figure F.2: Comparison of axial and tangential inductions as obtained by Actuator Disk (AD) simulations, the cylindrical wake model (KJ) and annuli-independent Stream-tube Theory (ST).

Several rotors In the previous paragraph, a rotor was modelled using a superposition of concentric cylindrical wake models. The method is here applied to 5 different rotors to show the possibility to study the velocity upstream of a column of turbines using the model. The absence of wake expansion in the model will affect the velocity field downstream of the rotors, but it is expected that reasonable agreement with actuator disk simulations will be obtained upstream of the rotor. Results as obtained by the cylindrical model with and without wake rotations are shown in figure F.3. These results will be compared to AD simulations in the near future. The velocity field is obtained directly using the closed form formulae of vortex cylinders.

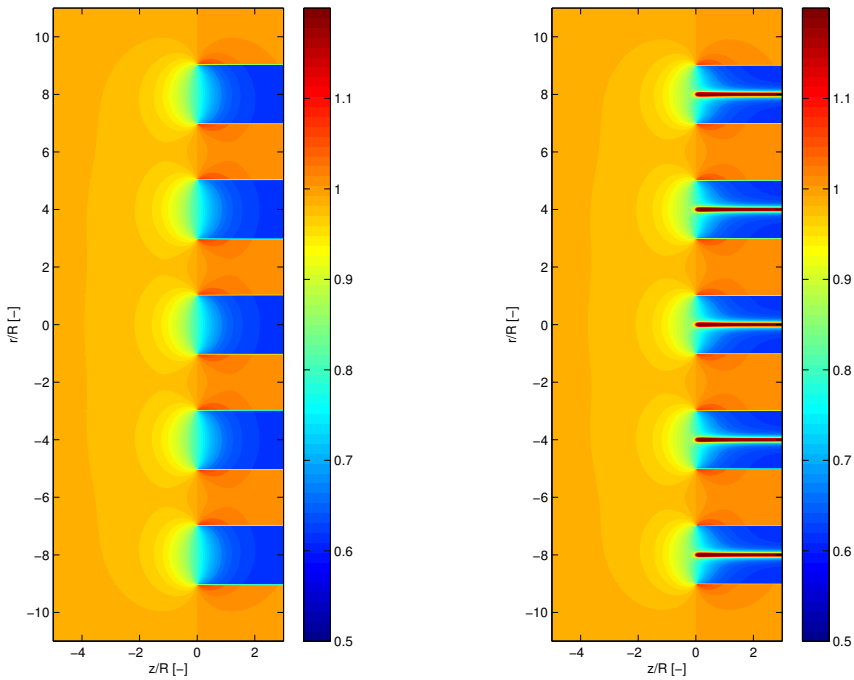

(a) (b)

Figure F.3: Velocity field as induced by five rotors without (a) and with (b) wake rotation using the cylindrical wake model (31 cylinders per rotor). All rotors have the same constant prescribed loading but for the case (b) the loading drops linearly to zero. The velocity field is obtained directly using the closed form formulae of a vortex cylinder. $\lambda = 6$, $C_T = 0.64$.

F.2 Helical model

Introduction In this section, the formulae for semi-infinite helical filaments are applied to model a wind turbine with straight lifting lines of constant circulation. By increasing the number of blades or the tip-speed ratios, the results are expected to converge towards a vortex cylinder model similar to an actuator disk. This approach as been used to validate either the vortex cylinder formulae or the helical filaments formulae. Results can also be compared to analytical and numerical actuator disk results.

Note on the helical model instability In the work of Okulov and Sørensen [151] the stability of helical vortex systems is studied. It is shown that the far wake described by the helical model of Joukowski is unconditionally unstable for all pitch values.

Problem definition For increasing number of blades and tip-speed ratio the following parameters can be used for the helices (neglecting the effect of the tangential induction)

$$\Gamma = \frac{C_T \pi R U_0}{B\lambda}, \qquad h = \frac{\pi R}{\lambda}\left[1 + \sqrt{1 - C_T}\right] \tag{F.1}$$

It is to be noted that no core model was used for the helices, and thus high induction are found in the vicinity of the helices. The linearized actuator disk results from the PhD thesis of Madsen (Madsen 1988, see also Madsen et al. [123, 122]) are used for comparison. They are given as:

$$\frac{v_r}{U_0} = \frac{\Delta p}{4\pi} \ln\left(\frac{z^2 + (r+1)^2}{z^2 + (r-1)^2}\right) \tag{F.2}$$

$$\frac{v_z}{U_0} = 1 - \frac{\Delta p}{2\pi}\left(\operatorname{atan}\frac{1-r}{z} + \operatorname{atan}\frac{1+r}{z}\right) - \Delta p \delta_{z>0} \tag{F.3}$$

and at the rotor, with $A = 2.24$, $z_0 = 0.04$:

$$\frac{v_r}{U_0} = \frac{C_T}{4\pi A} \ln\left(\frac{z_0^2 + (r+1)^2}{z_0^2 + (r-1)^2}\right) \tag{F.4}$$

$$\frac{v_z}{U_0} = 1 - \frac{C_T}{2\pi A}\left(\operatorname{atan}\frac{1-r}{z_0} + \operatorname{atan}\frac{1+r}{z_0}\right) \tag{F.5}$$

F.2.1 Influence of number of blades

Number of blades (helices) from 1 to 10 are used in this study. The axial induction is illustrated in figure F.4, the radial induction in figure F.5 and the tangential induction in figure F.6 and figure F.7.

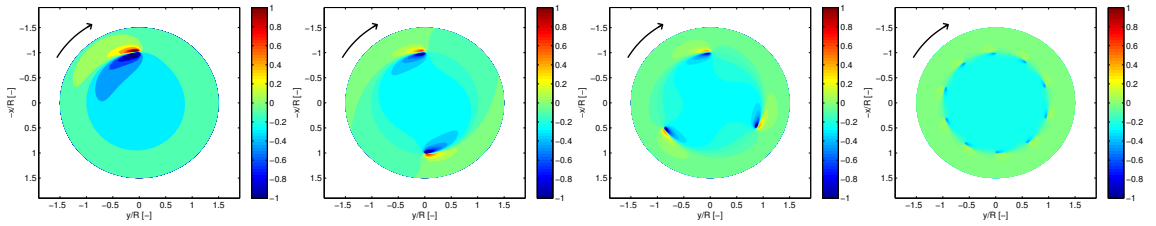

(a) (b) (c) (d)

Figure F.4: Axial induction for various number of blades (B={1,2,3,10}). Convergence towards a constant axial induction..

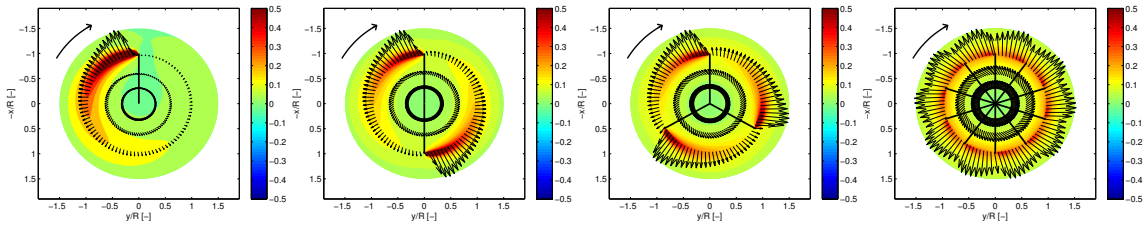

(a) (b) (c) (d)

Figure F.5: Velocity in the rotor plane for various number of blades ($B = \{1, 2, 3, 10\}$) and contour of the radial velocity.

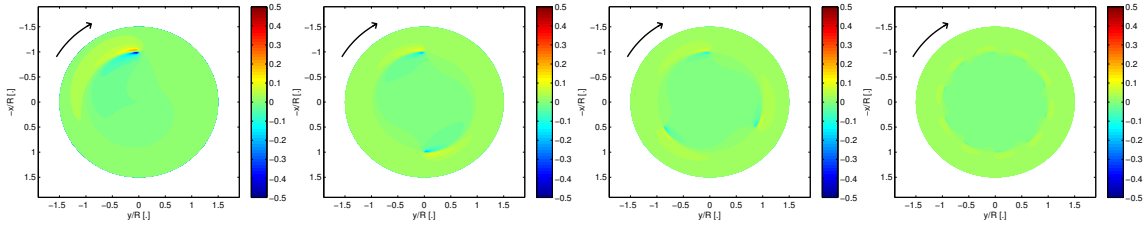

(a) (b) (c) (d)

Figure F.6: Tangential velocity for various number of blades - Influence of tip vorticity only. Results tending to 0 inside of the rotor disk as B increases. The tangential tends to a be proportional to $1/r$ outside of the rotor disk..

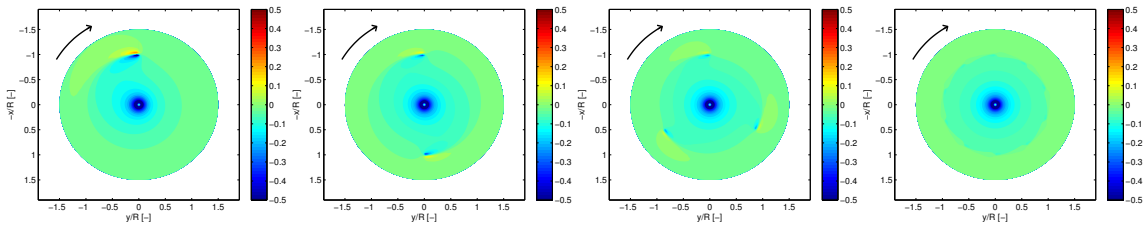

(a) (b) (c) (d)

Figure F.7: Tangential velocity for various number of blades - Influence of tip vorticity and root vortex. Results tending to zero outside of the rotor disk as B increases. A $1/r$ behavior inside the disk is observed (though desingularized at the root)..

F.2.2 Sensitivity to lambda

Overview of the velocity field at the rotor plane The velocity field in the rotor plane for a three bladed rotor and different tip-speed ratio is shown in figure F.8, figure F.10 and figure F.9 for the axial, tangential and radial induction.

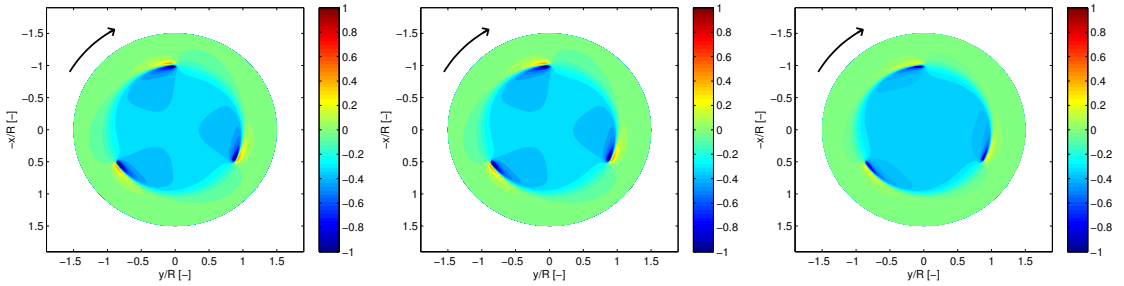

(a) $\lambda = 6$ (b) $\lambda = 10$ (c) $\lambda = 60$

Figure F.8: Axial velocity - Convergence towards a constant axial induction.

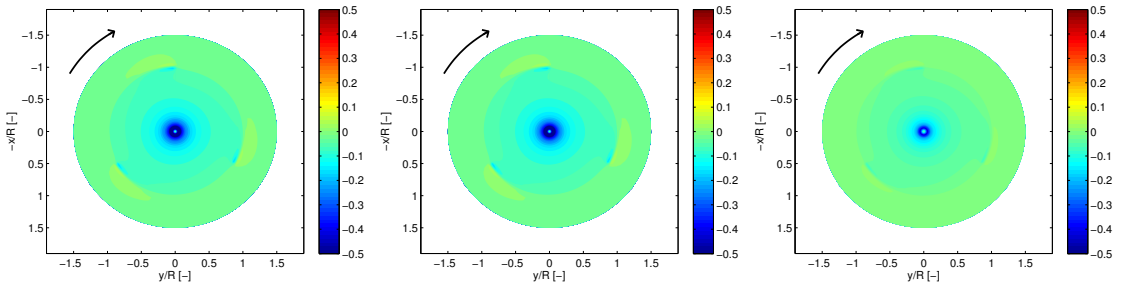

(a) $\lambda = 6$ (b) $\lambda = 10$ (c) $\lambda = 60$

Figure F.9: Tangential velocity (including root vortex) Convergence to 0 outside the rotor disk and $1/r$ behavior inside..

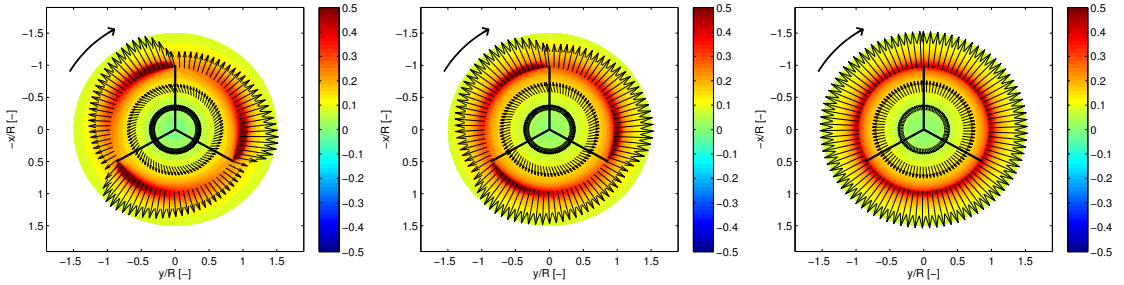

(a) $\lambda = 6$ (b) $\lambda = 10$ (c) $\lambda = 60$

Figure F.10: Radial velocity and in plane flow direction. The tangential induction tends to be negligible and the radial flow becomes axi-symmetric as the λ increases..

Variable on the lifting line The evolution of the axial, radial and tangential induction on the lifting line is shown in figure F.11.

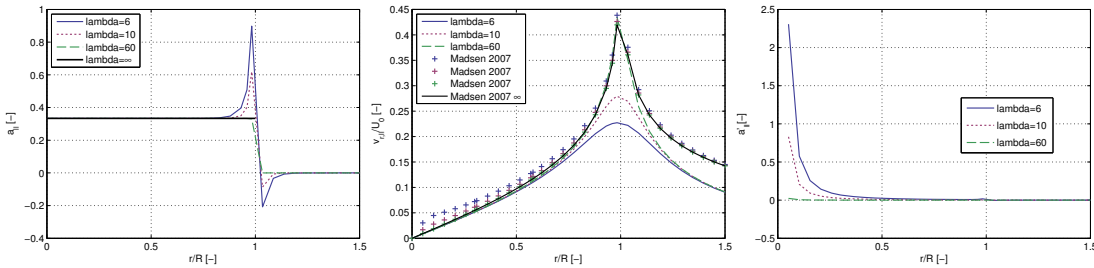

Figure F.11: Axial(a) - radial (b) and tangential (c) inductions on the lifting line.

F.2.3 Comparison to actuator disk results

The comparison between a rotor with $B = 100$ modeled with rigid helices of constant intensities and AD analytical and numerical results is shown in figure F.12. The simulation setup is similar to the one found in Madsen 1995 [125], upstream of the rotor at $x = 0.5R$.

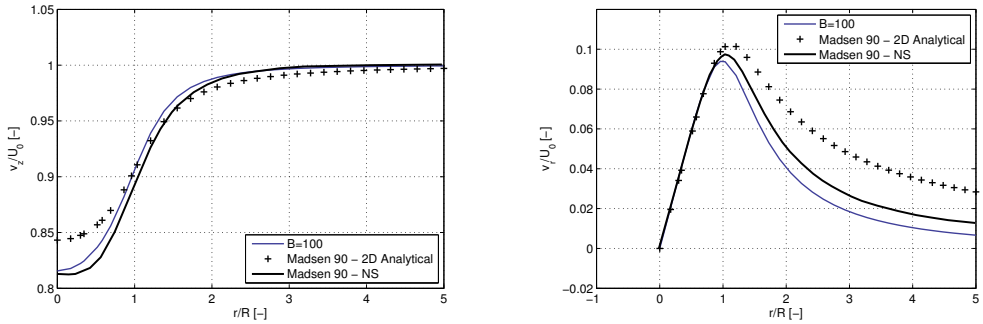

(a) (b)

Figure F.12: Axial (a) and radial (b) inductions upstream of an actuator disk using 100 helices, or AD numerical (NS) and linearized results (2D analytical).

The dissertation was submitted to the Technical University of Denmark, in partial fulfilment of the requirements for the obtainment of the PhD degree from the PhD School DTU Wind Energy. The PhD project was carried out between the 1 st of April 2012 and the 31st of March 2015 at the Aeroelastic Design Section of DTU Wind Energy, Department of Wind Energy (formerly Risø DTU, Wind Energy Department). The dissertation was submitted on the 1st of April 2015, and successfully defended on the 8th of June 2015.

Author: Emmanuel Branlard
Main Supervisor: Mac Gaunaa, DTU Wind Energy

DTU Wind Energy
Technical University of Denmark

Risø Campus 118
Frederikborgvej 399
DK-4000 Roskilde
Tlf. 45 25 25 25

www.vindenergi.dtu.dk
ISBN 978-87-93278-44-8